Sensorless Control of AC Machines for Low and Zero Speed Operation without Additional Test Signal Injection

by

Reiko Raute

Thesis submitted to the University of Nottingham
for the degree of Doctor of Philosophy, October 2009

To my parents, my girlfriend Marija Attard and her supportive family.

Acknowledgement

This research has been possible due to the financial support provided by the European Commission under a Marie Curie Research Training Network under the MEST-CT-2004-504243 Research Project. I am grateful for the given opportunity.

I would like to express my sincere gratitude to my supervisors Dr. Cedric Caruana, Dr. Cyril Spiteri Staines and Dr. Joseph Cilia at the University of Malta, and Dr. Mark Sumner and Prof. Greg Asher from the University of Nottingham. I am thankful for their guidance, support and constructive help during my work.

Further thanks for the support provided during the development stage of this study by the technical staff in the Department of Industrial Electrical Power Conversion at the University of Malta.

Contents

List of Figures

List of Tables

Abstract

This work considers the sensorless control of AC machines for the low and zero speed operation range. Two novel techniques have been developed that use the inherit nature of the inverter PWM to estimate the rotor position of the machine.

The inherent back EMF and the saliency of AC machines can be utilized to identify the rotor/flux position. The zero vector current derivative (ZVCD) technique for permanent magnet synchronous machines (PMSM) utilizes both of these effects. No additional test signals are injected into the machine and the difficulty in sensing the machine terminal voltage at low speed is eased. Only three standard current transducers are used in the drive system. For the position/ speed estimator only the machine current derivative during the relatively long (at low speed) zero voltage vectors is used for obtaining the rotor position. Practical results show the operation of the drive at several torque and speed conditions including stand still.

A further method has been developed for the sensorless control of induction machines. The high frequency harmonics present in a PWM inverter drive system can be used to detect an equivalent impendence saliency that shows modulation due to rotor/ flux position saliency. The proposed method focuses particularly on the extraction of spatial saliency modulation due to rotor bar slotting effect, which can

be used to determine the mechanical rotor position. No additional signal injection is required; the method simply employs some of the inherent PWM carrier harmonics.

Chapter 1
Introduction

1.1 Background

With vector controlled AC drives the torque can be controlled with a dynamic similar to DC drives [1]. The main requirement is that the rotor flux position is known and this creates the principle of field oriented control. In permanent magnet synchronous machines the rotor flux is directly related to the position of the permanent magnets and thus the rotor position. Therefore the rotor position has to be known for the field orientated control. In induction machines the rotor flux position can be detected with dedicated flux sensors inside the machine (direct rotor flux orientation) or derived from the measured machine currents and the rotor speed/ position (indirect rotor flux orientation). The principle of direct flux orientation did not find a wide application in practical drives, since incorporated flux sensors inside the machine are fragile and not appreciated by industry. Indirect rotor flux oriented (IRFO) is nowadays implemented in almost all dynamic induction motor drives. For IRFO vector control a rotor position or speed signal also needs to be provided. Additional sensors attached to the machine are not appreciated due to their additional wiring and costs. Furthermore the machines are often located in very rough industrial conditions. While the machine itself is very robust the speed/ position measurement sensors are rather fragile.

The term sensorless control means that the target is to operate the machine without the need of additional sensors attached to the machine. Therefore the machine flux,

rotor speed or position are not directly measured on the machine. The idea is to derive the rotor or rotor flux position directly from electrical measurements inside the drive.

Sensorless control of AC machines has been a challenging task for the last decades [2]. Many techniques have been developed that use the back EMF information of the machine. Several model based methods have been proposed and good results for medium and high speed application have been presented. However at very low and zero speed the back EMF amplitude is small and can not be detected accurately for a reliable position estimation. Errors in the current and voltage measurement decrease the signal to noise ratio and are significant at very low speeds. Furthermore the parameter dependency of the used machine model reduces the estimation quality at low speeds.

Therefore in recent years the magnetic saliency of the machines has attracted the attention of researchers [3], [4]. The magnetic saliency is a consequence of the mechanical design of the machine and/ or magnetic saturation inside the machine [5], [6]. The position of the detected magnetic saliency gives information of the rotor/ rotor flux position. The magnetic saliency affects the machine stator inductances. Therefore the focus is to detect the stator windings inductance variation. To detect the inductance an AC excitation signal is required. Many sensorless techniques have been reported that measure the stator inductances by injecting a sinusoidal high frequency signals or by pulse signal excitation. Thus extra test signals are continuously injected into the machine. These injected test signals are superimposed onto the fundamental voltages and currents and have a significant magnitude. Therefore parasitic machine interference can be observed. The effects are current/ torque ripple and increased electromagnetic noise. The biggest disadvantage is however strong audible noise that makes signal injection schemes unsuitable for many applications.

1.2 Objectives and Scope

The variable voltage in AC drives is generated by inverters that are controlled using pulse width modulation (PWM). Therefore the fundamental machine voltages are produced by the modulation of a high frequency carrier signal. Even if only the fundamental voltages and currents are needed for normal machine operation, the effects of the PWM carrier signal are still present in all drives.
The idea in this work is to investigate the high frequency signals available inherently due to the PWM and make use of them to detect the stator winding inductance saliency. The purpose is therefore to avoid any additional signal injection inside the machine, but estimate the machine saliency information by only applying some signal processing to the measured stator currents and voltages.

1.3 Structure of the Thesis

The thesis is structured in the following chapters:

Chapter 2 reviews the basics of three phase AC machines. The fundamental operation is explained and the principle of field orientation is introduced. A brief introduction to space vector theory that is widely used in this thesis is given. The Park and Clark transformation equations that are further used in this thesis are also given.

Chapter 3 summarises sensorless techniques presented over the last years by several researchers. Model based and non model based techniques are considered. Principles of high frequency and test pulse injection schemes are reviewed.

Chapter 4 describes the experimental setup used. In particular, the functionality of the designed FPGA control board is explained. The parameters of the test machines used are given.

Chapter 5 presents the zero vector current derivative method for sensorless control of permanent magnet synchronous machines. The method measures the stator current vector derivative during the zero vectors from two discrete current samples. During the zero vectors the inverter shorts the machine terminals and the current decay during this instance is affected by the back EMF and the saliency of the machine. Both effects are superimposed and give a common position estimation signal. A tracking scheme is implemented to track the mechanical rotor position. The method works down to zero speed in motoring operation. However in the regenerative operation quadrants a small operation range exists where no stable steady operation is possible. Results are shown for sensorless torque and speed control.

Chapter 6 presents a technique that utilises the harmonics created by the fundamental PWM voltage generation. The second PWM harmonic is used to measure a stator equivalent impedance that shows machine saliency modulation. The saliency modulation caused by the rotor bar slotting in induction machines is used for the mechanical position tracking. The rotor bar modulation is only approximately 1 % of the average impedance. However, with a PLL tracking scheme the rotor movement can be clear reconstructed. To decouple the very small rotor modulation from a large impedance offset and further modulation effects an extensive compensation look up table is used. Results of the sensorless induction motor drive operating in torque, speed and position control are shown.

Chapter 7 discusses the final conclusions of the Thesis and suggests further work.

Chapter 2
AC Machines and Their Control

2.1 General Model of Three Phase AC Machines

Figure 2.1 (a) shows a cross section of a principal model of a three phase AC machine with one pole pair. Three phase AC machines have three stator coils placed 120 electrical degrees apart from each other around the stator. In Figure 2.1 (a) the stator coils are only symbolized by one turn. The captions A, B and C indicate the input of the phase currents and the captions A', B' and C' indicate the output of the phase winding turns. In sinusoidal machines, the winding distributions of the stator coils are ideally sinusoidal over stator circumference. The rotor design of AC machines differs for different designs. In this work only permanent magnet synchronous machines (PMSM) and induction machines (IM) are considered. In permanent magnet synchronous machines the rotor is equipped with permanent magnets and in induction machines the rotor consist of a short circuit conductor cage. For the principal explanation of AC machines it is important that the rotor is penetrated by the rotor flux ϕ_R, also indicated in Figure 2.1 (a). The rotor flux distribution is ideally also sinusoidal. The rotor flux will also penetrate through the air gap the stator iron and rotate during the operation of the machine. The imposed AC currents in the stator coils are directly controlled in dependency of the rotor flux position. The scheme of rotor flux orientation is explained later in section 2.3.

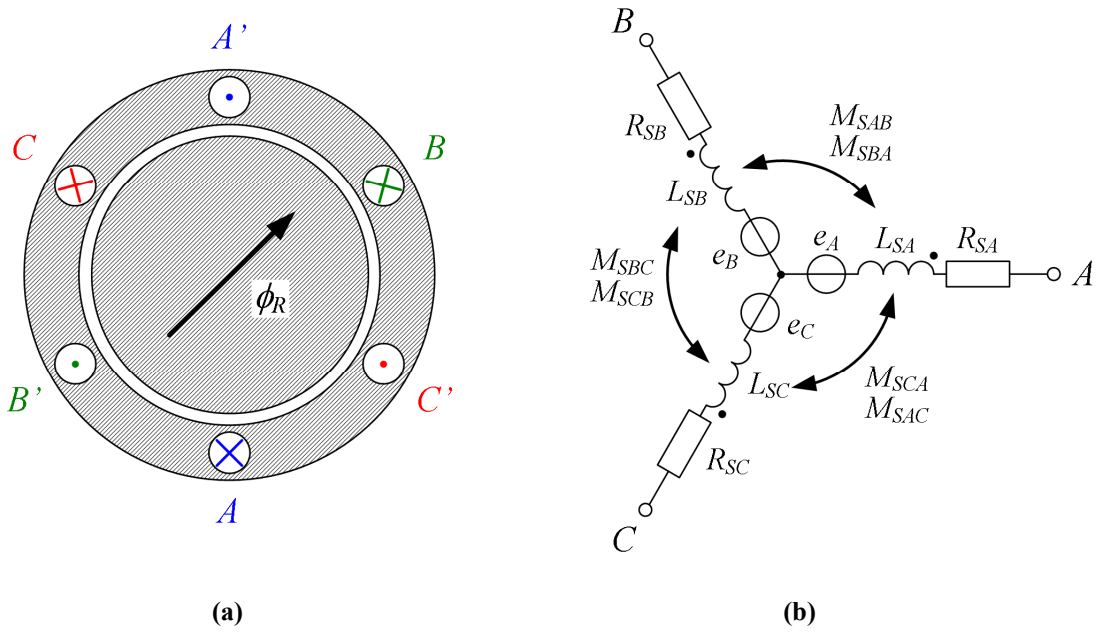

Figure 2.1: Principal model of three phase AC machine

Figure 2.1 (b) shows the star connection electrical equivalent circuit for the description of the electromagnetic machine. Each stator phase branch is represented by an ohmic resistor R_S, an inductance L_S and a voltage source e. The voltage source e represents the back EMF component induced in the stator coils by the rotor flux linkage variation. Equation (2.2) and (2.3) give the mathematical derivation of the back EMF value induced in the stator windings by the rotating rotor flux ϕ_R. L_{S0} is the stator inductance part that is coupled to the air gap. The stator coils are also magnetically coupled to each other indicated by the mutual inductances M_S. The resulting voltage equation system of the equivalent circuit shown in Figure 2.1 (b) is given by equation (2.1) [7]. In equation (2.1) v_S is the stator phase voltage and i_S is the stator phase winding current.

$$\begin{bmatrix} v_{SA} \\ v_{SB} \\ v_{SC} \end{bmatrix} = \begin{bmatrix} R_{SA} & 0 & 0 \\ 0 & R_{SB} & 0 \\ 0 & 0 & R_{SC} \end{bmatrix} \cdot \begin{bmatrix} i_{SA} \\ i_{SB} \\ i_{SC} \end{bmatrix} + \begin{bmatrix} L_{SA} & M_{SAB} & M_{SAC} \\ M_{SBA} & L_{SB} & M_{SBC} \\ M_{SCA} & M_{SCB} & L_{SC} \end{bmatrix} \cdot \frac{d}{dt} \begin{bmatrix} i_{SA} \\ i_{SB} \\ i_{SC} \end{bmatrix} + \begin{bmatrix} e_A \\ e_B \\ e_C \end{bmatrix} \qquad (2.1)$$

$$e = \frac{d\psi_{SR}}{dt} \tag{2.2}$$

$$\psi_{SR} = L_{S0}\phi_R \tag{2.3}$$

In an ideal machine it can be assumed that the three phase winding resistances are equal and thus equation (2.4) is valid. Further the simplifications of equation (2.5) and (2.6) can be made for a non-salient machine, also referred as smooth air gap machine.

$$R_{SA} = R_{SB} = R_{SC} = R_S \tag{2.4}$$

$$L_{SA} = L_{SB} = L_{SC} = L_{S0} + L_{S\sigma} \tag{2.5}$$

$$M_{SAB} = M_{SAC} = M_{SBA} = M_{SBC} = M_{SCA} = M_{SCB} = M_S \tag{2.6}$$

In equation (2.5) L_{S0} is the inductance that is linked through the air gap and $L_{S\sigma}$ is the leakage inductance of each phase winding, not couple to any other magnetic field. The sum of the balanced three phase currents is zero as stated by equation (2.7). Thus a further simplification can be made and the winding self and mutual inductances can be combined to the stator winding equivalent inductance L_S' given in equation (2.8).

$$i_{SA} + i_{SB} + i_{SC} = 0 \tag{2.7}$$

$$L_S' = L_{S0} + L_{S\sigma} - M_S \tag{2.8}$$

If the three phase winding distribution in the stator is ideally sinusoidal and the three

phase coils are exactly 2/3π displaced from each other, the mutual inductance between all three phase windings is given by (2.9) [1].

$$M_S = L_{S0}\cos\left(\frac{2}{3}\pi\right) = -\frac{1}{2}L_{S0} \tag{2.9}$$

After substituting equation (2.9) into (2.8), the stator winding equivalent inductance L_S' expression reduces to:

$$L_S' = \frac{3}{2}L_{S0} + L_{S\sigma} \quad . \tag{2.10}$$

Integrating the steps shown by equation (2.5) to (2.10) into the motor voltage equation (2.1) yields the simplified machine stator voltage equation system:

$$\begin{bmatrix} v_{SA} \\ v_{SB} \\ v_{SC} \end{bmatrix} = \begin{bmatrix} R_S & 0 & 0 \\ 0 & R_S & 0 \\ 0 & 0 & R_S \end{bmatrix} \cdot \begin{bmatrix} i_{SA} \\ i_{SB} \\ i_{SC} \end{bmatrix} + \begin{bmatrix} L_S' & 0 & 0 \\ 0 & L_S' & 0 \\ 0 & 0 & L_S' \end{bmatrix} \cdot \frac{d}{dt}\begin{bmatrix} i_{SA} \\ i_{SB} \\ i_{SC} \end{bmatrix} + \frac{d}{dt}\begin{bmatrix} \psi_{SRA} \\ \psi_{SRB} \\ \psi_{SRC} \end{bmatrix} \quad . \tag{2.11}$$

The resulting three phase stator flux linkage by the rotor flux can be described by equation (2.12) to (2.14).

$$\psi_{SRA} = \psi_{SR}\cos(\theta) \tag{2.12}$$

$$\psi_{SRB} = \psi_{SR}\cos\left(\theta - \frac{2}{3}\pi\right) \tag{2.13}$$

$$\psi_{SRC} = \psi_{SR}\cos\left(\theta - \frac{4}{3}\pi\right) \tag{2.14}$$

The imposed stator currents can be also described as balanced set of three phase currents, shown by equation (2.15) to (2.18).

$$i_{SA} = i_S \cos(\varphi) \tag{2.15}$$

$$i_{SB} = i_S \cos\left(\varphi - \frac{2}{3}\pi\right) \tag{2.16}$$

$$i_{SC} = i_S \cos\left(\varphi - \frac{4}{3}\pi\right) \tag{2.17}$$

The resulting equation for the electrical torque produced by the machine is given by equation (2.18). The variable *pp* is the number of the machine pole pairs. It can be seen that the developed machine torque depends not only on the magnitude of the rotor flux linkage ψ_{SR} and the stator currents i_S, but also on the phase angle φ-θ between these two balanced three phase sets. This angle is also referred as torque angle [1]. It can be seen that with a given current amplitude imposed to the stator, the maximum torque can be achieved if the torque angle is set to π/2. This criteria is used in the concept of rotor flux field orientated control.

$$T_e = pp\frac{3}{2} I_S \psi_{SR} \sin(\varphi - \theta) \tag{2.18}$$

2.2 Introduction to Space Vector Theory

Space vector theory supports the mathematical modelling and description of the electrical and magnetic relationships in AC motor drives. With the aid of space vector theory the machine quantities can be described as vectors in space. For the ease of mathematical handling the representation of two dimensional vectors as complex numbers in the complex plane can be used. Then the real axis of the complex plane is defined to be aligned with the abscissa of the referred reference frame.

2.2.1 Stationary Reference Frame

Poly phase AC machines have several phase coils distributed over the stator. The direction of the resulting magnetic flux set up by the current through the phase coil defines the magnetic axis of the phase winding. Therefore each phase current produces a flux vector, pointing in the direction of the winding magnetic axis with length proportional to the current magnitude. The referring current vectors for each phase are also defined in the direction of the winding magnetic axis. The resulting electro magnetic effect in the machine arises by the superposition of all flux components and therefore all phase currents. The single phase current vectors can be combined to one common current vector. Since a balanced three phase system is considered, the resulting vector moves only in the two dimensional plane around the motor shaft. For the ease of handling, a rectangular two dimensional coordinate system with the α axis as abscises and β axis as ordinate is used for the space vector description in the stator fixed space. The α axis is aligned to the magnetic axis of the phase *A* stator winding as shown in Figure 2.2. The $\alpha\beta$ coordinate system is also referred as stationary reference frame, since it is fixed to the stator position and thus not rotating in space.

In a balanced set of three phase currents the resulting stator current vector can be expressed as:

$$\vec{i}_{SABC} = \begin{bmatrix} i_{SA} \\ i_{SB} \\ i_{SC} \end{bmatrix} = \begin{bmatrix} I_S \cos\left(\lambda_{dq} + \varphi\right) \\ I_S \cos\left(\lambda_{dq} - \frac{2}{3}\pi + \varphi\right) \\ I_S \cos\left(\lambda_{dq} - \frac{4}{3}\pi + \varphi\right) \end{bmatrix}, \tag{2.19}$$

where I_S is the amplitude of the sinusoidal phase currents, λ_{dq} is the angular position of a rotating reference frame *dq* and φ is the relative angle between the resulting

stator current vector and the rotating *dq* reference frame. The elements of the balanced set of three phase currents are not linear independent of each other, but all are a function of the two parameters - current amplitude I_S and phase angle ($\lambda_{dq} + \varphi$). The vector projection of the stator currents from the balanced three phase *ABC* system to the *αβ* reference frame is expressed by equation (2.20) which is also shown in Figure 2.2.

$$\vec{i}_{S\alpha\beta} = \begin{bmatrix} i_{S\alpha} \\ i_{S\beta} \end{bmatrix} = \frac{2}{3}\begin{bmatrix} 1 & \cos\left(\frac{2}{3}\pi\right) & \cos\left(\frac{4}{3}\pi\right) \\ 0 & \sin\left(\frac{2}{3}\pi\right) & \sin\left(\frac{4}{3}\pi\right) \end{bmatrix} \cdot \begin{bmatrix} i_{SA} \\ i_{SB} \\ i_{SC} \end{bmatrix} = \frac{2}{3}\mathbf{A} \cdot \vec{i}_{SABC} \quad (2.20)$$

This equation is known as forward Clarke transformation. The choice of the constant in the transformation equation is arbitrary. Here, the value of 2/3 is chosen to preserve the phase current amplitude across the transformation. Therefore, sinusoidal phase currents with amplitude I_S produce a current space vector with magnitude I_S respectively. Substituting (2.19) into (2.20) gives equation (2.21) and (2.22) as the description of the stator current components in the stationary *αβ* reference frame.

$$i_{S\alpha} = I_S \cos\left(\lambda_{dq} + \varphi\right) \quad (2.21)$$

$$i_{S\beta} = I_S \sin\left(\lambda_{dq} + \varphi\right) \quad (2.22)$$

The stator current space vector can be also referred as complex number:

$$\underline{i}_{S\alpha\beta} = i_{S\alpha} + j\, i_{S\beta} \quad . \quad (2.23)$$

The resulting complex stator current vector in the stationary reference frame can be also directly derived from the three phase current values by:

$$\underline{i}_{S\alpha\beta} = \frac{2}{3}\left(i_{SA} + i_{SB}\, e^{j\frac{2}{3}\pi} + i_{SC}\, e^{j\frac{4}{3}\pi} \right) . \tag{2.24}$$

Equation (2.25) shows the result of $\underline{i}_{S\alpha\beta}$ for the assumed balanced three phase currents given in equation (2.19), which describes a circular trajectory in the stationary space vector plane. Due to the scaling factor 2/3 used, the radius of the circle equals the amplitude of the phase currents.

$$\begin{aligned} \underline{i}_{S\alpha\beta} &= i_S \cos\left(\lambda_{dq} + \varphi\right) + j\, i_S \sin\left(\lambda_{dq} + \varphi\right) \\ &= i_S\, e^{j(\lambda_{dq} + \varphi)} \end{aligned} \tag{2.25}$$

Equation (2.26) shows the reverse Clarke transformation to regain the three phase currents from the $\alpha\beta$ current vector. It should be noted that the reverse Clark transformation shown is only valid for a balanced three phase system. That means that the common mode component is assumed to be zero.

$$\vec{i}_{SABC} = \begin{bmatrix} i_{SA} \\ i_{SB} \\ i_{SC} \end{bmatrix} = \begin{bmatrix} 1 & 0 \\ \cos\left(\frac{2}{3}\pi\right) & \sin\left(\frac{2}{3}\pi\right) \\ \cos\left(\frac{4}{3}\pi\right) & \sin\left(\frac{4}{3}\pi\right) \end{bmatrix} \cdot \begin{bmatrix} i_{S\alpha} \\ i_{S\beta} \end{bmatrix} = \mathbf{A}^T \cdot \vec{i}_{S\alpha\beta} \tag{2.26}$$

Figure 2.2 summarises the above explained vector relation ships. The original stator phase winding currents magnitudes i_{SA}, i_{SB} and i_{SC} are aligned to the phase winding axes *A*, *B* and *C*. The three phase stator current values are drawn in the directions of the three phase axes and their super position, resulting into the vector $\vec{i}_{SABC}$, is also shown in the figure. The forward Clarke transformation results in the current space vector $\vec{i}_{S\alpha\beta}$, which is in phase with the three phase stator current vector $\vec{i}_{SABC}$ but has

only two third of the $\vec{i}_{SABC}$ current vector magnitude. The resulting current components $i_{S\alpha}$ and $i_{S\beta}$ are also shown in the figure.

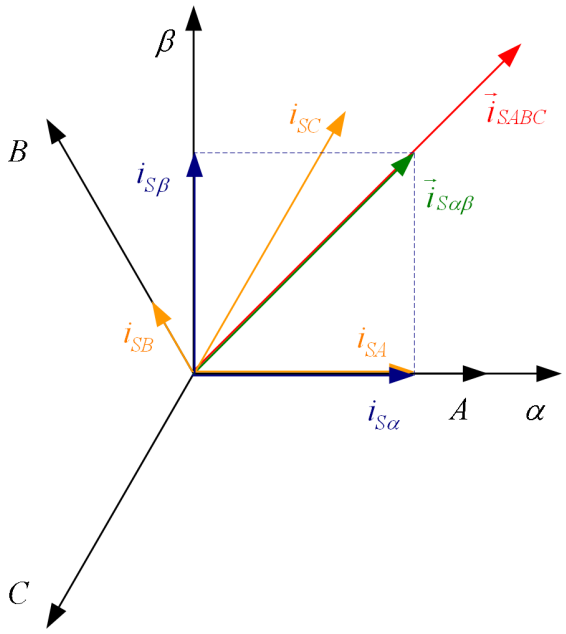

Figure 2.2: Relationship of stator current space vector and stator phase currents

The transformation between the three phase system and the stationary space vector reference system has been explained for the stator currents. However, the same space vector transformation is applicable to all other vector quantities in the machine.

The resistance and inductances in the stator voltage equation (2.1) are written as 3x3 matrixes. Therefore the impedances are not vector quantities but are described by tensors. Equation (2.27) shows the Clark transformation of the inductance tensor from the three phase ABC space to the two dimensional $\alpha\beta$ space. The same transformation applies to the resistance tensor. A unique back transformation of the $\alpha\beta$ tensor to the original ABC space is not possible as the common mode component has been omited from the two dimensional $\alpha\beta$ space.

$$\begin{bmatrix} L_{S\alpha} & M_{S\alpha\beta} \\ M_{S\beta\alpha} & L_{S\beta} \end{bmatrix} = \frac{2}{3}\mathbf{A}\cdot\begin{bmatrix} L_{SA} & M_{SAB} & M_{SAC} \\ M_{SBA} & L_{SB} & M_{SBC} \\ M_{SCA} & M_{SCB} & L_{SC} \end{bmatrix}\cdot\mathbf{A}^{T} \tag{2.27}$$

2.2.2 Rotating Reference Frame

For field orientated control it is desired to describe the motor states in the rotor flux position aligned *dq* reference frame. The position of the *d* axis is aligned to the rotor flux and therefore rotating with the rotor flux position λ_{dq} in the $\alpha\beta$ frame. For the stator current vector representation in the *dq* reference frame a further vector projection from the stationary $\alpha\beta$ frame to the rotating *dq* frame is applied:

$$\vec{i}_{Sdq} = \begin{bmatrix} i_{Sd} \\ i_{Sq} \end{bmatrix} = \begin{bmatrix} \cos(\lambda_{dq}) & \sin(\lambda_{dq}) \\ -\sin(\lambda_{dq}) & \cos(\lambda_{dq}) \end{bmatrix}\cdot\begin{bmatrix} i_{S\alpha} \\ i_{S\beta} \end{bmatrix} = \mathbf{B}\cdot\vec{i}_{S\alpha\beta} \quad . \tag{2.28}$$

This mathematical vector transformation can also be expressed with the complex operator:

$$\underline{i}_{Sdq} = i_{Sd} + j\,i_{Sq} = \underline{i}_{S\alpha\beta}\,e^{-j\lambda_{dq}} \quad . \tag{2.29}$$

Equation (2.28) and (2.29) imply mathematically a vector rotation by the angle $-\lambda_{dq}$. This vector rotation operation is also called Park transformation. For the back transformation of $\vec{i}_{Sdq}$ to $\vec{i}_{S\alpha\beta}$ equation (2.30) is used which is called the reverse Park transformation.

$$\vec{i}_{S\alpha\beta} = \begin{bmatrix} i_{S\alpha} \\ i_{S\beta} \end{bmatrix} = \begin{bmatrix} \cos(\lambda_{dq}) & -\sin(\lambda_{dq}) \\ \sin(\lambda_{dq}) & \cos(\lambda_{dq}) \end{bmatrix}\cdot\begin{bmatrix} i_{Sd} \\ i_{Sq} \end{bmatrix} = \mathbf{B}(\lambda_{dq})^{T}\cdot\vec{i}_{Sdq} \tag{2.30}$$

The Park back transformation for the complex number representation is:

$$\underline{i}_{S\alpha\beta} = \underline{i}_{Sdq}\, e^{j\lambda_{dq}} \quad . \tag{2.31}$$

The relationship between the vector description in the stationary and the rotating reference frame is shown in Figure 2.3. In the figure the stator current space vector in the stationary and rotating reference frame presentation is shown as a red arrow. This vector can be described by its i_α and i_β or i_d and i_q components, in reference to the $\alpha\beta$ or dq reference frame respectively.

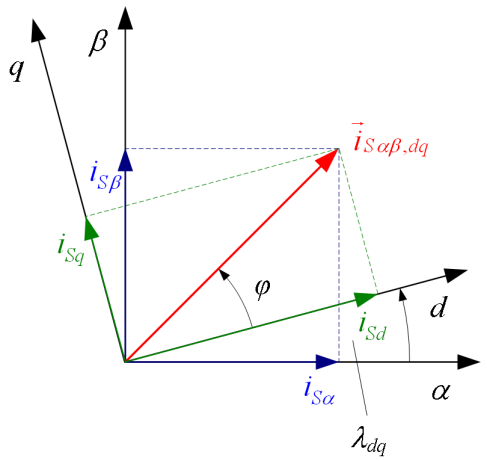

Figure 2.3: Relationship of current space vector components in stationary and rotating reference frames

If the vector rotation (2.29) is applied to the current space vector (2.25), derived for the balanced set of stator currents (2.19), the resulting current vector is given by:

$$\underline{i}_{Sdq} = I_S\, e^{j\varphi} \quad . \tag{2.32}$$

The d and q components of the resulting space vector in the rotating reference frame are then represented by equation (2.33) and (2.34).

$$i_{Sd} = I_S \cos(\varphi) \tag{2.33}$$

$$i_{Sq} = I_S \sin(\varphi) \tag{2.34}$$

The transformation from the stationary $\alpha\beta$ reference frame to the rotating dq reference frame has been explained for the stator current vector, but is also applicable for all other vector quantities in the machine.

The machine tensor quantities are also convertible into dq space. Equation (2.35) shows the forward Park transformation for the machine stator impedance tensor. As both vector spaces ($\alpha\beta$ and dq) have the same dimensions, the Park back transformation exists, given by equation(2.36). The same transformation can be also applied to the resistances of the machine.

$$\begin{bmatrix} L_{Sd} & M_{Sdq} \\ M_{Sqd} & L_{Sq} \end{bmatrix} = \mathbf{B} \cdot \begin{bmatrix} L_{S\alpha} & M_{S\alpha\beta} \\ M_{S\beta\alpha} & L_{S\beta} \end{bmatrix} \cdot \mathbf{B}^T \tag{2.35}$$

$$\begin{bmatrix} L_{S\alpha} & M_{S\alpha\beta} \\ M_{S\beta\alpha} & L_{S\beta} \end{bmatrix} = \mathbf{B}^T \cdot \begin{bmatrix} L_{Sd} & M_{Sdq} \\ M_{Sqd} & L_{Sq} \end{bmatrix} \cdot \mathbf{B} \tag{2.36}$$

2.3 Field Orientated Control of AC Machines

It was shown that the machine quantities can be described as two dimensional vectors that can be referred to different reference frames. In field orientated control the machine currents are controlled in a reference frame aligned to the machine excitation flux. According to the Lorentz force law the machine torque is then directly proportional to the current component orthogonal to the excitation flux. In DC machines the machine excitation flux is produced by the stator. Therefore the current control reference frame is fixed to the position of the stator. A torque

producing current is then imposed to the rotor windings orthogonal to the stator flux by the action of the mechanical commutator. In AC machines the excitation flux is rotating with the synchronous *dq* frame. For rotor flux orientation, which is used in this work, the *d* axis of the used synchronous reference frame is aligned to the position of the rotor flux. In rotor flux orientation, the rotor flux is assumed as machine excitation flux and the torque producing current vector is imposed into the stator windings in direction of the *q* axis, which is orthogonal to the *d* axis [8].

2.3.1 Control of Permanent Magnet Synchronous Machines

A permanent magnet synchronous machine (PMSM) has permanent magnets mounted on the rotor which produce the magnetic rotor flux $\underline{\phi}_R$. The air gap passing magnetic field of the rotor permanent magnets penetrates the stator and creates the flux linkage $\underline{\psi}_{SR}$ in the stator windings. No rotor currents are present in permanent magnet synchronous machines. The total flux linkage in the stator coils is the sum of the flux linkage caused by the stator windings self inductance and the rotor flux passing through the stator windings $\underline{\psi}_{SR}$:

$$\underline{\psi}_S = L_S \underline{i}_S + \underline{\psi}_{SR} \quad . \tag{2.37}$$

Equation (2.38) gives the PMSM stator voltage equation referred to an arbitrary reference frame rotating with ω_k. $\underline{v}_S$ and $\underline{i}_S$ are the complex stator voltage and current vectors. The parameters R_S and L_S are the stator winding resistance and equivalent inductance. Figure 2.4 shows the equivalent circuit [8].

$$\underline{v}_S = R_S \underline{i}_S + L_S \frac{d\underline{i}_S}{dt} + \frac{d\underline{\psi}_{SR}}{dt} + j\omega_k \underline{\psi}_S \tag{2.38}$$

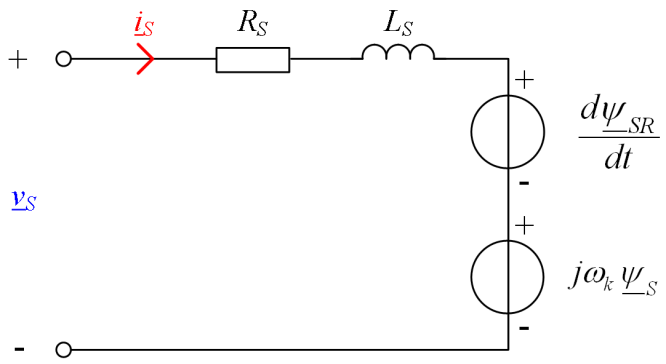

Figure 2.4: Equivalent circuit of a PMSM in arbitrary reference frame

The control of the stator currents is performed in the synchronous *dq* reference frame rotating with the rotor angular velocity ω_R. The *d* axis of the rotating reference frame is aligned to the rotor flux direction which is also the rotor position λ_R. Therefore under this condition $\psi_{SRd} = \psi_{SR}$ and $\psi_{SRq} = 0$. Equation (2.39) and (2.40) give the voltage equations for the *d* and *q* axis under rotor flux orientation and Figure 2.5 shows the equivalent circuit [8].

$$v_{Sd} = R_S\, i_{Sd} + L_S \frac{di_{Sd}}{dt} - \omega_R\, L_S\, i_{Sq} \tag{2.39}$$

$$v_{Sq} = R_S\, i_{Sq} + L_S \frac{di_{Sq}}{dt} + \omega_R\, L_S\, i_{Sd} + \omega_R\, \psi_{SR} \tag{2.40}$$

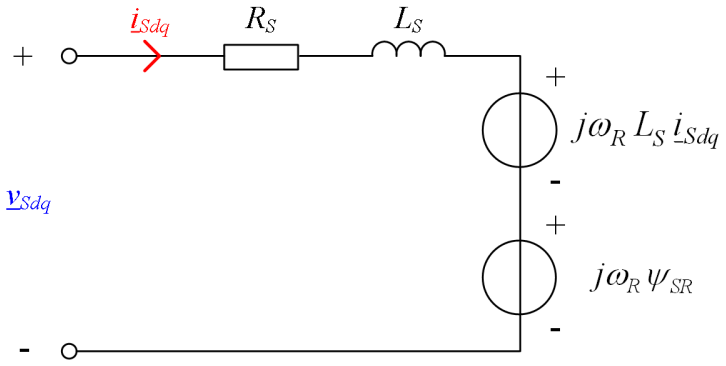

Figure 2.5: PMSM equivalent circuit in *dq* synchronous frame

In equation (2.39) and (2.40) the terms $\omega_R L_S i_{Sd}$ and $\omega_R L_S i_{Sq}$ describe the cross coupling between the *d* and *q* axis currents. The term $\omega_R \psi_{SR}$ describes the back EMF voltage induced into *q* direction.

If a stator current is introduced only into the *q* axis (therefore $i_{Sd} = 0$) the electromagnetic output torque of the machine can be calculated by:

$$T_e = pp\frac{3}{2}\psi_{SR}\, i_{Sq} \quad . \tag{2.41}$$

Equation (2.41) shows that the produced torque can be simply controlled directly by adjusting i_{Sq}. A current component into the machine *d* axis would affect the machine flux. This can be used for instance to weaken the excitation flux for high speed operation. However, since the relative air gap of permanent magnet synchronous machines is large the stator inductance L_S is small and a large current value is required to change the flux condition in the machine.

In practice equation (2.42) and (2.43) are used to calculate the machine's electromagnetic torque and back EMF. For simplicity the factors k_t (torque constant) and k_e (back EMF constant) are introduced which can be experimentally determined from the machine. Theoretical these constants should have the same value and be equal to the permanent magnet rotor flux linkage in the stator windings as given by equation (2.44).

$$T_e = pp\frac{3}{2}k_t\, i_{Sq} \tag{2.42}$$

$$e_q = k_e\, \omega_R \tag{2.43}$$

$$k_t = k_e = \psi_{SR} \tag{2.44}$$

Figure 2.6 shows the block diagram of the vector control system for a PMSM drive. As mentioned above, field weakening is not used. Therefore the reference value for i_{sd} is permanently set to zero. The i_{sq} stator current demand is adjusted proportional to the demanded torque T_e^*. The control of the stator currents is performed in the rotor flux position aligned *dq* reference frame. The information of the rotor flux position, which is fixed to the rotor position, is required. The rotor position can be measured for instance by a resolver or an encoder. The transformations of the voltage and current vectors between the stator fixed $\alpha\beta$ and *dq* reference frames are made by the Park transformation blocks. Further the Clark transformation blocks convert the vectors between the two dimensional $\alpha\beta$ space and the balanced three phase *ABC* space. The calculated three phase stator voltage values are converted to the inverter reference switching duty cycles d_A^*, d_B^* , and d_C^* by a pulse width modulation (PWM) scheme and fed to the voltage source inverter (VSI). A decoupling of the cross coupling terms $\omega_R L_S i_{Sd}$ and $\omega_R L_S i_{Sq}$ of equation (2.39) and (2.40) is not included in the block diagram. It is assumed that the fast current controllers compensate for the current cross coupling effects in the *dq* stator voltages. Even if a decoupling of the cross coupling terms can be implemented, the omission has no significant effect on the drive performance and simplifies the implementation.

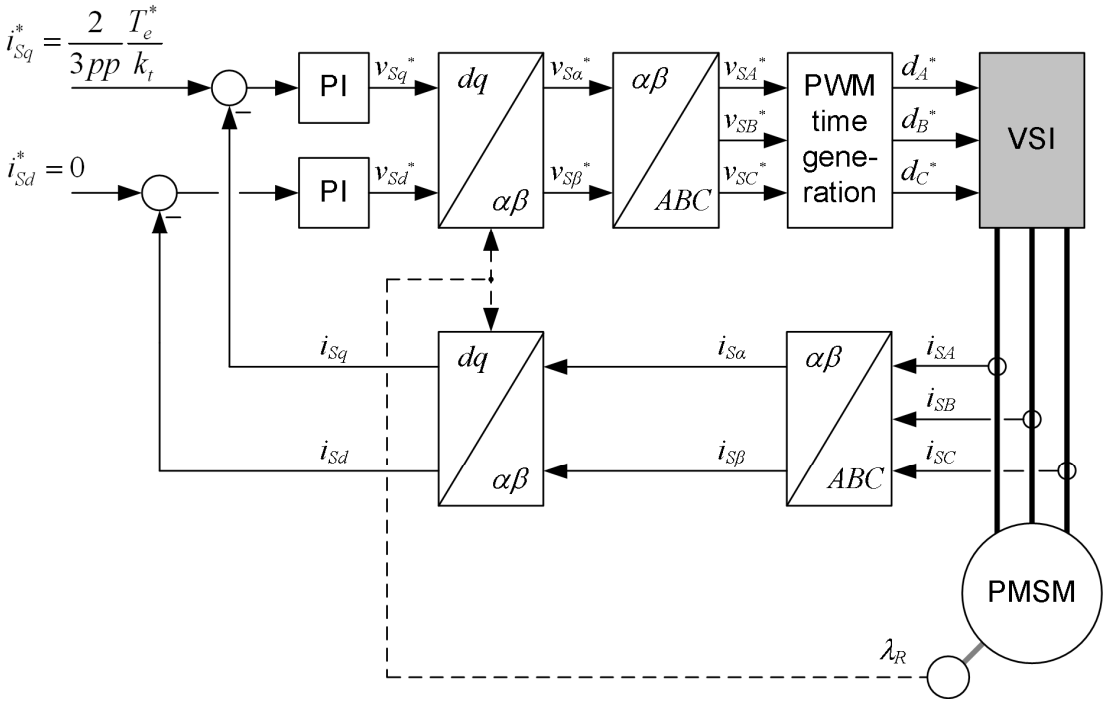

Figure 2.6: Block diagram of vector control system for PMSM drives

2.3.2 Control of Induction Machines

The stator and rotor voltage equations for a cage induction machine are shown in equation (2.45) and (2.46) respectively [9]. The equivalent circuit is shown in Figure 2.7. The rotor circuit is referred to stator side quantities. That means the stator/ rotor winding ratio is assumed to 1 : 1. Again the description is given in an arbitrary reference frame rotating with ω_k. The current vectors $\underline{i}_S$ and $\underline{i}_R$ describe the current quantities in the stator and rotor circuit. The complex stator voltage vector is $\underline{v}_S$ and the rotor voltage is zero due to the short circuit of the rotor bar cage. In the equations R_S is the stator and R_R the rotor resistance. The inductance parameters L_S and L_R describe the stator and rotor winding self inductances. L_0 is the inductance part that links the stator and the rotor winding through the air gap. The stator and rotor self inductances are the sum of the stator/ rotor coupling inductance L_0 and the windings

leakage inductance $L_{S\sigma}$ and $L_{R\sigma}$ as shown by equation (2.49) and (2.50). The stator flux linkage $\underline{\psi}_S$ and rotor flux linkage $\underline{\psi}_R$ describe the magnetic flux that passes thought the stator/ rotor inductances. They are both influenced by the self inductance flux and the mutual coupled flux that passes through the air gap from the stator/ rotor side. Equation (2.47) and (2.48) give the mathematical equations for the total rotor/ stator flux linkages [10].

$$\underline{v}_S = R_S \underline{i}_S + L_S \frac{d\underline{i}_S}{dt} + L_0 \frac{d\underline{i}_R}{dt} + j\omega_k \underline{\psi}_S \tag{2.45}$$

$$0 = R_R \underline{i}_R + L_R \frac{d\underline{i}_R}{dt} + L_0 \frac{d\underline{i}_S}{dt} + j(\omega_k - \omega_R)\underline{\psi}_R \tag{2.46}$$

$$\underline{\psi}_S = L_S \underline{i}_S + L_0 \underline{i}_R \tag{2.47}$$

$$\underline{\psi}_R = L_R \underline{i}_R + L_0 \underline{i}_S \tag{2.48}$$

$$L_S = L_0 + L_{S\sigma} \tag{2.49}$$

$$L_R = L_0 + L_{R\sigma} \tag{2.50}$$

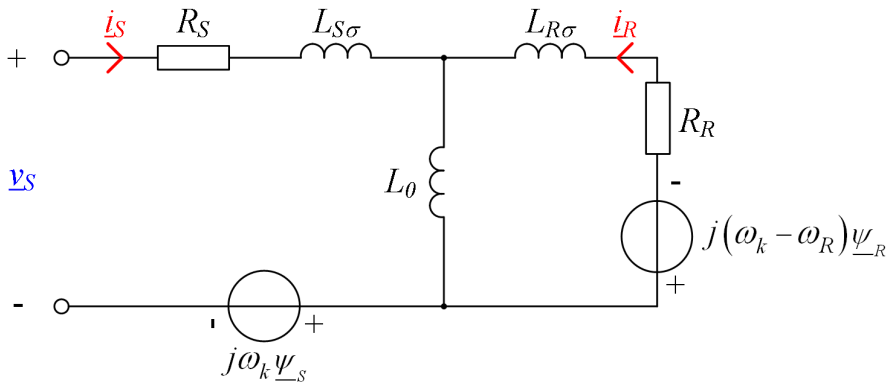

Figure 2.7: Induction machine equivalent circuit

In vector control the stator currents are imposed by current controllers. Therefore the current controllers adjust the stator voltages in order to set the demanded current values. Then the dynamic behaviour of the machine can be derived only from the rotor voltage equation which is in the *dq* frame:

$$0 = R_R \underline{i}_{Rdq} + L_R \frac{d\underline{i}_{Rdq}}{dt} + L_0 \frac{d\underline{i}_{Sdq}}{dt} + j\omega_{sl} \underline{\psi}_{Rdq} \quad . \tag{2.51}$$

As mentioned before, the rotor flux is used for orientation and the stator current vector is the controlled variable. Therefore the rotor flux and the stator currents are selected as state variables of the rotor circuit differential equation:

$$0 = \frac{R_R}{L_R} \underline{\psi}_{Rdq} - \frac{R_R}{L_R} L_0 \underline{i}_{Sdq} + \frac{d\underline{\psi}_{Rdq}}{dt} + j\omega_{sl} \underline{\psi}_{Rdq} \quad . \tag{2.52}$$

Under rotor flux field orientated control the *dq* reference frame is aligned to the rotor flux vector $\underline{\psi}_R$ and therefore $\psi_{Rd} = \psi_R$ and $\psi_{Rq} = 0$. Splitting the complex vector equation (2.52) into its real and imaginary part gives (2.53) and (2.54) as solution for the *d* and *q* axis components.

Re: $$0 = \frac{R_R}{L_R} \psi_R - \frac{R_R}{L_R} L_0 i_{Sd} + \frac{d\psi_R}{dt} \tag{2.53}$$

Im: $$0 = -\frac{R_R}{L_R} L_0 i_{Sq} + \omega_{sl} \psi_R \tag{2.54}$$

Equation (2.53) and (2.54) give two very important conclusions. First, the rotor flux is only affected by the stator current component in the direction of the rotor flux, i.e. i_{Sd}. The resulting rotor flux changes according to the linear first order differential equation given in (2.55). Second, the quadrature stator current component i_{Sq} does

not affect the rotor flux and changes proportional the slip frequency under constant rotor flux (2.56).

$$\frac{d\psi_R}{dt} = \frac{R_R}{L_R}\left(L_0\, i_{Sd} - \psi_R\right) \tag{2.55}$$

$$\omega_{sl} = \frac{R_R\, L_0}{L_R\, \psi_R} i_{Sq} \tag{2.56}$$

That means that the rotor flux can be directly controlled via i_{Sd}. The rotor flux dynamic is affected by a simple first order delay defined by the rotor time constant given in equation (2.57). The magnetising current i_{SMd} is defined that considers the dynamic properties of flux transitions and is proportional to the rotor flux (2.58). Figure 2.8 shows the relationship of i_{Sd}, i_{SMd} and the rotor flux ψ_R as block diagram.

$$\tau_R = \frac{L_R}{R_R} \tag{2.57}$$

$$i_{SMd} = \frac{\psi_R}{L_0} \tag{2.58}$$

Figure 2.8: Relation ship between rotor flux and i_{Sd}, and definition of magnetising current i_{SMd}

Including equation (2.57) and (2.58) into equation (2.56) gives (2.59) which is used to calculate the slip frequency of indirect rotor flux oriented (IRFO) induction machine drives.

$$\omega_{sl} = \frac{i_{Sq}}{\tau_R \, i_{SMd}} \tag{2.59}$$

Integrating the sum of the calculated slip frequency and the measured rotor speed gives the rotor flux position λ_{dq} in the stator fixed reference frame:

$$\lambda_{dq} = \int \left(\omega_R + \omega_{sl} \right) dt \quad . \tag{2.60}$$

The rotor flux linkage in the induction machine stator windings is:

$$\underline{\psi}_{SR} = \frac{L_0}{L_R} \underline{\psi}_R \quad . \tag{2.61}$$

The machine output torque can be calculated by equation (2.62) following the concept of rotor flux orientation.

$$\begin{aligned} T_e &= pp \frac{3}{2} \psi_{SR} \, i_{Sq} \\ &= pp \frac{3}{2} \frac{L_0}{L_R} \psi_R \, i_{Sq} \end{aligned} \tag{2.62}$$

Introducing also the machine torque constant k_t, equation (2.62) can be given as:

$$T_e = pp \frac{3}{2} k_t \, i_{Sq} \quad , \tag{2.63}$$

where the torque constant k_t is:

$$k_t = \psi_{SR} = \frac{L_0^2}{L_R} i_{SdM} \quad . \tag{2.64}$$

Figure 2.9 shows the block diagram of an IRFO vector control drives system. The stator currents are controlled in the *dq* reference frame. In normal operation i_{Sd}^* is kept constant at its rated value to retain a constant excitation flux (rotor flux). The reference value i_{Sq}^* is then proportional to the demanded machine torque T_e^*. In field weakening operation the rotor flux can be reduced, by simply reducing the i_{Sd}^* reference value. The position of the of the *dq* reference frame is calculated by equation (2.60) which uses the i_{Sq} proportional slip frequency and the measured rotor speed.

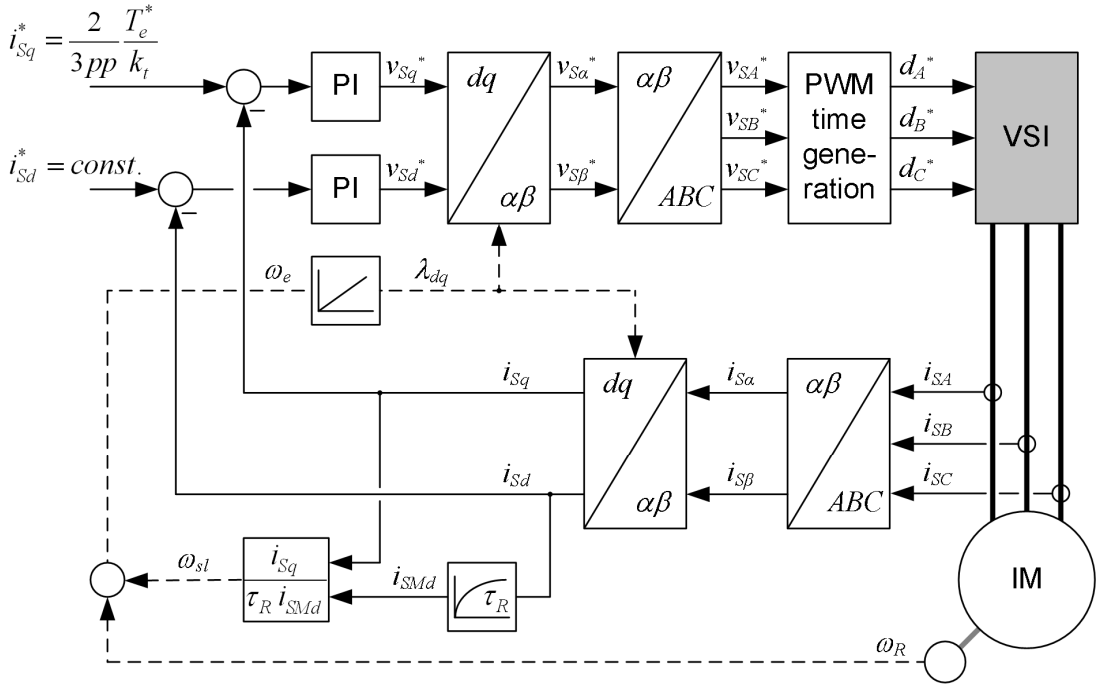

Figure 2.9: Block diagram of vector control system for induction machine drives with rotor flux position estimation by slip frequency calculation

An alternative approach to estimate the rotor flux position can be derived when the rotor voltage equation is transformed into the rotor fixed ($\alpha\beta$) reference frame,

rotating with ω_R as shown in equation (2.65) [1]. As can be seen the complex voltage equation forms a simple linear differential equation that can be easily calculated online in the drive control microcontroller. Figure 2.10 shows the block diagram of this implementation.

$$0 = \frac{1}{\tau_R}\underline{\psi}_{R(\alpha\beta)} - \frac{L_0}{\tau_R}\underline{i}_{S(\alpha\beta)} + \frac{d\underline{\psi}_{R(\alpha\beta)}}{dt} \tag{2.65}$$

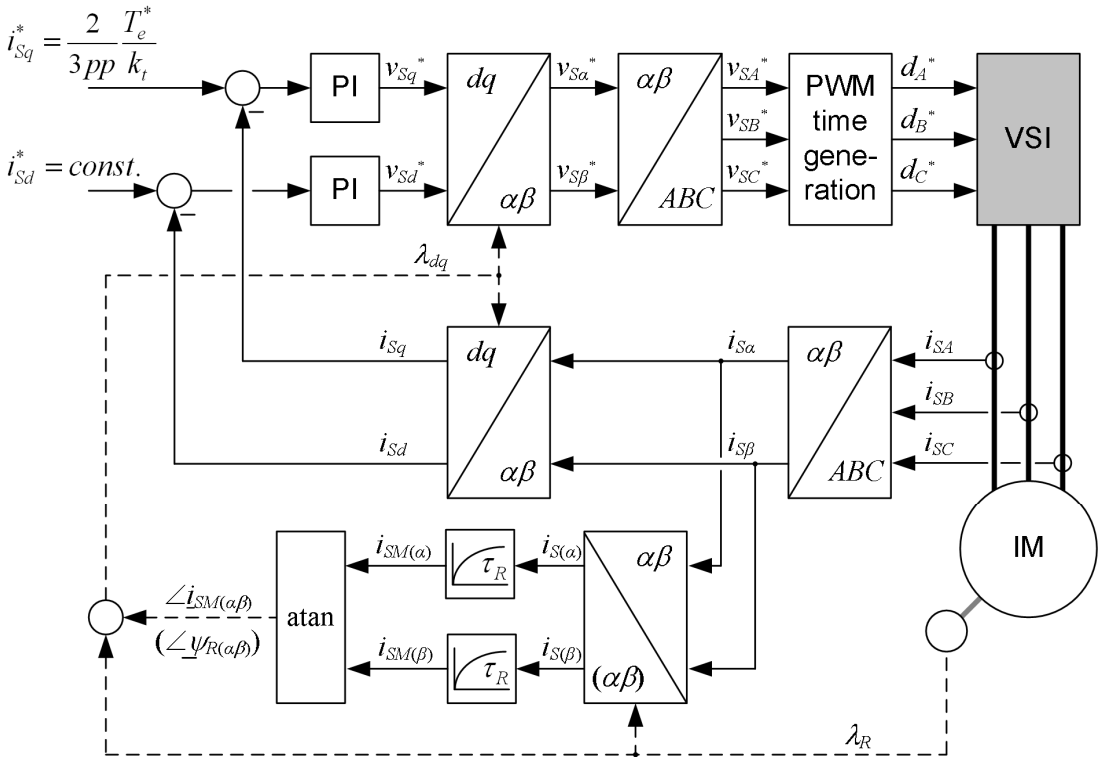

Figure 2.10: Block diagram of vector control system for induction machine drives with rotor flux position estimation by filtering current vector in rotor ($\alpha\beta$) frame

As shown above, the rotor flux position can be easily calculated from the measured rotor position λ_R and the stator currents. The rotor reference frame ($\alpha\beta$) stator current components are simply filtered by a first order delay low pass filter with $1/(2\pi\tau_R)$ as cut off frequency. The outputs give the components of the magnetising current vector

$\underline{i}_{SM}$ which is defined by equation (2.66). It can be seen that the argument of this current vector is directly the position of the rotor flux.

$$\underline{i}_{SM} = \frac{\underline{\psi}_R}{L_0} = i_{SMd}\, e^{j\lambda_{dq}} \tag{2.66}$$

In the above shown schemes it is shown that the rotor flux position can be estimated from the measured stator currents and the measured rotor position. This technique is called indirect rotor flux orientation (IRFO). Only one machine parameter, the rotor time constant τ_R is required for the indirect rotor flux position calculation. This parameter is directly dependent on the rotor inductance and rotor resistance. While the rotor inductance is constant over all operation conditions of the induction machine the rotor resistance changes significant with the temperature of the machine. This deteriorates the performance of the drive slightly. Also direct rotor flux orientation schemes exist. In there the air gap flux is directly measured by Hall effect sensors or search coils built into the machine. The rotor flux is then directly derived from the measured magnetic air gap flux. This calculation is not affected by the machine resistance. Therefore direct flux oriented drive shows a better performance in the rotor flux determination. However the requirement of additional machine sensors makes this technique unattractive for practical applications.

2.4 Speed and Position Control of Electric Drives

2.4.1 Cascade Control Structure

As shown in the section before the principle of field oriented control allows a very good control of the machine torque by directly controlling the applied stator current i_{Sq}. The current controllers have a very high bandwidth, reaching up to a few hundred

Hertz. The coupled mechanical system is usually much slower then the electrical system. An exact torque control is important to achieve a very dynamic drive system. Once a precise and dynamic control of the torque is achieved, speed and position control can be achieved by simply adding further control loops. Figure 2.11 shows the block diagram of a cascade control structure with additional speed and position controller. The speed of the drive is changed by the mechanical torque, therefore the speed controller sets the reference value of the torque (current controller). The position controller sets the reference value for the speed controller. Since the position is the integral of the rotor speed, the position is usually only a P controller. No steady state error will arise due to the pure integral part in the position transfer function. The basic idea of the cascade control structure is that each inner control loop can be considered as an ideal transfer function. The inner loop controllers compensate for delay functions of the subsystem and reject disturbances. The condition for a successful implementation is that each inner loop is always faster then the outer loop.

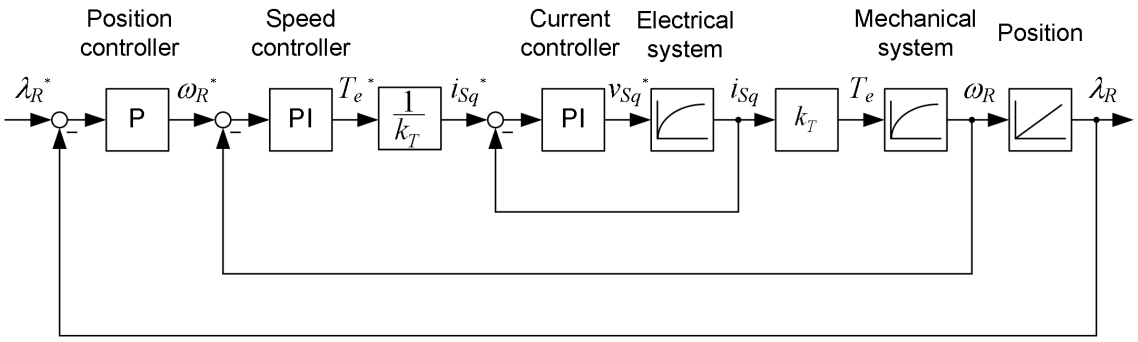

Figure 2.11: Cascade control structure with over laying speed and position control loops

In this work the above explained cascade control structure is used in all experiments of the implemented drive systems for speed- and position control.

2.4.2 Further Approaches for Speed and Position Control

There exist many more control structures to achieve a good speed and position control. Some of them do not use dedicated inner control loops, so that for instance no dedicated torque or speed controller is used. These implementations may be simpler and achieve sufficient performance for particular applications. However, if the inner control loops are replaced by only feed forward structures variable disturbances are not exactly compensated. Therefore the performance is expected to be worse. Also more sophisticated speed and position control structures exist for high precision applications. These are for instance state space controllers. State space controller use the maximum information provided by measurable, observable and controllable system states. Therefore a very good performance can be achieved. For the design the complete system needs to be precisely modelled by a linear state space system. However, non-linear subsystem components may make the approximation of the system by a linear model difficult. To compensate non-linear effects, compensation functions can be implemented. Further tools to tackle non-linearity effects are Fuzzy logic, artificial neural networks and look up tables [11].

2.5 Inverter Output Voltage Generation with Pulse Width Modulation

For the generation of the inverter switching signals several pulse width modulation (PWM) strategies are possible. Figure 2.12 shows a very basic principle of the PWM voltage pattern generation. In a first step the phase voltage reference signal v^* is scaled to the normalised unity amplitude signal m^*, given by equation (2.67). V_{DC} is the voltage of the inverter DC link. The maximum amplitude of the normalised reference voltage m^* is one. This normalised reference voltage signal is compared to a triangular carrier signal varying with the PWM carrier frequency. The PWM output signal v_{PWM} is set to high if the normalised reference voltage m^* is greater then the

triangle signal and set to low value if the triangle signal is greater than m^*. The inverter output will then switch to the positive DC link rail voltage ($V_{DC}/2$) if the PWM output signal is high and switch to the negative DC link rail voltage ($-V_{DC}/2$) if the PWM output signal is low. Figure 2.12 shows the PWM generation scheme. Graph (a) shows the normalised phase voltage reference m^* as blue line and the PWM carrier triangle waveform as green function. Plot (b) underneath shows the resulting inverter PWM output voltage. The dashed horizontal lines indicate the inverter switching instances. As can be seen in each PWM period, which is the period of the triangle carrier signal, one output voltage pulse is generated.

$$m^* = \frac{2v^*}{V_{DC}} \tag{2.67}$$

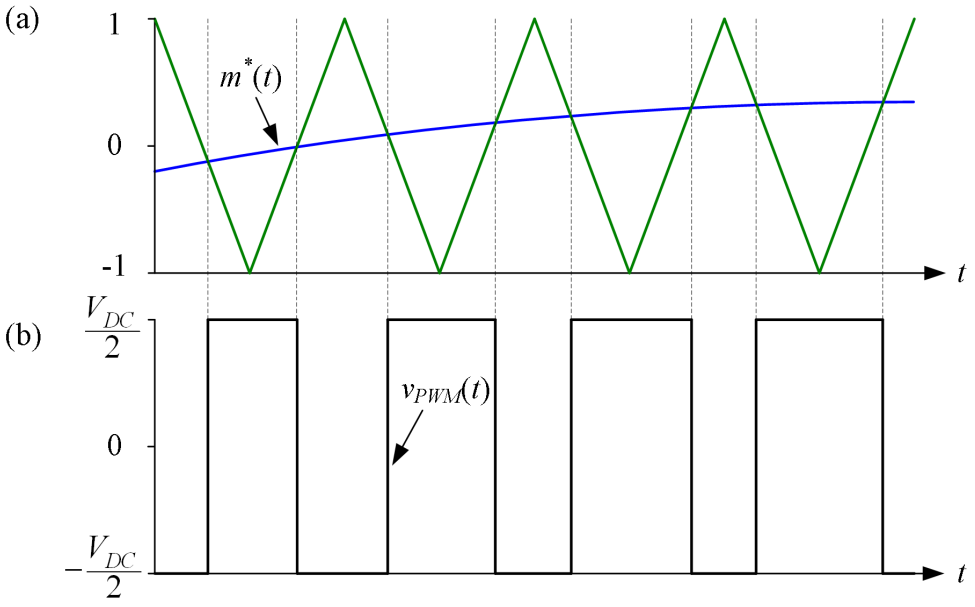

Figure 2.12: PWM voltage generation with comparison of reference voltage and carrier triangle wave form

In digital control systems the reference voltage is updated only at discrete time instances. Figure 2.13 visualises this. Similar to Figure 2.12 in plot (a) the continuous

normalised phase voltage reference m^* is shown as blue line and the PWM carrier triangle waveform is shown as green function. The additional dark blue line shows the normalised phase voltage reference when updated only at the sample instances k. As can be seen $m^*[k]$ is updated once every PWM cycle. If the discrete updated voltage reference is used the resulting PWM output voltage will be slightly different, due to the time quantisation error in the discrete sampled and hold reference voltage. However, the PWM frequency in voltage source inverter drive systems is usually much higher then the fundamental inverter output voltage and therefore this error is not significant.

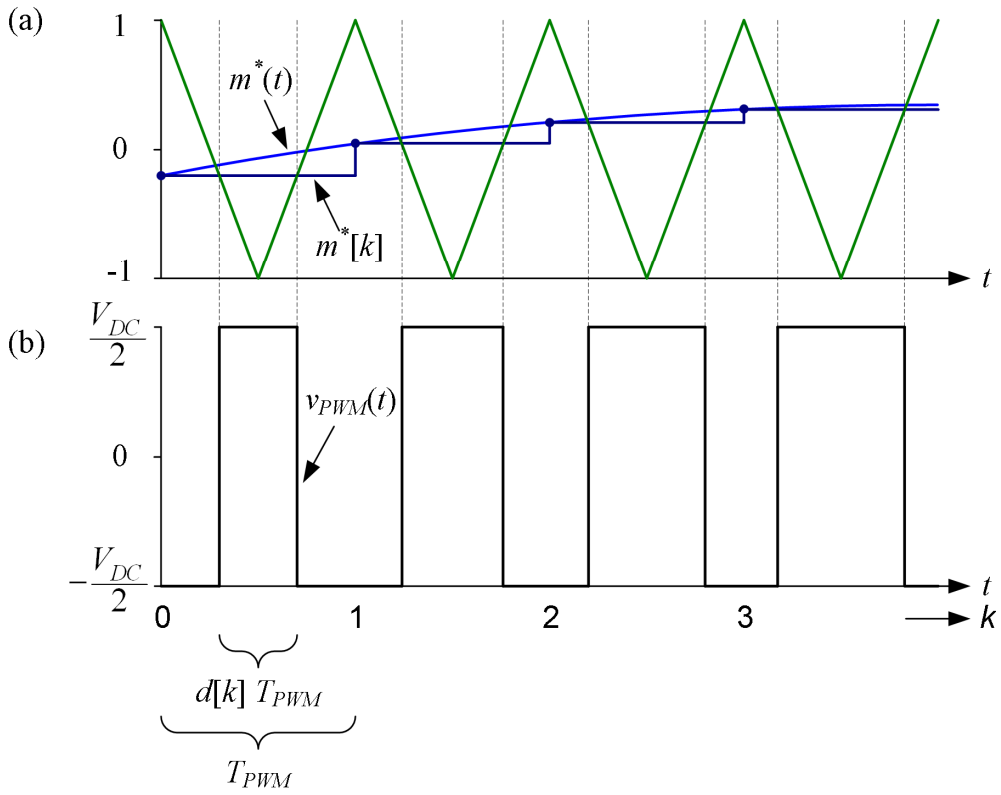

Figure 2.13: PWM voltage generation with discrete updated reference voltage

In digital microprocessor controlled drive systems the PWM switching instances are usually not computed by a comparison of the reference voltage with a carrier triangular function. The voltage switching duty cycle d is rather discrete calculated

with every PWM period. In order to make the average output voltage v_{PWM} follow the reference voltage v^*, the voltage time area per PWM cycle should be equal. Therefore the following condition should be met:

$$\int_{kT_{PWM}}^{(k+1)T_{PWM}} v^*(t)\,dt = \int_{kT_{PWM}}^{(k+1)T_{PWM}} v_{PWM}(t)\,dt \quad . \tag{2.68}$$

For the shown PWM generation scheme shown in Figure 2.13 equation (2.68) gives:

$$v^*[k]T_{PWM} = d[k]\frac{V_{DC}}{2}T_{PWM} - \left(1-d[k]\right)\frac{V_{DC}}{2}T_{PWM} \quad , \tag{2.69}$$

which gives as result for the inverter switching duty cycle:

$$d[k] = \frac{v[k]}{V_{DC}} + \frac{1}{2} = \frac{m[k]}{2} + \frac{1}{2} \quad . \tag{2.70}$$

The calculated phase switching duty cycle is the updated every PWM cycle to the PWM switching signals unit that generates the inverter device switching signals. The principle is similar to the comparator scheme shown in Figure 2.12 (a).

In practice many more PWM generation schemes exist. In some the three phase reference voltage signals are superimposed by a common mode voltage, e.g. a third harmonic component. This can be useful to achieve the maximal output voltage to the machine with the given DC link voltage [12]. Further schemes do not generate independent the phase voltage reference signal, but calculate rather an output voltage vector.

2.6 Conclusion

This chapter has provided an overview of the principles of operation of PM synchronous motors and induction machines, and their control as variable speed drives.

Chapter 3

Sensorless Control

As shown in Chapter 2 for the principle of field oriented control the position of the orientation field is required. This can be measured by dedicated sensors or derived from the machine model and the rotor speed/ position. Any of these methods required additional sensors mounted directly on the machine. This is highly undesirable since these sensors may also subject to very rough industrial conditions where the machine is located. Also additional wiring of these sensors is required which decreases further the reliability, since the cables and connectors are additional potential error sources. Therefore it is desirable to acquire the machine flux position without the need of sensors mounted on the machine. This is implied by using the term "sensorless control of AC machines".

3.1 Model Based Sensorless Control

Since each motor is also a generator one principle of detecting the machines flux position is by using the stator induced back EMF. The induced AC back EMF voltage $\underline{e}$ is directly related to the rotor flux linkage $\underline{\psi}_{SR}$ in the stator windings:

$$\underline{e} = \frac{d\underline{\psi}_{SR}}{dt} \quad . \tag{3.1}$$

From the machine stator voltage equations (2.38) and (2.45) the back EMF vector can be calculated through the measured stator voltages and the stator currents. Equation (3.2) shows the mathematical expression for permanent magnet synchronous machines and equation (3.3) for induction machines. Figures 3.1 and 3.2 shows the block diagrams of the back EMF computation.

$$\underline{e} = \underline{v}_S - R_S \underline{i}_S - L_S \frac{d\underline{i}_S}{dt} \tag{3.2}$$

$$\underline{e} = \underline{v}_S - R_S \underline{i}_S - \left(L_S - \frac{L_0^2}{L_R} \right) \frac{d\underline{i}_S}{dt} \tag{3.3}$$

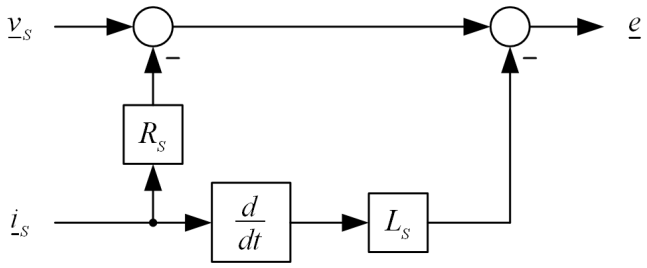

Figure 3.1: Block diagram of back EMF computation for PMSM

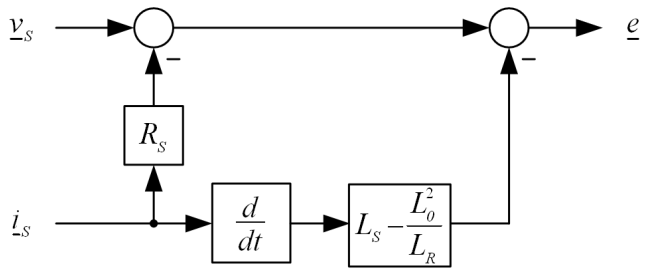

Figure 3.2: Block diagram of back EMF computation for induction machine

In sinusoidal AC machines under steady state the back EMF is 90 degrees in advance of the rotor flux vector. Therefore the integration of the back EMF vector is not

necessary, but can be replaced by the 90 degrees phase compensation. Problematic in the implementation is the computation of the fundamental stator current vector derivative. The currents shows ripple due to the PWM voltage. This ripple contains high frequency noise components that get amplified by the differentiation [10]. The measurement of the fundamental voltage is also difficult. Therefore in most cases the controller reference voltage is used. This avoids also the use of additional voltage sensors in the drive. Unfortunately the real machine voltage will not follow the reference voltage exactly due to inverter non-linearity distortions such as dead time effects, current clamping and the voltage drops over the switching devices. The inverter non-linearity effects are particular significant at low speed when the fundamental voltage is relatively small. Then the inverter voltage distortions can be larger then the machine back EMF amplitude.

Rearranging the stator equations (2.38) and (2.45) gives directly the rotor flux linkage in the stator windings for the PMSM (3.4) and the induction machine (3.5).

$$\underline{\psi}_{SR} = \int \left(\underline{v}_S - R_S \underline{i}_S \right) dt - L_S \underline{i}_S \tag{3.4}$$

$$\underline{\psi}_{SR} = \int \left(\underline{v}_S - R_S \underline{i}_S \right) dt - \left(L_S - \frac{L_0^2}{L_R} \right) \underline{i}_S \tag{3.5}$$

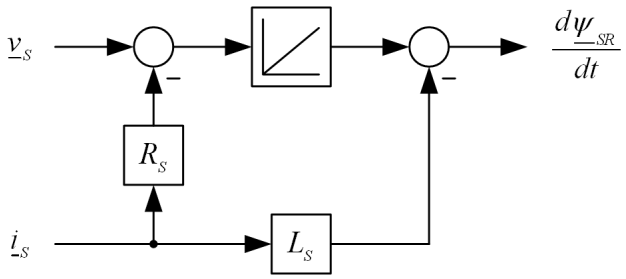

Figure 3.3: Calculation of rotor flux linkage in stator windings in the PMSM

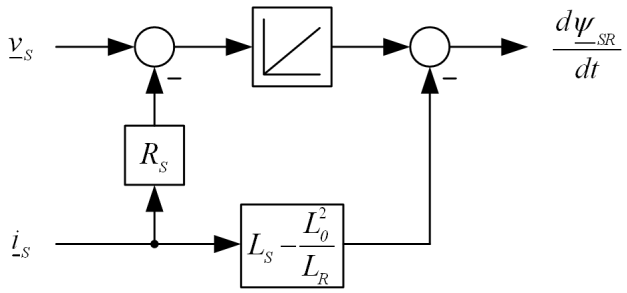

Figure 3.4: Calculation of rotor flux linkage in stator windings in the induction machine

Figures 3.3 and 3.4 shows the block diagrams for equations (3.4) and (3.5). Here the differentiation of the current is replaced by the integration of the voltage. The result is the rotor flux linkage in the stator winding that can be directly used for the field orientation. However, in practice also the integration gives problems. The current and voltage measurements contain small offset errors. In particular the voltage aquisition is less precise. Even if these offset errors are very small they cause the integration to drift [13]. Therefore in practice the integrator is replaced by a low pass filter as shown in Figures 3.5 and 3.6. The low pass filter behaves like an integrator at frequencies higher then the corner frequency. Below the corner frequency the gain is limited and surpresses the drift away by the voltage and current measurement offset errors. The corner frequency is usually set to a value of between 0.5 to 2 Hz [14] depending on the disturbances at low speed. Therefore the drift away due to small offset errors is limited.

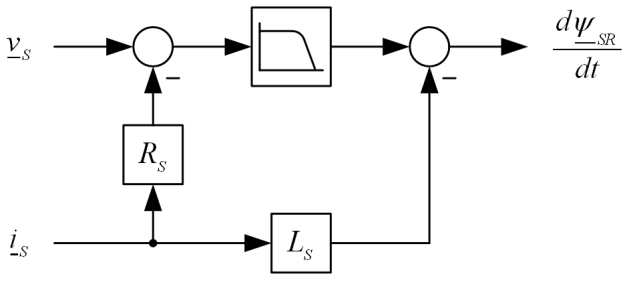

Figure 3.5: Practical implementation of rotor flux estimation with low pass filter for PMSM's

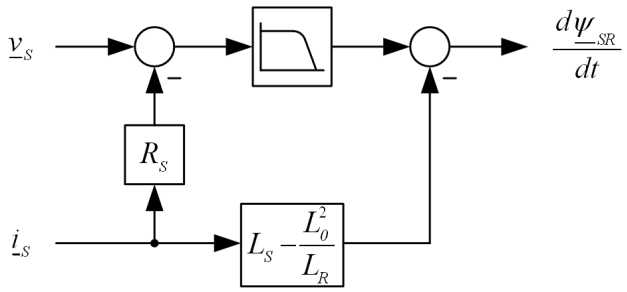

Figure 3.6: Practical implementation of rotor flux estimation with low pass filter for induction machines

Figure 3.7 shows a comparison in the frequency range of the integrator characteristic and a low pass filter. A cut off frequency of 1 Hz is used for this example. In the phase plot of Figure 3.7 it can be seen that not only the gain is limited at low speeds, but also the phase is affected. This phase shift gives an error in the estimated rotor flux position.

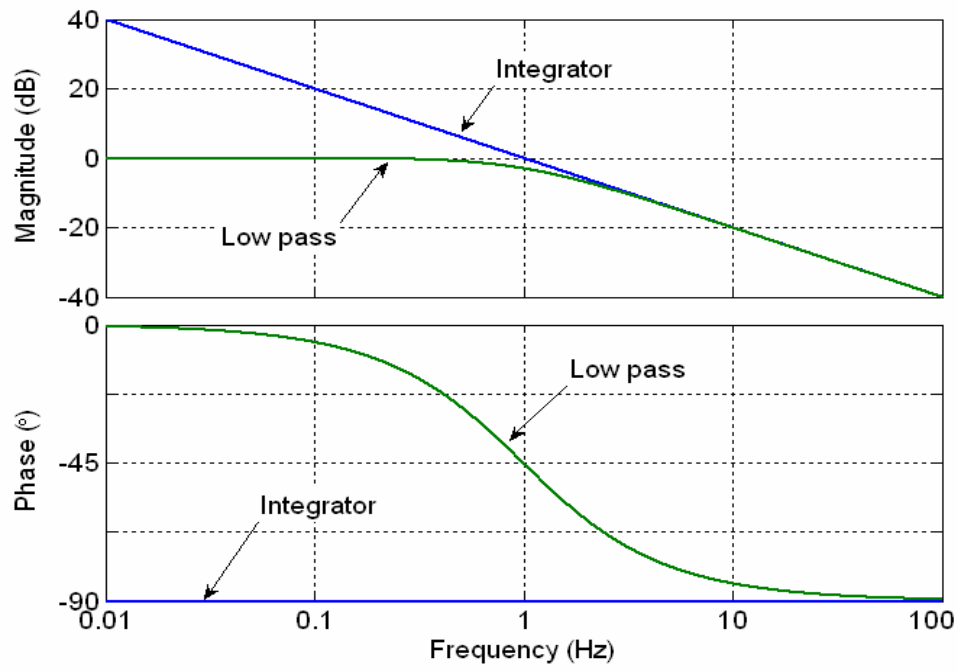

Figure 3.7: Bode plot of integrator and low pass filter

It is not only the offset errors in the current and voltage measurements that affect the position estimation quality, but also the machine parameter R_S. This parameter varies significantly with the machine temperature. Several resistance adaptation techniques have been reported to limit the resistance errors e.g. [14-17]. Further inverter non-linearity effects are also a significant disturbance as mentioned earlier. [14] presents a detailed study of the inverter disturbance and proposes a compensation scheme. In [18] operation of an induction machine at zero frequency excitation is shown that uses a DC offset voltage estimator and a noise compensator to generate undisturbed voltage and current signals, a resitance adaptation scheme, an inverter non-linearity compensation model and and ideal integrator.

The above shown principle is also called the voltage model observer. As shown the rotor flux position can be estimated from the fundamental stator voltage equation. This allows the implementation of field orientated control of AC machines. In permanent magnet synchronous machines the rotor flux position is directly related to the rotor position. Therefore the mechanical rotor position and speed is also known and sensorless speed control is also possible. In induction machines the mechanical rotor frequency is different by the slip frequency from the rotor flux frequency. However, by inverting the IRFO model explained in section 2.3.2 the slip frequency can be estimated from the imposed i_d and i_q currents. To improve the mechanical speed estimation several observer structures have been developed that combine different estimation models [19] also known as Model Reference Adaptive Systems (MRAS).

The above explained rotor flux position estimation based on the fundamental machine voltage equation works well at higher speeds (larger then 2 Hz electrical) [13]. It is well proven and implemented in many practical drives. However in practical applications, operation at very low and zero speed is not possible with the voltage model observer.

3.2 Non-model Based Sensorless Techniques

As shown, model based methods assume a linear machine model with defined parameters. In practice however these parameters are not exactly known and may also vary with the operation condition. One very common problem is the adjustment of the stator winding resistance which changes significantly with temperature. Furthermore the simplified models assume a sinusoidal distribution of the stator windings, a constant air gap and a homogeneous permeability of the iron in the machine. All these assumptions are not valid in practical machines, where the winding turns are semi sinusoidally distributed over the stator teeth or just concentrically. The rotor has usually discrete embedded rotor bars, permanent magnets or windings, depending on the type of machine. Furthermore the magnetic saturation in the iron of the machine causes a change of the local permeability which influences the magnetic flux paths and therefore the inductive parameters of the stator windings. Non-model based methods use these anisotropies that cause a magnetic saliency inside the machine.

3.2.1 Magnetic Saliencies in AC Machines

In electrical machines the magnetic properties are not homogenous over the radius. They are influenced by mechanical design features of the stator/ rotor and magnetic saturation in the machine iron. All machines exhibit both kinds of saliencies. However the amplitude and behaviour differs for different machine designs.

Mechanical rotor saliency is caused by a mechanical design saliency of the rotor. This is typical in salient-pole synchronous machines, in buried PM machines and in induction machines. The interaction between the mechanical rotor saliency and the stator teeth alters the local magnetic air gap flux in the machine and influences the magnetic coupling of the stator windings relative to the rotor position. This affects the stator windings self- and mutual inductances, which will exhibit a modulation

that is directly related to the rotor position. Furthermore the magnetic field created by the permanent magnets and currents in the machine cause saturation effects of the machine iron in different directions. The iron permeability is a non-linear function of the present magnetic condition. Figure 3.8 shows principally the *B*-*H* curve of iron. It can be seen that the magnetic flux density *B* does not increase linearly with the magnetic field strength *H*. With increasing *H* the flux density *B* reaches its maximum and saturates.

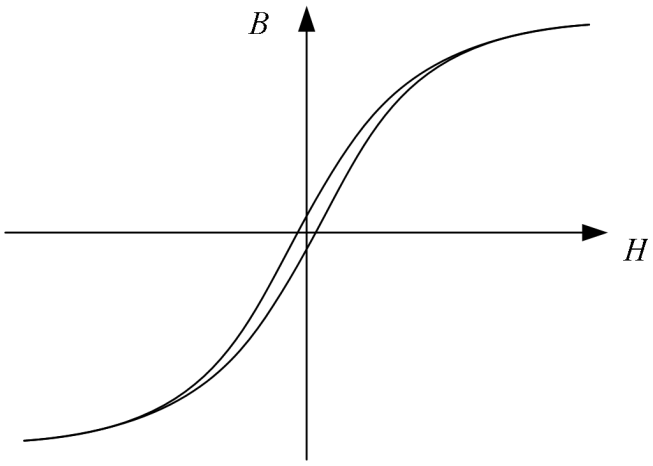

Figure 3.8: *B*-*H* curve of iron

The ratio between the magnetic field strength *H* and the magnetic flux density *B* is the permeability μ:

$$\mu = \frac{B}{H} \quad . \tag{3.6}$$

Therefore the permeability μ is also non-linear with the magnetic field strength *H*. The machine winding inductance depends directly of the machine's iron permeability μ and is hence a function of the magnetic field strength *H*. The magnetic field paths will modulate the resulting stator winding impedances. Since this modulation is created by the machines magnetic field and currents, this saliency is rotating with the

fundamental magnetic flux axis. The hysteresis effect shown in the *B-H* curve of Figure 3.8 is not considered for the saliency sensorless control schemes. This hysteresis effect causes magnetic losses due to the alternating magnetisation of AC machines.

3.2.2 Modelling of Magnetic Saliency in Three Phase Machines

A magnetic saliency modulates the stator windings self and mutual inductances. However for simplicity it is assumed that all the resulting self and mutual inductances can be combined in the equivalent inductance matrix shown in (3.7). The three phase equivalent inductances l_A, l_B and l_C are given by (3.8) to (3.10), which consist of a constant term L plus a sinusoidal modulation depending on ΔL and the saliency position $\lambda_{dq'}$. It is assumed that saliency causes a balanced sinusoidal three phase impedance modulation.

$$\mathbf{L}_{ABC} = \begin{bmatrix} l_A & 0 & 0 \\ 0 & l_B & 0 \\ 0 & 0 & l_C \end{bmatrix} \tag{3.7}$$

$$l_A = L - \Delta L \cos\left(2\lambda_{dq'}\right) \tag{3.8}$$

$$l_B = L - \Delta L \cos\left(2\lambda_{dq'} + \frac{2}{3}\pi\right) \tag{3.9}$$

$$l_C = L - \Delta L \cos\left(2\lambda_{dq'} - \frac{2}{3}\pi\right) \tag{3.10}$$

Figure 3.9 illustrates the assumed three phase equivalent modulation. Figure 3.9 (a) shows the cross section of a modelled machine indicating the three phase stator windings *A,B,C*. The shaded areas of the machine section symbolise areas with a high permeability (e.g. iron). The white area between the rotor and stator symbolise the relative air gap, where the permeability is assumed to be low. It can be seen that the relative air gap width changes with the position of the saliency *dq'* frame. The change of the relative air gap changes the values of the resulting three phase equivalent impedances l_A, l_B and l_C. Figure 3.9 (b) shows the variation of the three phase equivalent impedances plotted over the saliency frame position $\lambda_{dq'}$ relative to the stator frame. It can be seen that in each phase two sinusoidal modulation periods over one period of $\lambda_{dq'}$ occur. The modulation of the three phase impedances is shifted by 120 $°_{ele}$ for the assumed three phase machine model.

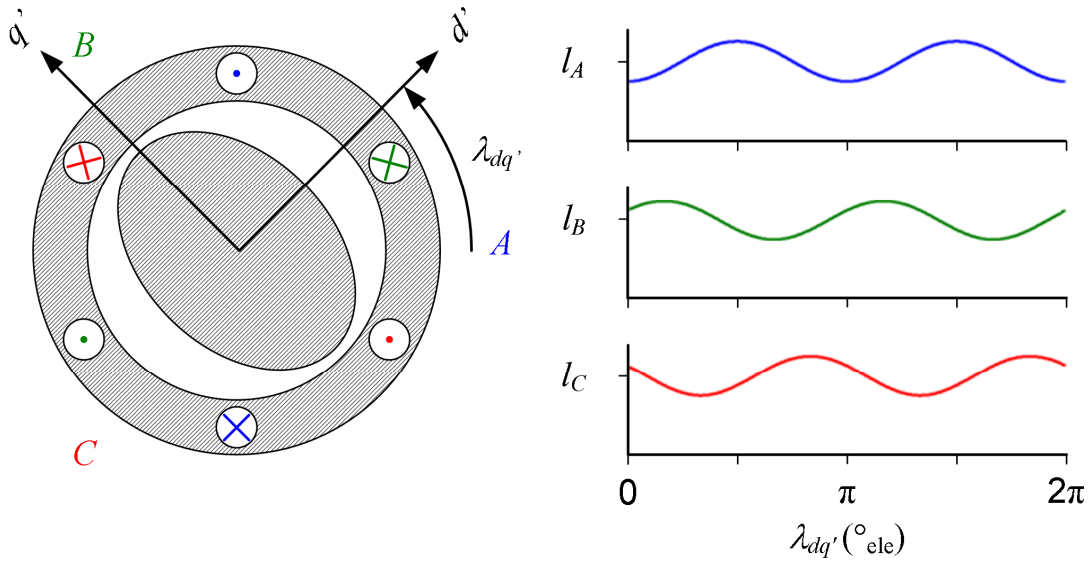

Figure 3.9: Modelled three phase equivalent inductance modulation by saliency

The polyphase machine model can be further described in the two phase $\alpha\beta$ frame. Transforming the three phase equivalent impedance tensor (3.7) into the $\alpha\beta$ frame gives (3.13) as result.

$$\mathbf{A} = \begin{bmatrix} 1 & \cos\left(\frac{2}{3}\pi\right) & \cos\left(\frac{4}{3}\pi\right) \\ 0 & \sin\left(\frac{2}{3}\pi\right) & \sin\left(\frac{4}{3}\pi\right) \end{bmatrix} \tag{3.11}$$

$$\mathbf{L}_{\alpha\beta} = \frac{2}{3}\mathbf{A}\cdot\begin{bmatrix} l_A & 0 & 0 \\ 0 & l_B & 0 \\ 0 & 0 & l_C \end{bmatrix}\cdot\mathbf{A}^T \tag{3.12}$$

$$\mathbf{L}_{\alpha\beta} = \begin{bmatrix} L-\frac{\Delta L}{2}\cos\left(2\lambda_{dq'}\right) & -\frac{\Delta L}{2}\sin\left(2\lambda_{dq'}\right) \\ -\frac{\Delta L}{2}\sin\left(2\lambda_{dq'}\right) & L+\frac{\Delta L}{2}\cos\left(2\lambda_{dq'}\right) \end{bmatrix} \tag{3.13}$$

The inductance tensor in the $\alpha\beta$ frame describes an elliptic shape rotating with the position of the saliency $\lambda_{dq'}$ as shown by Figure 3.10.

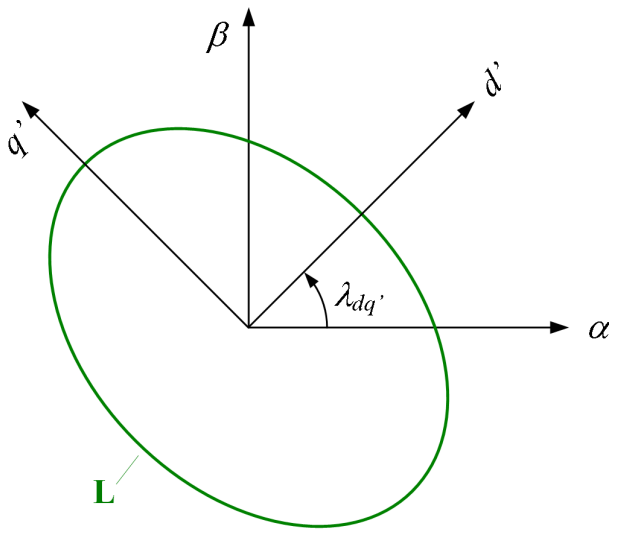

Figure 3.10: Modelled equivalent impedance saliency modulation in $\alpha\beta$ frame

Transforming the impedance tensor further into the saliency position defined dq' frame gives (3.16), which shows that the complete salient impedance inside the machine can be described by two variables $L_{d'}$ and $L_{q'}$ which define the equivalent impedance values into direction of saliency axis d' and its quadrature axis q'.

$$\mathbf{B} = \begin{bmatrix} \cos\left(\lambda_{dq'}\right) & \sin\left(2\lambda_{dq'}\right) \\ -\sin\left(2\lambda_{dq'}\right) & \cos\left(\lambda_{dq'}\right) \end{bmatrix} \tag{3.14}$$

$$\mathbf{L}_{dq'} = \mathbf{B} \cdot \begin{bmatrix} L - \frac{\Delta L}{2}\cos\left(2\lambda_{dq'}\right) & -\frac{\Delta L}{2}\sin\left(2\lambda_{dq'}\right) \\ -\frac{\Delta L}{2}\sin\left(2\lambda_{dq'}\right) & L + \frac{\Delta L}{2}\cos\left(2\lambda_{dq'}\right) \end{bmatrix} \cdot \mathbf{B}^{-1} \tag{3.15}$$

$$\mathbf{L}_{dq'} = \begin{bmatrix} L - \frac{\Delta L}{2} & 0 \\ 0 & L + \frac{\Delta L}{2} \end{bmatrix} = \begin{bmatrix} L_{d'} & 0 \\ 0 & L_{q'} \end{bmatrix} \tag{3.16}$$

The position of the saliency is defined by the indicated dq' frame. The assumed model shows a pure oval leakage impedance saliency. In practice however saliency loci with much more complex shapes can occur. Several saliencies effects exist in practical machines. These come from saturation of the iron and the mechanical design of the machine. As simple model it can be assumed that the different saliency effects are superimposing. However in practice the interactions between multiple saliencies in the machine are more complex.

The saliency can be caused by the mechanical machine construction or magnetic saturation. Therefore the saliency axes are related to either the mechanical anisotropy or to the position of the electro magnetic saturation. The saliency will rotate in the $\alpha\beta$ frame during the operation of the machine. The saliency rotational speed may be

a multiple of the electrical or mechanical speed of the machine [5]. In permanent magnet synchronous machines the saturation saliency and the mechanical saliency are rotating with the fundamental electrical frequency, which is also the mechanical frequency. Therefore both saliencies result into one overlapping saliency shape rotating synchronised. In induction machines the mechanical and fundamental exitation frequency is different. Therefore the mechanical saliency and the magnetic saturation saliency rotate with different speeds. Further the mechanical saliency caused by the interaction between the stator slots and rotor bar slots may rotate in opposite directions of the magnetic saturation saliency [5]. Therefore the mechanical and electrical saliency positions are not correlated. For the sensorless control the presence of multiply saliencies creates difficulties. In an ideal case only one circular impedance modulation occurs, as modelled above. Since this is not the case in practical machines, unwanted saliency components need to be compensated. Even if in most machines a good saliency signal can be detected, the separation of useful and unwanted saliency signals is a challenging task. In practice observer structures [20] and harmonic compensation schemes have been investigated [21]. However, the unwanted saliency compensation can be also achieved by using dedicated look up tables [22-24]. [25] uses a set of synchronous filters to separate the saliency modulations. It uses a memory algorithm that refines the quality of the disturbance waveforms as the motor's operational history is increased. The disturbance compensators are further used to reduce disturbances that are caused by inverter non-linearity effects.

For rotor flux orientated vector control of AC machines the magnetic rotor flux *dq* frame position is required. This vector control orientation frame can be derived from detecting the saliency *dq′* frame position. In synchronous machines the saliency *dq′* frame position is usually aligned to the rotor flux position. [26] reports that the angle between the rotor flux *dq* frame and the saturation saliency frame *dq′* is load

dependent for induction machines. The phase shift angle λ_{comp} is in [26] easily corrected by using a simple look up table, derived from commisioning tests.

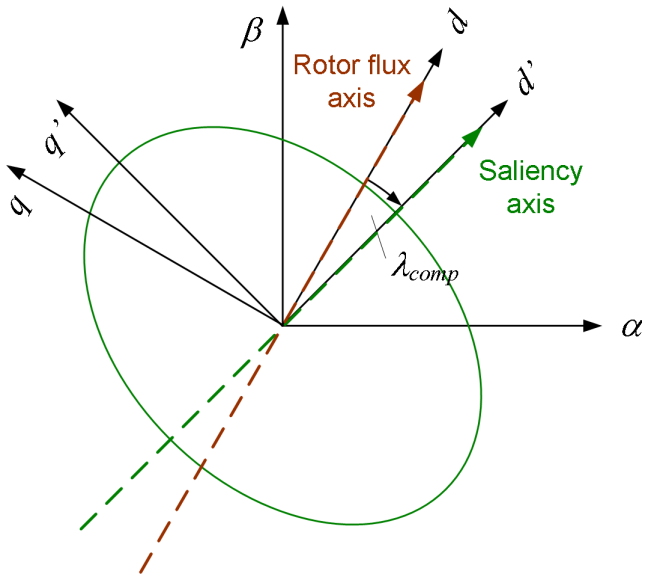

Figure 3.11: Relation between saliency *dq'* and rotor flux *dq* frame

Figure 3.11 shows the definition of the rotor flux *dq* frame used for the machine vector control and the *dq'* frame that is aligned with the maximal and minimal detected stator equivalent impedance. If a mechanical saliency is tracked which is not synchronised with the *dq* frame position, e.g. rotor bar modulation, the position of the rotor flux is not directly known. However, the acquired mechanical rotor position can be further used to estimate the vector control flux position by using for instance IRFO as achieved when using an encoder. Since the saliency modulation shows a modulation of double the *dq'* frame position, two minima and two modulation maxima occur in the detected saliency. This has to be taken into consideration for the sensorless position estimation to find only the wanted true position of the *dq'* frame.

3.3 Position Estimation with High Frequency Injection

In these sensorless position estimation schemes an additional high frequency (HF) carrier signal is added to the fundamental machine voltage. Under high frequency excitation the fundamental machine models presented in section 2.3 can not be used. The HF carrier frequency is usually much higher then the fundamental frequency (500 Hz ... 2.5 kHz). For the analysis of the machine saliency only the current response to the injected high frequency voltage is used. Thus the back EMF can be neglected. At the high frequency range the voltage drop over the ohmic resistance is much smaller than the voltage drop over the winding reactance. As result the simplified equation (3.17) is used to describe the relation of the high frequency stator voltage $\underline{v}_c$ and its high frequency current response $\underline{i}_c$. The resulting high frequency stator inductance tensor $\mathbf{L}_c$ is mainly determined by the windings leakage inductance. The stator winding inductance is assumed to be different in d' and q' direction due to machine saliency. Therefore the stator HF inductance is described as a tensor that includes the modulation due to the machine saliency. Equation (3.18) gives the high frequency stator iinductance tensor orientated in the saliency dq' frame.

$$\underline{v}_c = \mathbf{L}_c \frac{d\underline{i}_c}{dt} \tag{3.17}$$

$$\mathbf{L}_{cdq'} = \begin{bmatrix} L_c - \frac{\Delta L_c}{2} & 0 \\ 0 & L_c + \frac{\Delta L_c}{2} \end{bmatrix} = \begin{bmatrix} L_{cd'} & 0 \\ 0 & L_{cq'} \end{bmatrix} \tag{3.18}$$

Equation (3.19) to (3.22) show the derivation of the voltage equations that describe the relationship of the injected high frequency voltage signal and the resulting current response. It can be seen that the high frequency current signal is modulated

by the position of the saliency *dq'* frame. Equation (3.19) shows the voltage equation in saliency *dq'* frame orientation. Equation (3.20) shows the transformation into the stator fixed $\alpha\beta$ frame. Equation (3.21) shows the final voltage equation in the $\alpha\beta$ frame. Equation (3.22) shows the high frequency voltage equation rearranged, that shows the current response to the injected high frequency carrier voltage. It can be seen that the current response to a high frequency voltage vector of constant magnitude shows a modulation of $\sin(2\lambda_{dq'})$ and $\cos(2\lambda_{dq'})$ in the $\alpha\beta$ frame.

$$\begin{bmatrix} v_{cd'} \\ v_{cq'} \end{bmatrix} = \begin{bmatrix} L_c - \frac{\Delta L_c}{2} & 0 \\ 0 & L_c + \frac{\Delta L_c}{2} \end{bmatrix} \cdot \frac{d}{dt} \begin{bmatrix} i_{cd'} \\ i_{cq'} \end{bmatrix} \tag{3.19}$$

$$\begin{bmatrix} v_{c\alpha} \\ v_{c\beta} \end{bmatrix} = \begin{bmatrix} \cos(\lambda_{dq'}) & -\sin(\lambda_{dq'}) \\ \sin(\lambda_{dq'}) & \cos(\lambda_{dq'}) \end{bmatrix} \cdot \begin{bmatrix} L_c - \frac{\Delta L_c}{2} & 0 \\ 0 & L_c + \frac{\Delta L_c}{2} \end{bmatrix} \cdot \begin{bmatrix} \cos(\lambda_{dq'}) & \sin(\lambda_{dq'}) \\ -\sin(\lambda_{dq'}) & \cos(\lambda_{dq'}) \end{bmatrix} \cdot \frac{d}{dt} \begin{bmatrix} i_{c\alpha} \\ i_{c\beta} \end{bmatrix} \tag{3.20}$$

$$\begin{bmatrix} v_{c\alpha} \\ v_{c\beta} \end{bmatrix} = \begin{bmatrix} L_c - \frac{\Delta L_c}{2}\cos(2\lambda_{dq'}) & -\frac{\Delta L_c}{2}\sin(2\lambda_{dq'}) \\ -\frac{\Delta L_c}{2}\sin(2\lambda_{dq'}) & L_c + \frac{\Delta L_c}{2}\cos(2\lambda_{dq'}) \end{bmatrix} \cdot \frac{d}{dt} \begin{bmatrix} i_{c\alpha} \\ i_{c\beta} \end{bmatrix} \tag{3.21}$$

$$\begin{bmatrix} i_{c\alpha} \\ i_{c\beta} \end{bmatrix} = \frac{1}{L_c^{\,2} + \left(\frac{\Delta L_c}{2}\right)^2} \begin{bmatrix} L_c + \frac{\Delta L_c}{2}\cos(2\lambda_{dq'}) & \frac{\Delta L_c}{2}\sin(2\lambda_{dq'}) \\ \frac{\Delta L_c}{2}\sin(2\lambda_{dq'}) & L_c - \frac{\Delta L_c}{2}\cos(2\lambda_{dq'}) \end{bmatrix} \cdot \int \begin{bmatrix} v_{c\alpha} \\ v_{c\beta} \end{bmatrix} dt \tag{3.22}$$

3.3.1 Rotating $\alpha\beta$ Frame HF Voltage Injection

A well researched technique of using magnetic saliency in AC machines for the position estimation is by injecting a rotating high frequency voltage into the machine [5], [6], [20-22], [24], [25], [27-34]. A constant amplitude voltage vector rotating with a high frequency (500...2.5 kHz) is superimposed to the fundamental voltage vector. The injected high frequency voltage vector $\underline{v}_{c\alpha\beta}$ is defined by equation (3.23). Therefore a rotating HF current vector arises superimposed to the fundamental current vector. The high frequency current response is filtered out by a band pass filter from the measured machine currents and then demodulated to reconstruct the rotor or flux position. The same measured phase currents are used as feed back for the fundamental current controllers after the injected HF currents are filtered off by a low or band stop filter. Figure 3.12 shows the block diagram of the rotating HF voltage injection principle.

$$\underline{v}_{c\alpha\beta} = V_c e^{j\omega_c t} \tag{3.23}$$

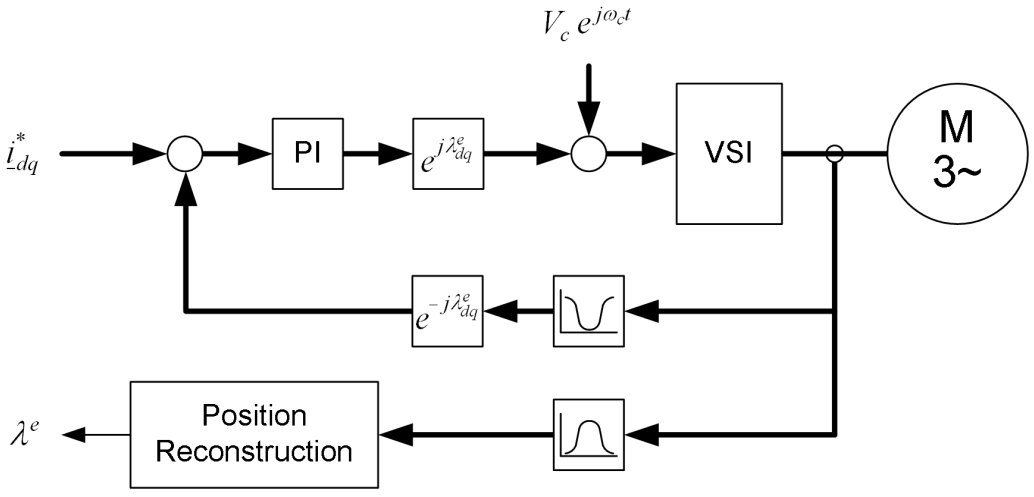

Figure 3.12: Block diagram of rotating HF voltage carrier injection

Since the injected HF voltage vector magnitude is constant the effect of the machine saliency is directly visible in the HF stator currents measured in the $\alpha\beta$ frame. Figure 3.13 shows the relationship between the injected rotating HF voltage vector and the resulting current response. The injected HF voltage vector is assumed to have constant amplitude rotating with the carrier frequency ω_c, describing a circular locus. The resulting current vector $\underline{i}_c$ will follow the injected rotating voltage vector with approximately 90 ° phase shift. However, the locus of the resulting HF current vector will not be exactly circular due to the stator inductance modulation.

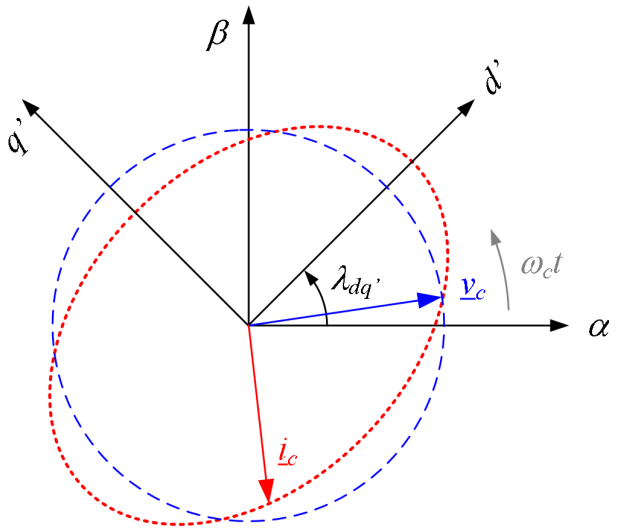

Figure 3.13: Relation between HF voltage and current vector $\underline{v}_c$ and $\underline{i}_c$ in rotating HF voltage injection

Equation (3.24) to (3.26) describe the resulting HF current response to the injected HF voltage $\underline{v}_c$ and modulated high frequency inductance tensor $\mathbf{L}_{c\alpha\beta}$.

$$\underline{i}_{c\alpha\beta} = \mathbf{L}_{c\alpha\beta}^{-1} \int \left(V_c e^{j\omega_c t} \right) dt \tag{3.24}$$

$$\begin{bmatrix} i_{c\alpha} \\ i_{c\beta} \end{bmatrix} = \frac{1}{L_c^{\,2} + \left(\frac{\Delta L_c}{2}\right)^2} \begin{bmatrix} L_c + \frac{\Delta L_c}{2}\cos\left(2\lambda_{dq'}\right) & \frac{\Delta L_c}{2}\sin\left(2\lambda_{dq'}\right) \\ \frac{\Delta L_c}{2}\sin\left(2\lambda_{dq'}\right) & L_c - \frac{\Delta L_c}{2}\cos\left(2\lambda_{dq'}\right) \end{bmatrix} \cdot \frac{V_c}{\omega_c} \begin{bmatrix} \sin\left(\omega_c t\right) \\ -\cos\left(\omega_c t\right) \end{bmatrix} \tag{3.25}$$

$$\underline{i}_{c\alpha\beta} = \frac{L_c}{L_c^{\,2} + \left(\frac{\Delta L_c}{2}\right)^2} \frac{V_c}{\omega_c} e^{\,j\left(\omega_c t - \frac{\pi}{2}\right)} + \frac{\frac{\Delta L_c}{2}}{L_c^{\,2} + \left(\frac{\Delta L_c}{2}\right)^2} \frac{V_c}{\omega_c} e^{\,-j\left(\omega_c t - 2\lambda_{dq'} - \frac{\pi}{2}\right)} \tag{3.26}$$

$$\underline{i}_{c\alpha\beta} = i_{cp}\, e^{\,j\left(\omega_c t - \frac{\pi}{2}\right)} + i_{cn}\, e^{\,-j\left(\omega_c t - 2\lambda_{dq'} - \frac{\pi}{2}\right)} \tag{3.27}$$

From equation (3.27) it can be seen that the resulting HF current contains two rotating vector components. One component is rotating with the injected voltage frequency in the same direction and one rotating at ($-\omega_c+2\lambda_{dq'}$) in the opposite direction to the injected HF voltage. The $\underline{i}_{cp}$ term is also referred to as positive sequence and the $\underline{i}_{cn}$ term as the negative sequence component [6].

Jansen and Lorenz [35] suggest an observer to track the saliency modulation in the HF currents. Figure 3.14 shows the block diagram of the proposed PLL observer structure. The algorithm uses an estimated dq^e frame with the angular position $\lambda_{dq'}{}^e$. The PLL adjusts the position of the estimated dq^e frame to be aligned with the saliency dq' frame. Therefore at lock in condition $\lambda_{dq'}{}^e$ equals $\lambda_{dq'}{}^e$.

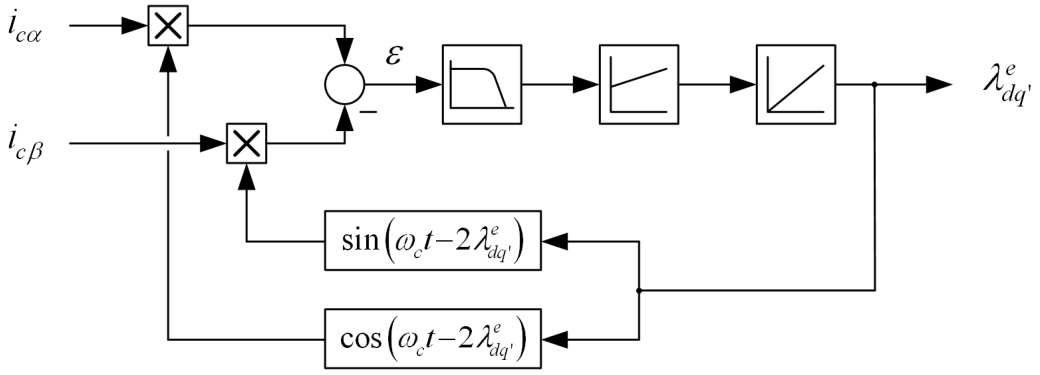

Figure 3.14: Observer to track saliency modulation in rotating HF currents

The error signal ε of the PLL can be given as function of the $\alpha\beta$ HF current components or the positive and negative sequence currents i_{cp} and i_{cn}:

$$\varepsilon = i_{c\alpha}\cos\left(\omega_c t - 2\lambda^{e}_{dq'}\right) - i_{c\beta}\sin\left(\omega_c t - 2\lambda^{e}_{dq'}\right) , \tag{3.28}$$

$$\varepsilon = i_{cp}\sin\left(2\omega_c t - 2\lambda^{e}_{dq'}\right) + i_{cn}\sin\left(2\lambda_{dq'} - 2\lambda^{e}_{dq'}\right) . \tag{3.29}$$

Due to the low pass filter and the limited bandwidth of the PI controller the first term of (3.29) resulting from the positive sequence HF currents can be neglected. Equation (3.30) states the final result for the effective error signal affecting the tracking PLL.

$$\varepsilon = k\sin\left(2\lambda^{e}_{dq'} - 2\lambda_{dq'}\right) \tag{3.30}$$

For small errors the error signal is almost directly proportional to the difference in the estimated position $\lambda_{dq'}{}^{e}$ and the real saliency position $\lambda_{dq'}$. The PLL error signal ε will decay to zero for the case that the correct saliency position is tracked.

Another approach is suggested by Teske [6]. The modulation of the HF current $\underline{i}_{c\alpha\beta}$ is decoupled via a heterodyning technique and the resulting position information is directly derived via an arcus tangens (atan) function. Figure 3.15 shows a block diagram of the proposed position estimation from the HF currents via heterodyning and atan function.

Figure 3.15: Block diagram of position estimator with heterodyning demodulation and atan

First the HF currents measured in the $\alpha\beta$ frame are transformed into the positive sequence reference frame rotating forward with ω_c. Therefore the negative sequence is shifted to about twice the injected HF frequency, while the positive sequence component appears as DC.

$$\underline{i}_{c\alpha\beta}\, e^{-j\omega_c t} \;=\; i_{cp} + i_{cn}\, e^{-j\left(2\omega_c t - 2\lambda_{dq'}\right)} \tag{3.31}$$

By high pass filtering the resulting current signal, the positive sequence HF carrier is filtered off. In a further step the signal is transformed to the negative sequence frequency which contains the desired modulation information.

$$i_{cn}\, e^{-j\left(2\omega_c t - 2\lambda_{dq'}\right)}\, e^{j2\omega_c t} \;=\; i_{cn}\, e^{j2\lambda_{dq'}} \tag{3.32}$$

Equation (3.32) shows that the desired saliency modulation information is directly available after the demodulation process. The final rotor position estimate is then derived by the atan function (3.33).

$$\lambda_{dq'} = \frac{1}{2}\operatorname{atan}\left(\frac{\operatorname{Im}\left(i_{cn}\, e^{j2\lambda_{dq'}}\right)}{\operatorname{Re}\left(i_{cn}\, e^{j2\lambda_{dq'}}\right)}\right) \tag{3.33}$$

Since in the atan function the real and imaginary part of the complex vector is used, the total vector amplitude does not affect the position estimation result.

Consoli [36] suggests another demodulation strategy. Only the HF current amplitude is detected. The measured $\underline{i}_c$ amplitude and the known direction of the HF voltage injection give information about the machine saliency position. The algorithm tracks the minimum and maximum of the resulting HF current amplitude. Figure 3.16 shows the block diagram of the method.

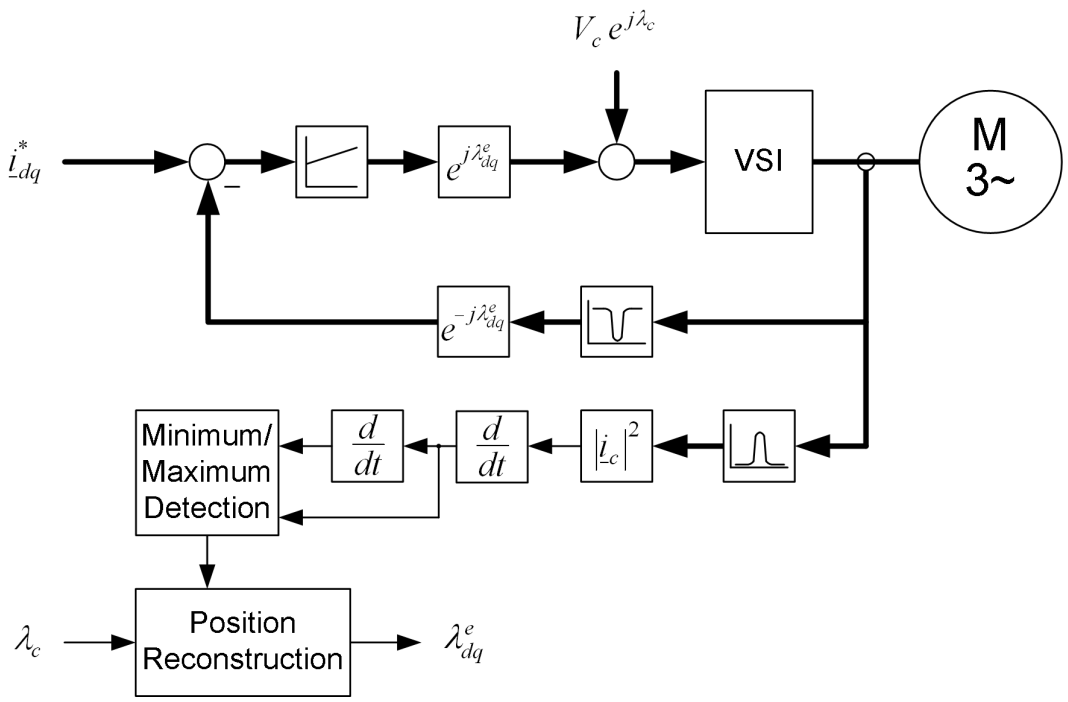

Figure 3.16: Demodulation of rotating HF current by detecting minimum and maximum amplitude

The modulated HF current signal frequency is the injected HF voltage frequency ω_c minus the dq' saliency modulation frequency $\omega_{dq'}$. Therefore the dq' saliency modulation velocity can be estimated from the stator HF currents. The HF current signal sampling is adjusted to take exactly four samples per period. Therefore the sample frequency is adjusted according to the modulation frequency $\omega_{dq'}$. The A look up table based algorithm is used in the implementation to adjust the sample instances to coincide with the maxima and minima of the HF current amplitude. Therefore the current sampling frequency is adjusted to the HF current negative sequence modulation frequency. The position of the injected HF voltage during the HF minima and maxima samples gives then the position of the detected saliency. Figure 3.17 shows the HF current amplitude sampling for a constant saliency position $\lambda_{dq'}$. The position λ_c during the maximum/ minimum detection of the HF current amplitude indicates the position of the saliency frame dq'. The HF current amplitude samples are indicated by the black dots in the figure and the dashed lines show the simultaneous registered position of the rotating HF voltage vector.

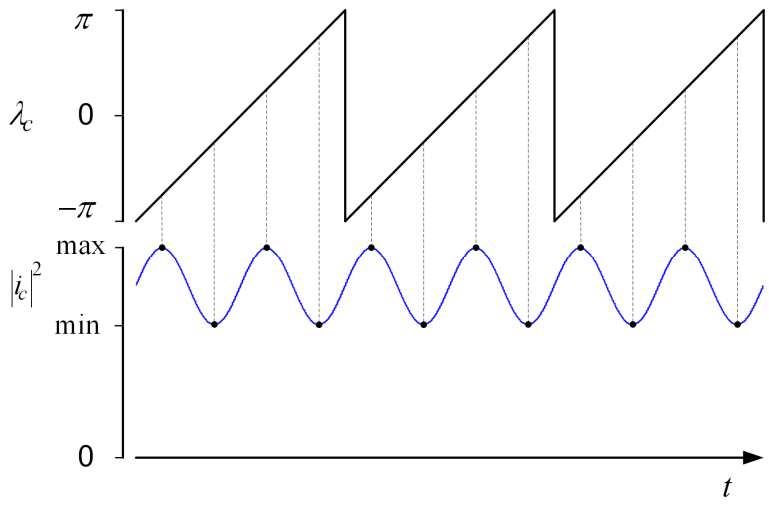

Figure 3.17: Sampling of HF current amplitude at minimum and maximum

3.3.2 Rotating $\alpha\beta$ Frame HF Voltage Injection and Zero-Sequence Carrier-Signal Detection

A further approach that uses the injection of a rotating high frequency voltage has been proposed by Consoli [37]. The method applies to star connected machines as shown in Figure 3.18. Due to the unbalance in the three phase inductances a HF signal is detectable in the zero sequence voltage v_0 (3.34), although a balanced rotating voltage is injected into the machine. For the detection of v_0 the three phase voltages v_A, v_B and v_C can be directly measured and summed up as shown in equation (3.34). Alternatively the star point voltage can be measured against a virtual zero voltage potential created by two capacitors in the DC link [37] or by measuring the machine star point potential against the star point of a balanced resistor network [38]. This results in only one additional voltage sensor required.

$$v_0 = v_A + v_B + v_C \tag{3.34}$$

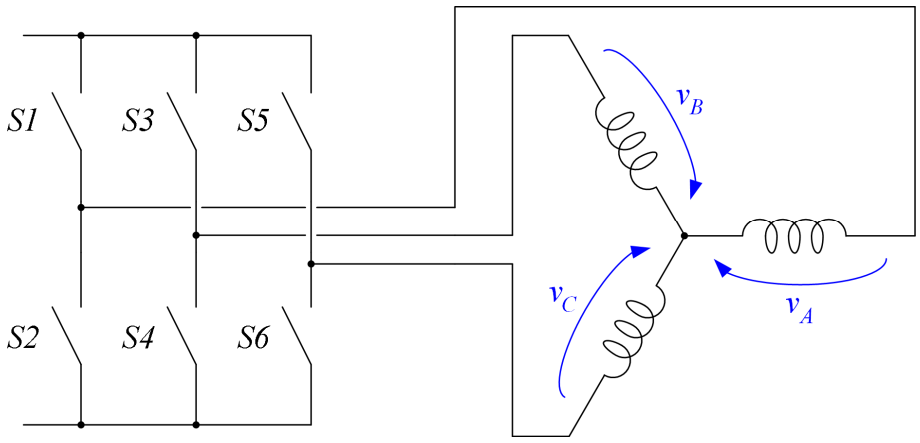

Figure 3.18: Equivalent circuit for zero sequence voltage measurement

Due to the interaction of the magnetic saliency and the injected high frequency voltage rotating with ω_c, the zero sequence voltage will also show a high frequency

component ω_c - $\omega_{\lambda dq'}$. Therefore, the velocity of the rotating dq' frame can be directly derived from the measured zero sequence voltage HF modulation. Consoli proposes in [37] for the demodulation a look up table based algorithm that samples the HF zero sequence voltage exactly four times per period, similar to the sensorless technique described in [36]. The zero sequence HF voltage is sampled at the maximum, the minimum and the two zero crossings per period. The zero crossing samples are used to track the modulation frequency and the minimum and maximum samples are used to derive the saliency frame position $\lambda_{dq'}$.
Consoli proposes in [39] an alternative procedure, where the zero sequence voltage is obtained from the voltage measurement between an artificial neutral point created by a balanced set of three star connected impedances and the midpoint of the DC bus. Hence, this method can be extended to drives in which the neutral of the stator winding is not available or additional wireing between the inverter and the machine star point is not allowed.

Briz [40] extended the principle to delta connected machines as shown in Figure 3.19 by measuring the zero sequence current. For the measurement of the zero sequence current i_0 (3.35) all three winding currents i_{AB}, i_{BC} and i_{CA} are summed through one single Hall-effect transducer [40]. The content of the HF signal in the zero sequence current then gives information about the position of the saliency frame dq'.

$$i_0 = i_{AB} + i_{BC} + i_{CA} \tag{3.35}$$

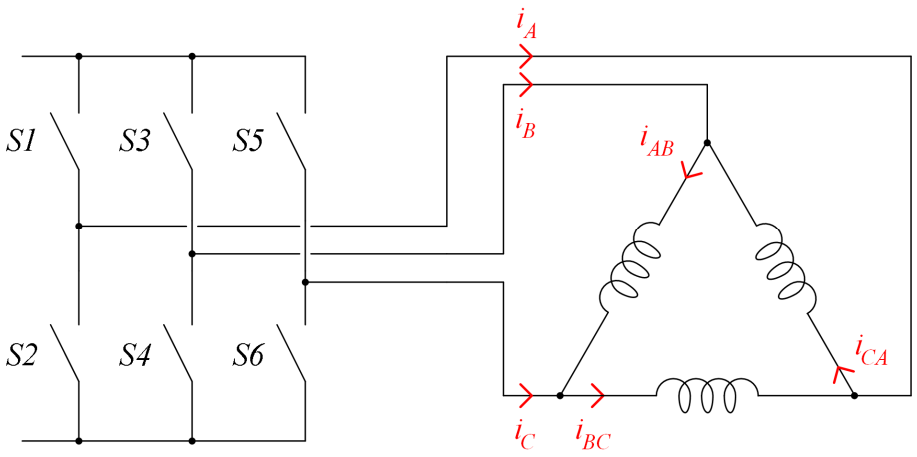

Figure 3.19: Equivalent circuit for zero sequence current measurement

3.3.3 Synchronous *dq'* Frame HF Voltage Injection

Synchronous frame injection has been reported in a number of publications e.g. [41-45]. The algorithm uses an estimated dq^e frame located at the position $\lambda_{dq'}{}^e$. The PLL tracking algorithm adjusts the position of the estimated dq^e frame to be aligned with the saliency dq' frame located at the position $\lambda_{dq'}$. Therefore, under correct position tracking $\lambda_{dq'}{}^e$ equals $\lambda_{dq'}$. The difference between the reference frames is λ_{err}, defined as:

$$\lambda_{err} = \lambda_{dq'}^{e} - \lambda_{dq'} \quad . \tag{3.36}$$

It is a tracking technique, that follows the minimum or maximum inductance designating the position of the dq' reference frame. The HF voltage is added to either the estimated d^e or q^e axis. Therefore in sensorless operation the injection of the HF voltage depends directly on the estimated dq^e reference frame position. Equation (3.37) shows the definition of the injected pulsating high frequency voltage vector for the case that the injection is done in d^e direction. Figure 3.20 shows the resulting

block diagram. The used HF voltage reference is added in software to the reference value of the fundamental voltages.

$$\underline{v}^{e}_{cdq'} = V_c \cos(\omega_c t) e^{j\lambda^{e}_{dq'}} \tag{3.37}$$

Equation (3.38) to (3.40) show the mathematical derivation for the resulting current response to the injected pulsating HF voltage into d^e direction.

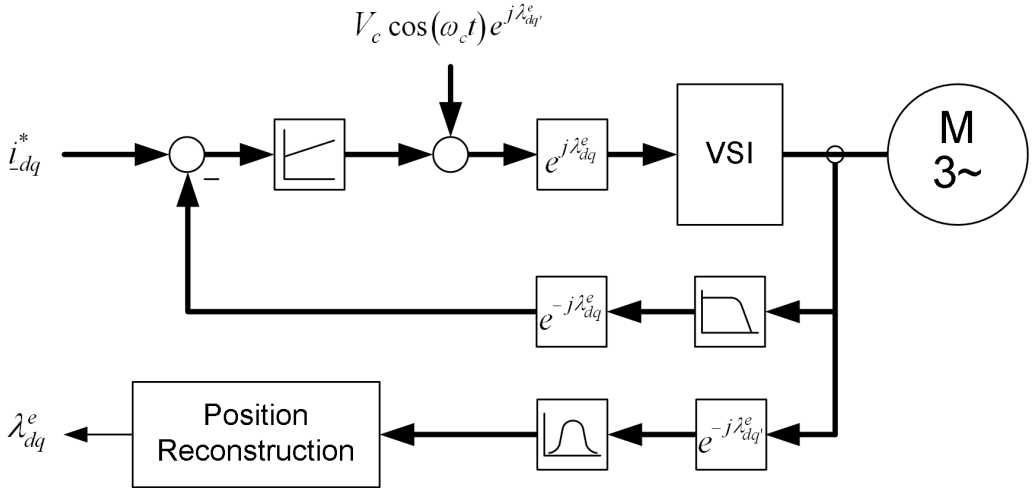

Figure 3.20: Block diagram of pulsating HF voltage carrier injection

$$\begin{bmatrix} i_{cd'}{}^{e} \\ i_{cq'}{}^{e} \end{bmatrix} = \frac{1}{L_c{}^2 + \left(\frac{\Delta L_c}{2}\right)^2} \cdot \begin{bmatrix} L_c + \frac{\Delta L_c}{2}\cos(2\lambda_{err}) & -\frac{\Delta L_c}{2}\sin(2\lambda_{err}) \\ -\frac{\Delta L_c}{2}\sin(2\lambda_{err}) & L_c - \frac{\Delta L_c}{2}\cos(2\lambda_{err}) \end{bmatrix} \cdot \frac{V_c}{\omega_c} \begin{bmatrix} \sin(\omega_c t) \\ 0 \end{bmatrix} \tag{3.38}$$

$$i_{cd'}{}^{e} = \frac{L_c}{L_c{}^2 + \left(\frac{\Delta L_c}{2}\right)^2}\frac{V_c}{\omega_c}\sin(\omega_c t) + \frac{\frac{\Delta L_c}{2}}{L_c{}^2 + \left(\frac{\Delta L_c}{2}\right)^2}\cos(2\lambda_{err})\frac{V_c}{\omega_c}\sin(\omega_c t) \tag{3.39}$$

$$i_{cq'}{}^{e} = \frac{-\frac{\Delta L_c}{2}}{L_c{}^2 + \left(\frac{\Delta L_c}{2}\right)^2}\sin(2\lambda_{err})\frac{V_c}{\omega_c}\sin(\omega_c t) \tag{3.40}$$

The resulting HF current component in the estimated quadrature axis q^e (for injection in d^e axis) is used for position tracking. It can be seen from equation (3.40) that this term decays to zero for the case in which $\lambda_{err} = 0$. Therefore, the sensorless algorithm adjusts continuously the direction of the pulsating voltage injection until this condition is met. The used tracking algorithm forms a PLL that keeps the estimated dq^e frame locked to the real dq' frame by forcing λ_{err} to zero. Figure 3.21 visualises the position tracking technique. The blue vector symbolises the injected pulsating voltage vector $\underline{v}_c$. The pulsating current response vector $\underline{i}_c$ will be also aligned with the d^e axis if $\lambda_{err} = 0$. Therefore the position of the estimated dq^e saliency frame is adjusted until $\underline{i}_{cq'}{}^{e} = 0$.

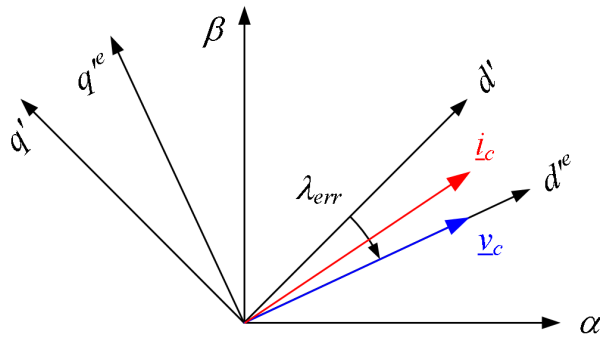

Figure 3.21: Relation between voltage and current vector $\underline{v}_c$ and $\underline{i}_c$ in pulsating HF carrier injection

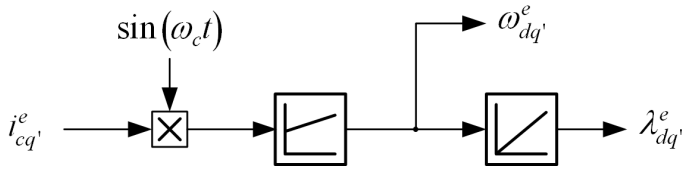

Figure 3.22: Block diagram of *dq'* frame tracking PLL

Figure 3.22 shows the structure of the PLL tracking algorithm for the case in which the pulsating HF voltage excitation is injected into the d^e direction. The high frequency current response in quadrature to the injected HF voltage is directly used as the input. The demodulated signal gives information of the position estimation error which is fed to the PLL PI controller. The PI controller adjusts the estimated speed until the HF current in q^e axis is zero. The integral of the estimated speed gives the estimated *dq'* frame position which is also used for the control of the HF voltage injection. The demodulation is done with a heterodyning scheme. A low pass filter can be implemented for the carrier frequency removal in the demodulated signal. However, some implementations [44], [45] do not use a low pass filter, but feed the HF signal directly into the PLL controller input. This minimizes phase lagging for the position estimation PLL that might be introduced by the low pass filter. The high frequency component is then inherently filtered out by the limited bandwidth of the PI controller. As an alternative [43] uses a bang-bang controller. In this case a low pass filter for the HF frequency of the demodulated signal is necessary due to the high bandwidth of the bang-bang controller.

The injection of the pulsating HF voltage is usually made on the d^e axis. Therefore the resulting HF current ripple affects mostly the flux producing fundamental current in *d* axis. In induction machines the rotor flux reaction of the machine is filtered by the rotor time constant and in PMSM's the variation of the *d* axis current has only a little effect on the rotor flux due to the relative larger air gap. Thus the effect on the resulting machine torque is minimal. In PMSM's the fundamental current into the *d*

axis is mostly set to zero. Therefore inverter non-linearity effects due to low current levels are more pronounced in the machine *d* axis. The final inverter disturbances for the sensorless position estimation scheme depend on the particular machine and inverter design. [46] suggests that injection of the pulsating HF voltage rather into the machine q^e axis can reduce inverter disturbances. However, the trade off are larger torque ripple caused by higher HF current ripple in the vector control *q* axis.

The synchronous frame injection is usually used for saliencies that rotate directly with the rotor flux position. It therefore finds many applications on synchronous permanent magnet machines [42-45]. For the use of this technique in induction machine drives only saturation saliency tracking has been reported [23], [41].

3.4 Transient Voltage Injection

A different approach to detect the saliency modulation of the machine leakage inductance is to introduce impulse transient conditions on the machine stator windings. In this case dedicated active voltage vectors are applied at certain points in time. The stator current response during the transient voltage excitation in the time domain gives information about the stator inductance modulation. The current sampling has to be synchronised to the applied test voltage impulses. Figure 3.23 shows a voltage source inverter (VSI) circuit diagram for a three phase drive as used in the techniques described below. All six active voltage vectors can be used as the test voltage as shown in Figure 3.24.

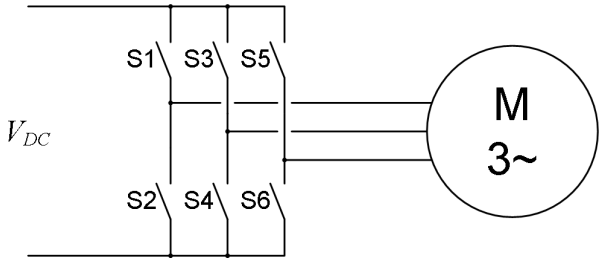

Figure 3.23: Principle circuit of three phase voltage source inverter

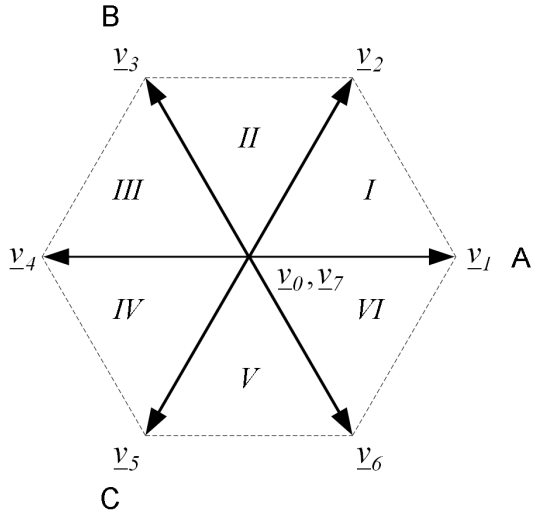

	A	B	C
$\underline{v}_0$	0	0	0
$\underline{v}_1$	1	0	0
$\underline{v}_2$	1	1	0
$\underline{v}_3$	0	1	0
$\underline{v}_4$	0	1	1
$\underline{v}_5$	0	0	1
$\underline{v}_6$	1	0	1
$\underline{v}_7$	1	1	1

Figure 3.24: Voltage space vectors in three phase voltage source inverters

Several test vector sequences are applied to estimate the machine saliency position. The active test voltage vectors are embedded between the fundamental generated PWM voltage switching. Furthermore the total voltage time integral of the additional voltage injection is zero and thus the value of the fundamental generated machine voltage is not changed. The duration of these active test vectors should be as short as possible to reduce resulting current distortions. However, due to transient conditions high frequency oscillations occur in the machine windings currents after the inverter switching instances. Therefore the stator current response measurements are necessarily delayed from the switching instances. The required delay determines the minimum test voltage duration.

3.4.1 The INFORM Method

This method has been introduced by Schroedl [47]. The abbreviation "INFORM" stands for "INdirect Flux detection by On-line Reactance Measurement". The magnetic saliency is detected by measuring the change of the complex stator current vector during a stator voltage test vector interval. The measurement is made in different test voltage vector directions. The stator winding circuit is represented by the complex INFORM admittance $\underline{y}_{INFORM}$ (3.41) that is subject to the machine saliency [47].

$$\underline{y}_{INFORM} = y_0 + \Delta y\, e^{j\left(2\lambda_{dq'} - 2\angle \underline{v}_s\right)} \tag{3.41}$$

The resulting INFORM admittance (3.41) describes a complex vector that consists of the constant offset y_0 plus a rotating Δy modulation that is defined by the saliency position $\lambda_{dq'}$ and the position of the applied voltage vector $\angle \underline{v}_s$. Equation (3.42) describes the general relation of the stator current derivative during the application of any stator voltage. As can be seen, the change of the stator current vector $\underline{i}_S$ is directly affected by the excitation stator voltage vector $\underline{v}_S$ and the saliency modulated stator admittance. Furthermore the back EMF $\underline{e}$ influence is taken into account in equation (3.42).

$$\frac{d\underline{i}_S}{dt} = \left(\underline{v}_S - \underline{e}\right)\left(y_0 + \Delta y\, e^{j\left(2\lambda_{dq'} - 2\angle \underline{v}_S\right)}\right) \tag{3.42}$$

Applying only an active voltage space vector in the direction of one of the three phases *A,B,C*, gives (3.43) to (3.45) as solutions for the current change in the phases of the applied voltage vector. If voltage vectors in the opposite direction to the three phase directions are applied, the resulting phase current changes are described by equation (3.46) to (3.48). The superscripts (1) to (6) indicate which voltage vector is

applied. For the basic principle explained in [47] only the phase current change of the test voltage vector direction is used. Therefore only the modulation of the real part of the INFORM admittance $\underline{y}_{INFORM}$ is considered.

$$\frac{\Delta i_A^{(1)}}{\Delta t} = \left(V - e_A\right)\left(y_0 + \Delta y \cos\left(2\lambda_{dq'}\right)\right) \tag{3.43}$$

$$\frac{\Delta i_B^{(3)}}{\Delta t} = \left(V - e_B\right)\left(y_0 + \Delta y \cos\left(2\lambda_{dq'} - \frac{2}{3}\pi\right)\right) \tag{3.44}$$

$$\frac{\Delta i_C^{(5)}}{\Delta t} = \left(V - e_C\right)\left(y_0 + \Delta y \cos\left(2\lambda_{dq'} + \frac{2}{3}\pi\right)\right) \tag{3.45}$$

$$\frac{\Delta i_A^{(4)}}{\Delta t} = -\left(V + e_A\right)\left(y_0 + \Delta y \cos\left(2\lambda_{dq'}\right)\right) \tag{3.46}$$

$$\frac{\Delta i_B^{(6)}}{\Delta t} = -\left(V + e_B\right)\left(y_0 + \Delta y \cos\left(2\lambda_{dq'} - \frac{2}{3}\pi\right)\right) \tag{3.47}$$

$$\frac{\Delta i_C^{(2)}}{\Delta t} = -\left(V + e_C\right)\left(y_0 + \Delta y \cos\left(2\lambda_{dq'} + \frac{2}{3}\pi\right)\right) \tag{3.48}$$

In equations (3.43) to (3.48) the applied voltage amplitude V is assumed as constant, only determined by the DC link voltage. The included back EMF terms are very small at very low/ zero frequency operation. However at higher speeds the back EMF influence becomes more significant. If the measurements in the positive and negative direction are made in a short interval of time, it can be assumed that in both measurements the back EMF values are the same. Combining the measurements in positive and negative directions allows cancelling the back EMF effect. The difference of the current derivative in positive and negative voltage excitation direction are shown by equations (3.49) to (3.51) which give directly the admittance modulation.

$$\frac{\Delta i_A^{(1)}}{\Delta t} - \frac{\Delta i_A^{(4)}}{\Delta t} = 2V\left(y_0 + \Delta y \cos\left(2\lambda_{dq'}\right)\right) \tag{3.49}$$

$$\frac{\Delta i_B^{(3)}}{\Delta t} - \frac{\Delta i_B^{(6)}}{\Delta t} = 2V\left(y_0 + \Delta y \cos\left(2\lambda_{dq'} - \frac{2}{3}\pi\right)\right) \tag{3.50}$$

$$\frac{\Delta i_C^{(5)}}{\Delta t} - \frac{\Delta i_C^{(2)}}{\Delta t} = 2V\left(y_0 + \Delta y \cos\left(2\lambda_{dq'} + \frac{2}{3}\pi\right)\right) \tag{3.51}$$

A further advantage of applying two opposite active voltage vectors in one measurement sequence is that the average volt time area does not change and the fundamental generated voltage is not affected. The applied measurement sequence is $\underline{v}_1$, $\underline{v}_4$, ... $\underline{v}_3$, $\underline{v}_6$, ... $\underline{v}_5$,$\underline{v}_2$. The measurement pairs are inserted between the fundamental control PWM cycles. The last three measurements pairs of the three phase directions are continuously combined to $\underline{P}$ shown by equation (3.52) whose argument gives the position of the detected INFORM admittance saliency modulation (3.53). As can be seen the amplitude of the applied voltage and the magnitude of the saliency modulation is not of interest. Only the argument of the detected INFORM admittance modulation is used for the position estimation.

$$\begin{aligned}\underline{P} &= \left(\frac{\Delta i_A^{(1)}}{\Delta t} - \frac{\Delta i_A^{(4)}}{\Delta t}\right)e^{j0} + \left(\frac{\Delta i_B^{(3)}}{\Delta t} - \frac{\Delta i_B^{(6)}}{\Delta t}\right)e^{j\frac{2}{3}\pi} + \left(\frac{\Delta i_C^{(5)}}{\Delta t} - \frac{\Delta i_C^{(2)}}{\Delta t}\right)e^{-j\frac{2}{3}\pi} \\ &= 2V\,\Delta y\, e^{j2\lambda_{dq'}}\end{aligned} \tag{3.52}$$

$$\angle\underline{P} = 2\lambda_{dq'} \tag{3.53}$$

This description of the INFORM method presents only the very basic principle. It considers only the real part of the saliency modulation, since only the current change into direction of the applied voltage test vector is used. [47] shows that the imaginary part can be additionally used to improve the position estimation. The position information derived from the measured real and imaginary parts in the INFORM

reactance is combined by means of a Kalman filter. In further work of Schroedl it is also shown that the applied test vector sequence can be enhanced to achieve better performance with normal fundamental machine current control [48].

3.4.2 Transient Zero Sequence Voltage Measurement

Holtz suggests a method that measures the zero sequence voltage to detect the leakage inductance saliency information. [49-51] show results for the rotor bar slot tracking of an induction machine that is connected in wye. The three phase voltages are measured as shown in Figure 3.18. The zero sequence voltage v_0 (3.54) is obtained under the application of dedicated active voltage test vectors. A measurement sequence, to test for the three phase winding inductance modulation, similar to the one described before is used. The active voltage test vectors are embedded during the zero vectors of the fundamental PWM control. Since one test vector sequence consists of two opposite direction voltage vectors with equal duration, the total voltage-time area is zero and the fundamental voltage is not changed.

$$v_0 = v_A + v_B + v_C \tag{3.54}$$

Equation (3.55) to (3.57) state the resulting measurement signals which reveal the saliency modulation in the three machine phases. The result per phase is the difference of the two measurements for the opposite test vector excitation along the phase axis.

$$v_0^{(1)} - v_0^{(4)} = 2V_{DC}\frac{l_A l_B + l_A l_C - 2 l_B l_C}{l_A l_B + (l_A + l_B) l_C} \tag{3.55}$$

$$v_0^{(3)} - v_0^{(6)} = 2V_{DC}\frac{l_B l_C + l_B l_A - 2 l_C l_A}{l_B l_C + (l_B + l_C) l_A} \tag{3.56}$$

$$v_0^{(5)} - v_0^{(2)} = 2V_{DC}\frac{l_C l_A + l_C l_B - 2 l_A l_B}{l_C l_A + (l_C + l_A) l_B} \tag{3.57}$$

Combining the measurements of all three phases to one complex signal $\underline{P}$ (3.58), gives as argument the detected saliency position (3.59).

$$\underline{P} = \left(v_0^{(1)} - v_0^{(4)}\right) + \left(v_0^{(3)} - v_0^{(6)}\right) e^{j\frac{2}{3}\pi} + \left(v_0^{(5)} - v_0^{(2)}\right) e^{-j\frac{2}{3}\pi} \tag{3.58}$$

$$\angle \underline{P} = 2\lambda_{dq'} \tag{3.59}$$

3.4.3 Transient Zero Sequence Current Measurement

An equivalent to the zero sequence voltage measurement technique, has been developed by Caruana [26] for delta connected machines as shown in Figure 3.19. In this method also dedicated test voltage vector sequences in the *A, B, C* phase directions are applied. The zero sequence current derivatives measured during the test voltage vectors (3.60) are used. For the current derivative acquisition a non-integrating Rogowsky coil is used. Only one Rogowsky coil is used that encloses simultaneously all three phase conductors and hence measures directly di_0/dt:

$$\frac{di_0}{dt} = \frac{di_{AB}}{dt} + \frac{di_{BC}}{dt} + \frac{di_{CA}}{dt} \quad . \tag{3.60}$$

The active voltage vector measurement sequence is also applied in pairs $\underline{v}_1$, $\underline{v}_4$, ... $\underline{v}_3$, $\underline{v}_6$, ... $\underline{v}_5$,$\underline{v}_2$. The resulting position signals are shown by equation (3.61) to (3.63). The superscripts (1) to (6) indicate which voltage vectors are applied.

$$\frac{di_0}{dt}^{(1)} - \frac{di_0}{dt}^{(4)} = 2V_{DC}\left(\frac{1}{l_A} - \frac{1}{l_C}\right) \tag{3.61}$$

$$\frac{di_0}{dt}^{(3)} - \frac{di_0}{dt}^{(6)} = 2V_{DC}\left(\frac{1}{l_B} - \frac{1}{l_A}\right) \tag{3.62}$$

$$\frac{di_0}{dt}^{(5)} - \frac{di_0}{dt}^{(2)} = 2V_{DC}\left(\frac{1}{l_C} - \frac{1}{l_B}\right) \tag{3.63}$$

These measurements of the three phase test vector excitations are also combined to a complex signal $\underline{P}$ (3.64), which gives as argument the detected saliency position (3.65).

$$\underline{P} = \left(\frac{di_0}{dt}^{(1)} - \frac{di_0}{dt}^{(4)}\right) + \left(\frac{di_0}{dt}^{(3)} - \frac{di_0}{dt}^{(6)}\right) e^{j\frac{2}{3}\pi} + \left(\frac{di_0}{dt}^{(5)} - \frac{di_0}{dt}^{(2)}\right) e^{-j\frac{2}{3}\pi} \tag{3.64}$$

$$\angle\underline{P} = 2\lambda_{dq'} \tag{3.65}$$

3.4.4 Saliency Measurement by Extended Modulation

Holtz presented [52] a technique that uses the transient excitation of active voltage vectors that are also used for the fundamental voltage generation. This avoids the generation of separate test voltage vectors and reduces the inverter switching instances. The used PWM scheme is denoted as extended modulation (EM). The available voltage vector space is devided into four overlapping 120° sectors as shown in Figure 3.25.

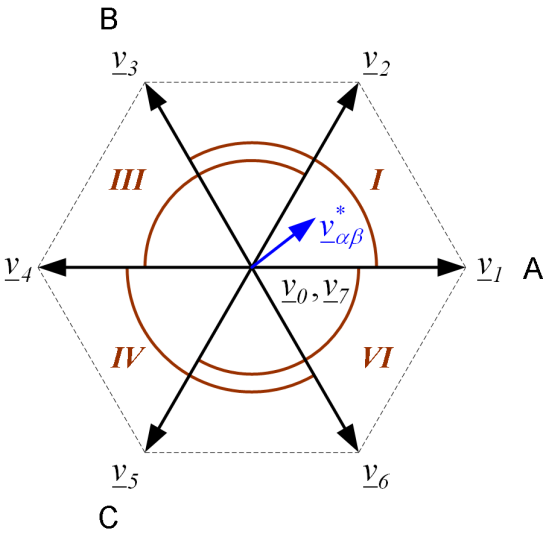

Figure 3.25: Definition of the 120 ° wide extended modulation sectors in VSI vector space

Table 3.1 states the inverter switching sequences for the four extended sectors. The used switching sequence is selected by the position of the fundamental reference voltage vector $\underline{v}_{\alpha\beta}^*$. For the saliency detection the current derivative is measured in all three motor phases. Very simple coaxial cable transformer coils are used for the measurement. The current derivatives are simultaneously sampled in all three phases during certain active voltage vectors. In the extended sector ***I*** the current derivatives are measured during the active vectors $\underline{v}_1$ and $\underline{v}_3$. The opposite direction voltage vectors $\underline{v}_6$ and $\underline{v}_4$ are only used to compensate for the extended duration of the measurement vectors $\underline{v}_1$ and $\underline{v}_3$. This ensures the required volt-time area during the PWM period for the fundamental voltage generation. The extension of the measurement voltage vectors is required due to high frequency oscillations in the currents after the inverter switching instances. Therefore the *di/dt* measurement is done a few µs after the last switching instance, which defines the minimum measurement vector duration. Table 3.1 states the measurement voltage vectors used and the resulting compensation vectors.

EM sector:	Inverter witching sequence:	Measurement:	Compensation:
I	$\underline{v}_0 \ldots \underline{v}_1 \ldots \underline{v}_6 \ldots \underline{v}_7 \ldots \underline{v}_4 \ldots \underline{v}_3 \ldots \underline{v}_0$	$\underline{v}_1, \underline{v}_3$	$\underline{v}_4, \underline{v}_6$
II	$\underline{v}_0 \ldots \underline{v}_1 \ldots \underline{v}_2 \ldots \underline{v}_7 \ldots \underline{v}_4 \ldots \underline{v}_5 \ldots \underline{v}_0$	$\underline{v}_2, \underline{v}_4$	$\underline{v}_1, \underline{v}_5$
III	$\underline{v}_0 \ldots \underline{v}_3 \ldots \underline{v}_4 \ldots \underline{v}_7 \ldots \underline{v}_6 \ldots \underline{v}_1 \ldots \underline{v}_0$	$\underline{v}_4, \underline{v}_6$	$\underline{v}_1, \underline{v}_3$
IV	$\underline{v}_0 \ldots \underline{v}_5 \ldots \underline{v}_4 \ldots \underline{v}_7 \ldots \underline{v}_2 \ldots \underline{v}_1 \ldots \underline{v}_0$	$\underline{v}_5, \underline{v}_1$	$\underline{v}_2, \underline{v}_4$

Table 3.1: Extended modulation switching patterns

The three phase current derivatives measured during the "test" vectors are used to calculate the complex saliency position signal $\underline{P}$ (3.66) that contains as argument the saliency modulation position (3.67). The calculations of p_A, p_B and p_C depend directly on the applied measurement voltage vectors and on the machine connection (wye or delta). Table 3.2 states the position signals derived from the applied active voltage vector for a wye connected machine and Table 3.3 shows the position signal equations for a delta connected machine [52]. The superscripts (1) to (6) indicate which voltage vector is applied. The coefficients *g* and *h* stated in Table 3.2 and Table 3.3 are given by equation (3.68) and (3.69). The inductance values *L* and ΔL refer to the assumed three phase equivalent inductance modulation stated in (3.8) to (3.10).

$$\underline{P} = p_A + p_B e^{j\frac{2}{3}\pi} + p_C e^{-j\frac{2}{3}\pi} \tag{3.66}$$

$$\angle \underline{P} = 2\lambda_{dq'} \tag{3.67}$$

$p_A = -g\frac{di_A}{dt}^{(1)} + 2$	$p_C = -g\frac{di_B}{dt}^{(1)} - 1$	$p_B = -g\frac{di_C}{dt}^{(1)} - 1$
$p_B = g\frac{di_A}{dt}^{(2)} - 1$	$p_A = g\frac{di_B}{dt}^{(2)} - 1$	$p_C = g\frac{di_C}{dt}^{(2)} + 2$
$p_C = -g\frac{di_A}{dt}^{(3)} - 1$	$p_B = -g\frac{di_B}{dt}^{(3)} + 2$	$p_A = -g\frac{di_C}{dt}^{(3)} - 1$
$p_A = g\frac{di_A}{dt}^{(4)} + 2$	$p_C = g\frac{di_B}{dt}^{(4)} - 1$	$p_B = g\frac{di_C}{dt}^{(4)} - 1$
$p_B = -g\frac{di_A}{dt}^{(5)} - 1$	$p_A = -g\frac{di_B}{dt}^{(5)} - 1$	$p_C = -g\frac{di_C}{dt}^{(5)} + 2$
$p_C = g\frac{di_A}{dt}^{(6)} - 1$	$p_B = g\frac{di_B}{dt}^{(6)} + 2$	$p_A = g\frac{di_C}{dt}^{(6)} - 1$

Table 3.2: Position signals for extended modulation (wye connection)

$$g = \frac{3L}{V_{DC}}\left(1-\left(\frac{\Delta L}{2L}\right)^2\right) \tag{3.68}$$

$p_B = h\frac{di_A}{dt}^{(1)} - 2$	$p_A = h\frac{di_B}{dt}^{(1)} + 1$	$p_C = h\frac{di_C}{dt}^{(1)} + 1$
$p_C = -h\frac{di_A}{dt}^{(2)} + 1$	$p_B = -h\frac{di_B}{dt}^{(2)} + 1$	$p_A = -h\frac{di_C}{dt}^{(2)} - 2$
$p_A = h\frac{di_A}{dt}^{(3)} + 1$	$p_C = h\frac{di_B}{dt}^{(3)} - 2$	$p_B = h\frac{di_C}{dt}^{(3)} + 1$
$p_B = -h\frac{di_A}{dt}^{(4)} - 2$	$p_A = -h\frac{di_B}{dt}^{(4)} + 1$	$p_C = -h\frac{di_C}{dt}^{(4)} + 1$

$p_C = h\frac{di_A}{dt}^{(5)} + 1$	$p_B = h\frac{di_B}{dt}^{(5)} + 1$	$p_A = h\frac{di_C}{dt}^{(5)} - 2$
$p_A = -h\frac{di_A}{dt}^{(6)} + 1$	$p_C = -h\frac{di_B}{dt}^{(6)} - 2$	$p_B = -h\frac{di_C}{dt}^{(6)} + 1$

Table 3.3: Position signals for extended modulation (delta connection)

$$h = \frac{L}{V_{DC}} \tag{3.69}$$

3.4.5 Position Estimation Based on Space Vector PWM Excitation

The latest approach of transient response saliency detection has been presented in [53]. There the current derivatives in all three machine phases are also measured by simple coaxial transformer coils. Also the active measurement vectors are embedded within the fundamental PWM. Therefore also no extra switching instances of the inverter occur. Table 3.4 shows the voltage space vector modulation for the six natural commutation sectors as shown in Figure 3.24. Per PWM period the current derivatives are sampled at two active voltage vectors and $\underline{v}_0$. The zero vector measurement is used to compensate for the back EMF influence. Also here the current derivative measurement occurs slightly delayed after the voltage switching to allow HF current oscillations to settle. Thus at very low speed the active measurement voltage vectors have to be extended. The required compensation is done in the second half of the PWM cycle. Table 3.4 states also the measurement and compensation vectors for each PWM cycle.

Commutation sector:	Inverter witching sequence:	Measurement:	Compensation:
I	$\underline{v}_0 \ldots \underline{v}_1 \ldots \underline{v}_2 \ldots \underline{v}_7 \ldots \underline{v}_4 \ldots \underline{v}_5 \ldots \underline{v}_0$	$\underline{v}_0, \underline{v}_1, \underline{v}_2$	$\underline{v}_4, \underline{v}_5$
II	$\underline{v}_0 \ldots \underline{v}_2 \ldots \underline{v}_3 \ldots \underline{v}_7 \ldots \underline{v}_5 \ldots \underline{v}_6 \ldots \underline{v}_0$	$\underline{v}_0, \underline{v}_2, \underline{v}_3$	$\underline{v}_5, \underline{v}_6$
III	$\underline{v}_0 \ldots \underline{v}_3 \ldots \underline{v}_4 \ldots \underline{v}_7 \ldots \underline{v}_6 \ldots \underline{v}_1 \ldots \underline{v}_0$	$\underline{v}_0, \underline{v}_3, \underline{v}_4$	$\underline{v}_6, \underline{v}_1$
IV	$\underline{v}_0 \ldots \underline{v}_4 \ldots \underline{v}_5 \ldots \underline{v}_7 \ldots \underline{v}_1 \ldots \underline{v}_2 \ldots \underline{v}_0$	$\underline{v}_0, \underline{v}_4, \underline{v}_5$	$\underline{v}_1, \underline{v}_2$
V	$\underline{v}_0 \ldots \underline{v}_5 \ldots \underline{v}_6 \ldots \underline{v}_7 \ldots \underline{v}_2 \ldots \underline{v}_3 \ldots \underline{v}_0$	$\underline{v}_0, \underline{v}_5, \underline{v}_6$	$\underline{v}_2, \underline{v}_3$
VI	$\underline{v}_0 \ldots \underline{v}_6 \ldots \underline{v}_1 \ldots \underline{v}_7 \ldots \underline{v}_3 \ldots \underline{v}_4 \ldots \underline{v}_0$	$\underline{v}_0, \underline{v}_6, \underline{v}_1$	$\underline{v}_3, \underline{v}_4$

Table 3.4: Space vector PWM excitation for saliency position estimation

Table 3.5 and Table 3.6 show the equations for the resulting three phase signals that are combined to one position signal (3.70). The factors *g* and *h* are the same stated for the extended modulation method given by equation (3.68) and (3.69).

$p_B = h\left(\frac{di_A}{dt}^{(1)} - \frac{di_A}{dt}^{(0)}\right) - 2$	$p_A = h\left(\frac{di_B}{dt}^{(1)} - \frac{di_B}{dt}^{(0)}\right) + 1$	$p_C = h\left(\frac{di_C}{dt}^{(1)} - \frac{di_C}{dt}^{(0)}\right) + 1$
$p_C = -h\left(\frac{di_A}{dt}^{(2)} - \frac{di_A}{dt}^{(0)}\right) + 1$	$p_B = -h\left(\frac{di_B}{dt}^{(2)} - \frac{di_B}{dt}^{(0)}\right) + 1$	$p_A = -h\left(\frac{di_C}{dt}^{(2)} - \frac{di_C}{dt}^{(0)}\right) - 2$
$p_A = h\left(\frac{di_A}{dt}^{(3)} - \frac{di_A}{dt}^{(0)}\right) + 1$	$p_C = h\left(\frac{di_B}{dt}^{(3)} - \frac{di_B}{dt}^{(0)}\right) - 2$	$p_B = h\left(\frac{di_C}{dt}^{(3)} - \frac{di_C}{dt}^{(0)}\right) + 1$
$p_B = -h\left(\frac{di_A}{dt}^{(4)} - \frac{di_A}{dt}^{(0)}\right) - 2$	$p_A = -h\left(\frac{di_B}{dt}^{(4)} - \frac{di_B}{dt}^{(0)}\right) + 1$	$p_C = -h\left(\frac{di_C}{dt}^{(4)} - \frac{di_C}{dt}^{(0)}\right) + 1$

$p_C = \quad h\left(\frac{di_A}{dt}^{(5)} - \frac{di_A}{dt}^{(0)}\right)+1$	$p_B = \quad h\left(\frac{di_B}{dt}^{(5)} - \frac{di_B}{dt}^{(0)}\right)+1$	$p_A = - \quad h\left(\frac{di_C}{dt}^{(5)} - \frac{di_C}{dt}^{(0)}\right)-2$
$p_A = - \quad h\left(\frac{di_A}{dt}^{(6)} - \frac{di_A}{dt}^{(0)}\right)+1$	$p_C = - \quad h\left(\frac{di_B}{dt}^{(6)} - \frac{di_B}{dt}^{(0)}\right)-2$	$p_B = - \quad h\left(\frac{di_C}{dt}^{(6)} - \frac{di_C}{dt}^{(0)}\right)+1$

Table 3.5: Position signals for SVPWM excitation (delta connection)

$p_A = - \quad g\left(\frac{di_A}{dt}^{(1)} - \frac{di_A}{dt}^{(0)}\right)+2$	$p_C = - \quad g\left(\frac{di_B}{dt}^{(1)} - \frac{di_B}{dt}^{(0)}\right)-1$	$p_B = - \quad g\left(\frac{di_C}{dt}^{(1)} - \frac{di_C}{dt}^{(0)}\right)-1$
$p_B = \quad g\left(\frac{di_A}{dt}^{(2)} - \frac{di_A}{dt}^{(0)}\right)-1$	$p_A = \quad g\left(\frac{di_B}{dt}^{(2)} - \frac{di_B}{dt}^{(0)}\right)-1$	$p_C = \quad g\left(\frac{di_C}{dt}^{(2)} - \frac{di_C}{dt}^{(0)}\right)+2$
$p_C = - \quad g\left(\frac{di_A}{dt}^{(3)} - \frac{di_A}{dt}^{(0)}\right)-1$	$p_B = - \quad g\left(\frac{di_B}{dt}^{(3)} - \frac{di_B}{dt}^{(0)}\right)+2$	$p_A = - \quad g\left(\frac{di_C}{dt}^{(3)} - \frac{di_C}{dt}^{(0)}\right)-1$
$p_A = \quad g\left(\frac{di_A}{dt}^{(4)} - \frac{di_A}{dt}^{(0)}\right)+2$	$p_C = \quad g\left(\frac{di_B}{dt}^{(4)} - \frac{di_B}{dt}^{(0)}\right)-1$	$p_B = \quad g\left(\frac{di_C}{dt}^{(4)} - \frac{di_C}{dt}^{(0)}\right)-1$
$p_B = - \quad g\left(\frac{di_A}{dt}^{(5)} - \frac{di_A}{dt}^{(0)}\right)-1$	$p_A = - \quad g\left(\frac{di_B}{dt}^{(5)} - \frac{di_B}{dt}^{(0)}\right)-1$	$p_C = - \quad g\left(\frac{di_C}{dt}^{(5)} - \frac{di_C}{dt}^{(0)}\right)+2$
$p_C = \quad g\left(\frac{di_A}{dt}^{(6)} - \frac{di_A}{dt}^{(0)}\right)-1$	$p_B = \quad g\left(\frac{di_B}{dt}^{(6)} - \frac{di_B}{dt}^{(0)}\right)+2$	$p_A = \quad g\left(\frac{di_C}{dt}^{(6)} - \frac{di_C}{dt}^{(0)}\right)-1$

Table 3.6: Position signals for SVPWM excitation (wye connection)

The position of the saliency modulation is then retrieved from the argument of the complex position signal $\underline{P}$ (3.70), as shown in (3.71).

$$\underline{P} \quad = \quad p_A + p_B\, e^{j\frac{2}{3}\pi} + p_C\, e^{-j\frac{2}{3}\pi} \tag{3.70}$$

$$\angle \underline{P} = 2\lambda_{dq'} \tag{3.71}$$

3.5 Conclusion of Sensorless Techniques Review

In this chapter the most common sensorless principles have been reviewed. It is shown that the rotor flux can be derived from the fundamental model of the machine due to the back EMF in the machine. However, it is explained that this principle can not be used at very low and zero speed where the back EMF is too small to be precisely detected. Furthermore the parameters of the model need to be precisely known for a good position estimation. This is particularly difficult to ensure for the required stator resistance parameters, since it changes significantly with the machine temperature.

To achieve operation at zero and very low speed, saliency based sensorless position estimation schemes have been developed. The nature of the saliencies is explained and it is shown that the saliency can be created by the mechanical machine design or magnetic saturation of the machine.

Several position estimation schemes with additional voltage signal injection are reviewed. For all of them, good practical results have been presented in a number of technical publications. The common idea is to apply some test voltage signal to the machine that excites the winding inductances. The current response is then used to retrieve the information about the saliency position. These saliency based methods are parameter insensitive and work also at zero mechanical speed and zero fundamental excitation. The implementation of HF injection schemes is simple and

can be made with standard low cost micro controllers. The implementation of the transient voltage methods requires a synchronised analogue signal sampling to the modified PWM inverter switching which may require a more advanced micro controller system. The main disadvantages are significant current distortions. With high frequency carrier injection the fundamental current shows also a significant carrier high frequency component. In test vector transient techniques the fundamental current is not disturbed by a fixed high frequency component, but shows significant spikes during the test vector instances. The main problem is the required minimum acquisition time for the measurement. The artificial extension of the active measurement voltage vectors causes significant current deviations. The current disturbances cause additional losses and in some cases also undesired torque ripple [40], [54]. The worst problem is however a significant audible noise, which can not be neglected for many applications.

Chapter 4

Experimental Rig

In this project an experimental rig has been set up in the Department of Industrial Electrical Power Conversion at the University of Malta. Figure 4.1 shows a block diagram of the setup. The three phase test machine is fed by a voltage source inverter. The inverter is a commercial Eurotherm S584 model. The internal PWM signal control of the inverter is not used. The inverter is modified so that external signals can be interfaced that control the switching of the IGBT's. In the experimental implementation the DSK 6713C evaluation board from Texas Instruments is used for the control of the drive system. The PWM switching signals are calculated by the machine real time control algorithm inside the DSP. For the interaction between the DSP control board, the inverter and other periphery a dedicated periphery control FPGA board has been designed. The three machine currents are measured by standard current Hall effect sensors. The three machine voltages are measured by commercial differential probes. The periphery control FPGA board provides also a general purpose digital input and output interface. A switch box is connected to the digital inputs of the periphery control FPGA board. This is used to change reference values and parameters during the experiments. The drive control algorithm runs on the DSK 6713C board. The program is loaded from the PC via the on board USB/ JTAG emulator. This direct PC/ DSK board can be also used for data capturing from the DSP control algorithm. However, it was found that this connection is rather slow and sensitive to electromagnetic interference that comes from the inverter. Therefore another PC/ DSK board connection is set up by

using the DSK USB 2.0 daughter card from AVNET. The USB 2.0 board is, as the FPGA periphery control board, connected to the DSK data and address bus. The USB 2.0 board is then connected to another USB port of the host PC. This set up data logging connection provides a data transfer rate of up to 480 Mb/s. This connection is also robust against electro magnetic interferences. The test machine used are a 4.4 kW permanent magnet synchronous machine (PMSM) from Yaskawa and a 5.5 kW induction machine from MEZ. The AC test machines are equiped with a standard 2500 pulse per revolution encoder. A DC drive from ABB is coupled to the shaft of the AC machine under test to act as mechanical load. This is not shown in the block diagram of Figure 4.1.

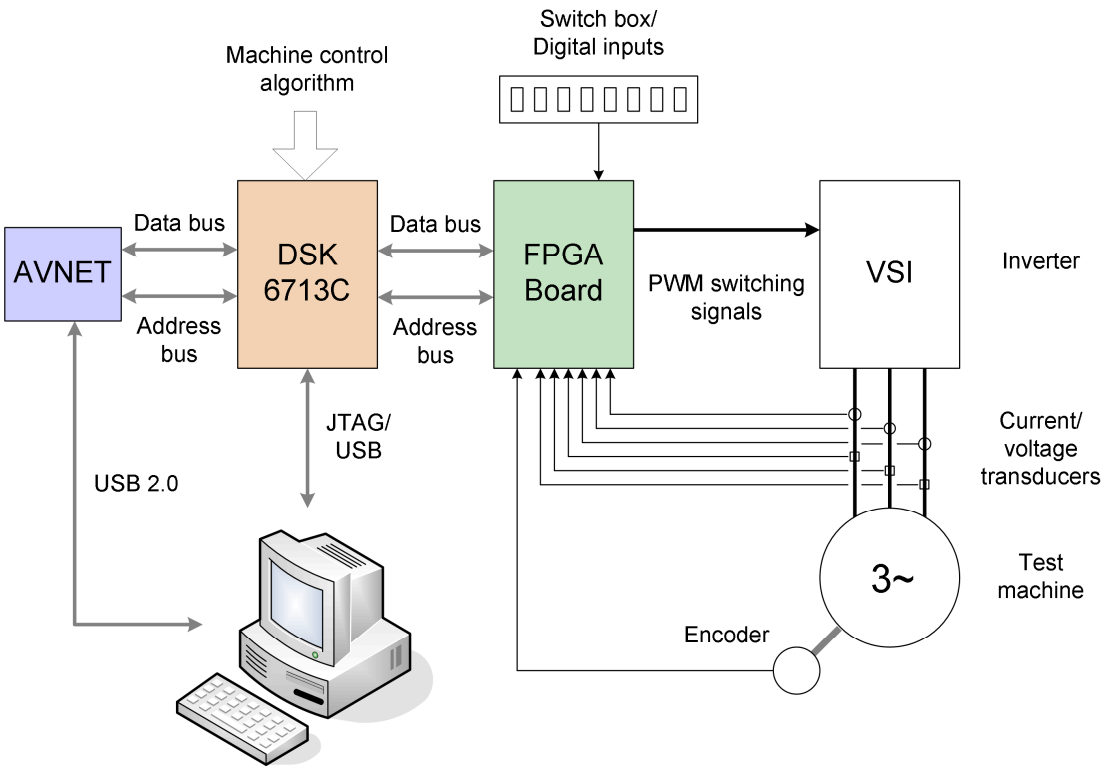

Figure 4.1: Setup of experimental rig

4.1 DSK 6713C Evaluation Board

The DSK 6713C board is a design from Spectrum Digital that provides a microprocessor evaluation platform with the TMS320C6713 digital signal processor (DSP) [55]. The 32-bit floating point DSP [56] runs at 225 MHz. 16 MB of external SDRAM [57] are provided on the evaluation board. Figure 4.2 shows a picture of the DSK 6713C evaluation board.

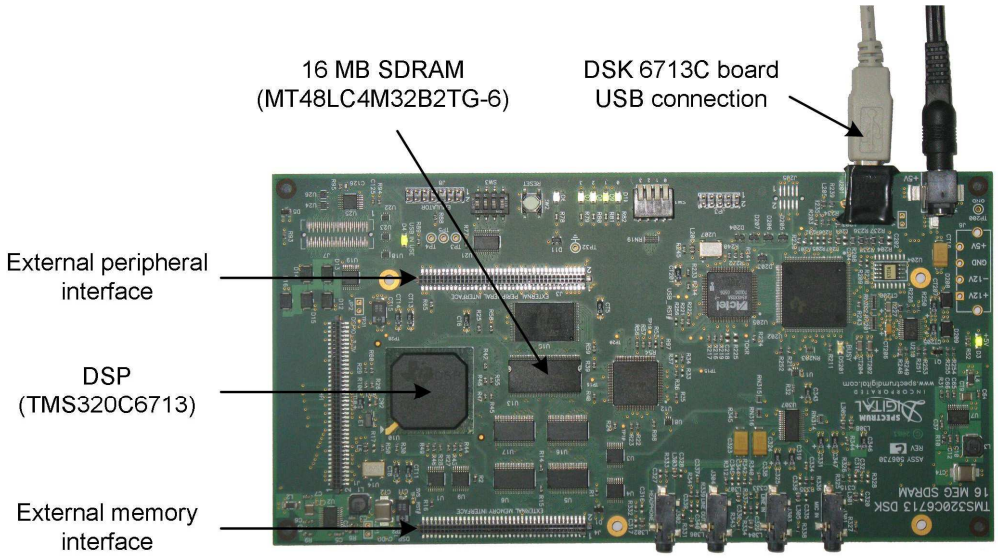

Figure 4.2: Picture of the DSK 6713C evaluation board

The programming is performed in C++ with the Texas Instruments software tool Code Composer Studio 3.1 [58]. The DSK 6713C board is a low cost evaluation platform that allows the easy and fast implementation of even complex control algorithms. Unfortunately no peripheral interfaces are provided to use the DSK 6713C evaluation board directly for drive control systems. However, dedicated extension connectors are provided to allow the easy design and integration of external periphery extension boards. The DSP system data and address bus is available on the external memory interface. The external peripheral interface

provides hardware interrupt pins and further daughter card control signals. The connectors are designed in such a way that extension boards can be directly plugged on top of the DSP evaluation board.

4.2 FPGA Periphery Control Board

The FPGA periphery control board was specifically designed and set up in this project. For integration of the DSK 6713C DSP board into practical motor control application, several interfaces such as PWM outputs, encoder interface and multi channel A/D converters are required. The FPGA periphery control board has been designed to provide adequate hardware periphery and interfaces for motor control systems. The two 80-pin connectors external memory interface and external peripheral interface are used for a memory mapped integration of the FPGA periphery board to the TMS320C6713 DSK micro processor platform. For achieving a highly integrated design a FPGA is used in which most digital periphery functions are implemented. A flash reprogrammable FPGA (Actel A3PE600) [59] has been selected, providing the possibility of in-system reprogramming [60]. Thus the peripheral configuration and the included hardware functionality of the C6713 DSK periphery is reconfigurable, providing maximum flexibility. All functional units inside the FPGA are accessed via 32-bit wide data word registers. Figure 4.3 shows a picture of the designed FPGA periphery control board.

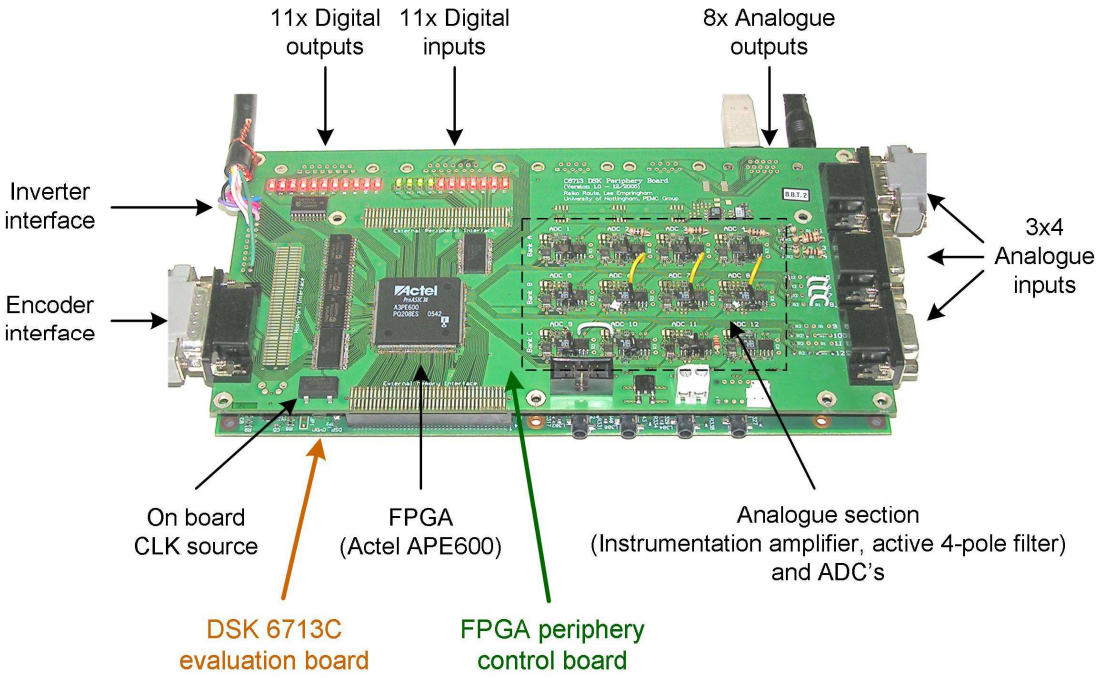

Figure 4.3: Picture of the DSP unit with periphery control FPGA board

The hardware design of the FPGA periphery control board PCB is described in detail in Appendix B. The selected Actel A3PE600 FPGA is a pure digital IC that provides 600,000 system gates and 13,824 D flip flops [59]. The used 208 pin PQ208 package version provides 147 digital inputs/ outputs. The programming is performed with the Actel design tool Libero IDE [61]. The FPGA program is based on VHDL language. However, with the provided programming tool all functions are implemented as block diagram design. The implemented functions are:

- **PWM timer unit** (generates the switching signals fed to the inverter)
- **ADC control unit** (controls the measurement of the analogue input signals, e.g. currents and voltages)
- **Encoder interface** (reads the encoder signal and provides the rotor position)
- **Watchdog and trip handling unit** (fault protection)
- **Digital in-/ outputs** (general purpose)

The cycle frequency of the FPGA algorithm is 45 MHz. The clock signal for the FPGA is derived from the DSK board. Therefore the FPGA algorithm runs synchronised to the DSP. However, there is also an on-board clock source available, that allows the use of the FPGA board as stand alone controller. The FPGA board is further connected to hardware interrupt pins 4 to 7 of the DSK 6713C evaluation board. Therefore four external interrupt request (IRQ) signals can be generated from the FPGA program. In the drive control system the external interrupts 5 and 6, initiated by the PWM unit and the ADC unit are used to trigger the DSP real time program loops. The external IRQ 6 is used to initiate the PWM loop algorithm and IRQ 5 is used for the algorithm that runs with the analogue signal sampling. The DSP algorithm that runs with ADC sampling is set to a higher priority. The ADC sampling algorithm runs with a faster cycle frequency and can interrupt the PWM cycle DSP algorithm. The IRQ control can be further modified in the DSP software tool Code Composer.

Figure 4.4 shows the global FPGA program control register. The address is 0xB000 0000 and it is a read write register indicated by (R/W) behind the address. By writing a 1 or 0 to the dedicated bits the PWM interface, the ADC control unit, the encoder interface and the watch dog timer can be enabled or disabled. In addition several trip signal sources can be selected for global system trip handling.

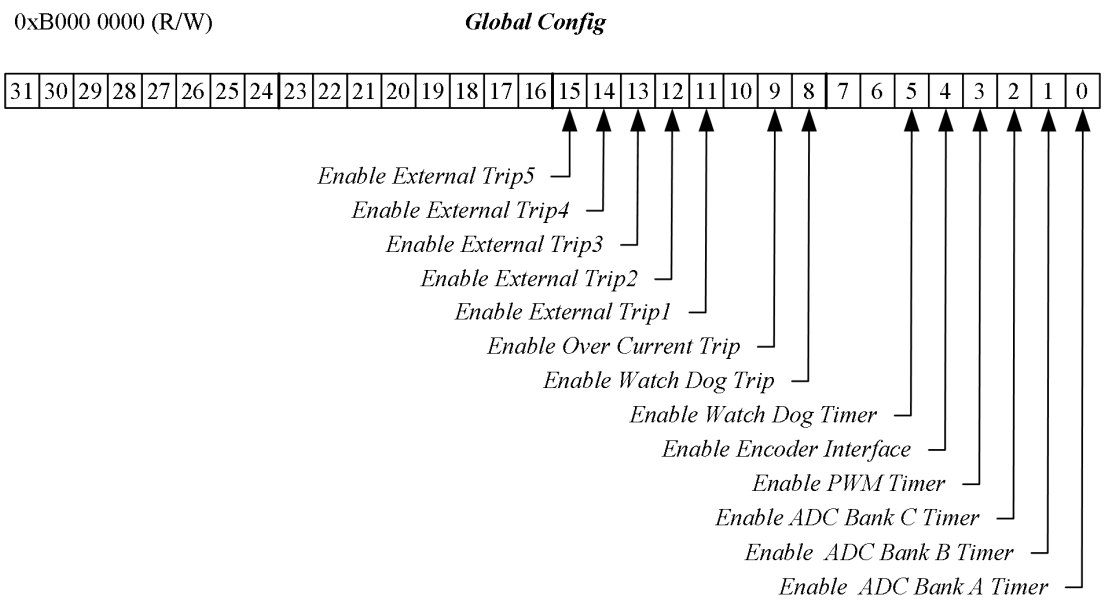

Figure 4.4: Global configuration register of FPGA functional units

4.2.1 PWM Timer Unit

The implemented PWM unit is developed for the control of a standard three phase voltage source inverter. The PWM unit produces the inverter IGBT actuation signals from the switching times calculated by the DSP program. The function is implemented by using a timer block (discrete counter) and several comparators. The dead time lock out between the two complement switching signals per phase is also included in the signal generation. The PWM frequency can be adjusted and also test vectors, used for some sensorless techniques, can be applied. Figure 4.5 shows the PWM unit control register *PWM Config*.

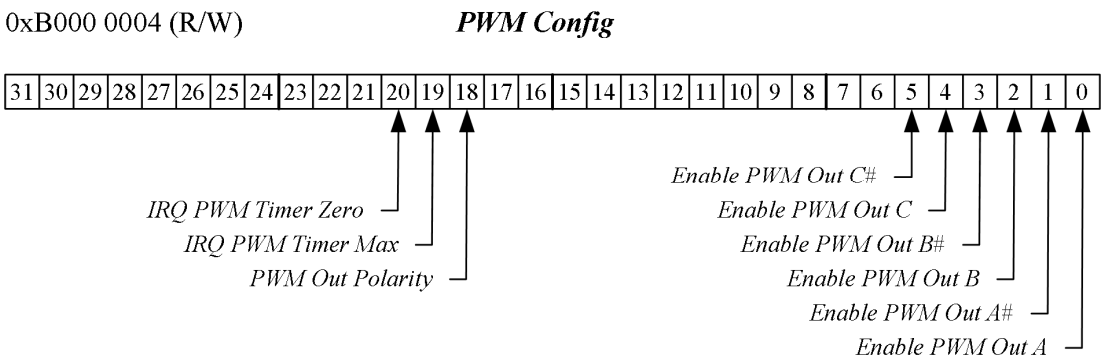

Figure 4.5: PWM configuration register

The address of the *PWM Config* register is 0xB000 0004. The register is also a read/ write (R/W) register. Bit 0 to 5 are used to enable the six PWM output signals. A 0 in the Enable *PWM Out* bit keeps the referring IGBT in off state. Bit 18 in the *PWM Config* register defines the polarity for the PWM signal logic. If the *PWM Out Polarity* bit is set to 0, then the PWM output signal is high if the referring IGBT is to be switched on. A 1 in the *PWM Out Polarity* bit means that negative logic is used and the IGBT on signal is low at the PWM output pins. The used timer runs up and down from zero to a defined maximum value during the operation. The PWM hardware interrupt is connected to the external interrupt pin 5 of the DSK board. The *PWM Config* register bits 19 and 20 are used to select the *PWM Timer Max* or *PWM Timer Zero* signal as hardware PWM interrupt source. Figure 4.6 shows the logic signal combination for the *PWM IRQ* signal. If both bits are set to 1, the interrupt request (IRQ) signal provides a pulse at the beginning and in the middle of each PWM cycle. This can be useful when a double update mode is used for the current control. The PWM times are then updated twice within one PWM period and the duty cycle of each PWM half cycle is independently controlled. The discrete current controller sampling frequency is then double the PWM switching frequency.

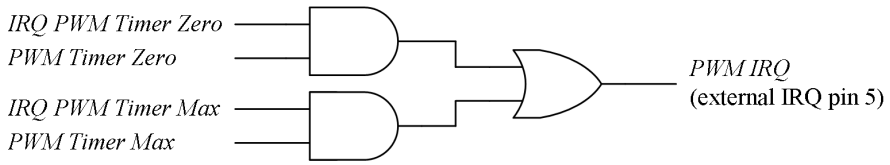

Figure 4.6: PWM unit interrupt signal configuration

Table 4.1 shows the addresses of the PWM unit timing registers. All timing register values are referred to the used clock frequency of 45 MHz. The table below states the register addresses, the names and a brief description of the timing value.

Address	**Register name**	**Description**
0xB000 0008 (R/W)	*PWM Period*	PWM period
0xB000 000C (R/W)	*PWM Dead Time*	Dead time between upper and lower IGBT on signal
0xB000 0010 (R/W)	*Phase A T1*	Switching time T_1 for phase *A*
0xB000 0014 (R/W)	*Phase A T2*	Switching time T_2 for phase *A*
0xB000 0018 (R/W)	*Phase A T3*	Switching time T_3 for phase *A*
0xB000 001C (R/W)	*Phase B T1*	Switching time T_1 for phase *B*
0xB000 0020 (R/W)	*Phase B T2*	Switching time T_2 for phase *B*
0xB000 0024 (R/W)	*Phase B T3*	Switching time T_3 for phase *B*
0xB000 0028 (R/W)	*Phase C T1*	Switching time T_1 for phase *C*
0xB000 002C (R/W)	*Phase C T2*	Switching time T_2 for phase *C*
0xB000 0030 (R/W)	*Phase C T3*	Switching time T_3 for phase *C*

Table 4.1: PWM timing registers

The PWM unit has been designed to allow test pulse injections additional to the fundamental PWM switching signal. This can be used for instance to embed additional test voltage vectors in between the zero vectors, as used in certain sensorless techniques, e.g. [26], [38], [47-51]. During the operation the PWM timer value is compared to the set switching times. Figure 4.7 shows the logic diagram of the implemented function. Only Phase *A* is shown as example, but the same function is also implemented for phase *B* and *C*. The PWM timer value is the value of the discrete PWM timer that runs up and down during the operation. The outputs of the three comparators *A z1*, *A z2* and *A z3* go high as soon as the PWM timer value is greater or equal the phase timing values. The comparator output signals are combined via a 3-input XOR-OR gate. Table 4.2 shows the truth table of the signal combination.

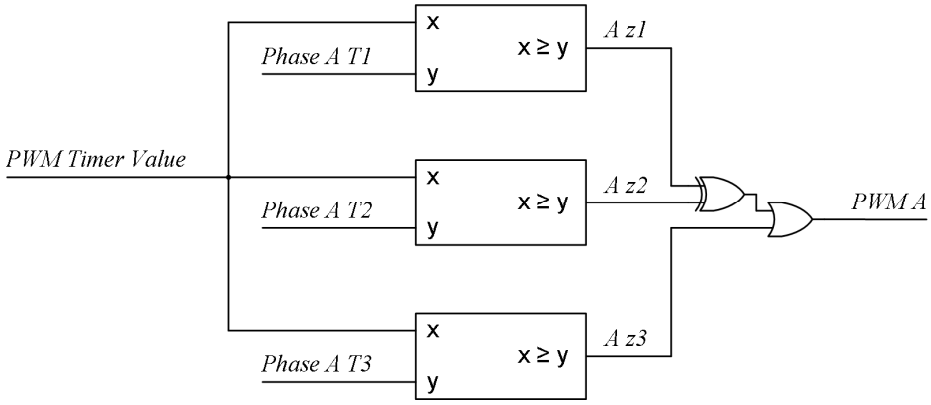

Figure 4.7: Logical combination for PWM signal generation

It is intended to use the T_3 signal for the fundamental PWM voltage generation. The switching times T_1 and T_2 are provided to allow test voltage vectors during the low zero vectors. The value T_1 is the start time of the test pulse and the value T_2 is the end time of the test pulse. If no test pulses are used the T_1 and T_2 timing registers can be ignored. All PWM registers are initialised to zero at power on of the system.

A z1	*A z2*	*A z3*	*PWM A*
0	0	0	0
0	1	x	1
1	0	x	1
1	1	0	0
x	x	1	1

Table 4.2: Truth table of 3-input XOR-OR gate

The PWM output signal is further adjusted by the set dead time and the PWM output signal polarity. Figure 4.8 shows the PWM output signal conditioning block for phase *A* as example. The final signals *PWM Out A* and *PWM Out A#* are interfaced to the inverter. This block requires also the clock signal to include the dead time between the two IGBT control signals per phase. The same function block is also implemented for phase *B* and *C*.

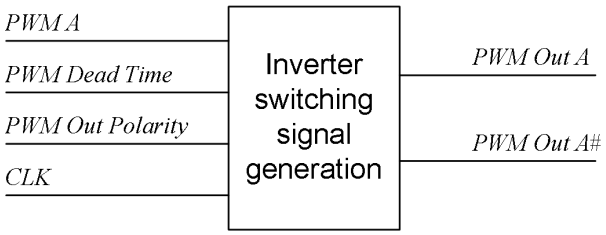

Figure 4.8: Inverter switching signal generation with dead time and output polarity adjustment

Figure 4.9 shows a theoretical example of the PWM unit operation. Only the phase *A* switching signal generation is shown as example. The PWM switching frequency is set to 1.125 MHz. The PWM Period register value is calculated by equation (4.1) and is therefore 19 for the given example.

$$PWM\ Period\ =\ \frac{45\,\mathrm{MHz}}{2\,f_{PWM}} - 1 \tag{4.1}$$

Figure 4.9 shows in the top plot the time varying *PWM Timer Value*. The discrete timer counts from zero up to the value set in the *PWM Period* register in the first half of the PWM cycle and down to zero again in the second PWM half cycle. When the *PWM Timer Value* is zero or equal the *PWM Period* register value the *PWM Timer Max* or *PWM Timer Zero* bit becomes set to 1. There is a small delay of 1 clock cycle (22.2 ns) due to the implemented logic. The *PWM Timer Count Up/ Down* signal indicates if the PWM timer is counting up (1) or down (0). The signal is delayed by half a clock cycle (11.1 ns). As stated before the *PWM Timer Max* or *PWM Timer Zero* signals can be used to trigger the *PWM IRQ* of the DSP real time program. In the shown example bit 19 and 20 of the *PWM Config* register are both set to 1. Therefore the external interrupt pin 5 of the DSP system provides a trigger pulse at the beginning and middle of every PWM cycle. Equation (4.2) shows how the *Phase PWM T* switching time register values are calculated from the real switching times *T*.

$$Phase\ PWM\ T\ =\ 45\,\mathrm{MHz}\,T - 1 \tag{4.2}$$

In the shown example of Figure 4.9 the demanded switching times for phase *A* are T_1 = 88.8 ns, T_2 = 222.2 ns and T_3 = 333.3 ns. Therefore the switching time registers *Phase A T1*, *Phase A T2* and *Phase A T3* are set to 3, 9 and 14. The figure shows the comparator output signals *A z1*, *A z2* and *A z3*, and the PWM signal *PWM A*. It can be seen that the switching instances occur at the time instances T_1, T_2 and T_3. At the second PWM half cycle the reverse switching sequence occurs at T_{PWM}-T_1, T_{PWM}-T_2 and T_{PWM}-T_3. It can be seen that the switching instances occur symmetrical to the PWM cycle centre. The pulse between T_3 and T_{PWM}-T_3 is considered as fundamental PWM pulse. The pulses between T_1 and T_2 and between T_{PWM}-T_2 and T_{PWM}-T_1 are considered as test vectors. The signals *PWM Out A* and *PWM Out A#* are shown for

the condition that the *PWM Out Polarity* bit of the *PWM Config* register is set to 0, therefore defining positive logic. The dead time T_{DT}, that ensures that both IGBT's per inverter leg are switched off for a minimum duration, is set to 44.4 ns. The *PWM Dead Time* register is initialised set 1 according to:

$$PWM\ Dead\ Time\ =\ 45\,\text{MHz}\,T_{DT}-1\ \ . \tag{4.3}$$

The final switching signals *PWM Out A* and *PWM Out A#* are delayed by two clock cycle due to the dead time adjustment.

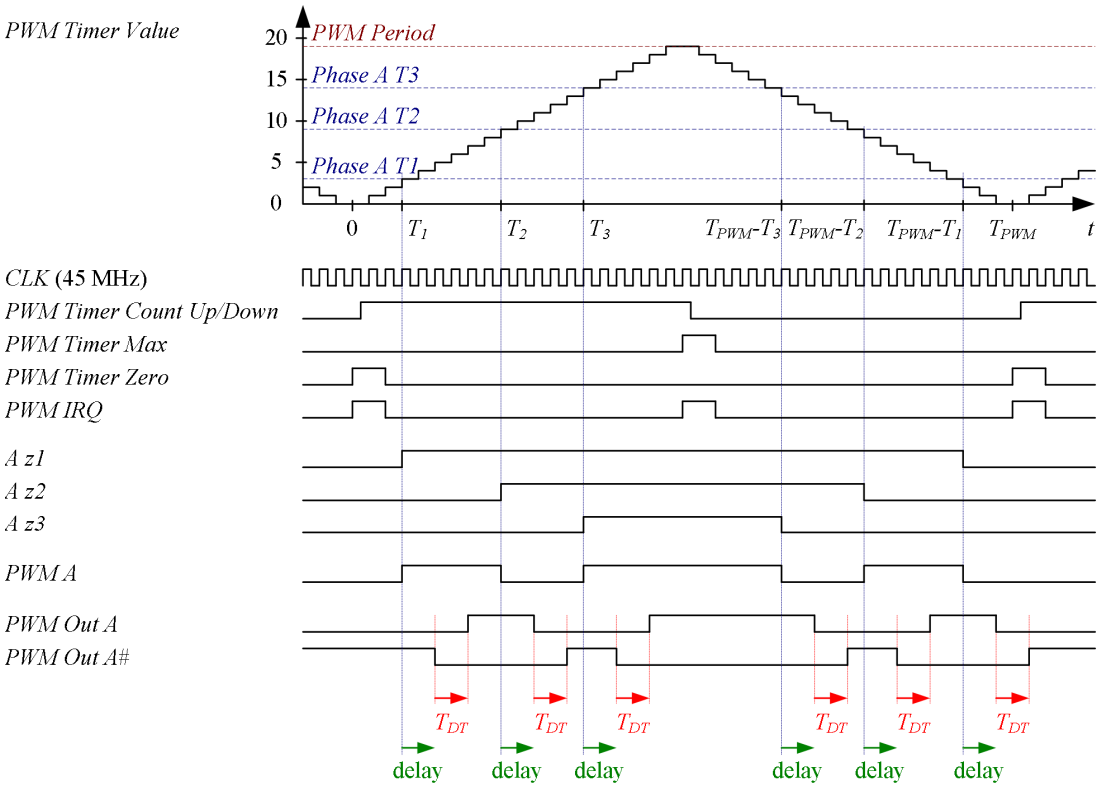

Figure 4.9: Example of PWM unit operation

Figure 4.10 shows a second example for the PWM signal generation. The same conditions as in the example above are used, except that no test vectors are required and only the fundamental PWM pulse is used. Therefore *Phase A T1*, *Phase A T2* are

set to zero and only *Phase A T3* is set to 14. It can be seen that the *A z1* and *A z2* are both permanent high. According to the truth table shown in Table 4.2 the *PWM A* output equals then *A z3*. As second difference to the previous example the *PWM Out Polarity* bit of the *PWM Config* register is set to 1, therefore defining negative logic for the inverter actuation signals *PWM Out A* and *PWM Out A#*.

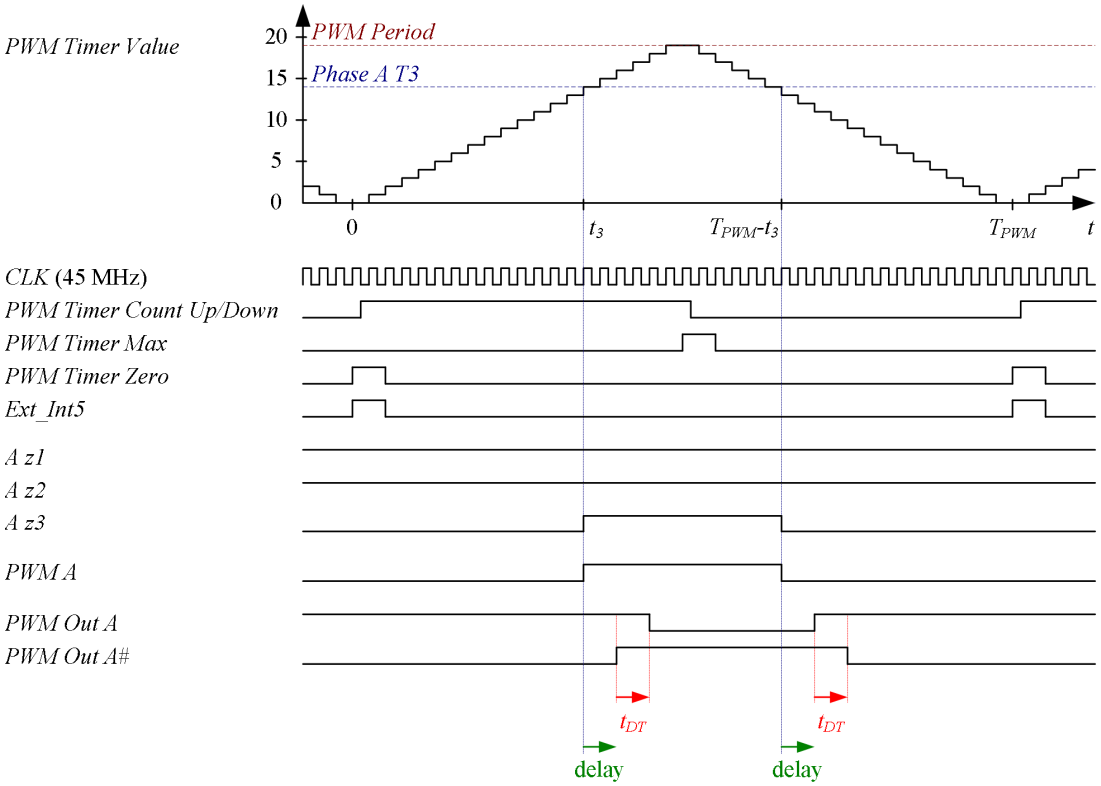

Figure 4.10: Second example of PWM unit operation

The example of Figure 4.10 shows the operation mode that is used in all experiments with the provided hardware setup. The fundamental PWM switching time register values are directly calculated from the demanded duty cycle *d* by:

$$Phase\,T3 = (1-d)\frac{45\,\mathrm{MHz}}{2\,f_{PWM}} \quad . \tag{4.4}$$

4.2.2 ADC Control Unit

On the designed FPGA periphery control board are twelve analogue input channels accommodated. For each channel an individual analogue to digital converter (ADC) AD7686 from Analog Devices [62] is used, which provides 16-bit resolution and a sampling rate of up to 500 kS/ s. For the analogue signal conditioning each analogue input channel has an input voltage divider, an instrumentation amplifier and a 4-pole active filter stage. Figure 4.11 shows the schematic of the analogue signal conditioning. The voltage divider resistor network can be used to adjust the voltage range of the input signal v_{in} and to convert current input signals to voltage signals. The instrumentation amplifier provides very high input impedance, so that also sensors with very low output power can be connected. The resistor *Rg* connected to the instrumentation amplifier IC can be used to increase the input gain. The Texas Instruments INA 128 IC's [63] are used in the design. The active filter stage consist of two multiple feedback circuits. The used operational amplifiers are Texas Instruments OPA2228 [64]. The gain and the characteristic of this filter stage can be individual adjusted according to the need of the user by selecting the required *R* and *C* values. Not needed components can be also left out. The purpose was to design a very flexible solution for future needs. Therefore all these signal conditioning stages are provided on the PCB.

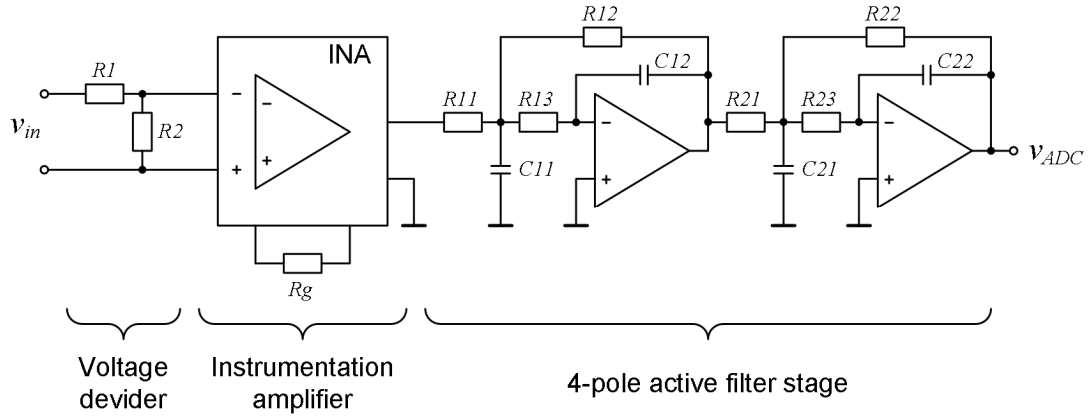

Figure 4.11: Circuit diagram of analogue input signal conditioning

The output of the analogue signal condition circuit v_{ADC} is directly connected to the input of the ADC IC's. Figure 4.12 shows the arrangement of the ADC channels. The twelve ADC channels are organised into tree independent controllable banks. Each back has its own convert start signal. The digital data from the ADC IC's is transmitted via a synchronous serial data connection. Each ADC serial data output is connected to a dedicated pin of the FPGA. The serial data clock signal *SCLK* is common for all ADC's.

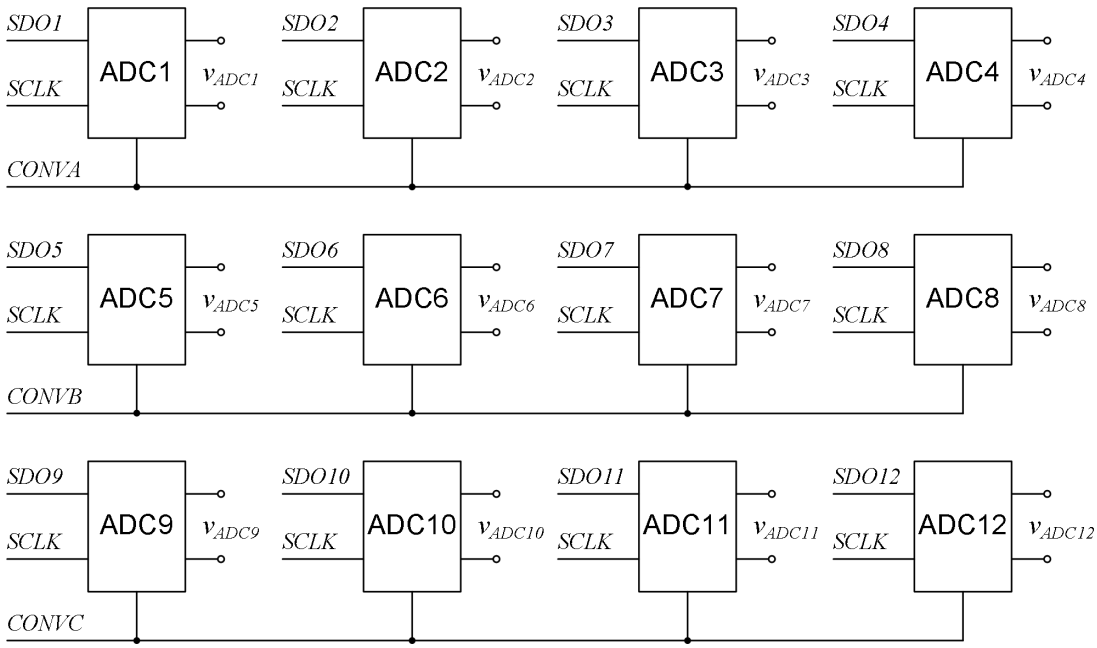

Figure 4.12: Organisation of ADC channels

Figure 4.13 shows the ADC unit control register *ADC Config* and Table 4.3 shows the used timing registers to control the ADC sampling.

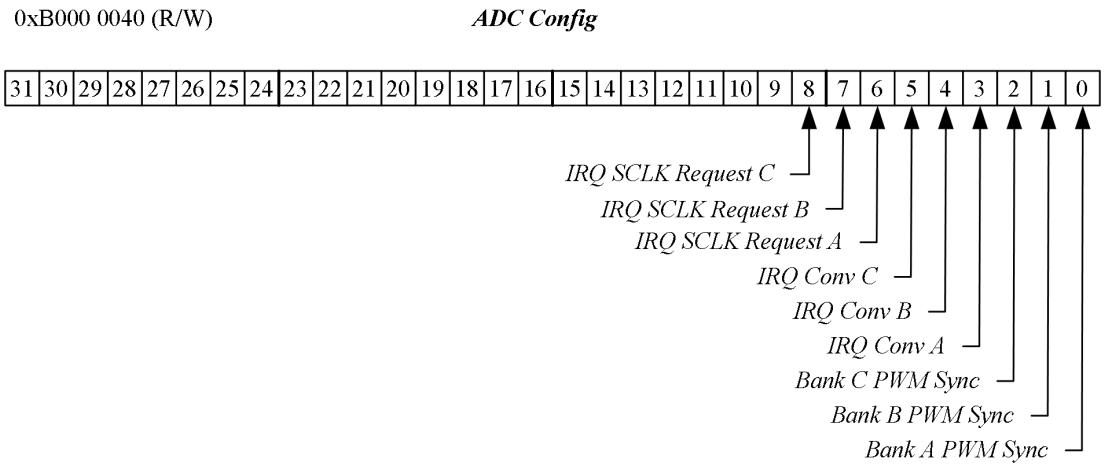

Figure 4.13: ADC unit control register *ADC Config*

Address	Register name	Description
0xB000 0044 (R/W)	*Bank A Period*	Sampling period of ADC bank *A*
0xB000 0048 (R/W)	*Bank A Shift*	Time shift of ADC bank *A* sample to PWM cycle synchronisation
0xB000 0050 (R/W)	*Bank B Period*	Sampling period of ADC bank *B*
0xB000 0054 (R/W)	*Bank B Shift*	Time shift of ADC bank *B* sample to PWM cycle synchronisation
0xB000 005C (R/W)	*Bank C Period*	Sampling period of ADC bank *C*
0xB000 0060 (R/W)	*Bank C Shift*	Time shift of ADC bank *C* sample to PWM cycle synchronisation

Table 4.3: Timing registers for ADC sampling

The sampling period of each ADC bank is defined by the *Bank Period* register. The *Bank Period* register value is calculated from the ADC sampling period T_{ADC} by:

$$Bank\ Period \quad = 45\,\text{MHz}\, T_{ADC} - 1 \quad . \tag{4.5}$$

The *Bank Shift* register can be used to align the ADC sampling to the PWM cycle. If the *Bank PWM Sync* bits in the *ADC Config* register are set to 1, the ADC sampling is triggered at the given time in the first half cycle of the PWM period. The *Bank Shift* register value can be calculated from the desired time shift between the start of the PWM cycle and the ADC sampling T_{Shift} by:

$$Bank\ Shift \quad = 45\,\text{MHz}\, T_{Shift} - 1 \quad . \tag{4.6}$$

Table 4.4 shows the addresses of the ADC result registers. Two 16-bit results are combined to one 32-bit register. The results of the two channels in one results register are updated at the same time, since they belong to the same ADC bank. The advantage is that only one read cycle has to be executed by the DSP to read both results at the same time from the external FPGA register. The (R) behind the address indicates that these are read only registers and can not be initialised by the DSP program.

Address	**Register name**	**Description**
0xB000 0070 (R)	*Result ADC1&2*	Bit [31-16] result of ADC1 Bit [15-0] result of ADC2
0xB000 0074 (R)	*Result ADC3&4*	Bit [31-16] result of ADC3 Bit [15-0] result of ADC4
0xB000 0078 (R)	*Result ADC5&6*	Bit [31-16] result of ADC5 Bit [15-0] result of ADC6

0xB000 007C (R)	*Result ADC7&8*	Bit [31-16] result of ADC7 Bit [15-0] result of ADC8
0xB000 0080 (R)	*Result ADC9&10*	Bit [31-16] result of ADC9 Bit [15-0] result of ADC10
0xB000 0084 (R)	*Result ADC11&12*	Bit [31-16] result of ADC11 Bit [15-0] result of ADC12

Table 4.4: ADC result registers

Figure 4.14 shows a theoretical example of the ADC unit timing operation. In the example the ADC bank *A* sampling frequency is set to 4.5 MHz. Therefore the *Bank A Period* register is set to 9. The sampling of ADC bank *A* is set to be synchronised to the PWM wave form. Therefore the *Bank A PWM Sync* in the *ADC Config* register is set to 1. It is desired that the first ADC sample occurs 111.1 ns after the PWM cycle start. Therefore the *Bank A Shift* register is set to 4. As can be seen in the figure, the *Bank A Timer Value* resets to zero after the set *Bank A Period* value is reached. The timer becomes further reset in the first PWM half cycle after the *PWM Timer Value* passes the set value in *Bank A Shift* register. This function can be very useful if the ADC sampling is required to be synchronised to the PWM wave form. Since the PWM period duration is a multiple of the ADC bank *A* period the next ADC bank *A* sampling synchronisation occurs at the same instance of the *Bank A Timer Value* roll over. When the *Bank A Timer Value* is zero a convert start impulse (*CONVA*) is initiated that starts the analogue signal sampling and digitalisation. In the shown example of Figure 4.14 the *Bank B Period* register is set to 11. Therefore the ADC sampling frequency of bank B is 3.75 MHz. A synchronisation of the sampling to the PWM wave form is not required and therefore the *ADC bank B PWM Sync* bit in the *ADC Config* register is set to 0. It can be seen that the *Bank B Timer value* resets only after the set sampling period and is not affected by the *PWM Timer Value*.

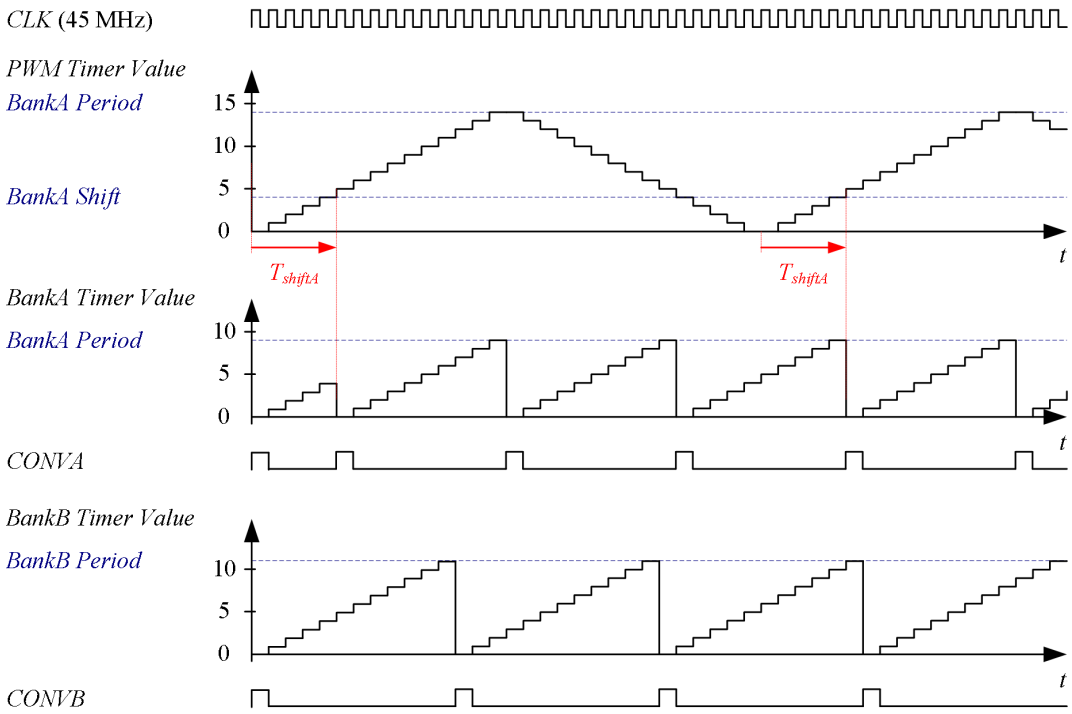

Figure 4.14: ADC sampling timing operation

Figure 4.15 shows an example of the serial data transfer from the ADC's to the FPGA. Only bank *A* is shown as example. The digital data from the ADC's is transferred to the FPGA by using the /CS mode 3-wire with busy indicator explained in the data sheet [62]. After the convert start pulse the ADC's sample the analogue input signal and start the digital conversion. The conversion ready is indicated by the ADC by setting the SDO output pin to low level. If all ADC's in bank *A* give the ready SDO low signal, the *SCLK Request A* signal becomes set by the Bank. If all ADC banks that started a conversion indicate the *SCLK Request* signal the 45 MHz FPGA system clock becomes put through to the *SCLK* pin. The serial data bits become then clocked out by the ADC's and are sampled by the FPGA data input pins at the falling edge. The bits in the SDO streams are marked by their number 0 to 15. Bit 15 is the most significant bit [62]. After 17 clock cycles the data is available in the FPGA ADC result registers shown in Table 4.4. It should be noted that several

ADC banks can start the conversion at the same time. However it is not suggested that another bank starts the ADC conversion during the data clock in time. This time is very small (seventeen 45 MHz clock cycles, approximately 0.4 µs) and therefore a sampling before or after should be done.

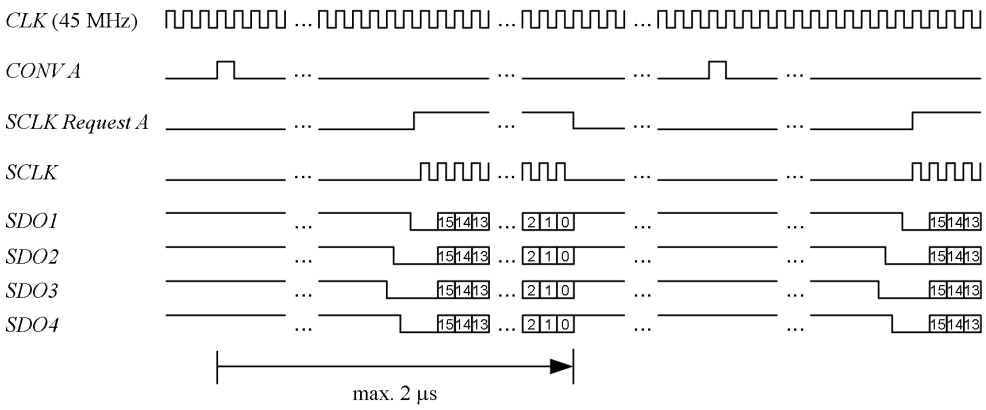

Figure 4.15: Serial interface of ADC data

For the IRQ generation the convert start pulses or the *SLK Request* signal can be linked to the external interrupt pin 6. The signals can be selected by the *ADC Config* register bits 3 to 8. All enabled IRQ signal are OR combined. The *CONV* signal can be used to call a DSP interrupt routing at the beginning of the analogue signal sampling. The falling edge of *SLK Request* signal can be used to call an interrupt directly after the ADC result registers have been updated. Figure 4.16 shows the logic function block diagram of the ADC IRQ signal generation.

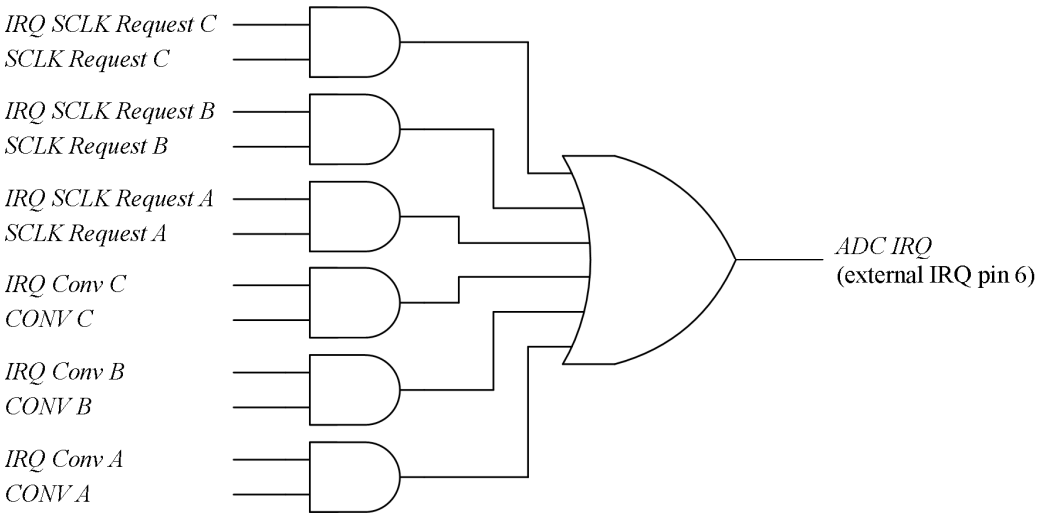

Figure 4.16: ADC unit interrupt signal configuration

4.2.3 Encoder Interface

The encoder interface has three read registers (R) and one write register (W) as shown in Table 4.5

Address	Register name	Description
0xB000 00A0 (W)	*Encoder Max Position*	Maximal position value per mechanical revolution
0xB000 00A4 (R)	*Encoder Position*	Actual encoder position
0xB000 00A8 (R)	*Zero Position*	Encoder counter value at zero marker
0xB000 00AC (R)	*Encoder Stop Time*	Time of last encoder pulse

Table 4.5: Encoder interface unit registers

The encoder interface is designed for a standard three channel quadrature encoder. The encoder gives two 90 degrees shifted square wave signals that indicate the

movement of the rotor. The zero position is defined by an additional channel that gives only one impulse at a certain position of the rotor. Each channel has as positive and negative logic signal from the encoder for noise reduction. Therefore six digital input signals are used, *A, A#* and *B, B#* as incremental pulse signals and *Z, Z#* as zero position marker. The signals with the 'hash' indicate the negative logic signals. Figure 4.17 shows the logic block diagram that is used inside the FPGA to convert the differential *A* and *A#* into one single digital signals *A2*. The same logic function is applied to the *B* and *Z* channel. Therefore the *B*, *B#* signals result into one *B2* signal and the *Z* and *Z#* into a *Z2* signal. Only if the positive input signal is high and the negated signal is low the resulting latch becomes set. On the contrarily *A* must be low and the *A#* must be high to set the latch to 0. This condition avoids errors if only one of the complementary signals is affected by noise.

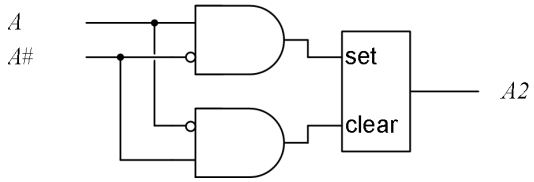

Figure 4.17: Input stage of differential encoder signal

Spikes or glitches can be interpreted as additional encoder impulses that would interfere with the drive operation. To increase the noise immunity of the encoder interface, the filter unit shown in Figure 4.18 is implemented. Again only the signal conditioning for channel *A* is shown, but the same is applied for the *B* and *Z* channel. The signal *A2* is passed though a shift register and the last 12 signal states are compared. Only if all 12 signals are low or high the output signal *A3* becomes high or low. The unit is clocked by the 45 MHz FPGA clock signal. Therefore the encoder input signal must be stable for at least 266.7 ns.

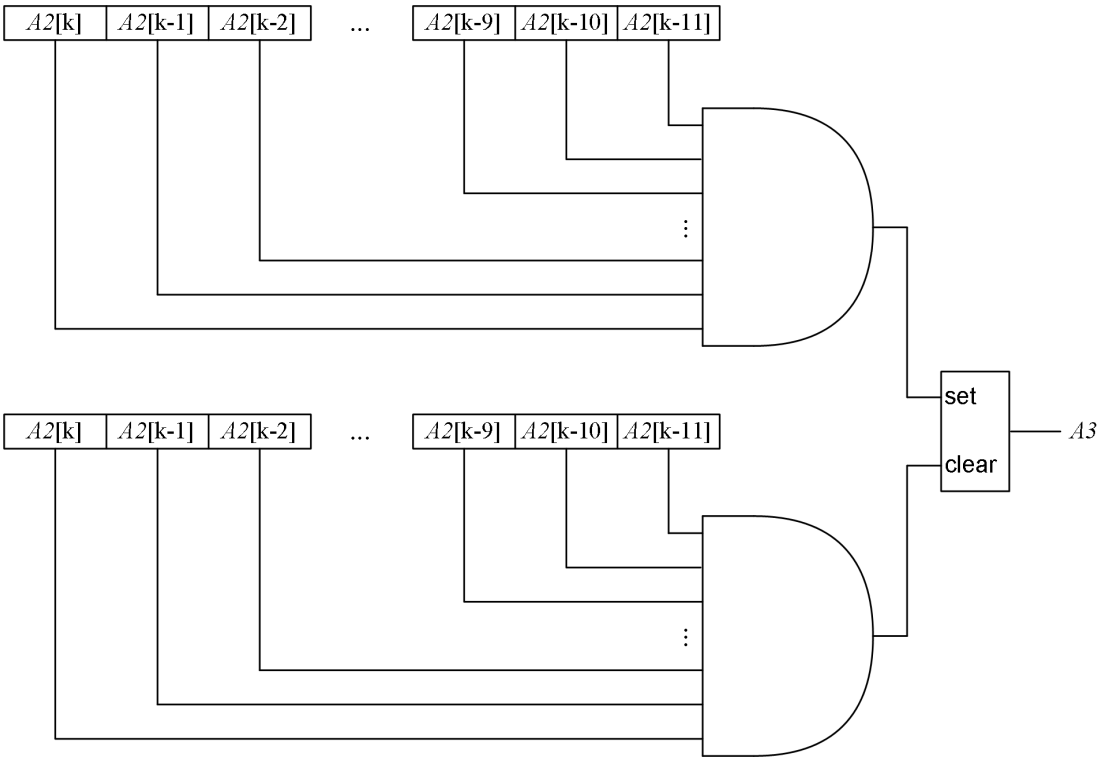

Figure 4.18: Spike and glitch filter in encoder signals

The two pulsating *A* and *B* channel square waves are 90 degrees offset shifted as shown by Figure 4.19 (a). Therefore the total encoder pulses per revolution resolution can be multiplied by four if the quadrature states of the *AB* signal constellations are used. Figure 4.19 (b) shows the logical quadrature state detection.

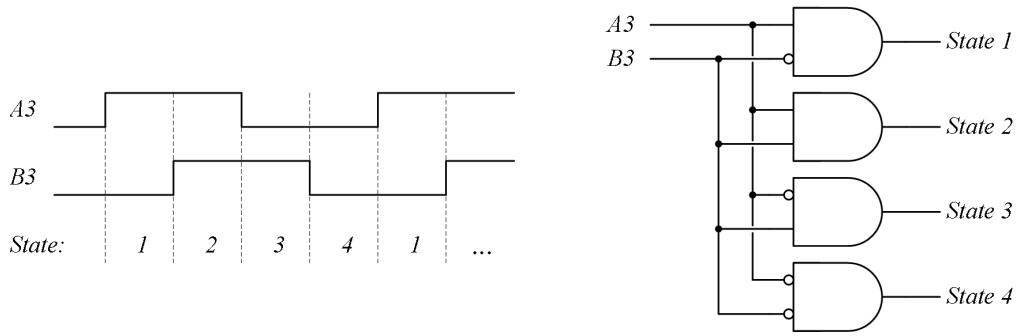

(a) **(b)**

Figure 4.19: Quadrature state detection

If a transition from state *1* to *2*, *2* to *3*, *3* to *4* or *4* to *1* is detected the position counter value is incremented by 1. On the contrary if the state transitions *4* to *3*, *3* to *2*, *2* to *1* or *1* to *4* is detected, the position counter is decremented by 1. Concluding the direction of rotor movement is also detected from the quadrature signal transition. The encoder interface unit has the following registers:

During the operation the *Encoder Position* register is incremented or decremented at each detected state transition. Thus it is the integral the encoder pulses which equals the actual rotor position. The used counter is 31-bit wide. The most significant bit in the *Encoder Position* register gives the direction of rotation. Figure 4.20 shows the bit allocation of the *Encoder Position* register.

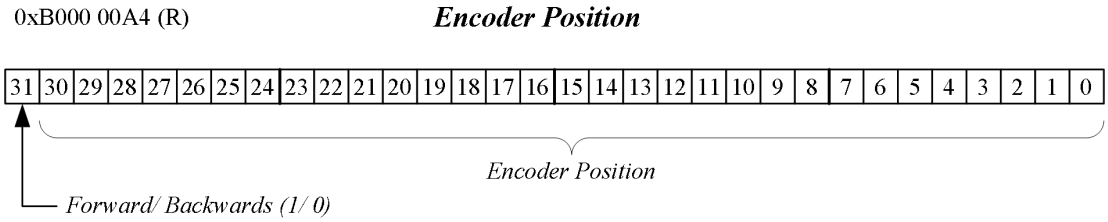

Figure 4.20: Encoder Position register

The mechanical rotor position λ_R can be calculated for a quadrature encoder counter with *PPR* pulses per revolution by:

$$\lambda_R = \frac{Encoder\ Position[30:0]}{4\,PPR} 360°_{mech} \quad . \tag{4.7}$$

In the *Encoder Max Position* register one can write the maximal position counter value. In forward direction the encoder position counter becomes reset to zero after the maximal position counter value stored in the *Encoder Max Position* register has been reached. If the rotor is rotating backwards and the encoder position counter value is zero its value is set to the *Encoder Max Position* value at the next decrement.

The encoder position becomes also set to zero at the occurrence of the zero index impulse *Z*. If the rotational direction is forward the counter value reset occurs at the rising edge of the *Z* impulse and in reverse direction at the falling *Z* pulse edge. Therefore the position counter value is always initialised to zero at the same position. The *Zero Position* register is provided for error testing. When the zero marker position reset edge is detected the actual *Encoder Position* register is latched. Ideally the encoder position should be always zero, unless it is the first revolution, since the roll over and under function at the *Encoder Max Position* value should reset the encoder position counter at the correct zero position. However, if some encoder pulses are missed or additional pulses are detected due to disturbances, the value will be different. This register can be tested during the drive control operation. A larger number in the *Zero Position* register means problems with the encoder signals.

As additional feature an encoder stop timing function is implemented. This can be very useful for the machine speed measurement, particular at low speeds. The speed can be derived from the number of position increments during a certain time. However if the speed is required to be updated at a high sampling frequency, at low speed just a few position increments occur during the sampling period. Thus the speed resolution will be poor. A better approach for low speed is to measure the time for a certain position increment. The encoder timing unit measures the time between two state 1 to 2 transitions in forward direction or the time between two state 2 to 1 transitions in backwards direction. The timer is clocked by the 45 MHz FPGA system clock. Therefore the time measurement has a precision of 22.2 ns. The value in the *Encoder Stop Time* register is the number of clock cycles per one encoder pulse width. The 31 least significant bits of the *Encoder Stop Time* register give the number of FPGA clock cycles per encoder pulse width. The most significant bit shows the direction of the rotor rotation. This allows calculating positive and negative speed values.

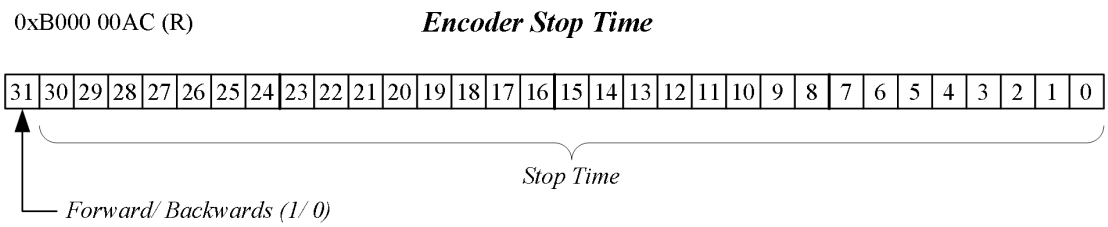

Figure 4.21: Encoder Stop Time register

The time for the last encoder pulse can be calculated from equation (4.8). For a given encoder the resulting mechanical rotor frequency can be calculated from equation (4.9).

$$t_{Encoder\ pulse} = \frac{Encoder\ Stop\ Time[30:0]}{45\,\mathrm{MHz}} \tag{4.8}$$

$$f_R = \frac{45\,\mathrm{MHz}}{Encoder\ Stop\ Time[30:0]\ PPR} \quad \text{if} \quad Encoder\ Stop\ Time[31] = 1$$

$$f_R = -\frac{45\,\mathrm{MHz}}{Encoder\ Stop\ Time[30:0]\ PPR} \quad \text{if} \quad Encoder\ Stop\ Time[31] = 0 \tag{4.9}$$

4.2.4 Watchdog and Trip Handling Unit

The trip handling unit observes the system for trip occurrences and brings the system into a safe state to avoid damage after a trip has been detected. Several trip sources are available. All trip signals are low active. That means that a healthy state is if the trip signals are 1 and a 0 indicates the trip instance. The negative logic variables are indicated by a 'hash' at the end of the name.

To observe if the microcontroller has crashed a watch dog timer unit is implemented. The watch dog checks if the DSP algorithm is executed at regular frequency. The watch dog consist of a timer that is continuously counting down. If the count reaches zero, the *Watch Dog Count Zero#* signal goes low and the trip signal it released. To avoid that the watch dog counter reaches zero, the timer value is reloaded during a repeating program cycle. In the implementation the PWM cycle is used for the watch dog timer update. The watch dog timer value is in every PWM cycle reloaded to a time slightly larger then the PWM period. Equation (4.10) shows the equation for the *PWM Watch Dog Period* timing register value calculation. The register is a 32-bit value register at the address 0xB000 0034 where the *PWM Watch Dog Period* timing is written every PWM cycle. As can be seen in equation (4.10) the value is exactly how many FPGA system clock occur during one PWM period plus some margin x.

$$PWM\ Watch\ Dog\ Period = \frac{45\ \text{MHz}}{f_{PWM}} + x \tag{4.10}$$

Figure 4.22 shows a theoretical example to explain the watch dog unit operation. The PWM cycle frequency is set to 4.5 MHz. Therefore the PWM period is ten clock cycles wide and the watch dog timer decrements its value by 10 per PWM period. The update value of the watch dog timer per PWM period is 13 ($x = 3$). Therefore the watch dog timer is updated under normal operation before it reaches zero, indicated by the three update instances in the figure. If the DSP system crashes, the PWM cycle algorithm is not executed and thus the watch dog timer is not updated. Following the watch dog timer reaches zero, only a few clock cycles after the last PWM period. As shown in the figure, the *Watch Dog Count Zero#* signal goes low and indicates the trip instance to the trip handling unit.

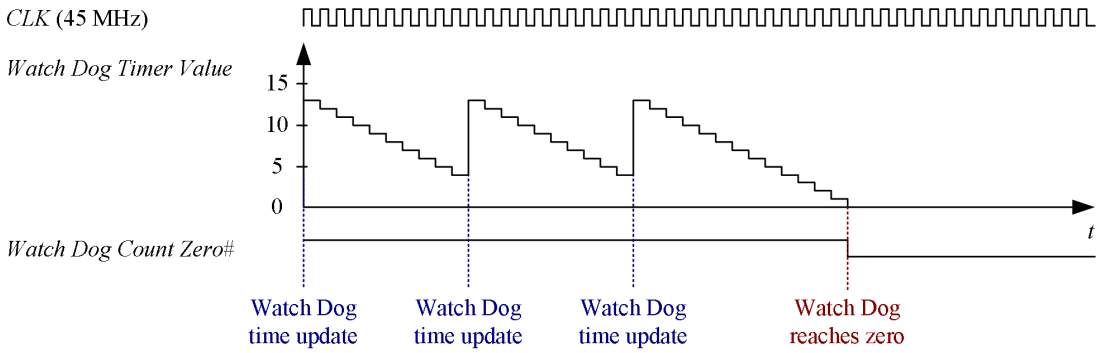

Figure 4.22: Watch dog operation

Besides the watch dog trip signal, an on board over current comparator and five external trip input signals are available. The bits 8, 9 and 11 to 15 of the global configuration register *Global Config* are used to enable the trip signals. Figure 4.23 shows the trip unit signal logic. At the instance of a trip signal that is enabled a global trip becomes latched. This latched global trip signal is connected to the *Trip IRQ#* signal. This trip signal is also connected to the external IRQ pin 7 of the DSK 6713C board and available at the inverter interface connector. If the *Trip IRQ#* trip signal is 0 all PWM outputs are disabled. That means that all inverter IGBT signals are set to off state. To reset the latched trip condition a read access to address 0xB000 0034 has to be executed by the DSP. The trip latch is clear dominant. Thus the reset condition is further that no enabled trip signals are active.

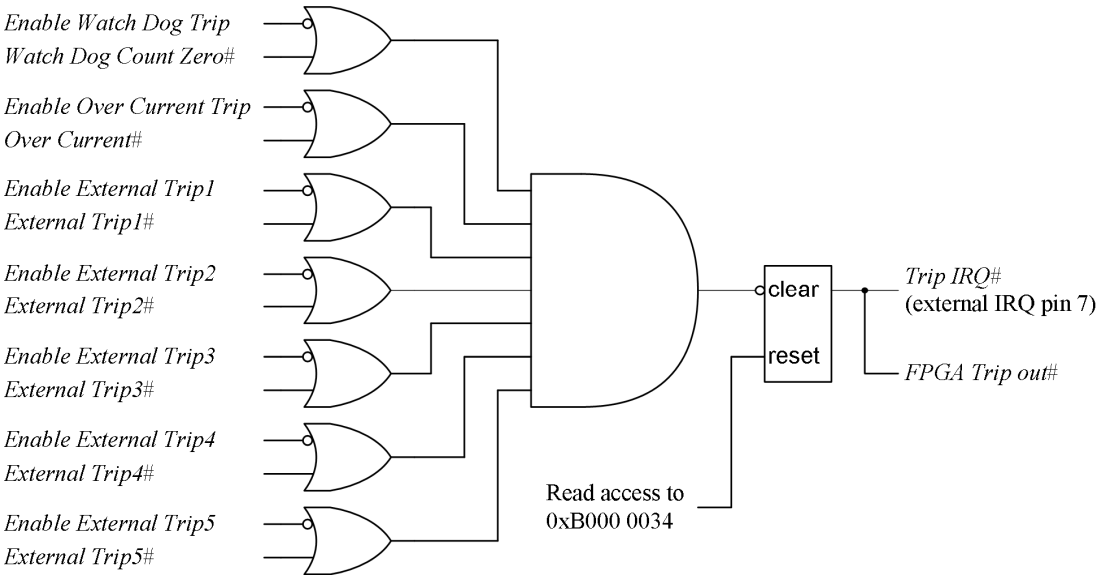

Figure 4.23: Trip unit interrupt signal configuration

The registers *Trip Status Current* and *Trip Status Latched* are shown in Figure 4.24. They show the status of the trip source signals and the PWM unit timer conditions. The *Trip Status Current* register can be read to detect the current trip signal status. The *Trip Status Latched* register latches the *Trip Status Current* register at the instant of a global trip release. Thus the system condition at the trip instance is captured and can be later analysed.

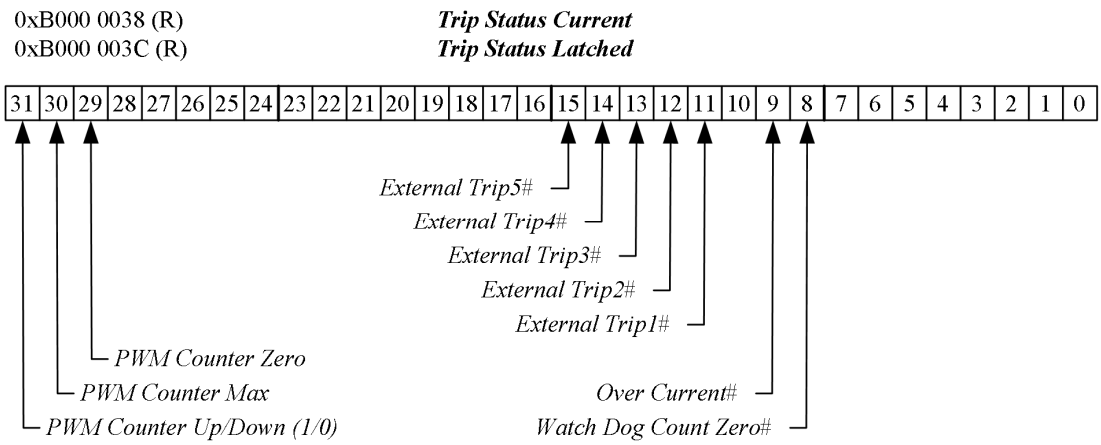

Figure 4.24: Trip status registers

4.2.5 Digital In-/ Outputs and Switch Box

The DSK 6713C periphery board provides a general purpose digital input and a digital output connector. Each connector provides 11 channels. Figures 4.25 and 4.26 show the FPGA program registers that control the digital input and out put pins. The digital output pins status is set by writing the desired logic level to the bits 0 to 10. The *Digital Out* register state can be also read back by the DSP. The *Digital In* register is a read only (R) register that reflects the digital states of the input pins. A 1 means high voltage level and a 0 means low voltage level. The states are also indicated by LED's soldered on the FPGA periphery board.

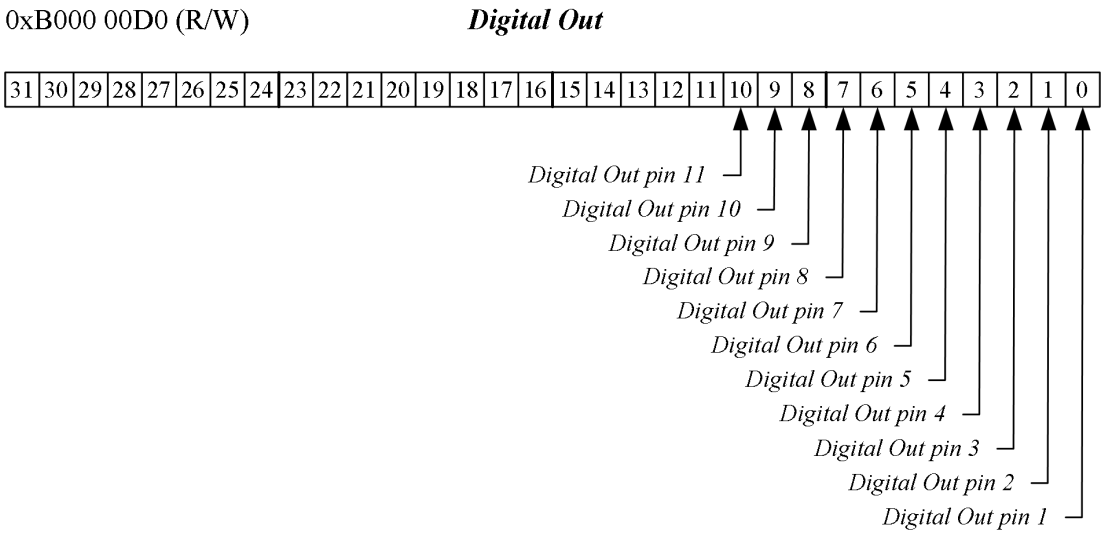

Figure 4.25: Digital output signals register

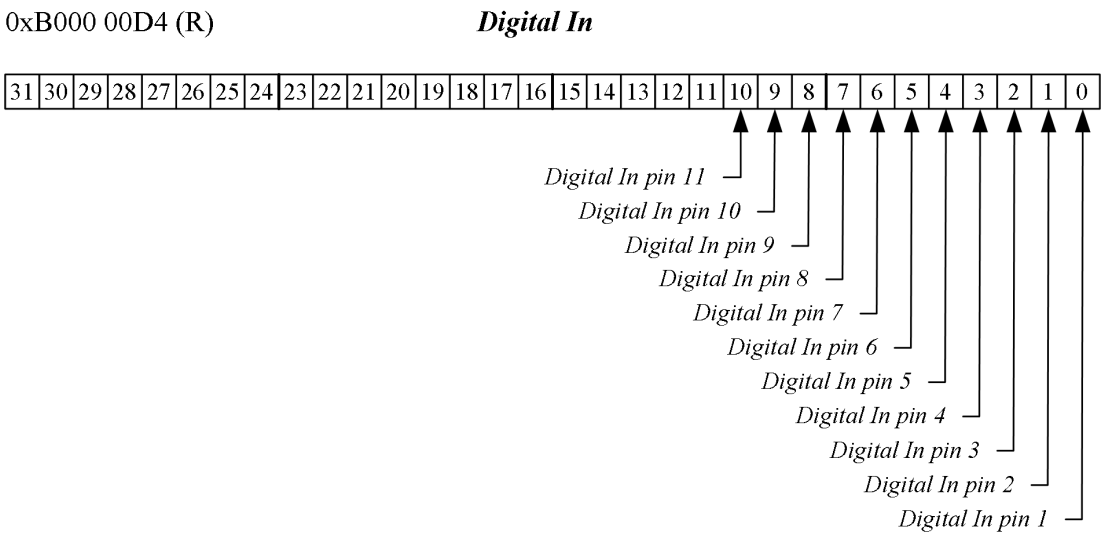

Figure 4.26: Digital input signals register

Figure 4.27 shows a picture of the used switch box that is connected to the FPGA periphery control board. The 8 switches are directly connected to the digital input pins 0 to 7. The digital input signal are used the set reference values in the drive control program and to initiate the data capturing.

Figure 4.27: Picture of the connected switch box

4.3 AVNET DSK to USB 2.0 Daughter Card

The DSK 6713C board provides a communication interface to the PC with the used programming tool Code Compose and the RTDX link. However it was found that this communication is rather slow and very sensitive to noise. The maximal achieved date transfer rate is only about 17 KB/s and crashes occur frequently when the inverter is switched on.

For setting up a faster and more robust PC interface for data capturing the DSK to USB 2.0 Daughtercard from AVNET [65] is used. This daughter card is also directly connected to the DSK 6713C board external memory and periphery interface connectors. Figure 4.28 shows a picture of the AVNET DSK to USB 2.0 daughter that is plugged directly on the external peripheral and memory interface of the DSP/ FPGA board unit.

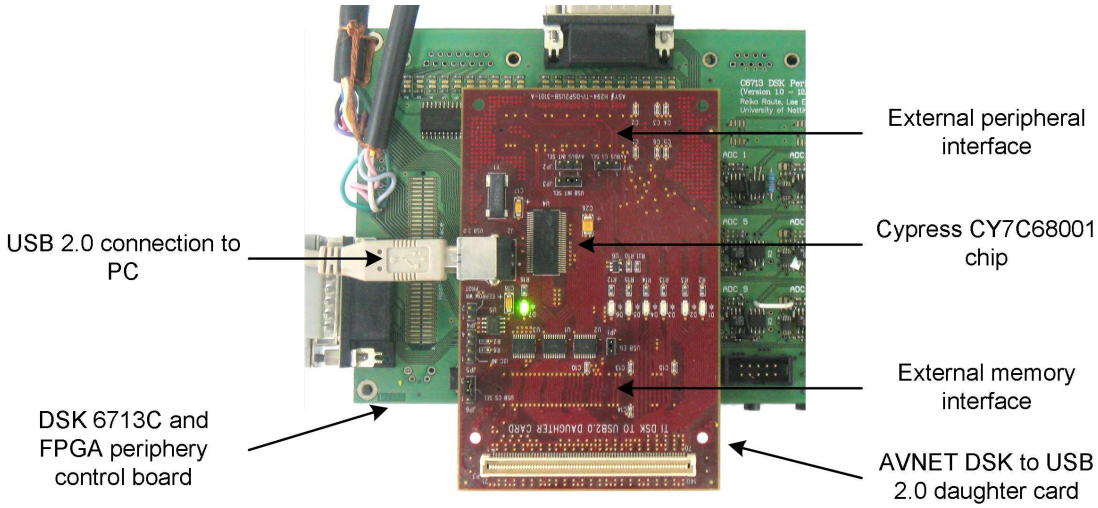

Figure 4.28: Picture of AVNET DSK to USB 2.0 daughter card on DSP/ FPGA boards

The DSK to USB 2.0 Daughtercard accommodates the Cypress CY7C68001 USB 2.0 controller [66] that provides a parallel to USB 2.0 interface. The registers of the Cypress CY7C68001 controller are memory mapped to the DSK microprocessor board. Therefore the communication from the DSP system is done by reading from

and writing to certain memory addresses. The communication to the PC side is established by using dedicated driver libraries. The driver files are provided by AVNET. Also program examples are provided that are used for the software development. The PC host application is programmed with the Dev-C++ compiler from Bloodshed Software [67]. For the project only a data transfer from the DSK 6713C DSP system to the PC is implemented. This is used to log data from the experiments on the PC for offline analysis. The data capturing during the experiments is initiated by setting a switch on the switch box. The in the DSP program defined variable values are then continuously stored into the 16 MB external RAM of the DSK 6713C board as 16-bit numbers until a defined maximum number of samples is reached. The experiment is then automatically stopped and the data transfer to the PC is activated. After the USB 2.0 daughter board is initiated the data array stored in the external DSK board memory is one by one transferred to the USB 2.0 daughter card. On the PC the created program file "DataCapture_1a.exe" has to be started which reads the data from the USB port and stores it into the file "Data.mat" in the local directory. The file "Data.mat" contains then the same data array captured during the experiment as Matlab data array. This file can be easily imported into Matlab and the experimental data can be analysed offline.

4.4 Power Electronics

Figure 4.29 shows a picture of the set up power electronics unit. A commercial inverter, model Eurotherm Drives 584 S [68], is used. For the experimental use the external generated PWM signals are fed into the inverter by a customised created interface. The inverter internal PWM signals are disconnected and the external PWM signals are fed instead to the IGBT driver circuits. The inverter internal protection unit is still enabled. The external PWM signals, generated by the DSK/ FPGA control unit are passed trough an optocoupler stage before interfaced to the inverter.

This provides a galvanic isolation of the experimental DSP/ FPGA control unit and the power electronics side. The optocoupler board is also shown in Figure 4.29. Figure 4.29 shows also the three used current transducers (LEM LAH 25-NP) [69] and voltage probes (Hameg HZ 115) [70].

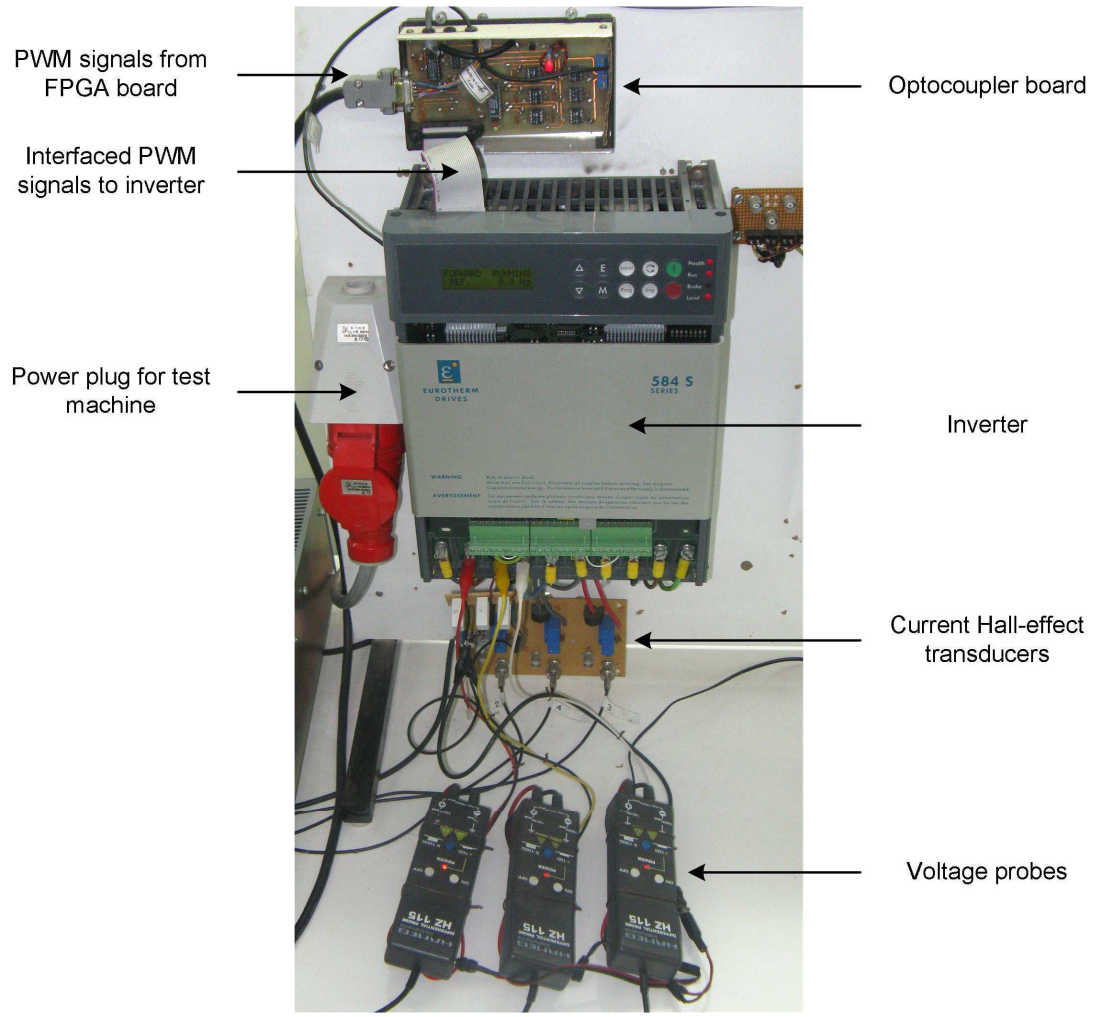

Figure 4.29: Picture of the inverter and used current and voltage transducers

Table 4.6shows the specifications taken from the manual of the used inverter.

Manufacturer:	Eurotherm drives
Type:	584S /0055
Rated output power:	5.5 kW
Rated input voltage:	380 ... 460 V
Rated input current:	15 A
Rated output voltage:	0 - 380 ... 460 V
Rated output current:	13 A

Table 4.6: Inverter specifications

4.5 Permanent Magnet Synchronous Machine

Figures 4.30 and 4.31 show a picture of the used permanent magnet synchronous machine and its nameplate.

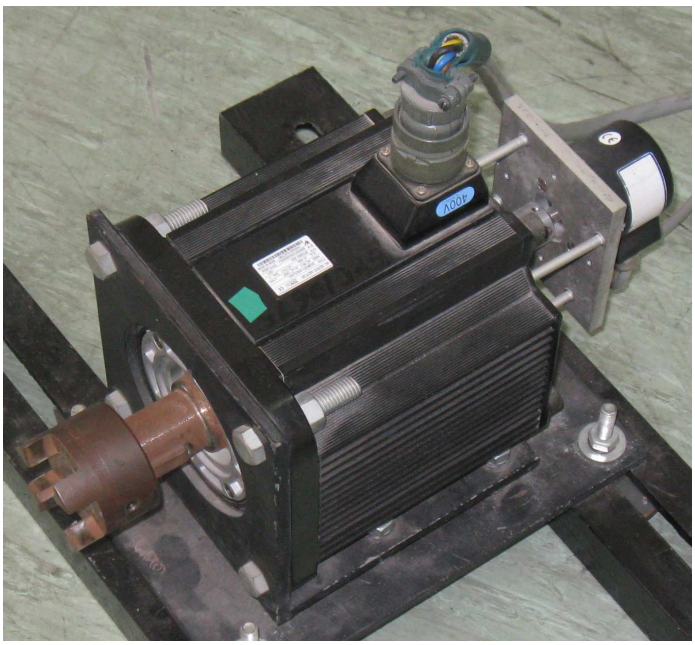

Figure 4.30: Picture of PMSM

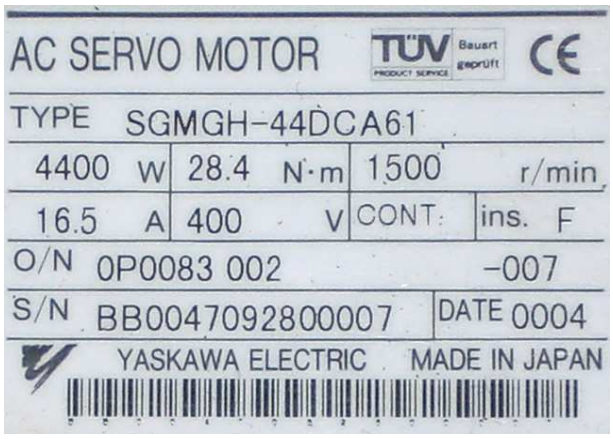

Figure 4.31: Nameplate of PMSM

The machine has four pole pairs. Therefore the electrical frequency at rated speed is 100 Hz. The per phase resistance is 0.23 Ω. The winding equivalent inductance is 4.6 mH when the *d* axis is aligned to winding and 3.6 mH when the *q* axis is aligned to the winding. The windings resistance and inductance values for the PMSM were determined in [71].

In an experiment the back EMF constant was determined. Figure 4.32 shows an experiment where the machine is driven by the DC machine to 150 rpm. The frequency is 10 Hz electrical. The terminals of the PMSM machine are open and the three terminal voltages are measured against earth. Figure 4.32 shows the measured rotor position and the measured voltages between the *A*, *B* and *C* terminals and earth.

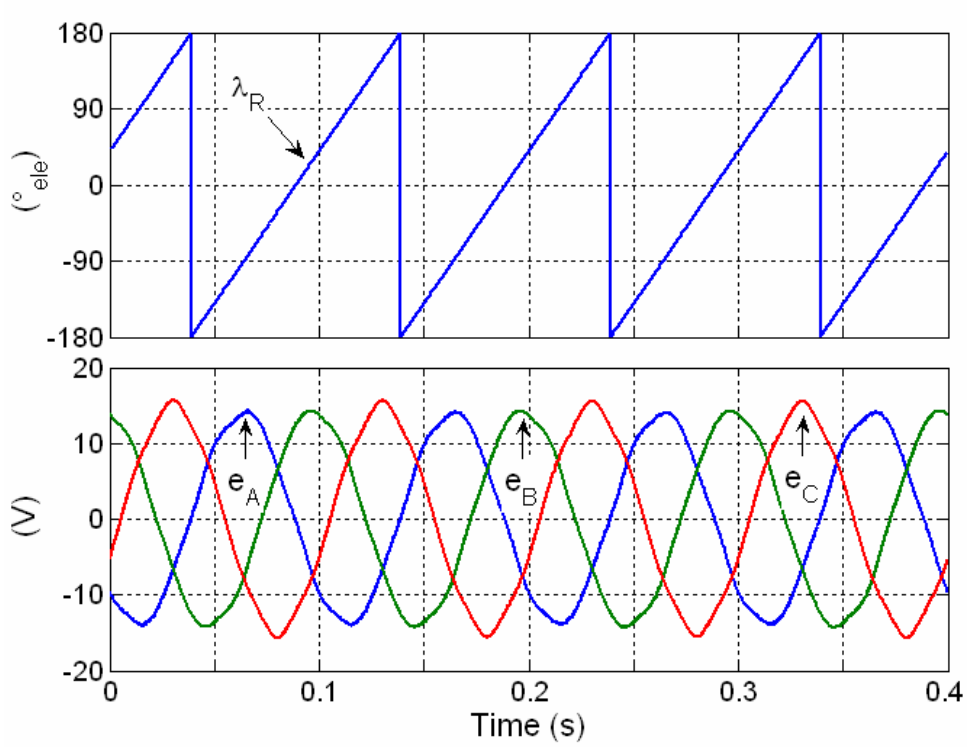

Figure 4.32: PMSM back EMF of all three phases at 150 rpm

It can be seen that the three phase back EMF waveforms are almost sinusoidal. Figure 4.33 shows the locus of the complex back EMF vector $\underline{e}_{\alpha\beta}$ calculated by:

$$\underline{e}_{\alpha\beta} = \frac{2}{3}\left(e_A + e_B e^{j\frac{2}{3}\pi} + e_C e^{j\frac{4}{3}\pi} \right) . \tag{4.11}$$

The locus of the complex back EMF vector is almost ideal circular. However, some small distortions are still visible. The distortion shapes the locus a bit hexagon like. This is due to the practical three phase designs of the machine.

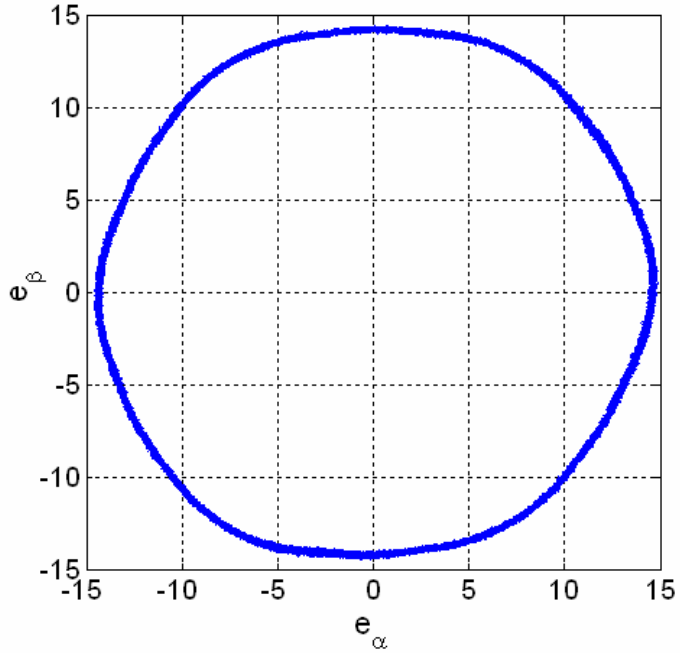

Figure 4.33: Locus of back EMF

It can be seen that the phase back EMF amplitude at 10 Hz electrical is about 14.3 V. Therefore the back EMF constant k_e can be calculated by:

$$k_e = \frac{\hat{e}_{phase}}{\omega_R} = \frac{14.3\,\mathrm{V}}{2\pi 10\,\mathrm{Hz}} = 0.228\frac{\mathrm{Vs}}{\mathrm{rad}} \quad . \tag{4.12}$$

4.6 Induction Machine

Figures 4.34 and 4.35 show a picture and the nameplate of the used induction machine. The machine has two pole pairs.

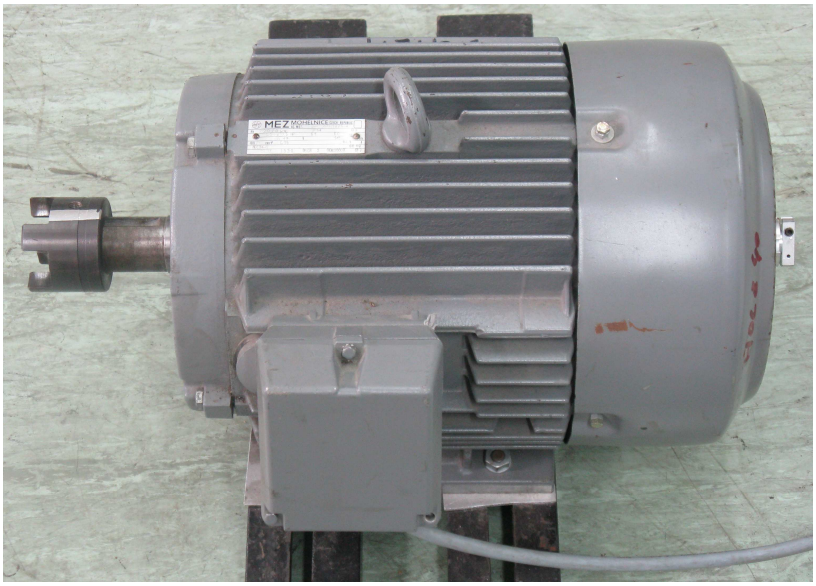

Figure 4.34: Picture of induction machine

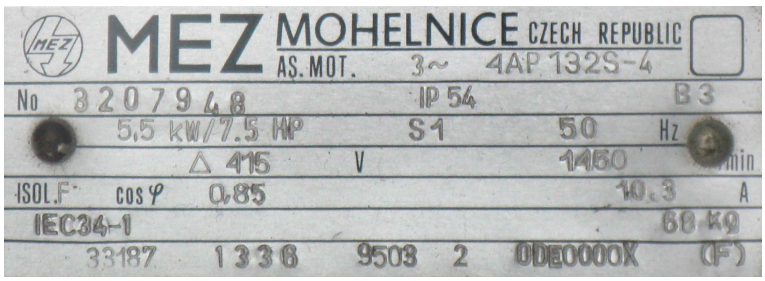

Figure 4.35: Nameplate of induction machine

The rotor of the machine is a skewed semi opened squirrel cage design with 32 rotor bars. The stator has 36 teeth to carry the stator windings. The stator airgap is about 0.3 mm wide. Figures 4.36 and 4.37 show a picture of the rotor and stator.

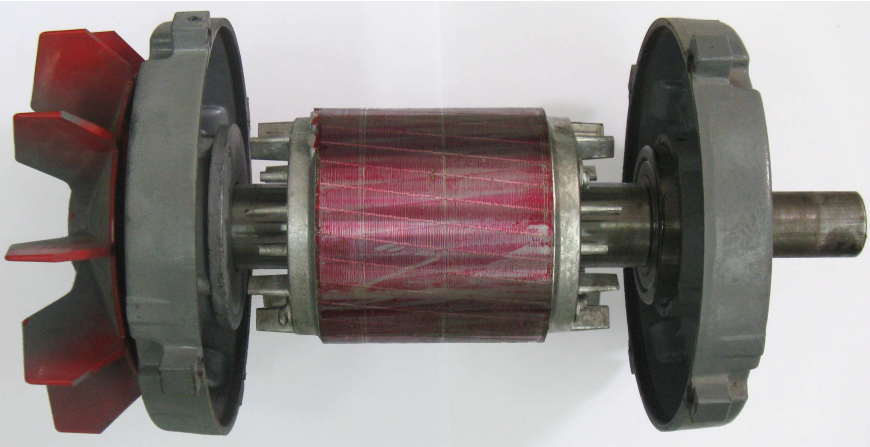

Figure 4.36: Rotor of induction machine

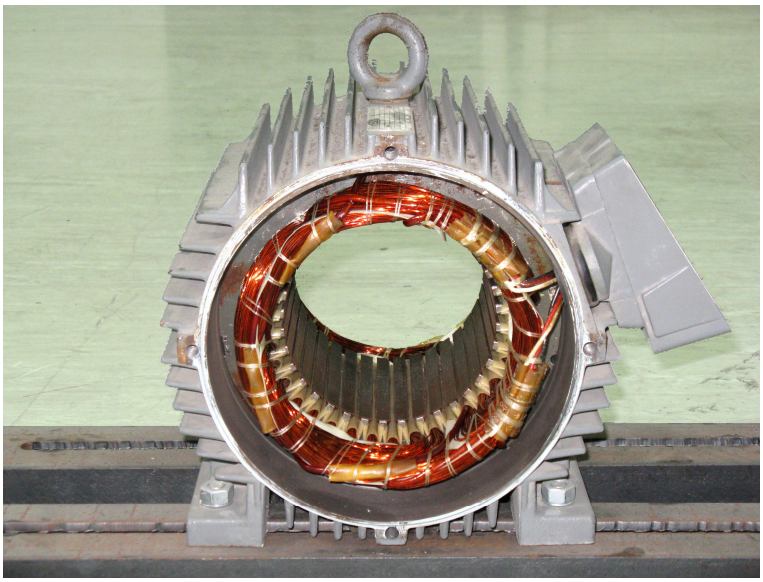

Figure 4.37: Stator of induction machine

Table 4.7 stated the machine parameter derived from the machine test described in Appendix A.

Stator resistance	R_S = 3.38 Ω
Rotor resistance	R_R = 2.91 Ω
Stator leakage inductance	$L_{S\sigma}$ = 20.25 mH
Rotor leakage inductance	$L_{R\sigma}$ = 20.25 mH
Air gap resistance	R_0 = 1166.7 Ω
Air gap inductance	L_0 = 415.5 mH
Stator time constant	τ_R = 150 ms
Magnetising stator current	i_{Sd} = 7.6 A
Torque producing stator current	i_{Sq} = 12.5 A

Table 4.7: Determined machine parameters

4.7 DC Drive

A DC drive is used to load the AC machines under test. The used ABB DC machine and its nameplate is shown in Figures 4.38 and 4.39. The machine is supplied by the ABB DCS 400 four-quadrant thyristor power converter [72]. No modifications of the industrial DC drive are done. It is only operated as recommended by the manufacturer. The drive can be operated in torque and speed control. The drive parameters and reference values are either set by the local panel on the converter or by the connected PC with the provided software Drive Window Light [73]. The Drive Window Light software allows also capturing of the drive parameters during the operation.

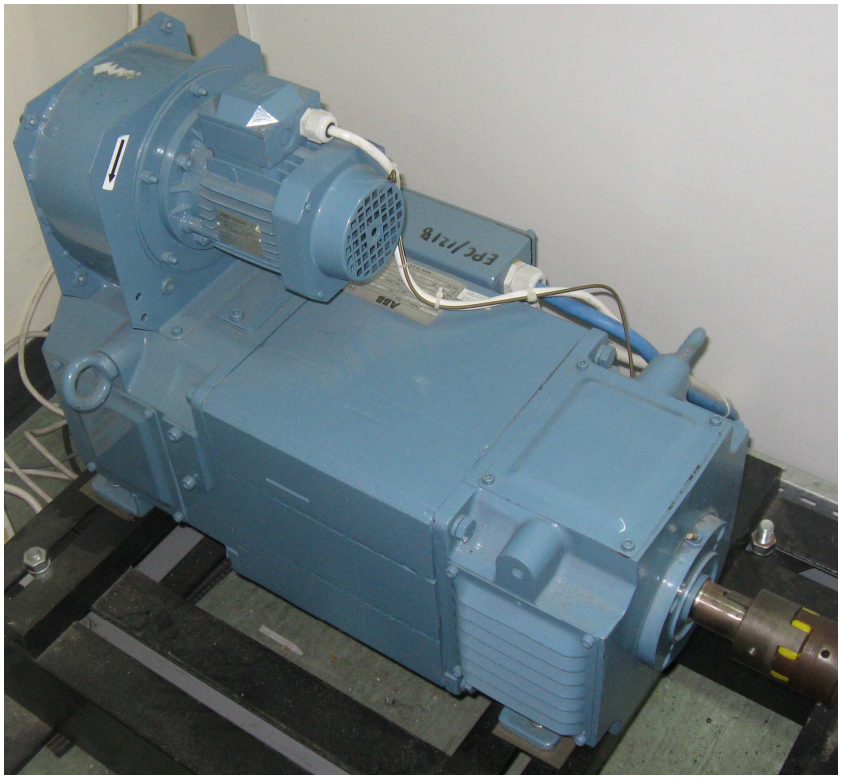

Figure 4.38: Picture of DC machine

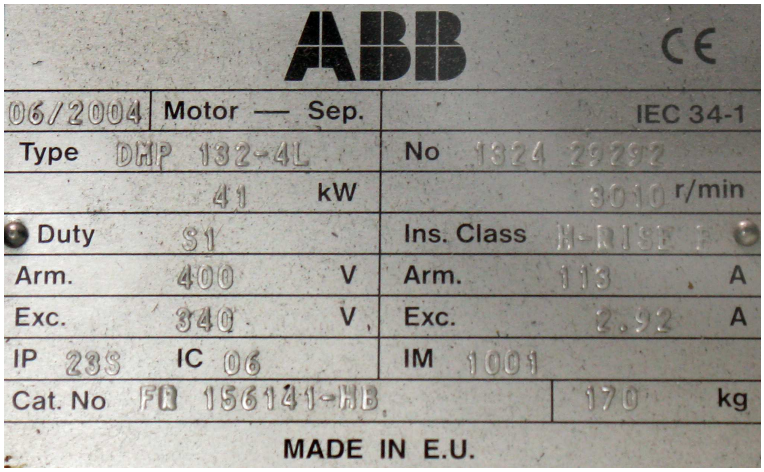

Figure 4.39: Nameplate of DC machine

Figure 4.40: DC drive converter

From the rated power P_{rated} and the rated speed n_{rated} the rated torque T_{rated} can be calculated:

$$T_{rated} = \frac{P_{rated}\,60}{n_{rated}\,2\pi} = \frac{41\text{kW}\,60}{3010\text{ rpm}\,2\pi} = 130\text{ Nm} \quad . \tag{4.13}$$

The DC machine output torque is under constant field proportional to the armature current i_{arm}. Therefore the torque constant k_T can be calculated by:

$$k_T = \frac{T_{rated}}{i_{arm\,rated}} = \frac{130\,\text{Nm}}{113\,\text{A}} = 1.15\frac{\text{Nm}}{\text{A}} \quad . \tag{4.14}$$

Thus the electrical DC machine torque can be calculated from the DC machine armature current.

Chapter 5
Zero Vector Current Derivative Method

The inherent back EMF and the saliency of AC machines can be utilized to identify the rotor/ flux position. The zero vector current derivative (ZVCD) method for sensorless control of permanent magnet machines, utilizing both of these effects [74], is proposed in this chapter. No additional test signals are injected into the machine and the difficulty in sensing the machine terminal voltage at low speed is eased. Only three standard current transducers are used in the drive system. For the position/ speed estimator only the machine current derivatives detected during the relatively long (at low speed) zero voltage vectors are used for obtaining the rotor position. The measured current derivatives are affected by the machine saliency and the back EMF. Practical results show the operation of the drive at several torque and speed conditions including stand still.

In the used machine the considered saliency is directly orientated with the mechanical rotor position aligned to the real *dq* frame position. Therefore the saliency position $\lambda_{dq'}$ equals the real rotor flux position λ_{dq}. Thus in this chapter the *dq* frame is referred as saliency frame and rotor flux vector control frame. Furthermore only stator current values are considered. Therefore the index "*S*" to indicate stator variables, as used in Chapter 2, is omitted for simplicity.

5.1 Practical Implementation of the Current Derivative Acquisition

For measuring the motor currents and their derivatives, three standard current hall effect transducers are used. No analogue low pass filters are used. Since the zero voltage vector duration is relatively long at low speed, calculation of the current derivative from two consecutive samples, taken during each zero voltage vector, yield a useable $\Delta i/\Delta t \approx di/dt$ signal. In contrast, [26], [52], [53] directly measure the di/dt by dedicated current derivative sensors as the active vectors during which the measurement is required are quite short. The maximum fundamental output voltage is limited to approximately 30 % of rated as the technique is intended for low and zero speed operation. This ensures a sufficient zero voltage vector duration, even under transients.

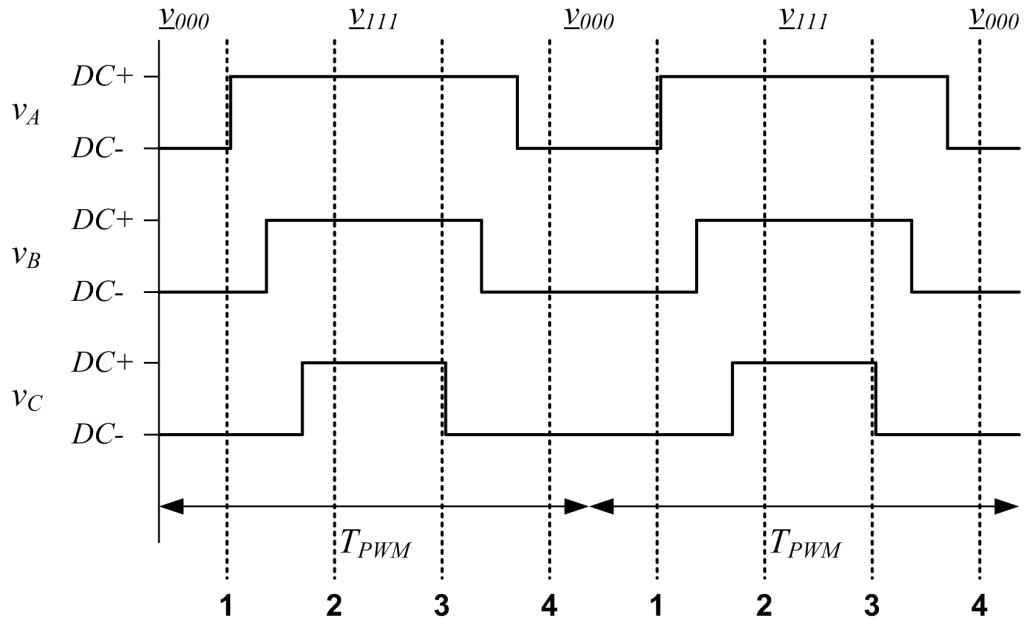

Figure 5.1: Discrete current sampling synchronized to the voltage switching

Figure 5.1 shows the current sampling instances with reference to the inverter PWM waveforms. In order to allow a precise current derivative measurement during the zero vectors, in this work a relative low PWM switching frequency is applied. A PWM switching frequency of 3.75 kHz is used and the sampling frequency of the A/D converters is set to four times faster. Therefore, the time between successive current samples is 66.6 µs. The first measurement occurs at least 20 µs delayed from the end of the last active voltage vector. This allows current oscillations following switching to settle and gives the current transducers time to follow the current trend precisely. The current derivative is computed for each zero voltage vector. Thus, there are two $\Delta i_0/\Delta t \approx di_0/dt$ measurements made in each PWM period. In Figure 5.1 the dashed vertical lines numbered 1 to 4 per PWM period show the current sampling instances. Samples 2 and 3 are used for calculating the current variation during $\underline{v}_{111}$ (all motor phases connected to positive DC link rail *DC*+) and sample 1 and 4 of the previous PWM period are used for calculating the current variation during $\underline{v}_{000}$ (all phases connected to negative DC rail *DC*-). The two measurements per PWM period are then averaged to give the position error signal.

5.2 Derivation of the Sensorless Algorithm

The derivation starts from the fundamental voltage equations in the *dq* frame shown in equation (5.1). It should be noted here that the cross coupling terms in (5.1) are left out for simplicity. For completeness of the theoretical explanation the influence of the cross coupling term is in detail discussed in section 5.9 and results will show that the influence is insignificant in the practical implemented sensorless drive.

$$v_d = R i_d + L_d \frac{di_d}{dt} \tag{5.1}$$

$$v_q = R i_q + L_q \frac{di_q}{dt} + k_e \omega_R \tag{5.2}$$

In equation (5.1) R is the stator resistance, L is the total leakage inductance, ω_R is the rotor speed and k_e represents the back EMF constant. The inductance parameters L_d and L_q are different due to the machine saliency, caused by the mechanical rotor construction and/ or magnetic saturation. When a zero voltage vector is applied, the inverter shorts the motor terminals driving both v_d and v_q to zero. The stator voltage equations (5.1) and (5.2) can then be simplified to equation (5.3) and (5.4) which reveal two different time constants dependent on the difference in L_d and L_q of the machine. The subscript "*0*" refers to zero voltage vector condition.

$$\frac{di_{d0}}{dt} = -\frac{R}{L_d} i_d \tag{5.3}$$

$$\frac{di_{q0}}{dt} = -\frac{R}{L_q} i_q - \frac{k_e \omega_R}{L_q} \tag{5.4}$$

Equation (5.3) and (5.4) only apply in the real dq frame, which is not known when using sensorless operation. Considering an estimated dq frame such as dq^e in Figure 5.2, offset from the real dq frame by an angle λ_{err}, equations (5.3) and (5.4) transform into equation (5.5) and (5.6).

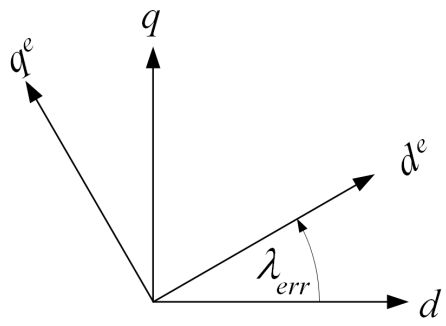

Figure 5.2: Relation of real *dq* and estimated dq^e reference frame

$$\frac{di_{d0}^{e}}{dt} = \frac{R}{L_d L_q}\left(\left(\left(L_d - L_q\right)\cos\left(\lambda_{err}\right)^2 - L_d\right) i_d^e - \left(L_d - L_q\right)\sin\left(\lambda_{err}\right)\cos\left(\lambda_{err}\right) i_q^e\right) - \sin\left(\lambda_{err}\right)\frac{k_e \omega_R}{L_q} \tag{5.5}$$

$$\frac{di_{q0}^{e}}{dt} = -\frac{R}{L_d L_q}\left(\left(L_d - L_q\right)\sin\left(\lambda_{err}\right)\cos\left(\lambda_{err}\right) i_d^e + \left(\left(L_d - L_q\right)\cos\left(\lambda_{err}\right)^2 + L_q\right) i_q^e\right) - \cos\left(\lambda_{err}\right)\frac{k_e \omega_R}{L_q} \tag{5.6}$$

In the assumed operation of the PMSM motor only a torque producing current is introduced and thus the vector controller is set to force i_d^e to zero as shown by Figure 5.3. Hence equation (5.5) and (5.6) can be simplified to (5.7) and (5.8).

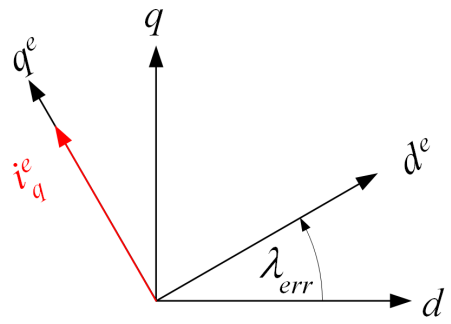

Figure 5.3: Current vector in the assumed operation

$$\frac{di_{d0}^{e}}{dt} = -\frac{R}{2}\left(\frac{1}{L_q} - \frac{1}{L_d}\right)\sin\left(2\lambda_{err}\right) i_q^e - \frac{k_e \omega_R}{L_q}\sin\left(\lambda_{err}\right) \tag{5.7}$$

$$\frac{di_{q0}^{e}}{dt} = \underbrace{\frac{R}{2}\left(\left(\frac{1}{L_q} - \frac{1}{L_d}\right)\left(1 + \cos\left(2\lambda_{err}\right)\right) + \frac{2}{L_d}\right) i_q^e}_{Saliency} \underbrace{- \frac{k_e \omega_R}{L_q}\cos\left(\lambda_{err}\right)}_{Back\ EMF} \tag{5.8}$$

Here, the current derivative in the estimated d^e axis is of particular interest. From equation (5.7) can be seen that it depends on two terms, a component of the quadrature current resulting from the machine saliency and a component of the back EMF in the real q direction. The former is proportional to $\sin(2\lambda_{err})$, while the latter is proportional to $\sin(\lambda_{err})$. Hence, both provide the opportunity to identify the position error in the assumed orientation. Thus, this method forms a hybrid technique which utilizes both rotor position dependent properties (saliency and back EMF).

Equation (5.7) also shows that the identified position error signal goes to zero under correct rotor flux orientation. A possible approach is then to force this signal to zero and hence lock the dq^e coordinate system to the real machine rotor dq frame as in [41], [43-45]. This is done through the phase locked loop (PLL) structure shown in Figure 5.4. The PI controller adjusts the rotation velocity of the estimated dq^e frame which leads, after integration, to an estimated rotor position for vector orientation. After passing the PI controller output signal through a low pass filter, a smoothed speed feedback signal $\omega_{RF}{}^e$ is obtained suitable for further control loops. The need for the error signal polarity block in Figure 5.4 is explained in the following section.

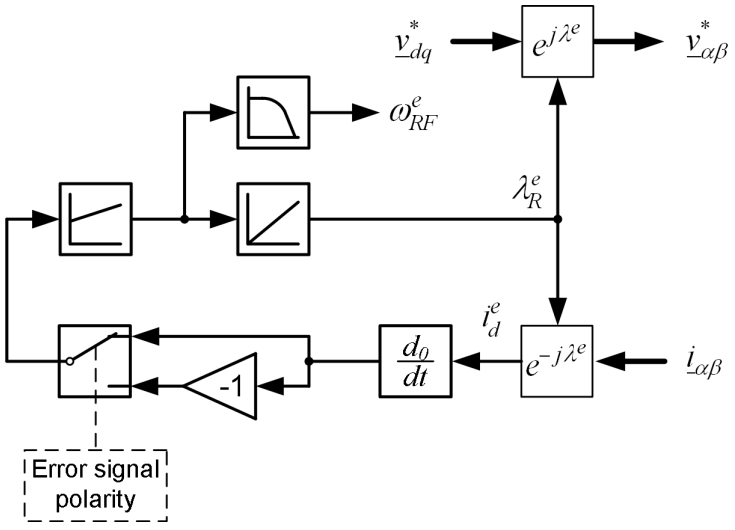

Figure 5.4: Block diagram of *dq* frame tracking scheme

5.3 Four Quadrant Operation

As shown in equation (5.7) the error signal is the sum of two effects, a back EMF and a saliency term. In motoring operation, where i_q^e and ω_R have the same sign, the error signal terms have the same polarity for small orientation errors (-90 ° < λ_{err} < 90 ° electrical). At higher speed the back EMF signal effect has much higher amplitude then the saliency effect. That means that the sensorless drive relies only on the back EMF information at higher speeds. However the sign of the back EMF signal will change with speed reversal. Thus the speed needs to be observed and the error signal polarity needs to be adjusted [75]. Generally, only the back EMF effect of this method could be used for any synchronous machine without saliency. The only restriction would be that a minimum speed needs to be achieved in order to detect the back EMF di_0/dt signal properly. Therefore zero speed operation would not be possible.

In a salient machine the saliency effect is super imposed with the back EMF error signal. It is speed independent and also present at zero speed. Only a small current is required in the machine. The polarity of the error signal depends only on the i_q^e current polarity and which of the quadrature inductance is larger, L_d or L_q. Figure 5.5 summarizes the di_{d0}^e/dt signal influences in all 4 operation quadrants for the condition that $L_d > L_q$ (as for the machine used in this work). In Figure 5.5 the small graphs symbolize the back EMF influence and the saliency effect of the di_{d0}^e/dt signal. As can be seen in motoring operation these two functions reinforce each other for small λ_{err} angles. By contrast these two signals will be opposing if i_q^e and ω_R have different sign (operation in quadrants *II* and *IV*). That means that in regeneration mode there is a speed/ torque range in which $di_d^e/dt(\lambda_{err})$ can not be directly used as the error signal. However, at very low speed the saliency signal is dominating and gives enough information for the position tracking and at above a certain speed the back EMF effect is much stronger than the saliency. That means

that there will be only a small operating region in quadrant *II* and *IV* that the proposed scheme does not cover which is indicated by the shaded areas in Figure 5.5. In all other regions only the dominating effect needs to be known and the error input sign accordingly selected.

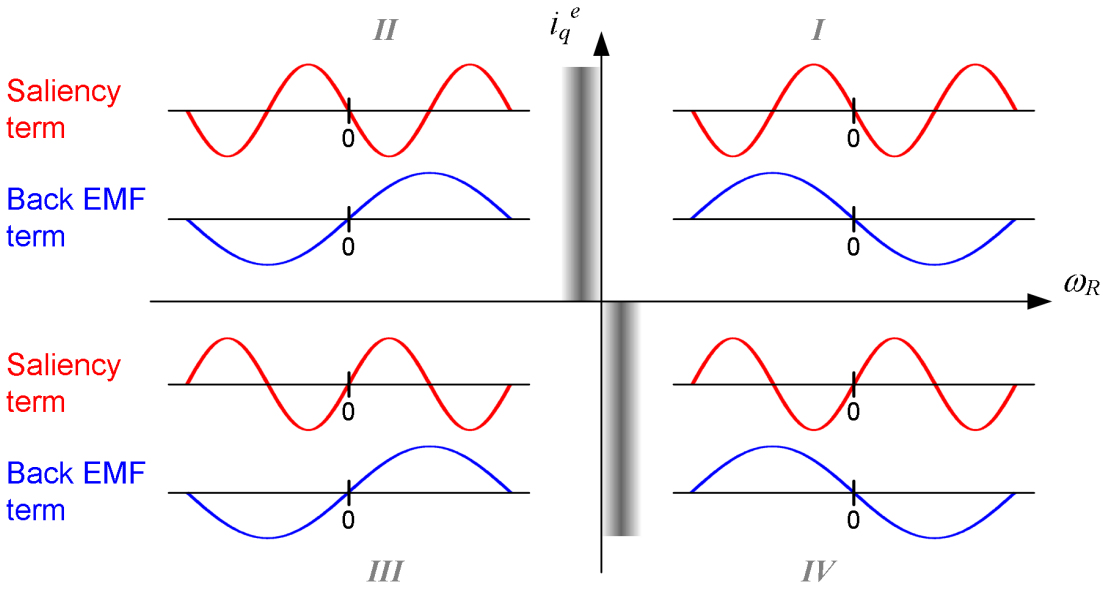

Figure 5.5: Estimation frame error signal di_{d0}^e/dt components in four quadrant operation

It can be concluded that the correct setting of the position error signal polarity is crucial for the successful operation of the method. Figure 5.6 shows the suggested error signal polarity correction function for four quadrant operation. At higher speeds, the back EMF effect is dominant, hence the position error signal polarity can be set by the speed polarity. The enclosed area shows the operating points where the saliency term is dominant. In there, the polarity of the position error signal can be set to reflect the polarity of i_q^e. The grey areas in the regenerative operation quadrants identified in Figure 5.6 are the 'no–go' regions where the di_{d0}^e/dt position error signal is not useable. The position error signal polarity will then be a function of the speed and the imposed current. Since the saliency error signal strength depends also on the magnitude of the imposed current, the error signal polarity thresholds also

incorporate a function of the imposed machine current amplitude, not shown in Figure 5.6.

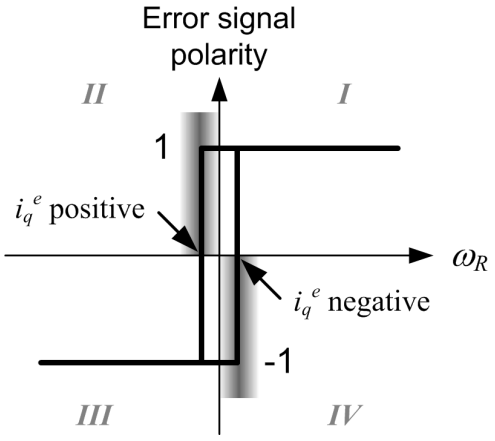

Figure 5.6: Error signal polarity correction function depending on imposed current i_q^e polarity and rotor speed ω_R

In practical experiments it was found that for the machine used the unstable 'no–go' region is in the range of approximately -0.4 to -0.1 Hz electrical for positive i_q^e values and 0.1 to 0.4 Hz for negative i_q^e values respectively. Hence above 0.4 Hz electrical, which refers to 0.4 % of rated speed for the PMSM used, the back EMF component in equation (5.7) is dominant. The operating range is then further extended by the saliency term in the range of -0.1 to 0.4 Hz electrical for positive torque values and in the range of -0.4 to 0.1 Hz electrical for negative torque values. Therefore the unstable operation range is approximately 0.3 Hz electrical wide.

5.4 Experimental Analysis of Measured Zero Vector Current Derivative

The first experiments test the relative size of the components of the position error signal. In these experiments, the q^e axis is assumed aligned to the stationary α axis. The inverter is controlled to impose a constant current into the α axis, i.e. q^e axis. The PMSM rotor is turned by the coupled DC motor and the di_0/dt signal is captured for both forward and backward rotation in order to measure the effect of the real dq frame misplacement to the injected current position, which is orientated in the estimated dq^e frame. Figure 5.7 visualizes the condition of the experiment with the reference frames used.

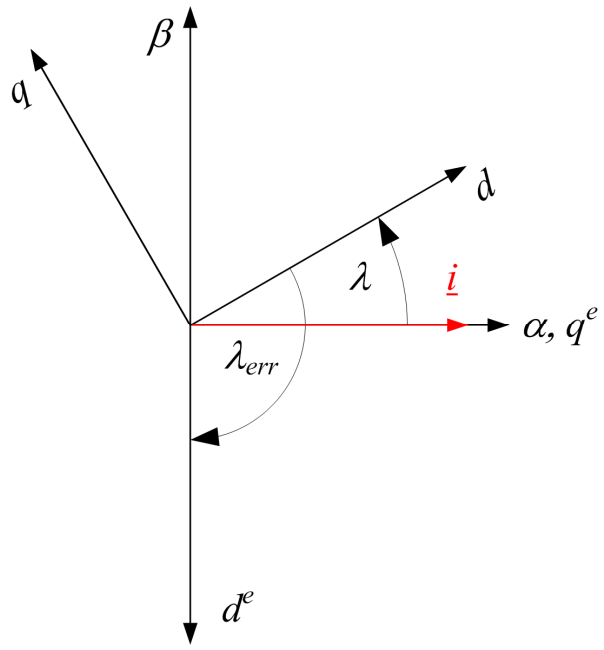

Figure 5.7: Reference frame relations in experiment with stator current constant aligned into α axis

Figure 5.8 shows the recorded experimental data plotted over the time for an imposed zero current demand (i_q^{e*} = 0 A). Plot (a) shows the recorded encoder rotor position, plot (b) contains the complex $\alpha\beta$ stator currents and (c) shows the DSP calculated current vector derivative during the zero vectors in the $\alpha\beta$ frame. It is already visible in the time plot that the di_0/dt signals are affected by the rotor position. In the experiment the rotor rotational direction is reversed at one point in time in order to investigate the effect of the back EMF, since it changes polarity with rotational direction.

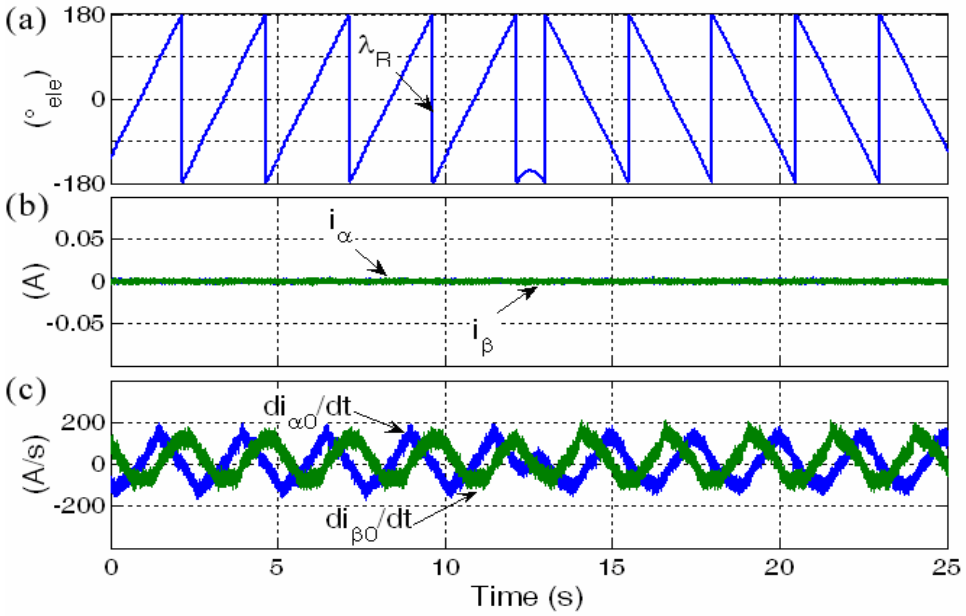

Figure 5.8: Time plot i_α^* = 0 A, i_β^* = 0 A, +/-6 rpm

In Figure 5.9 the current derivative in the estimated d^e axis is plotted as a function of the respective estimation frame position error λ_{err}. The blue dots show the current derivative values for the forward and the green dots for the backward rotation. The position error signal arises solely due to the back EMF effect as there is no fundamental current imposed on the machine. It can be seen that the back EMF dependent $di_{d0}^e/dt(\lambda_{err})$ signal changes its polarity with the rotational direction. The

resulting sin(λ_{err}) signal is quite pronounced and can be used for the proposed sensorless tracking algorithm, even if the speed in this experiment is just 0.4 % of rated value. The back EMF amplitude at this speed is about 0.57 V.

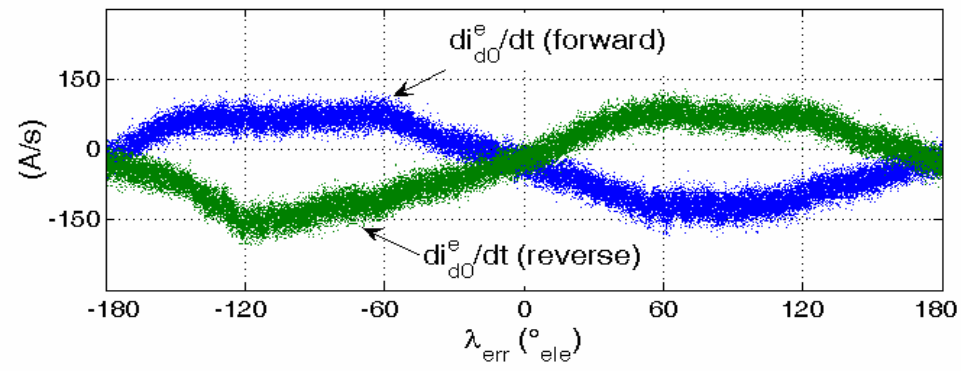

Figure 5.9: $di_{d0}^e/dt(\lambda_{err})$ over rotor position i_q^e = 0 A, +/-6 rpm

In Figure 5.10 the same experiment as shown in Figure 5.8 is carried out, but with a non-zero stator current demand (i_q^{e*} = 1 A). In the time plot it can be seen that the measured zero vector current derivatives look slightly different from the previous experiment. Figure 5.11 shows the resulting di_{d0}^e/dt signal plotted over the misalignment angle λ_{err}. The result is similar to Figure 5.9 in that the sin(λ_{err}) signal due to the back EMF is clearly visible, however a sin(2λ_{err}) pattern due to the saliency can also be observed in this case. The saliency effect is now visible due to the non-zero i_q^e current. It is visible from Figure 5.11 that at this speed the back EMF term of equation (5.7) is still superior to the saliency di_{d0}^e/dt portion. Therefore under this condition only the back EMF signal can be used for the position tracking.

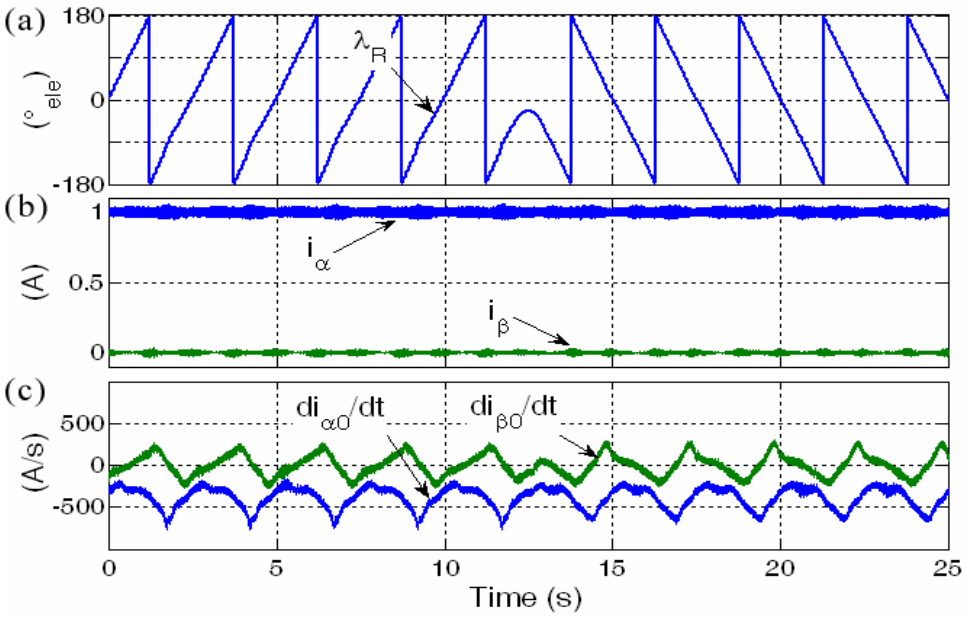

Figure 5.10: Time plot i_α^* = 1 A, i_β^* = 0 A, +/-6 rpm

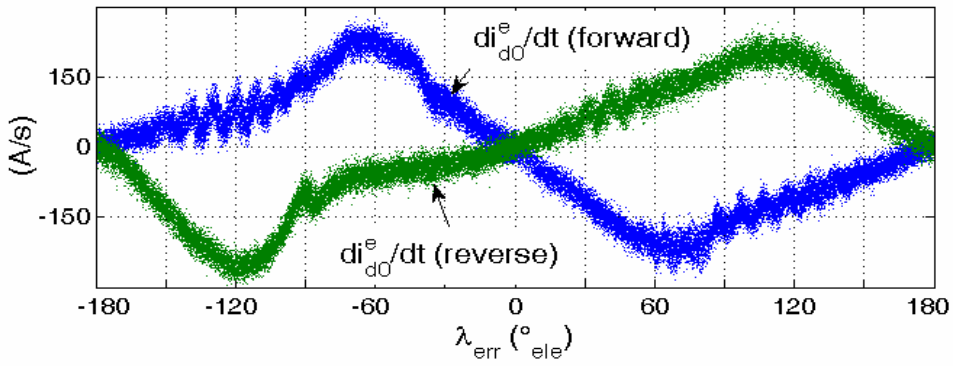

Figure 5.11: $di_{d0}^e/dt(\lambda_{err})$ over rotor position i_q^e = 1 A, +/-6 rpm

Figure 5.12 shows the results of a further experiment where the speed is reduced to +/-1 rpm, whilst keeping the demand current at 1 A. Figure 5.13 shows the resulting di_{d0}^e/dt signal plotted over the misalignment angle λ_{err}. Only a sin($2\lambda_{err}$) effect is now visible for both directions of rotation as derived in equation (5.7). This shows that in this experiment the saliency effect is dominant. This is due to the non-zero i_q^e current and the very low speed of operation.

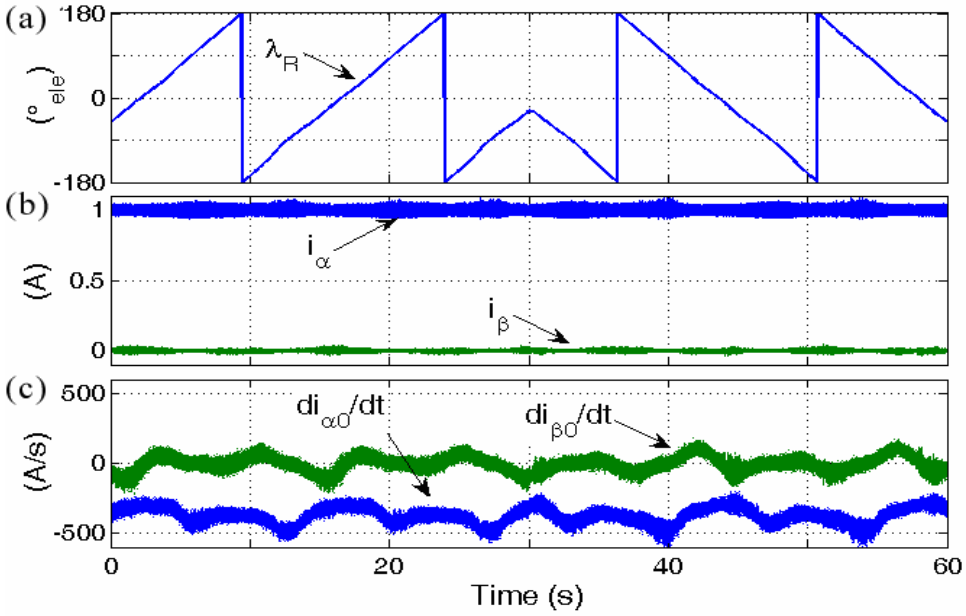

Figure 5.12: Time plot $i_\alpha^* = 1$ A, $i_\beta^* = 0$ A, +/-1 rpm

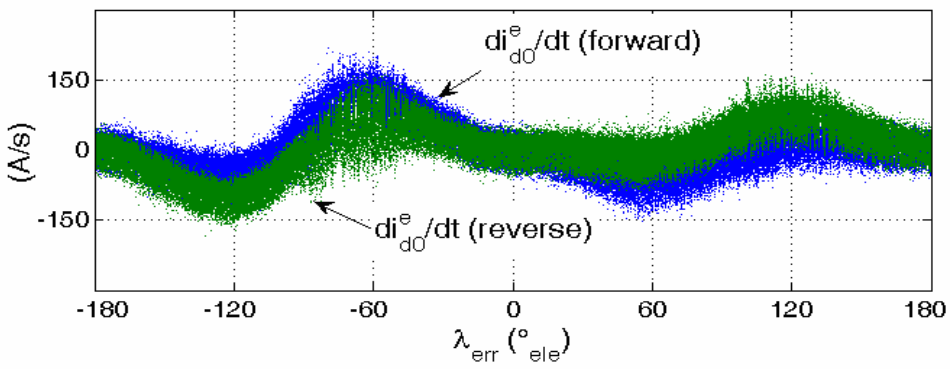

Figure 5.13: $di_{d0}^e/dt(\lambda_{err})$ over rotor position $i_q^e = 1$ A, +/-1 rpm

Figure 5.9 to 5.13 show that the detected di_0/dt signal is very noisy, but the position dependent information is visible and can be used for sensorless control of the PMSM drive. The useful $di_0/dt(\lambda_{err})$ function amplitude during the zero vectors can be as low as 100 A/s, depending on the stator current amplitude and operation speed. That means that the maximum phase current change during the 66.6 µs sampling interval of the discrete current measurement can be as low as 6.6 mA. This points out that a precise current measurement is required and 16-bit ADC's, as used in the

implementation, are recommended. In the experimental setup the current measurement range is set from -18.2 A to 18.2 A. Therefore the resolution of the digital current measurement is 0.56 mA.

5.5 Observed Inverter Non-linearity Effects

It was found that the current derivative measured during the zero voltage vectors depends not only on the current vector orientation in the rotor *dq* frame, but is also affected by the current vector position in the stator fixed $\alpha\beta$ frame. Figure 5.14 shows the current derivative components in *d* and *q* direction under sensored mode where the drive is always controlled in true orientation. The PMSM motor is set to a constant torque with $i_q^* = 1$ A, while the speed is controlled by the coupled DC machine to 1 rpm. Therefore di_{d0}/dt should be permanently zero and di_{q0}/dt should be constant under constant speed. In Figure 5.14 plot (a) shows the measured rotor position, plot (b) shows the applied machine currents in the true *dq* axes and plot (c) shows the measured di_{d0}/dt and di_{q0}/dt values. It can be seen that there is a significant modulation in the measured zero vector current derivative signals. Figure 5.15 shows the measured di_{d0}/dt samples plotted against the stator current vector position. From Figure 5.15 it can be seen that the modulation pattern is directly associated with the current vector position in the stator fixed $\alpha\beta$ frame. It can be seen that a predominant pattern repeats every 60 electrical degrees and is associated with the six current commutation sectors, where one of the phase currents changes its polatity. The magnitude of the modulation changes and needs to be compensated. Figure 5.15 shows also an averaged $di_{d0}/dt(\angle \underline{i}_{\alpha\beta})$ function (green line), calculated from the measured samples. It was found that the amplitude of the inverter non-linearity varies with the stator current vector amplitude.

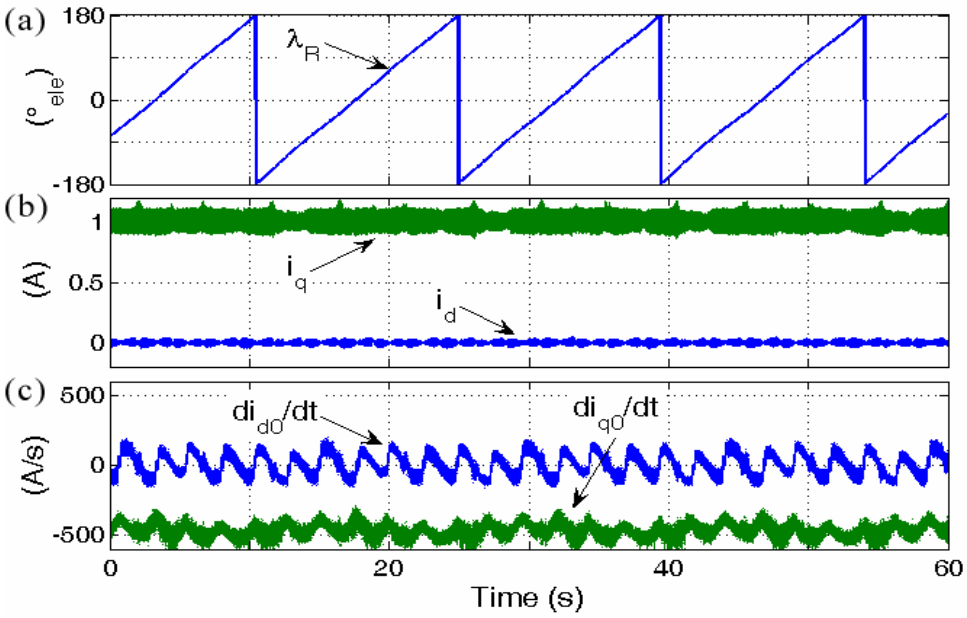

Figure 5.14: PMSM drive running in sensored torque control ($i_d^* = 0$ A, $i_q^* = 1$ A) at 1 rpm

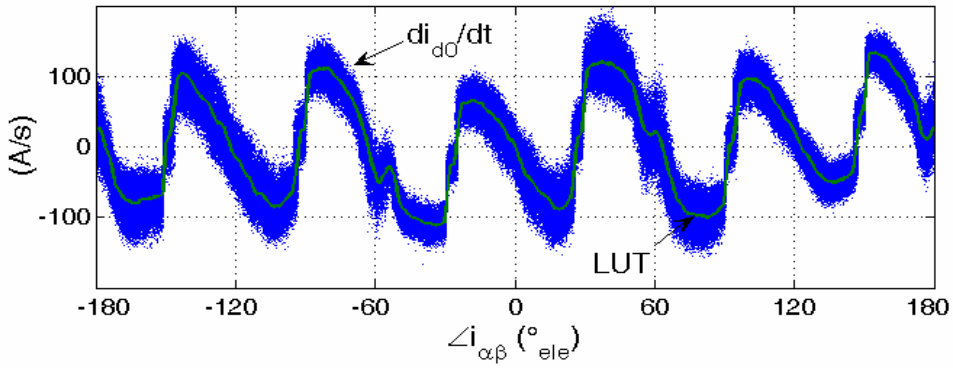

Figure 5.15: di_{d0}^e/dt over current vector position for 1 A current vector magnitude

Figure 5.16 shows the resulting di_{d0}/dt inverter non-linearity function for the torque producing current range of 0.1 to 11 A. The shown profile in Figure 5.16 is the combination of the averaged $di_{d0}/dt(\angle \hat{i}_{\alpha\beta})$ functions that were measured in several experiments in sensored mode (similar to Figure 5.14) with different i_q^* reference values. It might also be possible to generate such a table using sensorless control by operating at a slightly higher speed using a back EMF based technique for drive commissioning. A model based method can be used to control the machine in vector

control at a speed were the back EMF observer provides a precise position estimation for vector control. It can be assumed that under this condition the di_{d0}/dt signal is measured under "true" orientation. Therefore the di_{d0}/dt inverter non-linearity function could be also measured without an encoder. However, the quality of the generated di_{d0}/dt inverter non-linearity function will be not as precise as done under sensored condition with a directly measured position signal.

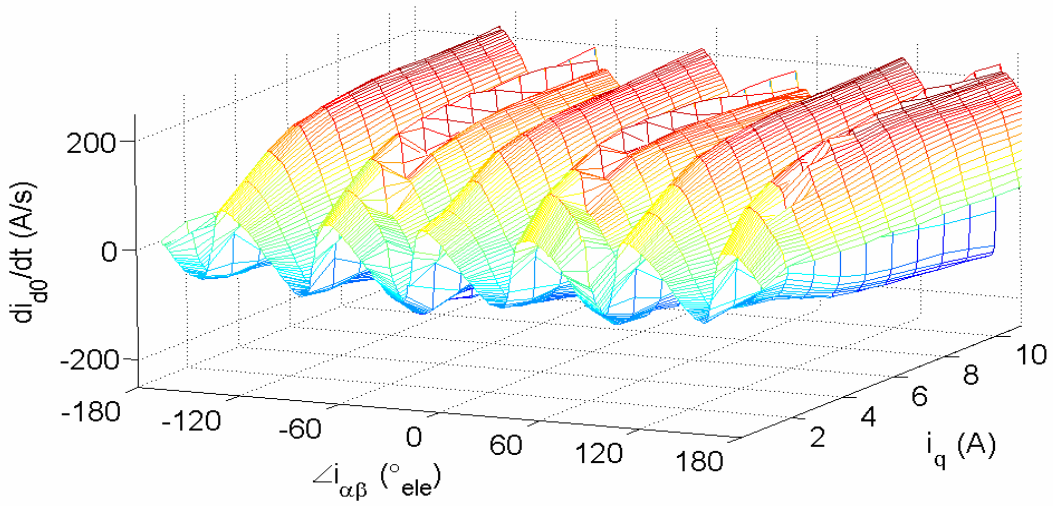

Figure 5.16: Measured $di_{d0}/dt(\underline{i}_{\alpha\beta})$ function in the range of 0.1 A to 11 A

5.6 Results with Direct Measured Inverter Non-linearity Compensation

The measured $di_{d0}/dt(\underline{i}_{\alpha\beta})$ average functions shown in the section before are used to decouple the inverter effects from the position error signal and are stored in the DSP as a look up table (LUT) as shown in Figure 5.17. The di_{d0}/dt look up table is referenced directly by the measured current vector magnitude and position.

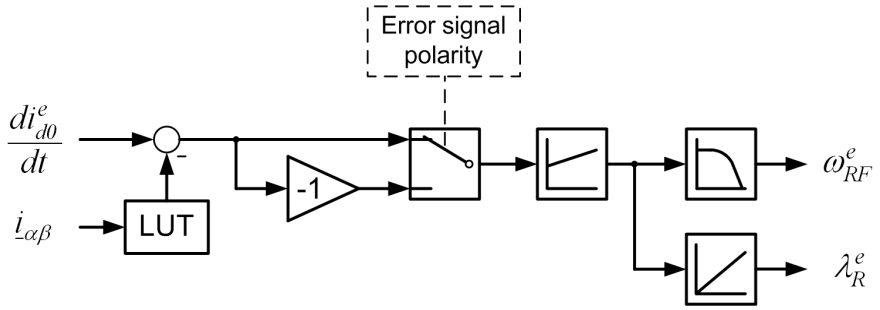

Figure 5.17: Block diagram of *dq* frame tracking estimator with LUT compensation

The parameters of the PI controller shown in Figure 5.17 are adjusted by trial and error. K_P is set in the range of 0.1 to 0.3 rad/ A and T_I is set between 0.05 to 0.3 s. The values were adjusted individually in each experiment to achieve the best performance. The filter for the estimated speed feedback is a first order low pass Butterworth design implemented directly in the DSP algorithm with a cut off frequency of 2 Hz.

5.6.1 Sensorless Torque Control

Figures 5.18 to 5.31 show experiments with the implemented PMSM drive operating with sensorless torque control. In torque control the speed of the machine rig is controlled by the coupled DC machine. The sensorless PMSM drive i_q reference variable is set to a value proportional to the required torque. At a fixed i_q reference value the stator current amplitude is approximately constant set by the current controllers. In the experiments for each set i_q reference value, a single di_{d0}/dt compensation look up table is used as shown in Figure 5.15. The quantisation of the di_{d0}/dt compensation look up table is 0.1 electrical degrees for the stator current vector position. Therefore each compensation look up table has 3600 values. In Figures 5.18 to 5.31 plot (a) shows the measured and estimated rotor position (λ_R and λ_R^e), plot (b) shows the difference between measured and estimated rotor position

(λ_{err}) and plot (c) shows the applied machine currents in the estimated dq^e reference frame.

Figures 5.18 to 5.21 show the performance of the sensorless controlled drive system only in motoring operation, thus in operation quadrants *I* or *III*. As shown in Figure 5.5 in operation quadrants *I* and *III* the di_{d0}^e/dt saliency and back EMF component give a combined position error feedback. Therefore sensorless operation down to zero speed is possible with the salient PMSM motor used. Figures 5.18 to 5.20 show the operation of the sensorless PMSM drive at constant torque and very low and zero speed with minimum and high machine current. The error signal polarity of the tracking PLL system shown in the block diagram of Figure 5.17, is set manually to be a positive value.

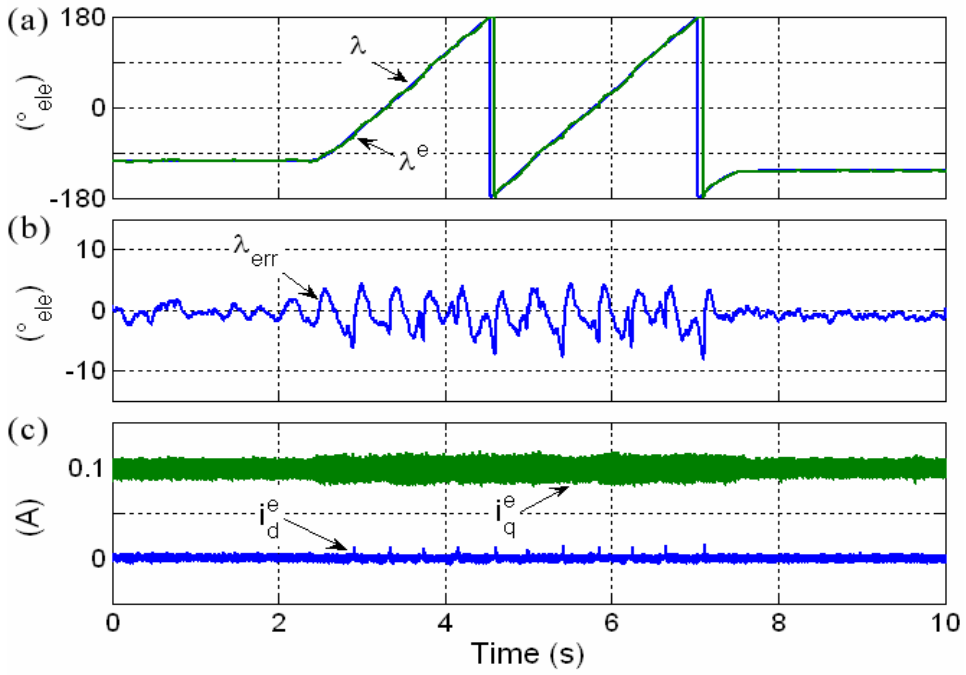

Figure 5.18: Sensorless operation of the drive at zero speed and 0.4 Hz electrical (6 rpm) with low current (i_q^* = 0.1 A)

In Figure 5.18 to 5.31 the applied current amplitude of 0.1 A corresponds to less then 1 % of rated machine current. As can be seen from equation (5.7) the amplitude of

the imposed machine current amplifies directly the zero vector current derivative saliency term. It can be seen from the experiment in Figure 5.18 that the di_{d0}^{e}/dt error signal from the saliency term is still strong enough to enable sensorless control of the drive at zero speed.

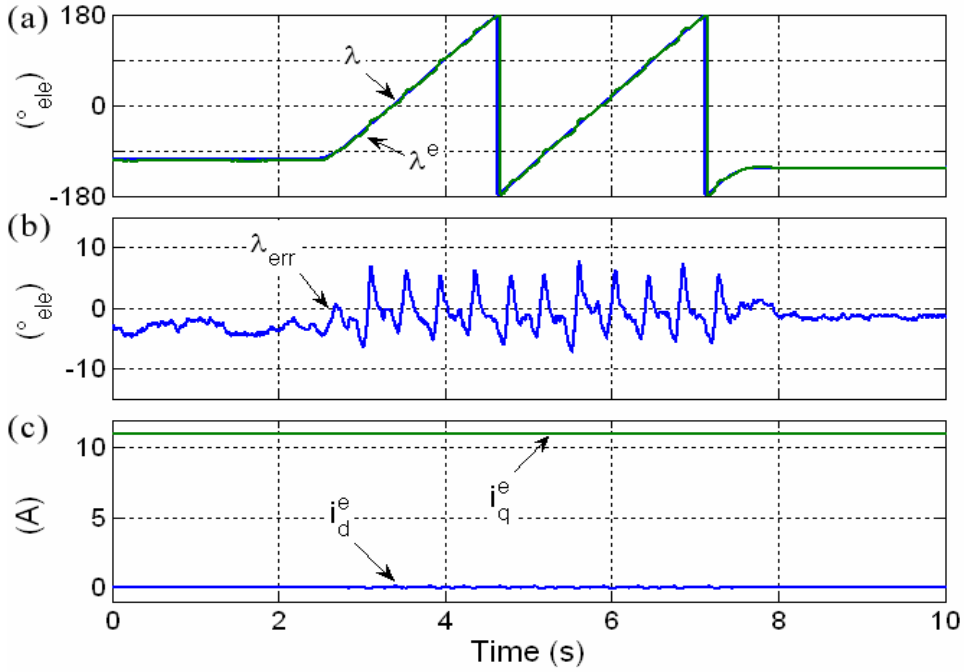

Figure 5.19: Sensorless operation of the drive at zero speed and 0.4 Hz electrical (6 rpm) with $i_q^* = 11$ A

Figure 5.19 shows the same experiment as Figure 5.18, but for high torque ($i_q^* = 11$ A). Both of the above experiments show stable operation of the sensorless drive at zero and very low speed at very low and high torque. As can be seen, the current controllers keep the machine currents constant in the estimated dq^e reference frame. It can be seen that the estimated position matches the real rotor position. This shows that the sensorless algorithm is capable of tracking reliably the machine's rotor position. The position error plots show that there are estimation errors of up to 8 electrical degrees which correspond to 2 mechanical degrees for the 8 pole machine. One can notice that the position error shows a 6 f_e pattern, which repeats with the

current commutation sectors. This leads to the conclusion that there are further disturbance effects related to the current position in the $\alpha\beta$ frame, which are not completely compensated by the basic LUT compensation scheme. However, the drive system shows stable operation and the resulting toque ripple may be acceptable in certain applications.

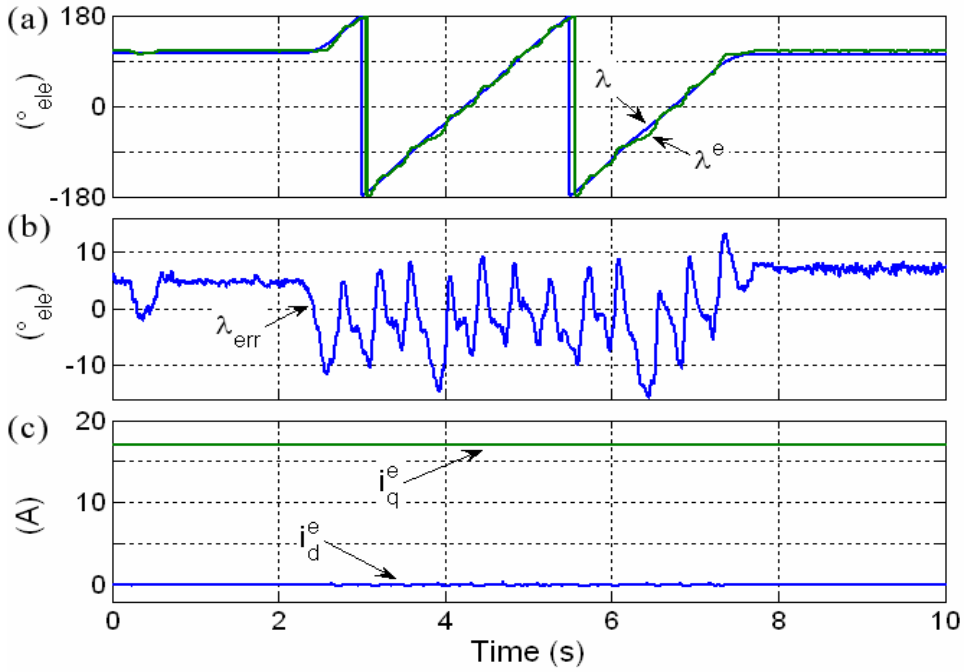

Figure 5.20: Sensorless operation of the drive at zero speed and 0.4 Hz electrical (6 rpm) with $i_q^* = 17$ A

Figure 5.20 shows a result of the sensorless drive operating in torque control at the maximum current possible with the set up hardware. It can be seen that the position error has increased. Also the tracking at zero speed is less accurate. However, the position estimation scheme also tracks the rotor position down to zero zpeed.

The results shown in Figure 5.21 represent one of the most critical conditions for a sensorless PMSM drive system, high load steps at zero speed operation. The i_q^e reference is changed from 0.1 A to -11 A, to 11 and to -0.1 A as indicated in the

figure. The position tracking PLL error input polarity is changed to positive when i_q^* is positive (0.1 A, 11 A) and negative when i_q^* is negative (-0.1 A, -11 A).

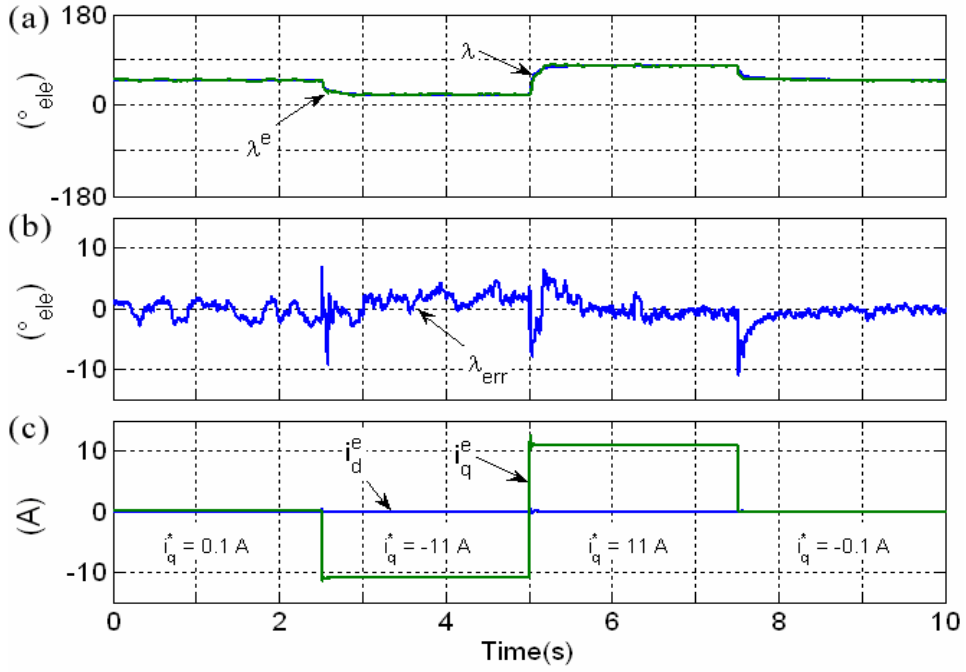

Figure 5.21: Load step response at stand still with torque steps

As can be seen from the experiment, the current controllers set the demanded currents with a fast dynamic response, since the current control loops have a high bandwidth. In Figure 5.21 some position error oscillations can be seen at the step instances, which reflect the dynamic response of the tracking PI controller to the speed transitions. However, it can be seen that the sensorless position estimation PLL system has no difficulties in keeping locked to the correct rotor position. In the position error plot the estimation error is within the range of +/-10 electrical degrees, which corresponds to a precision of +/-2.5 mechanical degrees.

In the experiments shown in Figures 5.18 to 5.21 at zero speed, the back EMF amplitude is zero too. Therefore under this condition only the saliency term of di_{d0}^{e}/dt in (5.7) provides information for the position tracking scheme.

Figures 5.22 and 5.23 show the drive in motoring and generating operation in the forward and reverse directions with torque transients imposed. The i_q^e reference current is also changed between 0.1 A , -11 A, 11 A and -0.1 A. The PMSM drive runs under sensorless torque control and the speed is set by the coupled DC drive. In Figure 5.22 the DC drive is set to a reference speed of 12 rpm in the forward direction and in Figure 5.23 in the reverse direction. Therefore in Figure 5.22, operation in quadrants *I* and *IV* is achieved whilst in Figure 5.23 the operation is in quadrants *II* and *III*. The di_{d0}^{e}/dt error signal polarity at this speed is only determined by the back EMF sign, which depends on the direction of rotation. Therefore in the experiment of Figure 5.22 the error signal polarity is constant and set to positive and in the experiment of Figure 5.23 it is set to negative.

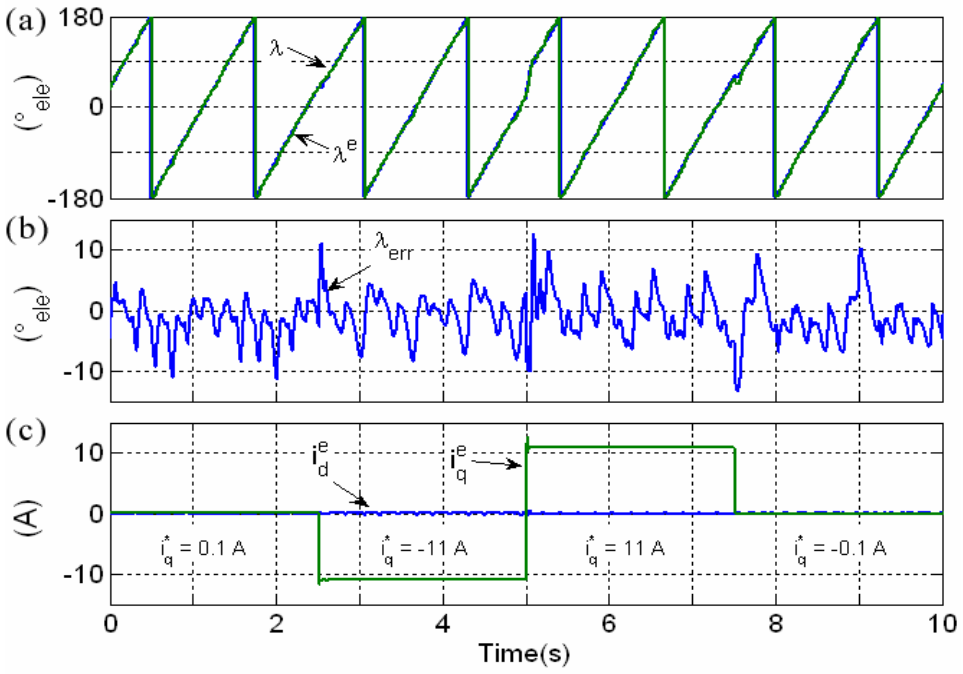

Figure 5.22: Torque steps in forward direction at 0.8 Hz electrical (12 rpm)

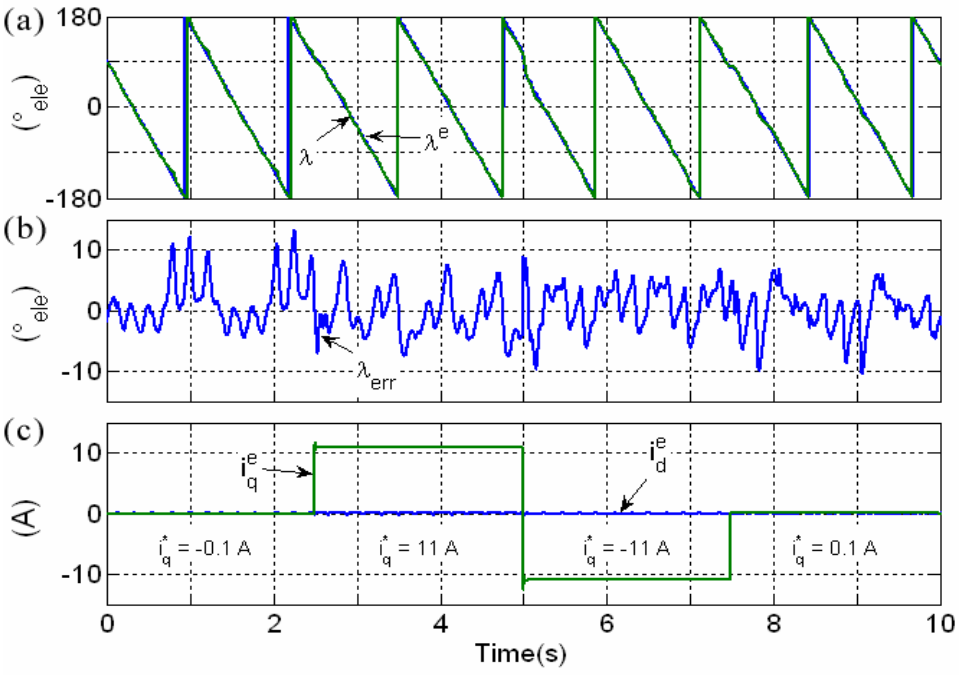

Figure 5.23: Torque steps in reverse direction at -0.8 Hz electrical (-12 rpm)

As can be seen in Figures 5.22 and 5.23, the i_q^e polarity change does not affect the position tracking algorithm significantly since the back EMF is the dominant term in the di_{d0}^e/dt error signal under the shown operating conditions. The ripple pattern in the estimated position changes slightly with the different i_q^e current values. However, the position error is kept in the range of about +/-12 electrical degrees.

Figures 5.24 to 5.31 show the sensorless algorithm initialisation from standstill. For the experiments in the forward direction the di_{d0}^e/dt error signal polarity is manually set to positive and in the experiments with backwards rotation to negative polarity. At the beginning of the experiments the estimated position is initialised manually to a wrong position value as indicated in the figures. The initial value is set deliberately to λ_{err} = 180 electrical degrees. This is the worst case for the algorithm to start from

unknown rotor position. The experiments are only intended to explain the behaviour of the position tracking algorithm at start up from unknown rotor position.

Figures 5.24 to 5.27 show the operation at zero torque, therefore zero current. Thus the position estimator relies only on the back EMF component. It can be seen that the algorithm fails to estimate the position at zero speed due to the lack of both back EMF (zero speed) and saliency signals (no load). However, as soon as there is some rotation, the back EMF component provides a suitable signal. In Figures 5.24 and 5.25 the rotor speed is +/-6 rpm, which corresponds to +/-0.4 % of rated speed. At this low speed the back EMF amplitude is only approximately 0.57 V. A correct position initialisation and tracking is achieved, even if the estimated position signal is quite noisy and the error values reach up to +/-27 electrical degrees. Figures 5.26 and 5.27 show the same zero current experiments at double the speed (+/-12 rpm). It can bee seen that the position estimation quality improves significantly, even if the speed is still less then 1 % of rated value and the back EMF voltage amplitude is just a bit more then 1 V. The amplitude of the position estimation error is about +/-11 electrical degrees.

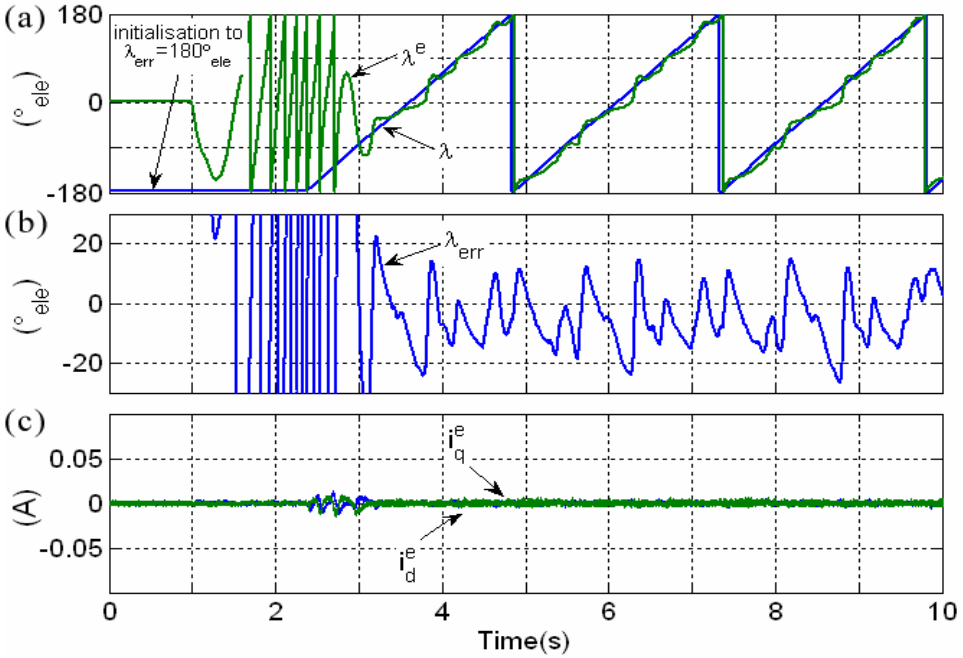

Figure 5.24: Sensorless operation of the drive from zero speed to 0.4 Hz electrical (6 rpm) with zero current (forward rotation)

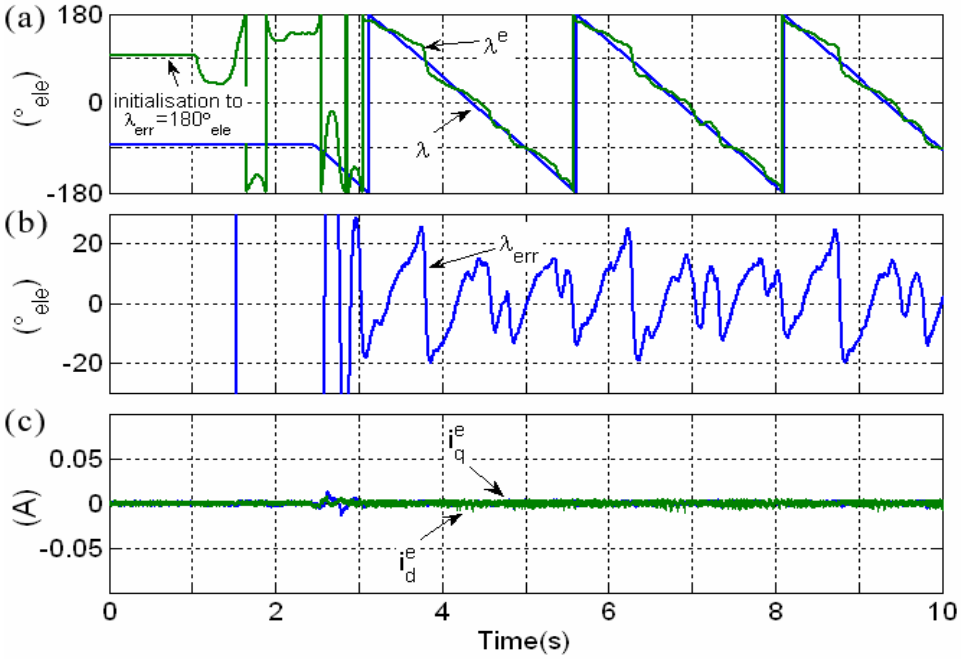

Figure 5.25: Sensorless operation of the drive from zero speed to -0.4 Hz electrical (-6 rpm) with zero current (reverse rotation)

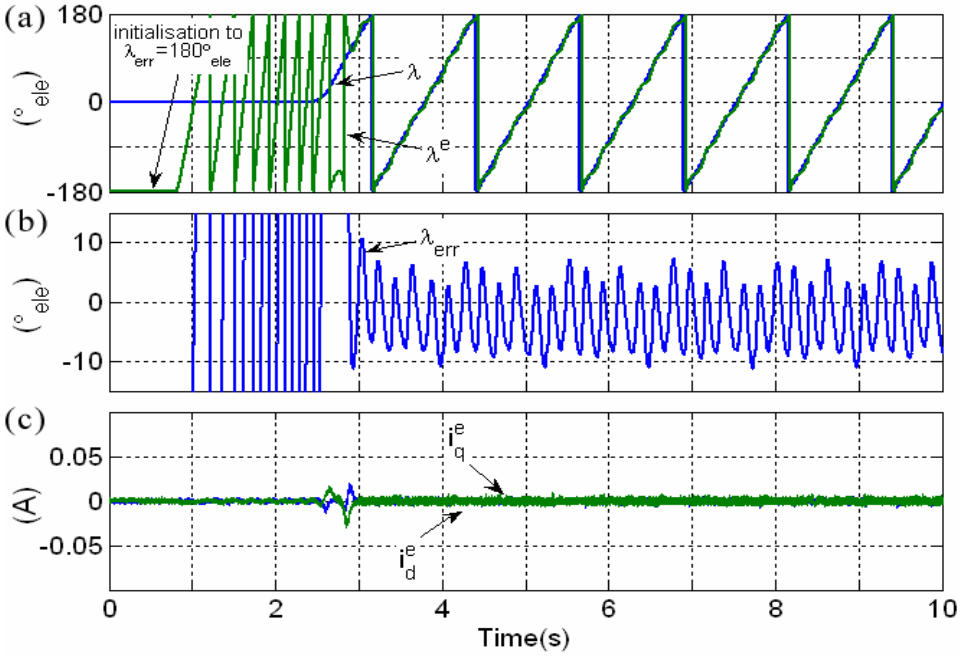

Figure 5.26: Sensorless operation of the drive from zero speed to 0.8 Hz electrical (12 rpm) with zero current (forward rotation)

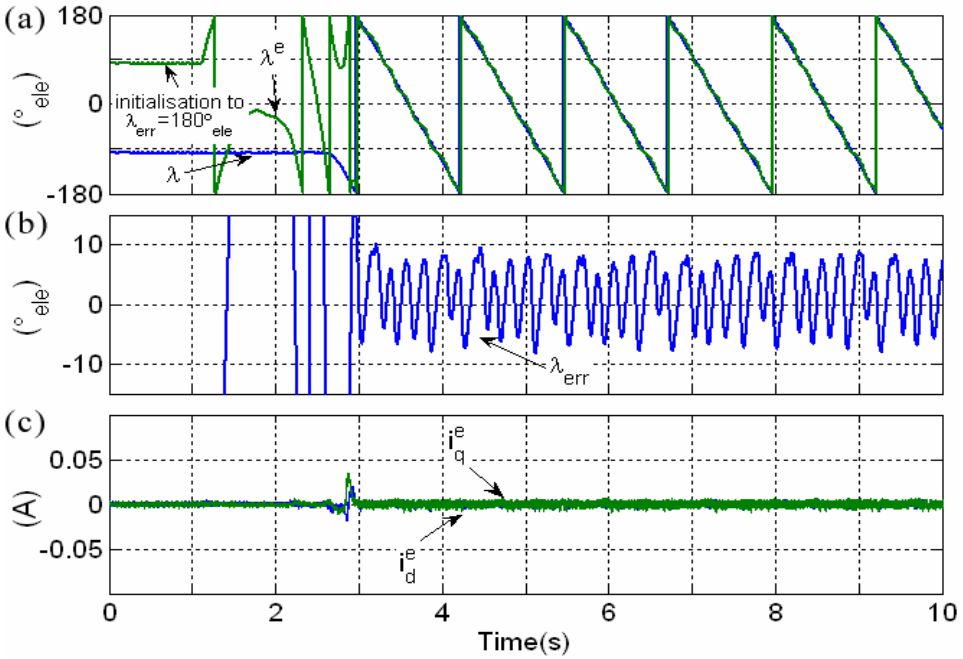

Figure 5.27: Sensorless operation of the drive from zero speed to -0.8 Hz electrical (-12 rpm) with zero current (reverse rotation)

Figures 5.28 and 5.29 show position initialisation experiments with minimum stator current (0.1 A), and Figures 5.30 and 5.31 with high stator current (11 A). It can be seen that the position tracking PLL locks (under zero speed) to a stable value due to the now pronounced saliency term.

In Figures 5.28 and 5.30 the PLL keeps locked to λ_{err} = 180 electrical degrees due to the condition $\sin(2\lambda_{err}) = 0$. This is a general issue of saliency based methods, since the saliency modulation has two minima and maxima per electrical period. However, in this method also the back EMF contributes to the position estimation, which has only one stable operation point, $\sin(\lambda_{err}) = 0$, at the true orientation. Therefore as soon as there is some rotor movement the back EMF forces the position estimator to the correct rotor position. It can be seen that once the position tracking PLL is locked to the true rotor position value, it follows the correct position back to zero speed if the drive is operating under motoring condition.

In Figures 5.29 and 5.31 the di_{d0}^{e}/dt error signal polarity is set to negative since operation is reverse direction is regarded. Since the applied currents are positive, the saliency error signal function is positive. As a result the estimated position keeps locked at zero speed at about λ_{err} = +/-90 electrical degrees, which are stable $di_{d0}^{e}/dt = 0$ tracking points (see Figure 5.5). As soon as there is some rotation the back EMF signal takes over and forces the sensorless algorithm to the correct rotor position value.

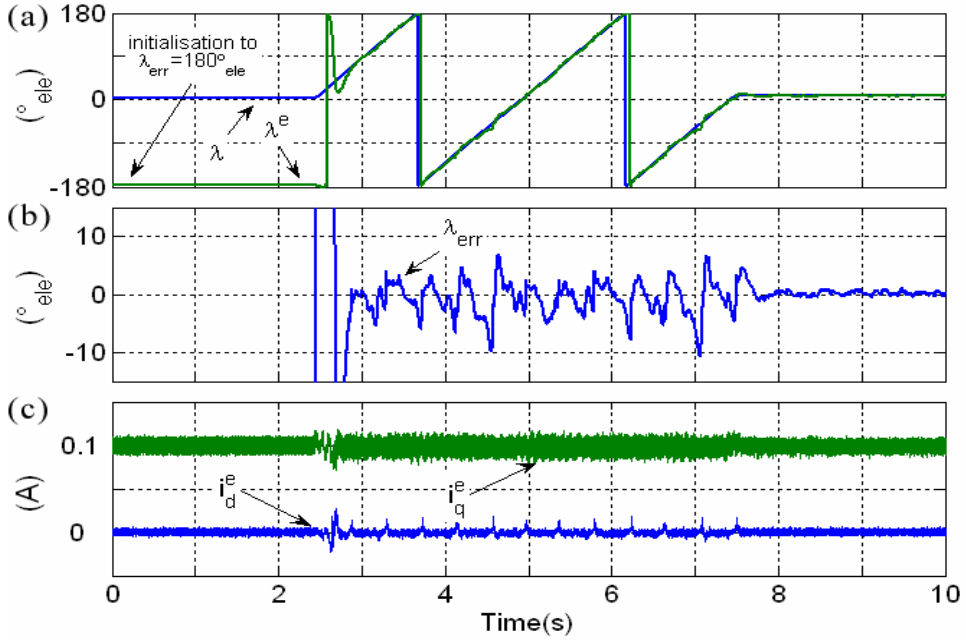

Figure 5.28: Sensorless operation of the drive from zero speed to 0.4 Hz electrical (6 rpm) with low current (i_q^* = 0.1 A) (forward rotation)

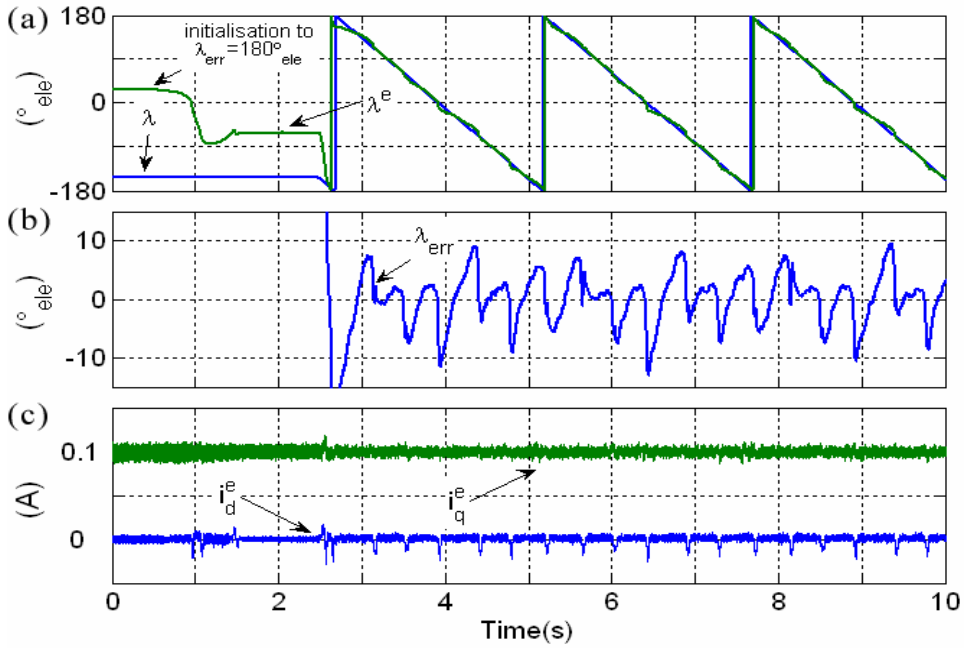

Figure 5.29: Sensorless operation of the drive from zero speed to -0.4 Hz electrical (-6 rpm) with low current (i_q^* = 0.1 A) (reverse rotation)

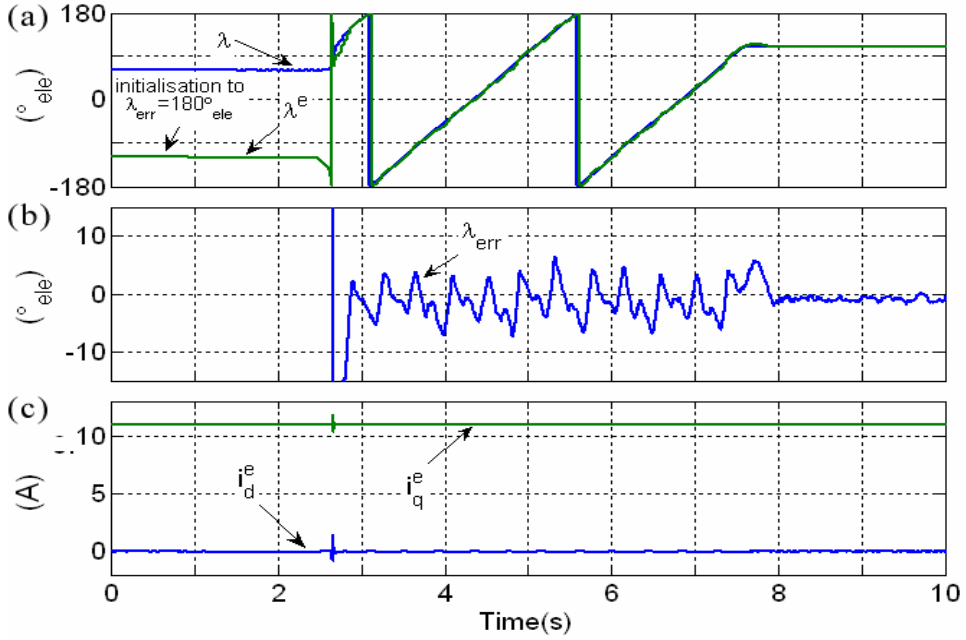

Figure 5.30: Sensorless operation of the drive from zero speed to 0.4 Hz electrical (6 rpm) with high current (i_q^* = 11 A) (forward rotation)

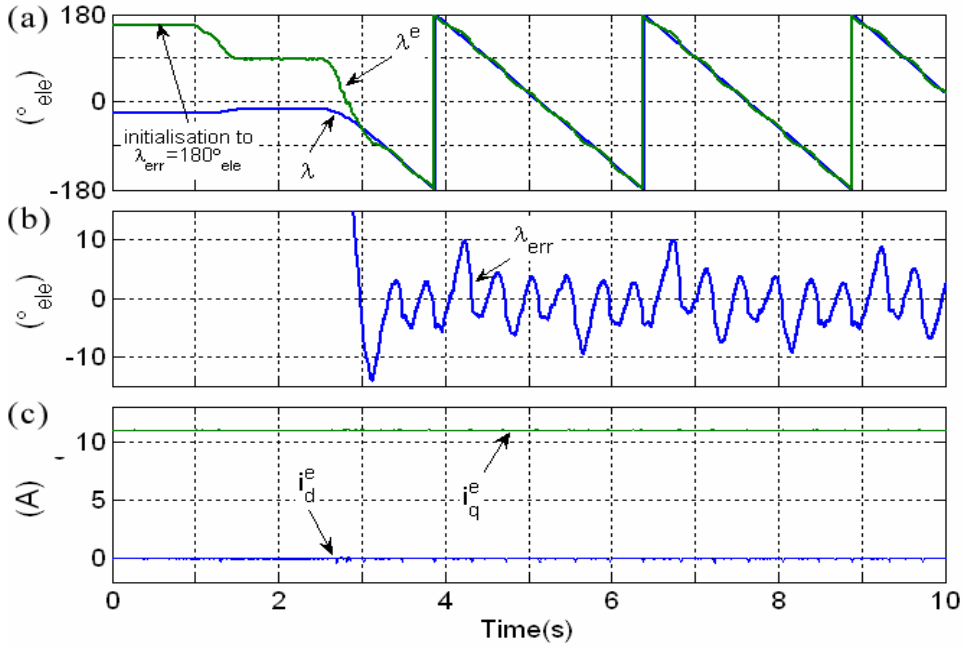

Figure 5.31: Sensorless operation of the drive from zero speed to -0.4 Hz electrical (-6 rpm) with high current (i_q^* = 11 A) (reverse rotation)

Figures 5.28 to 5.31 are only shown to demonstrate the superimposing influence of the back EMF to the saliency effect for the correct rotor position initialisation from an unknown value. During the experiments the drive torque changed rapidly at the instant of the position error correction. This is not desired in practical drives. For a practical implementation it is suggested that the drive becomes initialised by only the back EMF and zero current as shown in Figures 5.24 to 5.27. Also other techniques can be implemented to find the correct rotor position at zero speed before starting the drive. This can be done for instance by high frequency injection as suggested e.g. in [45], [76-79]. As soon as the true rotor position has been found, a torque producing current i_q^e can be introduced to the machine. Since the tracking PLL keeps the estimation error small, the speed can then be reduced back to zero in motoring mode.

5.6.2 Sensorless Speed Control

For the speed control a PI controller cascade loop is implemented as explained in section 2.4.1. The output of the speed controller adjusts the torque producing current reference i_q*. As feedback for the speed controller only the sensorless estimated speed ω_{RF} as shown in block diagram of Figure 5.17 is used. The low pass filter used is a digital Butterworth design with 2 Hz cut of frequency. In all the experiments the coupled load DC machine is set to a constant current level to provide a constant electrical torque. Under speed control the torque and thus the current amplitude is changed by the speed controller. Therefore the current amplitude dependent di_{d0}/dt inverter non-linearity compensation function shown in Figure 5.16 is used as a two dimensional look up table inside the DSP algorithm. The quantisation for the current amplitude is 1 ampere and 1 electrical degree for the stator current vector position. Thus, the used LUT shown in Figure 5.16 consists of 12 x 360 values, which require 8640 byte memory allocation in 16-bit precision. Values between the discretised LUT current values are calculated by linear interpolation.

Figures 5.32, 5.35 and 5.36 show results when the PMSM drive is operated in sensorless speed control. In the figures plot (a) shows the measured and estimated rotor position λ_R and λ_R^e and plot (b) shows the difference between these position signals λ_{err}. Plot (c) shows the current vector components in the estimated dq^e reference frame used for the vector control. Plot (d) shows the encoder signal i.e. the rotor speed n_R and the low pass filtered estimated speed n_{RF} used for the sensorless speed control. Since the speed derivation from the discrete encoder impulses produces a high amount of high frequency noise the measured speed signal n_R is also shown following a low pass filter. However in this case the cut of frequency for the first order Butterworth filter is set to 200 Hz. This is a rather high value and therefore the speed signal shown can be regarded as true rotor speed. The resulting filter delay is very small and should be not recognisable in the plots.

Figure 5.32 shows the result when the reference speed is changed from 30 rpm (2 Hz electrical) to 375 rpm (25 Hz electrical) and vice versa. The reference speed change is limited by a 300 rpm per second ramp. No ramp limitation on the reference torque is applied, but the total range is limited to 0.1 A to 11 A, since only a di_{d0}/dt compensation look up table for this current range is used as shown in Figure 5.16. During the acceleration maximum torque is applied and during the deceleration period the i_q^e reaches the minimal set reference value. It can be seen from the results in Figure 5.32, that the sensorless drive settles at the demanded speed with a good precision. The position errors visible in Figure 5.32 (b) are in the range of approximately +/-12 degrees electrical and no significant steady state offset error is visible. Only during the acceleration and deceleration transition the estimated position lags/ advances slightly. This is due to the dynamic properties of the tracking PLL. The estimated rotor speed is adjusted by PLL's PI control loop that is subject to a limited bandwidth. However, the observed delay in the position estimation during the speed dynamics is small and does not affect the drive performance significantly.

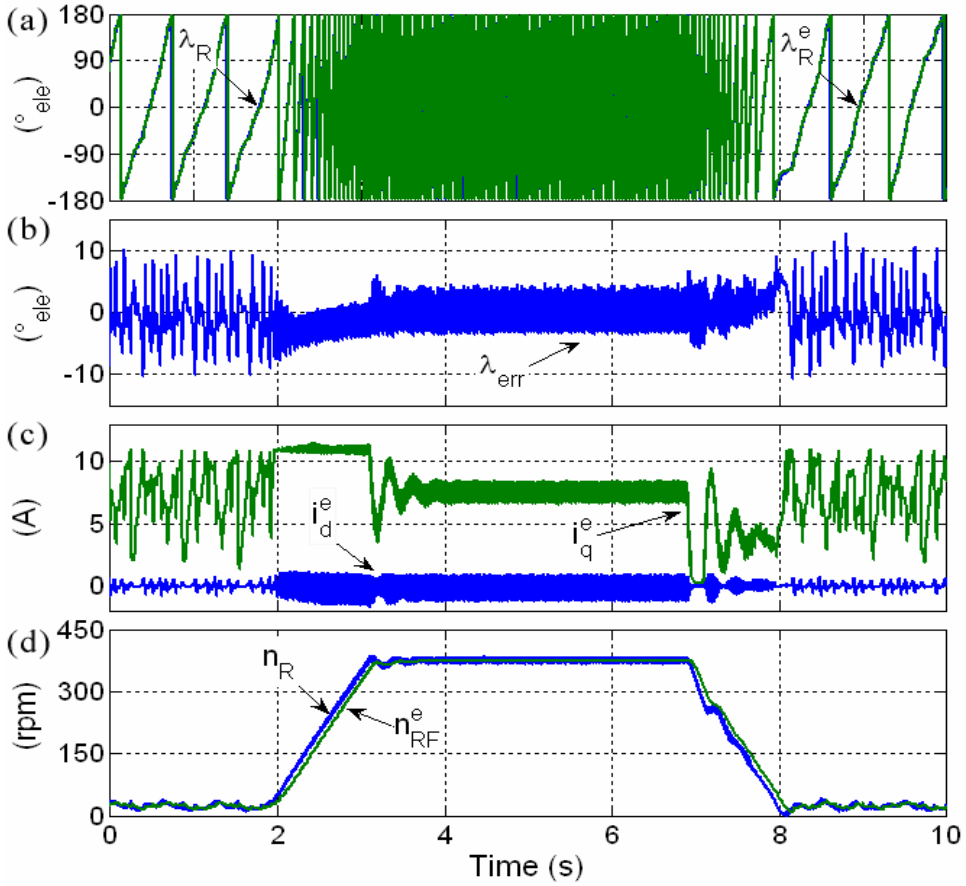

Figure 5.32: Sensorless PMSM drive in speed control (30 to 375 rpm)

Figure 5.32 shows a tendency for oscillations in the speed transients which are due to the low cut off frequency of the speed filter. This is not desired for a dynamic speed controlled drive. However due to the noise in the sensorless algorithm, particular due to the inverter disturbances, a good filtering of the estimated speed is required. It can be seen that during the overshoot at deceleration almost zero speed is reached for a short time. Significant torque ripple are created by the mechanical machine coupling. This is reflected in the i_q^e plot of Figure 5.32 (c), particularly visible at low speed. As can be seen due to the torque ripple also a strong ripple in the set rotor speed is visible. In sensorless speed control only operation down to 30 rpm (2 Hz electrical) is achieved. This is also affected by the strong mechanical torque ripple. When the reference speed is further decreased the torque ripple can cause the drive speed to

reach the unstable operation range indicated in Figure 5.5 which may result into a loss of stability. Figure 5.33 shows the same experiment as in Figure 5.32 under sensored operation. The speed signal is derived from the encoder position and also passed through a 2 Hz low pass filter to demonstrate the same operation condition. It can be seen that the performance is very similar to Figure 5.32. That proves that the use of the estimated position does not deteriorate the drive performance under this operation condition significantly. The torque ripple is caused by the mechanical coupling also visible at low speed.

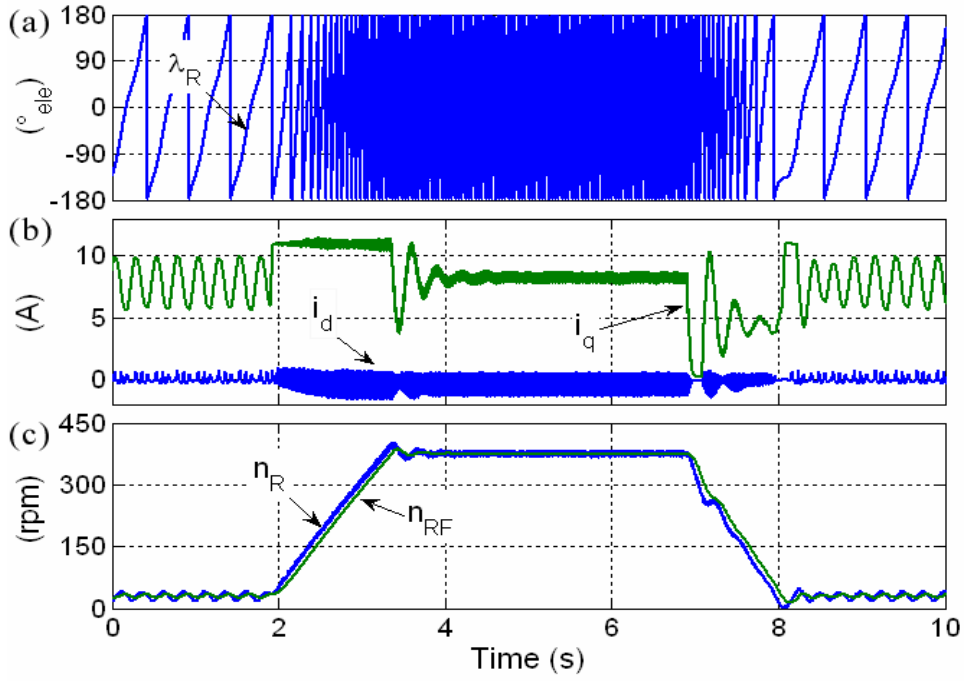

Figure 5.33: Sensored PMSM drive in speed control (30 to 375 rpm)

The high speed of 375 rpm (25 Hz electrical) is the maximum tested speed since only low and zero speed is considered in this work. The maximum speed is in general limited due to the reference voltage limitation explained in section 6.1. This is required to ensure the minimum duration for the current derivative measurement during the zero voltage vectors. The voltage limitation can be increased if the relative

duration of the zero vectors to the active voltage vectors can be reduced. This can be achieved by for instance reducing the PWM switching frequency, a different PWM scheme or a measurement of the current derivative over a shorter time. Higher speeds can be achieved by using for example novel developed current derivative sensors that are cheap and easy to implement [26], [52], [53], [80], [81].

As explained before, there is a small operating range where the di_{d0}^{e}/dt position error signal cancels. Hence no information for position tracking is provided, due to the opposing saliency and back EMF component polarities. It is not possible to obtain sustained sensorless operation in these regions. However it is desirable to pass through them without losing stability. The sensorless algorithm is based on a PLL structure that is subject to the dynamic response of the PLL's PI controller. The idea is to set the bandwidth of the position estimator to allow a speed transient to pass through the grey operation ranges without the algorithm losing orientation. Moreover, the PLL input polarity needs to be changed at the instant when the di_{d0}^{e}/dt error signal changes its polarity. Since the PLL estimates the rotor speed, this information can be assumed to be known as the sensorless algorithm is locked to the rotor position [75].

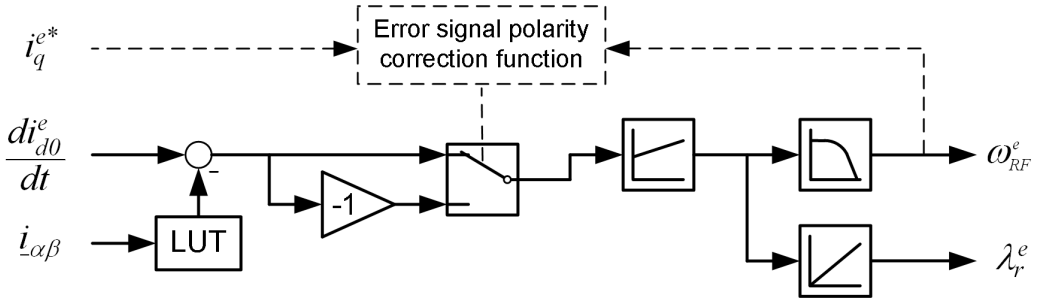

Figure 5.34: Block diagram of the implemented algorithm with error signal polarity selection for four quadrant operation.

Figure 5.34 shows the block diagram of the implemented algorithm for four quadrant operation. The polarity of the saliency term is set by the i_q^e current polarity. Since the current controllers have a high bandwidth the i_q^{e*} demand value is used. The estimated speed is used to set the back EMF term polarity. Due to the noise in the position tracking the speed estimate needs to be filtered using a low pass filter as shown in the block diagram. This filter is implemented as first order Butterworth design with 2 Hz cut of frequency. The filter delay will affect the dynamics of the polarity correction. It was found that the unstable operation range is about 0.3 Hz electrical wide for the machine used. Although sustained operation in this unstable region is not possible, the bandwidth of the position control PLL allows a fast 'pass through' to take place with the resulting estimated position error being small. As shown in the previous sections, the algorithm is capable of regaining stability after a 'safe' operating range has been reached.

Figure 5.35 shows experimental results obtained with the setup of Figure 5.34. The speed demand for the fully sensorless PMSM drive is changed between +/-30 rpm (+/-2 Hz electrical). As expected the position error increases for a short time during the speed reversals. The experiment shows that the algorithm successfully tracks the position estimate and returns to a stable condition after the speed transients. As can be seen in plot (d) of Figure 5.35 the estimated speed value shows a significant delay due to the 2 Hz low pass filtering. This delay needs to be taken into account, since the filtered estimated speed is used to adjust the error signal polarity as shown in Figure 5.34. In order to balance the introduced delay the speed threshold at which the error signal polarity is corrected is different for the positive to negative and the negative to positive speed transitions. For the experiment in Figure 5.35 the error polarity switching threshold for the positive to negative speed transition is 1.3 Hz electrical (20 rpm) and for the negative to positive speed transition -1.6 Hz electrical (-24 rpm). These values were adjusted experimentally to compensate the speed filter delay in the estimated speed signal. From the measured drive speed shown in Figure

5.35 (d) it can be seen that the true speed value is in the speed range between -0.4 to -0.1 Hz electrical when the error signal polarity switching occurs. Therefore the error signal polarity correction occurs during the pass through of the unstable operation range as suggested in Figure 5.6.

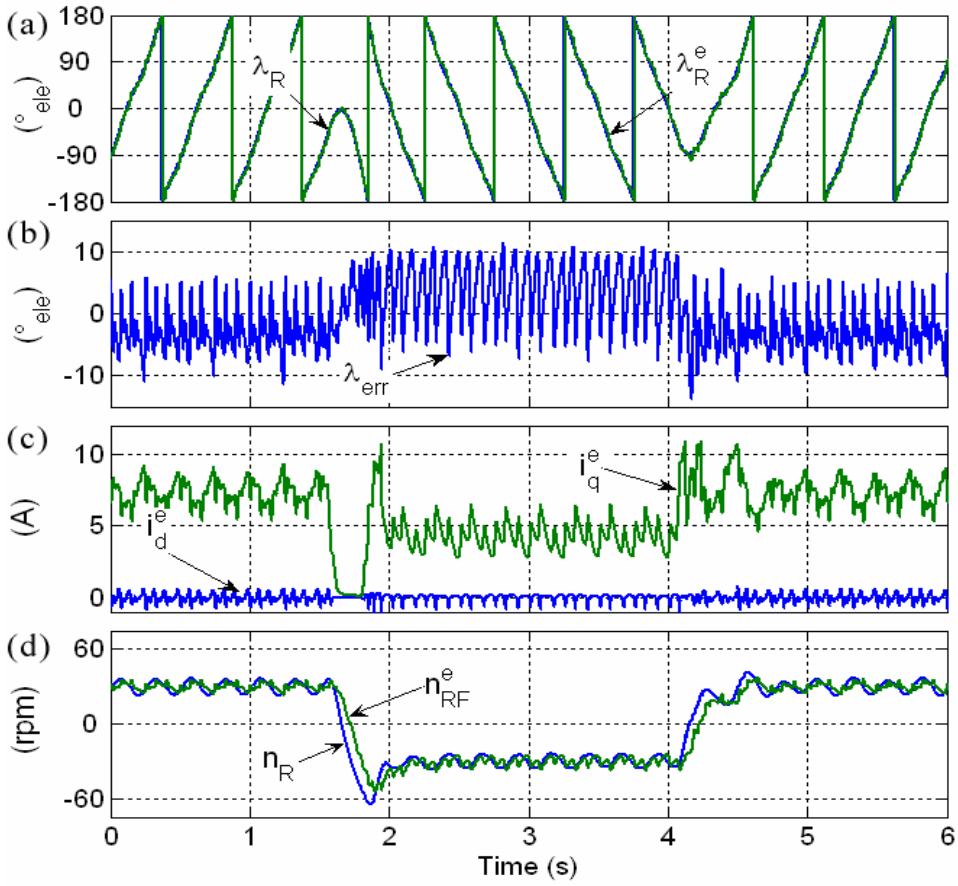

Figure 5.35: Sensorless speed controlled PMSM drive with speed reversal (+/-30 rpm)

Figure 5.36 shows the same speed reversal experiment as described before. However, the reference speed is changed between +/-75 rpm (+/-5 Hz electrical). The polarity correction speed thresholds are set to 2 Hz electrical (30 rpm) for positive to negative speed transitions and -2.2 Hz electrical (-33 rpm) for negative to positive speed transitions. These values are again adjusted by trial and error to compensate for the delay in the used feedback speed signal.

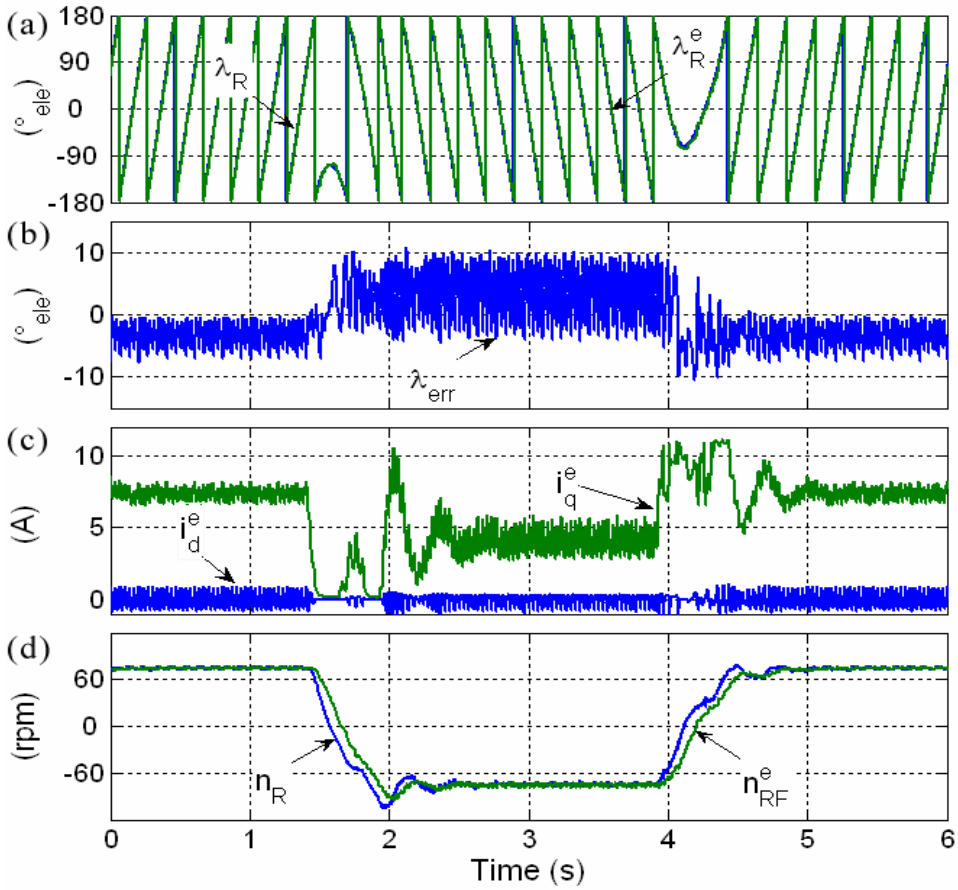

Figure 5.36: Sensorless speed controlled PMSM drive with speed reversal (+/-75 rpm)

Figures 5.37 and 5.38 show the experiments of Figures 5.35 and 5.35 repeated under sensored operation. It can be seen that the performance is similar to sensorless operation. This shows that the sensorless position tracking does not deteriorate the drive performance significantly.

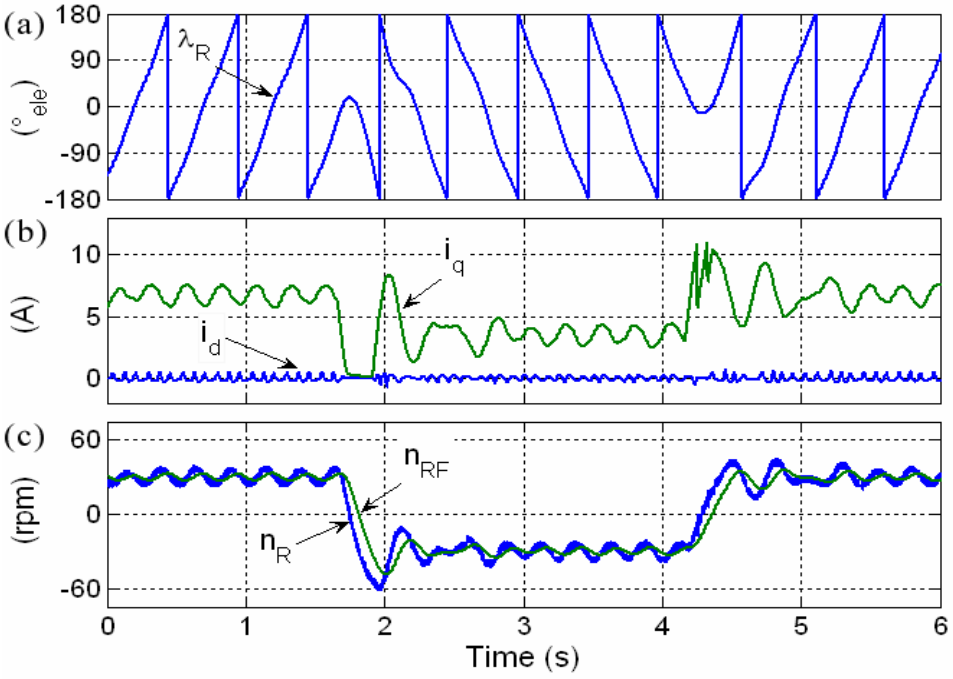

Figure 5.37: Sensored speed controlled PMSM drive with speed reversal (+/-30 rpm)

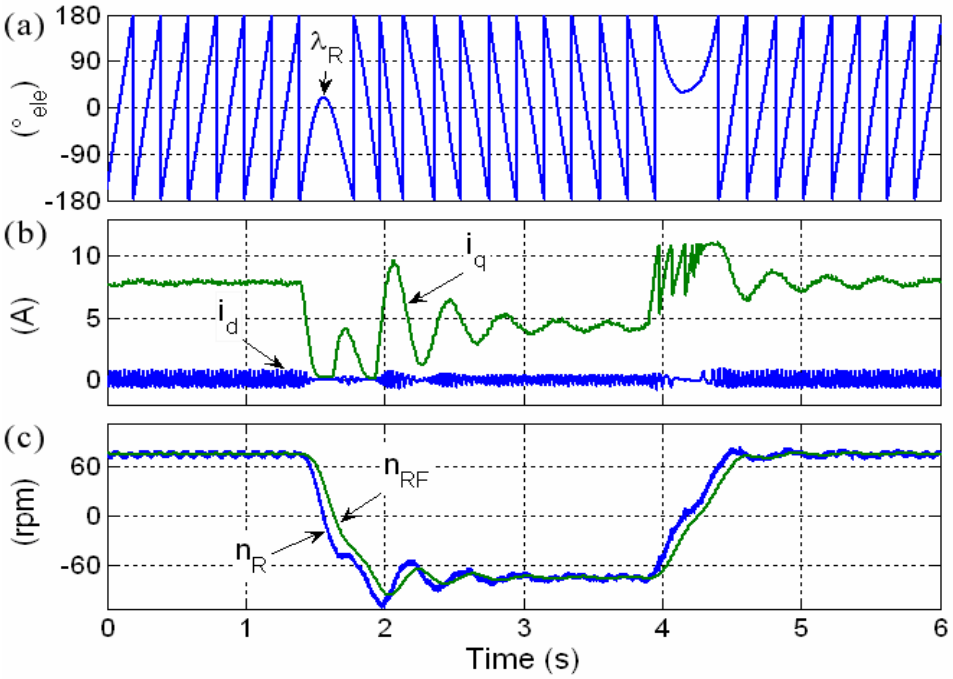

Figure 5.38: Sensored speed controlled PMSM drive with speed reversal (+/-75 rpm)

As can be seen in Figures 5.35 and 5.36 speed reversal in sensorless mode by correcting the error signal polarity works without the drive losing orientation. The position estimation error during the pass through of the unstable operation range increases only slightly and does not seem critical for the operation. However due to the delay in the estimated speed feedback signal the thresholds need to be adjusted to the speed transient behaviour. The performance of this operation may be significantly improved if a mechanical based speed observer is introduced [42]. By using an observer model the delay in the estimated speed could be removed and therefore no variable speed values need to be defined for the error signal correction.

5.7 Analysis of the Inverter Non-linearity Effect

It was observed that the current derivative during the zero voltage vectors depends not only on the frame misalignment λ_{err} as given by (5.7) but is also affected by the current position in the stator fixed $\alpha\beta$ frame. It was found that this di_{d0}/dt modulation is mainly caused by the on-state voltages across the inverter semiconductors [82]. Figure 5.39 shows the schematic of an inverter connected to a PMSM machine represented as its equivalent circuit. In Figure 5.39 *T* stands for the active inverter switching devices and *D* for the respective free wheel diodes. In the machine circuit diagram *R* represents the winding resistance, *L* the phase equivalent inductance and *e* the phase back EMF component. The subscripts *A*, *B* and *C* refer to the respective phases. For analysis purposes, assume phase *A* current to be positive and the currents in phases *B* and *C* to be negative, as indicated by the arrows i_A, i_B and i_C. The inverter state is 111 (all upper switches on as indicated by the green caption) meaning that at this instance a zero vector is applied, effectively connecting the machine terminals to the *DC*+ rail. In the ideal case this would be a short circuit between all phases. However, in practice this is not the case due to the resistance in the inverter

semiconductors. In the described arrangement *T1*, *D2* and *D3* are conducting. Therefore all three phase currents are passing semiconductors before they arrive at the *+DC* rail. At this instant *T1*, *D2* and *D3* conduct the machine's three phase currents to the common upper rail. At the next zero vector, the inverter state becomes 000 (all lower switches on) and devices D4, T5 and T6 conduct the machine currents.

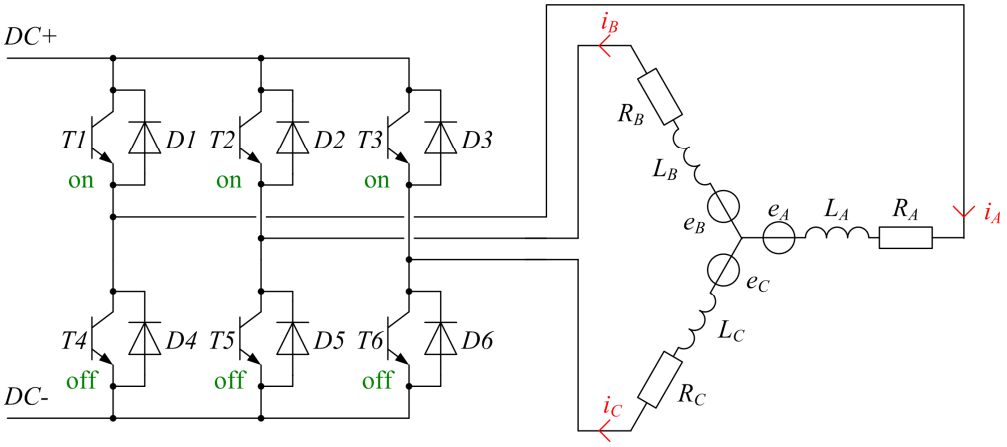

Figure 5.39: Schematic of inverter and PMSM equivalent circuit

Figure 5.40 shows the variation of the observed inverter di_{d0}/dt non-linearity signal and the stator currents. The PMSM is run in sensored mode and a constant current of 1A is imposed into the real *q* axis as shown in Figure 5.14. The rotor is slowly rotated at 1 rpm. All graphs are plotted against the measured stator current vector position. Plot (a) shows the measured three phase currents while (b) and (c) show the acquired current derivative in the real *d* axis during the two zero voltage vector states $\underline{v}_{111}$ and $\underline{v}_{000}$. Plot (d) shows the averaged function from the two zero vector di_{d0}/dt measurements during one PMW period, as used in the sensorless algorithm. The current and current derivative signals are filtered by a 10 Hz low pass filter to reduce noise for illustrative purpose only. The dashed lines in the figure indicate the six current commutation sectors of the three phase system. The conducting inverter devices are also stated in Figure 5.40. It can be observed that the corrupting signal is linked to the commutation sectors and differs for the cases when two IGBT's and a

diode or two diodes and an IGBT are conducting current. This indicates that the inverter devices are contributing directly to the modulation of the di_{d0}/dt signal.

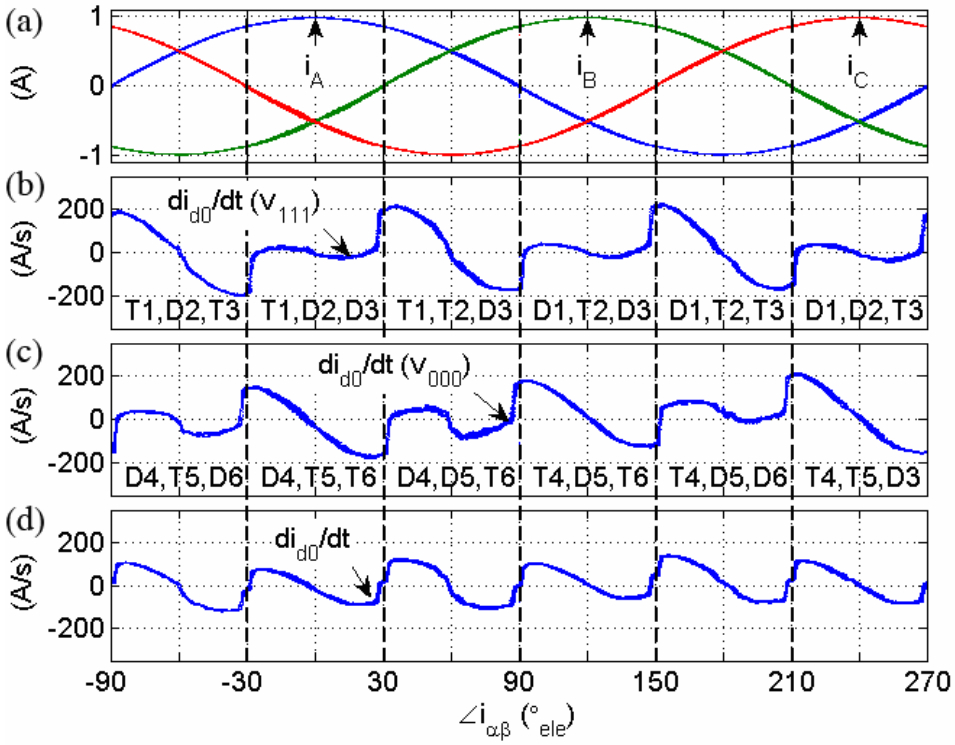

Figure 5.40: Inverter effect on di_{d0}/dt over the current vector position

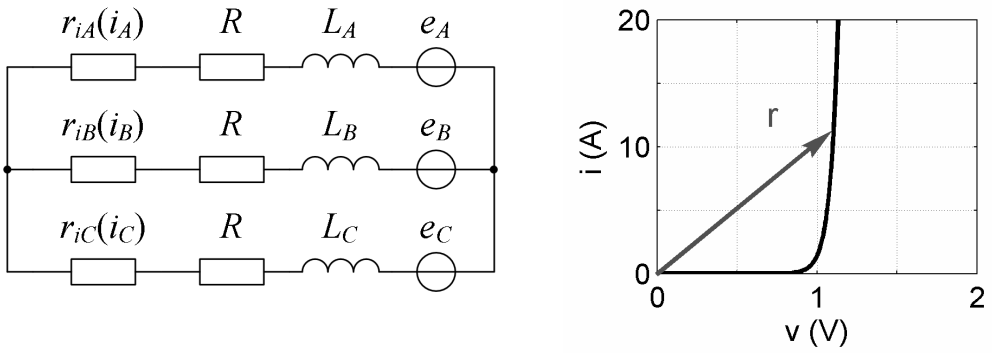

(a) **(b)**

Figure 5.41: (a) equivalent three phase impedance circuit, (b) diode voltage current curve

As a basic approximation, the conducting devices can be represented by their on state resistances as shown in Figure 5.41 (a). r_{iA}, r_{iB} and r_{iC} represent the on-resistances of the conducting semiconductors in the respective inverter leg. These resistances are non-linear and depend on the instantaneous current value in the semiconductors. The ohmic resistances of the three stator windings are assumed to be equal the value R. L_A, L_B, L_C represent the three winding equivalent inductances and e_A, e_B and e_C the phase back EMF terms. Figure 5.41 (b) shows the assumed non-linear voltage-current curve of a diode or IGBT as is used for the following simulations. For the basic voltage-current curve modelling only a basic exponential function is used. Since the instantaneous current values in the three phases are different, the point of operation on Figure 5.41 (b) will be different for each device resulting in different values of resistance. This results in an unbalanced three phase set of resistances. The total resistance in the current decay path is an essential factor in the current derivative saliency effect, as shown in equation (5.7). The per phase winding resistance R of the machine is 0.23Ω. The on-resistance of a semiconductors r_i can be in the range of a few mΩ at high current to several Ω's at very low current. Since the current in one phase of the machine is very low every 60 electrical degrees, a strong unbalance effect in the three phase resistance network occurs.

As explained before, during the zero vectors the three phases are not ideally short circuit, but are affected by the voltage drops over the inverter semiconductors. The voltage drops over the three inverter phase legs v_{iA}, v_{iB} and v_{iC} are stated by equation (5.9). The values r_{iA}, r_{iB} and r_{iC} are the resistances of the conducting devices in the inverter legs, which are dependent on the actual phase current.

$$\begin{bmatrix} v_{iA} \\ v_{iB} \\ v_{iC} \end{bmatrix} = -\begin{bmatrix} r_{iA}\, i_A \\ r_{iB}\, i_B \\ r_{iC}\, i_C \end{bmatrix} \tag{5.9}$$

Therefore equation (5.10) can be used as simplified three phase voltage equation system under application of a zero vector.

$$-\begin{bmatrix} r_{iA}\, i_A \\ r_{iB}\, i_B \\ r_{iC}\, i_C \end{bmatrix} = \begin{bmatrix} R & 0 & 0 \\ 0 & R & 0 \\ 0 & 0 & R \end{bmatrix} \cdot \begin{bmatrix} i_A \\ i_B \\ i_C \end{bmatrix} + \begin{bmatrix} L_A & 0 & 0 \\ 0 & L_B & 0 \\ 0 & 0 & L_C \end{bmatrix} \cdot \begin{bmatrix} \frac{di_{A0}}{dt} \\ \frac{di_{B0}}{dt} \\ \frac{di_{C0}}{dt} \end{bmatrix} + \begin{bmatrix} e_A \\ e_B \\ e_C \end{bmatrix} \tag{5.10}$$

Equation (5.11) gives then the solution for the current derivative in the three phases during the inverter zero vectors.

$$\begin{aligned} \begin{bmatrix} \frac{di_{A0}}{dt} \\ \frac{di_{B0}}{dt} \\ \frac{di_{C0}}{dt} \end{bmatrix} &= -\begin{bmatrix} L_A & 0 & 0 \\ 0 & L_B & 0 \\ 0 & 0 & L_C \end{bmatrix}^{-1} \cdot \left(\begin{bmatrix} r_{iA}\, i_A \\ r_{iB}\, i_B \\ r_{iC}\, i_C \end{bmatrix} + \begin{bmatrix} R_A & 0 & 0 \\ 0 & R_B & 0 \\ 0 & 0 & R_C \end{bmatrix} \cdot \begin{bmatrix} i_A \\ i_B \\ i_C \end{bmatrix} + \begin{bmatrix} e_A \\ e_B \\ e_C \end{bmatrix} \right) \\ &= -\begin{bmatrix} \frac{1}{L_A} & 0 & 0 \\ 0 & \frac{1}{L_B} & 0 \\ 0 & 0 & \frac{1}{L_C} \end{bmatrix} \cdot \left(\begin{bmatrix} r_{iA}+R & 0 & 0 \\ 0 & r_{iB}+R & 0 \\ 0 & 0 & r_{iC}+R \end{bmatrix} \cdot \begin{bmatrix} i_A \\ i_B \\ i_C \end{bmatrix} + \begin{bmatrix} e_A \\ e_B \\ e_C \end{bmatrix} \right) \end{aligned} \tag{5.11}$$

5.7.1 Under True Orientation

In equation (5.11) the resulting equivalence resistance matrix is not balanced. Therefore transforming (5.11) into the form used to orientate on the *dq* frame gives

(5.12), which contains a non-diagonal matrix with cross coupling elements between the *d* and *q* axis, r_{dq} and r_{qd}.

$$\begin{bmatrix} \frac{di_{d0}}{dt} \\ \frac{di_{q0}}{dt} \end{bmatrix} = -\begin{bmatrix} \frac{1}{L_d} & 0 \\ 0 & \frac{1}{L_q} \end{bmatrix} \cdot \begin{bmatrix} r_{dd} & r_{dq} \\ r_{qd} & r_{qq} \end{bmatrix} \cdot \begin{bmatrix} i_d \\ i_q \end{bmatrix} - \begin{bmatrix} \frac{1}{L_d} & 0 \\ 0 & \frac{1}{L_q} \end{bmatrix} \cdot \begin{bmatrix} 0 \\ e_q \end{bmatrix} \tag{5.12}$$

The *dq* frame equivalent impedance matrix calculation is shown by equation (5.15) which includes the transformation matrixes (5.13) and (5.14). The three phase resistances r_A, r_B and r_C in equation (5.15) are the sum of the phase winding resistances *R* and the respective inverter leg resistances r_i.

$$\mathbf{A} = \begin{bmatrix} 1 & \cos\left(\frac{2}{3}\pi\right) & \cos\left(\frac{4}{3}\pi\right) \\ 0 & \sin\left(\frac{2}{3}\pi\right) & \sin\left(\frac{4}{3}\pi\right) \end{bmatrix} \tag{5.13}$$

$$\mathbf{B}(\lambda_R) = \begin{bmatrix} \cos(\lambda_R) & \sin(\lambda_R) \\ -\sin(\lambda_R) & \cos(\lambda_R) \end{bmatrix} \tag{5.14}$$

$$\begin{bmatrix} r_{dd} & r_{dq} \\ r_{qd} & r_{qq} \end{bmatrix} = \frac{2}{3} \cdot \mathbf{B} \cdot \mathbf{A} \begin{bmatrix} r_A & 0 & 0 \\ 0 & r_B & 0 \\ 0 & 0 & r_C \end{bmatrix} \cdot \mathbf{A}^T \cdot \mathbf{B}^T \tag{5.15}$$

The solutions for the *dq* equivalent resistances are:

$$\begin{aligned} r_{dd} &= \frac{2}{3}\cos^2\left(\lambda_R\right) r_A\left(i_A\right) \\ &\quad + \frac{2}{3}\cos^2\left(\lambda_R - \frac{2}{3}\pi\right) r_B\left(i_B\right) \\ &\quad + \frac{2}{3}\cos^2\left(\lambda_R + \frac{2}{3}\pi\right) r_C\left(i_C\right) \end{aligned} \quad , \tag{5.16}$$

$$\begin{aligned} r_{qq} &= \frac{2}{3}\sin^2\left(\lambda_R\right) r_A\left(i_A\right) \\ &\quad + \frac{2}{3}\sin^2\left(\lambda_R - \frac{2}{3}\pi\right) r_B\left(i_B\right) \\ &\quad + \frac{2}{3}\sin^2\left(\lambda_R + \frac{2}{3}\pi\right) r_C\left(i_C\right) \end{aligned} \quad , \tag{5.17}$$

$$\begin{aligned} r_{dq} = r_{qd} &= -\frac{1}{3}\sin\left(2\lambda_R\right) r_A\left(i_A\right) \\ &\quad - \frac{1}{3}\sin\left(2\lambda_R + \frac{2}{3}\pi\right) r_B\left(i_B\right) \\ &\quad - \frac{1}{3}\sin\left(2\lambda_R - \frac{2}{3}\pi\right) r_C\left(i_C\right) \end{aligned} \quad . \tag{5.18}$$

Assuming true orientation, the current derivative signal along the *d* axis is given by equation (5.19). It can be seen that there is an extra term as compared to the original equation given by equation (5.3).

$$\frac{di_{d0}}{dt} = -\frac{r_{dd}\left(i_q, \lambda_R\right)}{L_d} i_d - \frac{r_{dq}\left(i_q, \lambda_R\right)}{L_d} i_q \tag{5.19}$$

Since vector control is applied, the stator current vector is a function of the imposed i_q current component and the orientation angle λ_R. Therefore the resulting resistance

components can be also assumed to be dependent on i_q and λ_R as indicated in equation (5.19).

The problem was initially investigated through simulation. For the simulations, a simple current-voltage curve approximation is used for all 12 inverter switching devices which is shown in Figure 5.41 (b). Figures 5.42 and 5.44 show simulated results for an i_q current of 0.1 A and 11 A. Plot (a) shows the simulated three phase currents and plot (b) indicates the resulting total phase resistances, which is the inverter resistance plus winding resistance. Plot (c), (d) and (e) show the calculated *dq* frame resistance values. Plot (f) shows the final result for the theoretical current derivative in the *d* direction under true orientation. All variables are plotted against the stator current vector angle. Figures 5.43 and 5.45 show the experimentally measured $di_{d0}/dt(\angle \underline{i}_{\alpha\beta})$ functions and their average (solid line) over the rotor position for the same i_q values of Figures 5.42 and 5.44 respectively. It can be seen that the experimental measured signal follows the pattern of the simulated signal. At high currents the magnitude of the simulated function differs more from the measured values. This is due to the simple assumed voltage current curve approximated by a basic exponential function. However the characteristic modulation pattern repeating with each current commutation sector is the same.

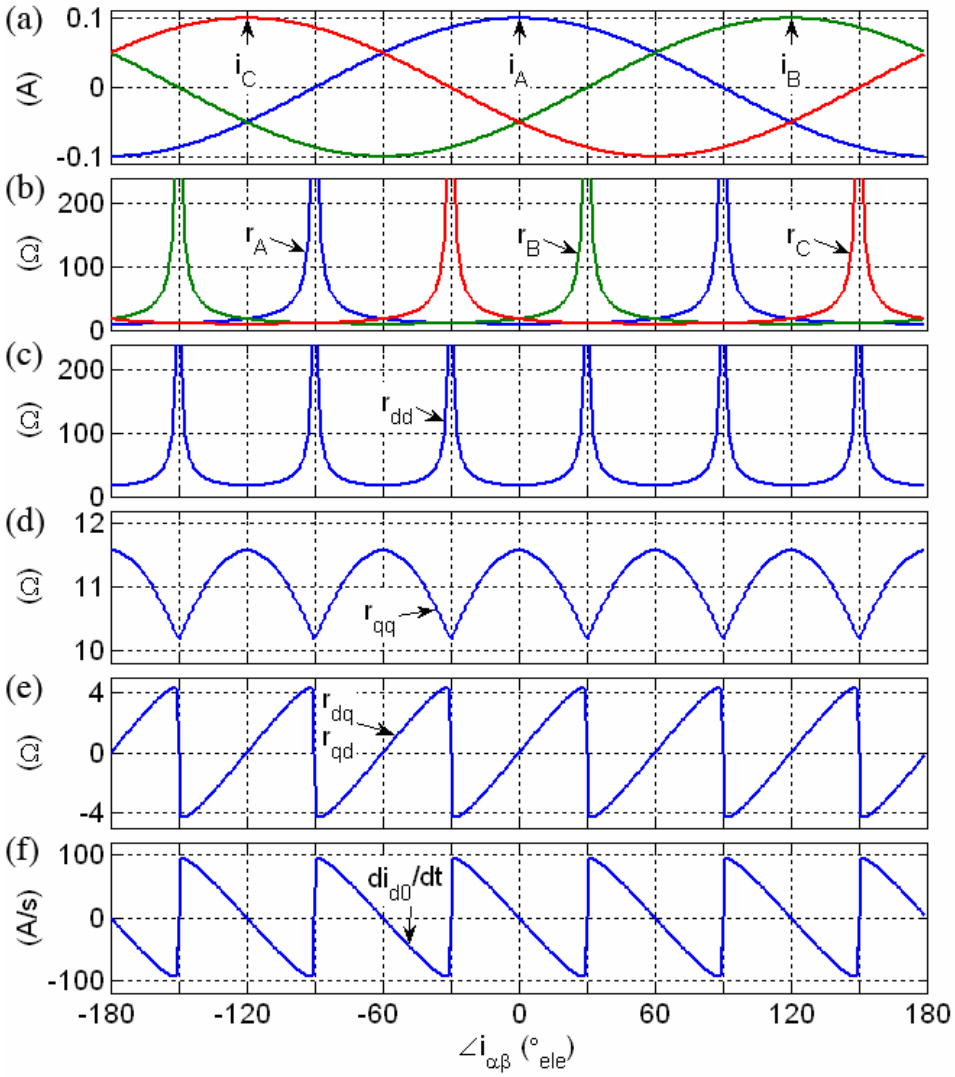

Figure 5.42: Simulated inverter non-linearity effect for i_q = 0.1 A

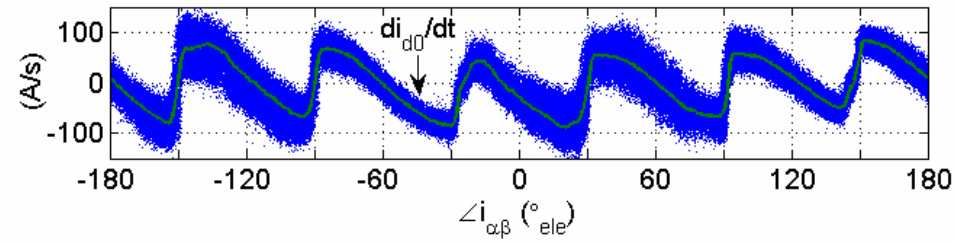

Figure 5.43: Measured $di_{d0}/dt(\angle i_{\alpha\beta})$ for i_q = 0.1 A

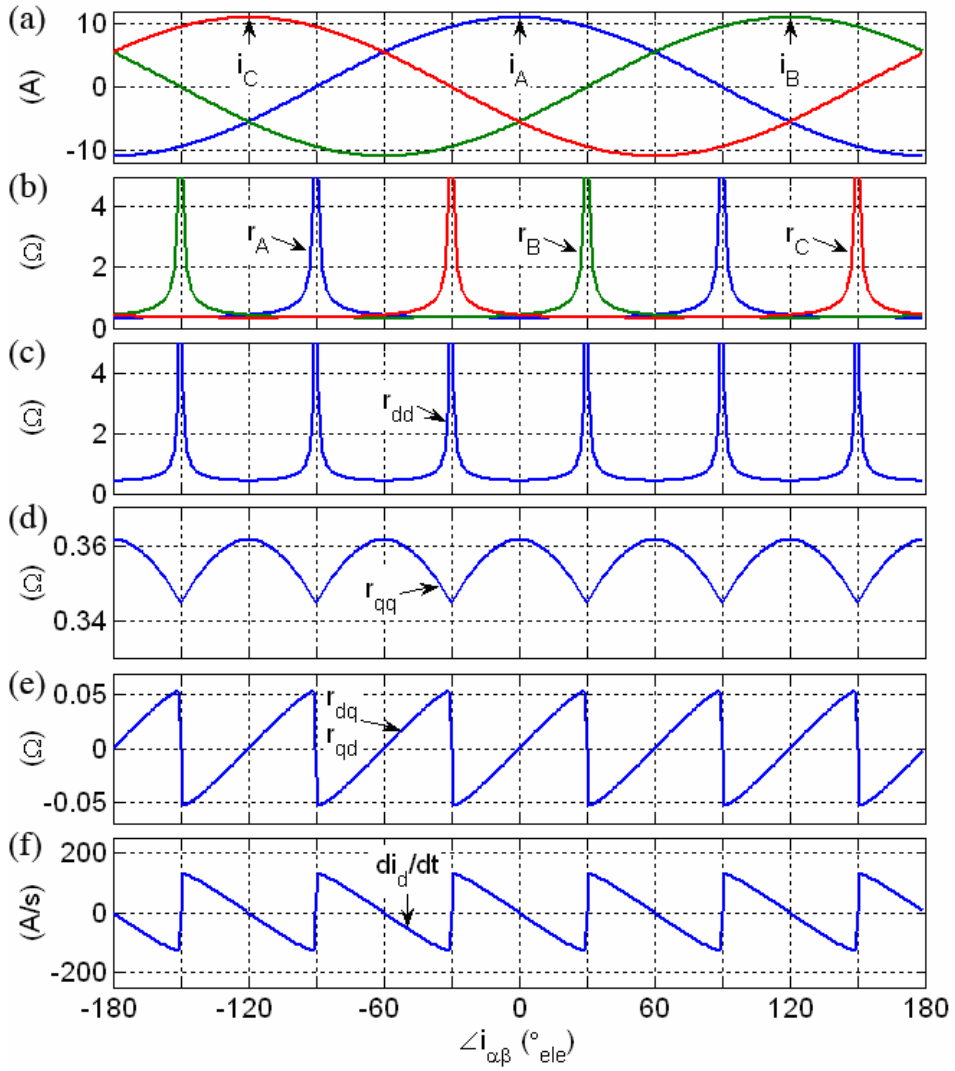

Figure 5.44: Simulated inverter non-linearity effect for i_q = 11 A

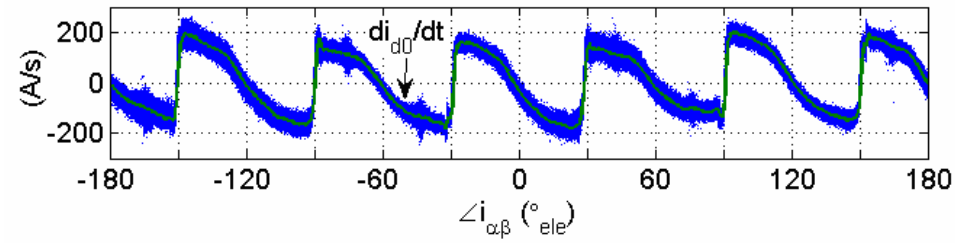

Figure 5.45: Measured $di_{d0}/dt(\angle \underline{i}_{\alpha\beta})$ for i_q = 11 A

The comparison is extended to i_q values in the range from 0.1A to 11A. The simulated profile of $di_{d0}/dt(\underline{i}_{\alpha\beta})$ is shown in Figure 5.46. Comparing the simulated profile to the measured $di_{d0}/dt(\underline{i}_{\alpha\beta})$ function, shown in Figure 5.16, shows that the simulation results match the practical measurements. Both functions show the same repeated pattern over the six current commutation sectors. Visible differences are due to the approximations made in representing the semiconductor voltage current curve and further effects such as current clamping that might occur at very low phase current values.

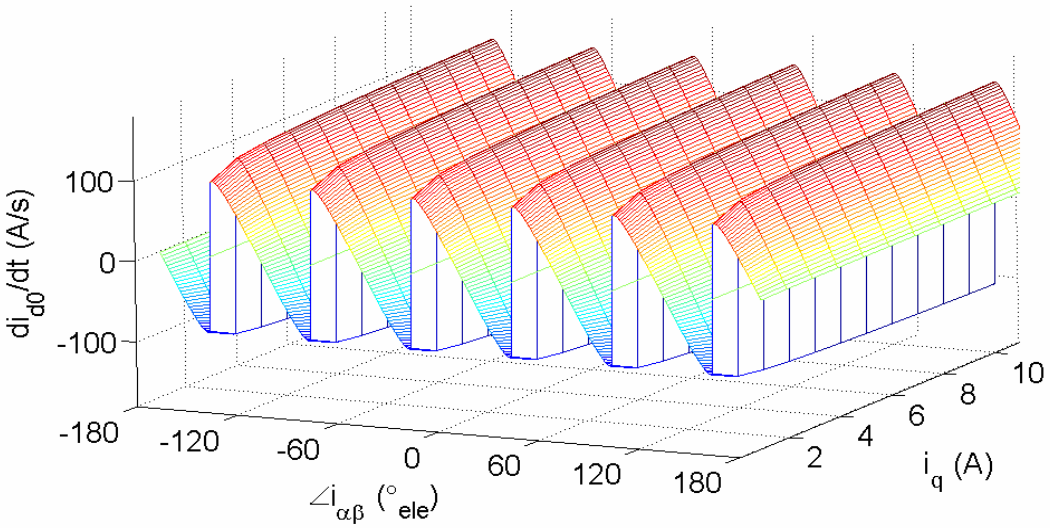

Figure 5.46: Simulated $di_{d0}/dt(\underline{i}_{\alpha\beta})$ function for current vector amplitudes from 0.1 A to 11 A

5.7.2 Under Sensorless Orientation

Under sensorless control, the machine current is controlled in the estimated dq^e reference frame and the values of i_q^e and λ^e determine the stator phase currents and thus the inverter resistance modulation. Therefore in equation (5.20) the resistance matrix is directly related to the estimated referenced frame and expressed as a function of λ^e and i_q^e. The back EMF set up by the permanent magnet flux and the

rotor inductances L_q and L_q are aligned with the real dq frame. Therefore the transformation matrix (5.21) is required that adjusts the misplacement of these two reference frames.

$$\begin{bmatrix} \frac{di_{d0}^e}{dt} \\ \frac{di_{q0}^e}{dt} \end{bmatrix} = -\mathbf{B}(\lambda_{err}) \cdot \begin{bmatrix} \frac{1}{L_d} & 0 \\ 0 & \frac{1}{L_q} \end{bmatrix} \cdot \mathbf{B}^T(\lambda_{err}) \cdot \begin{bmatrix} r_{dq}^e(i_q^e, \lambda^e) & r_{dq}^e(i_q^e, \lambda^e) \\ r_{qd}^e(i_q^e, \lambda^e) & r_{qq}^e(i_q^e, \lambda^e) \end{bmatrix} \cdot \begin{bmatrix} 0 \\ i_q^e \end{bmatrix} - \mathbf{B}(\lambda_{err}) \cdot \begin{bmatrix} 0 \\ \frac{k_e \omega_R}{L_q} \end{bmatrix} \quad (5.20)$$

$$\mathbf{B}(\lambda_{err}) = \begin{bmatrix} \cos(\lambda_{err}) & \sin(\lambda_{err}) \\ -\sin(\lambda_{err}) & \cos(\lambda_{err}) \end{bmatrix} \quad (5.21)$$

For the required vector space transformation the Park transformation matrix $\mathbf{B}(\lambda_{err})$ given in equation (5.21) is used. The impedance matrix and the back EMF vector are transformed to the dq^e space by the Park transformation as explained in section 2.2.2. Assuming i_d^e is forced to zero by the vector controller, the resulting current derivative signal in the d^e axis is given by (5.22). The equation shows an extra term compared to the original equation given by equation (5.7), that results from the inverter resistance unbalance. The influence of the extra term originating from the inverter resistance effect is simulated in the next section.

$$\frac{di_{d0}^e}{dt} = \underbrace{-i_q^e \frac{r_{qq}^e}{2}\left(\frac{1}{L_q} - \frac{1}{L_d}\right)\sin(2\lambda_{err})}_{\text{Saliency}} \underbrace{-i_q^e \frac{r_{dq}^e}{2}\left(\frac{1}{L_d} + \frac{1}{L_q} + \left(\frac{1}{L_d} - \frac{1}{L_q}\right)\cos(2\lambda_{err})\right)}_{\text{Inverter resistance unbalance}} \underbrace{-\frac{k_e \omega_R}{L_q}\sin(\lambda_{err})}_{\text{Back EMF}} \quad (5.22)$$

As is shown in the theoretical derivation above the final $di_{d0}^{e}/dt(\lambda_{err})$ signal under sensorless condition (5.22) is a complex expression affected by r_{qq}^{e} and r_{dq}^{e}. The following analysis confirms that the di_{d0}/dt function measured under sensored condition can be used to compensate the inverter resistance influence, to ensure that the sensorless algorithm shown in Figure 5.17 keeps locked to the correct position value. Since equation (5.22) seems quite complex for $\lambda_{err} \neq 0$, the function is also simulated. Figure 5.47 shows the simulation for zero speed (back EMF term neglected) and i_q^e = 1 A. The plot shows the $di_{d0}^{e}/dt(\lambda_{err})$ functions and the $di_{d0}/dt(\angle \underline{\hat{i}}_{\alpha\beta})$ LUT compensation value for different current vector positions in the $\alpha\beta$ frame. Again the simple voltage-current curve shown in Figure 5.41 (b) is used. The graph shows the solution for three current vector positions. From Figures 5.42 and 5.44 can be seen that for the simulation results at $\angle \underline{\hat{i}}_{\alpha\beta}$ = -28 ° and $\angle \underline{\hat{i}}_{\alpha\beta}$ = 28 ° electrical the r_{dq} influence is largest, where as for $\angle \underline{\hat{i}}_{\alpha\beta}$ = 0 ° electrical r_{dq} is zero. It can be seen in the figure that the resistance unbalance term in (5.22) causes not only an offset, but also a phase shift of the $\sin(2\lambda_{err})$ shape. The error signal fed to the tracking PLL as shown in the block diagram in Figure 5.17 is the difference between the detected di_{d0}^{e}/dt value (solid line) and that of the LUT stored $di_{d0}/dt(\underline{i}_{\alpha\beta})$ value (dashed line). As can be seen for small positive errors the error signal used always has negative polarity and for small negative estimation errors the PLL error signal polarity is positive. Under true orientation the error signal is zero, which is the lock in condition for the position estimator PLL.

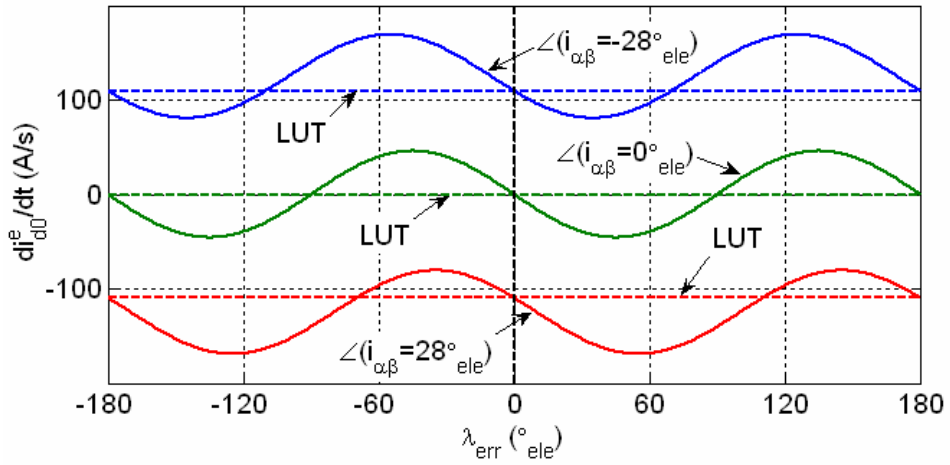

Figure 5.47: Simulation results for $di_{d0}^{e}/dt(\lambda_{err})$ function for i_q^e = 1 A at different current vector positions and referring LUT $di_{d0}/dt(\underline{i}_{\alpha\beta})$ compensation values

Figure 5.48 shows the measured $di_{d0}^{e}/dt(\lambda_{err})$ function and the used $di_{d0}/dt(\angle\underline{i}_{\alpha\beta})$ LUT compensation values for 1 A current vector amplitude as in Figure 5.47. In the experiments the current controller is set to impose a constant DC current vector into the stator windings. The rotor is then moved by the coupled DC machine at 1 rpm as shown in Figure 5.12. As was shown before at this low speed the back EMF is very small and its influence can be neglected. It was found that the extreme points of the inverter resistance unbalance in the practical drive are at $\angle\underline{i}_{\alpha\beta}$ = -24 ° electrical and $\angle\underline{i}_{\alpha\beta}$ = 24 ° electrical. The results in Figure 5.48 show the measured $di_{d0}^{e}/dt(\lambda_{err})$ functions and the used LUT compensation values of the practical drive. The measured di_{d0}^{e}/dt values are passed through a 10 Hz low pass filter to reduce the noise for illustration purposes only. It can be seen that the measured results are similar to the simulation results shown in Figure 5.47. It can further be seen that the saliency function is not an ideal $\sin(2\lambda_{err})$. However, it can be seen that with the subtraction of the correct $di_{d0}/dt(\angle\underline{i}_{\alpha\beta})$ LUT compensation value the error signal can be used for position tracking.

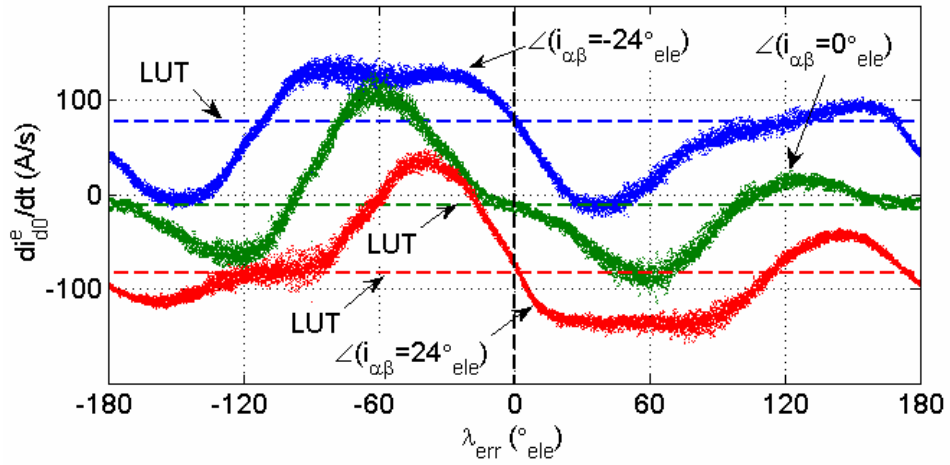

Figure 5.48: Measured results for $di_{d0}^e/dt(\lambda_{err})$ function for i_q^e = 1 A at different current vector positions and referring LUT $di_{d0}/dt(\underline{i}_{\alpha\beta})$ compensation values

The desired component of equation (5.22), for zero speed position tracking, is the $\sin(2\lambda_{err})$ dependent saliency term which is multiplied by the parameter r_{qq}^e. That means that the parameter r_{qq}^e contributes directly to the error signal strength. In Figures 5.42 and 5.44, simulation results for the resistance values are shown for 0.1 A and 11 A applied i_q to the machine. It can be seen that r_{qq}^e is much greater at low current than at large current values. Therefore even if the error signal in equation (5.22) is also directly dependent on the imposed i_q^e amplitude, the greater inverter resistances at lower current vector amplitudes amplifies the final error signal and counteracts the current amplification. Figure 5.49 shows the case for simulated i_q^e currents from 0 to 11 A imposed in alignment with the phase A axis (λ^e = -90 ° electrical). In plot (a) the calculated r_{qq}^e function is shown. One can notice clearly that the resistance rises exponentially at low current which is due to semiconductor resistance. Plot (b) below shows the final amplification factor of the desired $\sin(2\lambda_{err})$ saliency component in equation (5.22). It can be seen that this factor drops with lower current. However at a small current vector amplitude such as 0.1 A it still gives about 20 % of the saliency term amplification factor amplitude as at i_q^e = 11 A.

This simulation result reaffirms the possibility of experimental sensorless control even at a small current vector amplitude of less then 1 % of rated value.

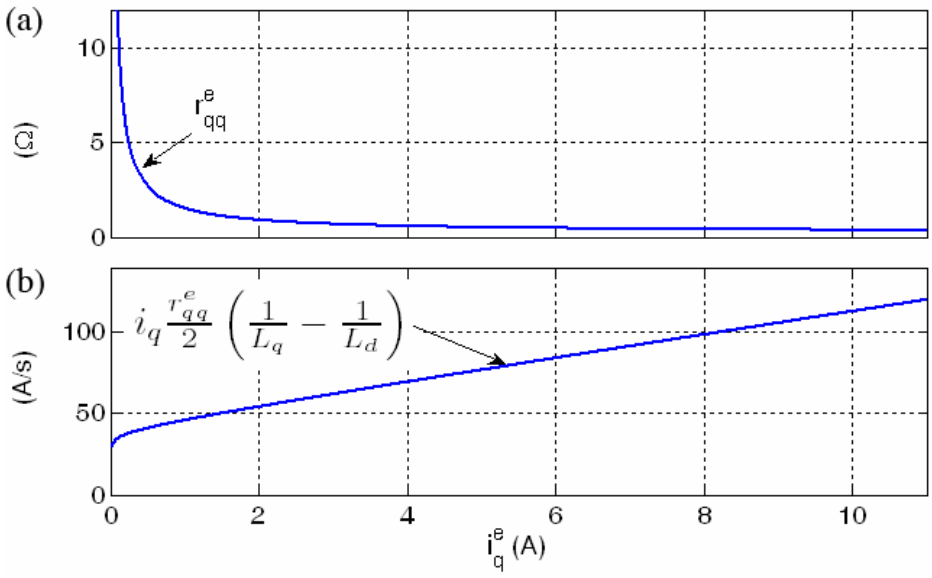

Figure 5.49: Simulated saliency term amplification factor of $di_{d0}^e/dt(\lambda_{err})$ in dependency of imposed current i_q^e aligned to phase *A* direction (λ^e = -90 ° electrical)

Figures 5.50 and 5.51 show the measured saliency $di_{d0}^e/dt(\lambda_{err})$ function for 0.1 A and 2 A current vector amplitude. The same experiment as shown in Figure 5.12 is carried out, but with different i_q^* reference values. As can be seen in Figure 5.50 the saliency influence in the $di_{d0}^e/dt(\lambda_{err})$ function is still visible, even if its amplitude is smaller than for the case of i_q^e = 1 A as shown in Figure 5.13. The amplitude of the saliency modulation in Figure 5.51 seems larger then in Figure 5.13, due to the larger current amplitude. As expected it can be seen that the saliency modulation in the $di_{d0}^e/dt(\lambda_{err})$ signal increases with larger current amplitude. However the increase of the saliency modulation is not directly proportional to the current amplitude. Comparing Figures 5.50 and 5.51 shows that in the practical drive the $di_{d0}^e/dt(\lambda_{err})$ saliency modulation at 0.1 A is still about half the modulation amplitude as at 2 A current amplitude. This practical observation agrees with the theoretical conclusion

that the increasing phase resistances at lower current values contribute to the zero vector current derivative saliency signal amplitude.

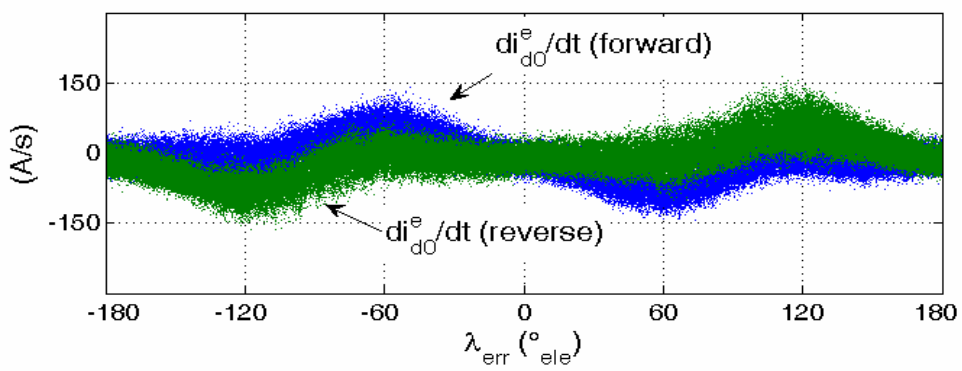

Figure 5.50: $di_{d0}^e/dt(\lambda_{err})$ over rotor position i_q^e = 0.1 A, +/-1 rpm

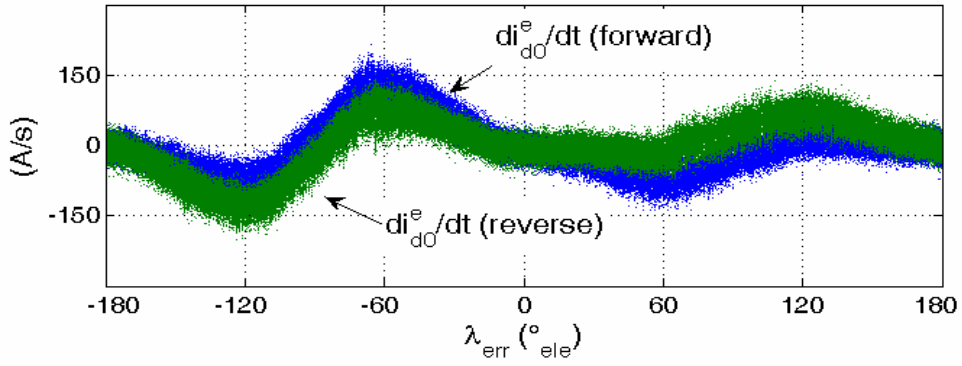

Figure 5.51: $di_{d0}^e/dt(\lambda_{err})$ over rotor position i_q^e = 2 A, +/-1 rpm

5.7.3 Compensation by Current-Resistance Function

As shown the inverter non-linearity effect has to be compensated. Therefore a dedicated di_{d0}/dt function has been acquired in sensored operation of the drive. This is undesired for practical sensorless drives. Therefore it is investigated if a more simple compensation function can be used that requires no sensored operation for the commissioning. As shown in the theoretical derivation most of the zero vector current derivative inverter non-linearity modulation arises from the non-linear

resistances of the inverter phase legs, which depend on the phase currents. In a numerical process an inverter leg resistance function $r(|i|)$ is calculated from the acquired di_{d0}/dt signal shown in Figure 5.16 and the simultaneous measured phase currents. This function could be also derived from the voltage-current characteristic of the inverter switching devices if exact information is provided. This could be for instance an accurate SPICE model. However, only basic information for the inverter module used was available [83].

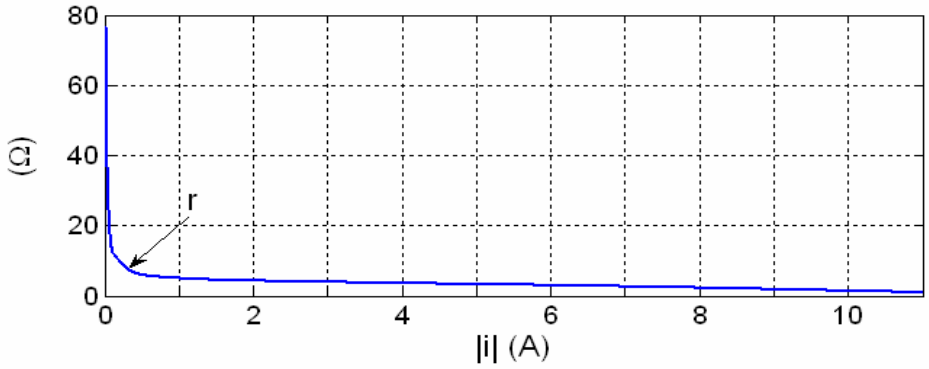

Figure 5.52: Calculated phase current-resistance function $r(|i|)$

Figure 5.52 shows the calculated $r(|i|)$ function in the range of 0 A to 11 A. It can be seen that the function looks as expected. Figure 5.52 was determined by applying a backwards transformation of the dq frame's values of r_{dq} back into the ABC frame's values of resistance. The calculation implies a backwards transformation from the two axis dq space to the three phase ABC space. Therefore the common mode component, which results in an offset of the three phase resistance values, can not be determined. That means that the offset shown in Figure 5.52 does not reflect the true value. However, a different offset value in all of the three phases does not influence the r_{dq} function that causes the di_{d0}/dt inverter non-linearity effect.

The generated function in Figure 5.52 could be approximated by a high order analytical function. This would require a rather long computation time for the online

operation. Therefore the generated $r(|i|)$ function is also stored as a look up table in the DSP memory with a discretisation of 20 mA. For values in between these currents, linear interpolation is used. The resulting di_{d0}/dt compensation value is then calculated by:

$$\frac{di_{d0}}{dt} = \frac{|\underline{i}_{\alpha\beta}|}{3L_d}\left(\sin\left(2\angle\underline{i}_{\alpha\beta}\right)r\left(|i_A|\right)+\sin\left(2\angle\underline{i}_{\alpha\beta}+\frac{2}{3}\pi\right)r\left(|i_B|\right)+\sin\left(2\angle\underline{i}_{\alpha\beta}-\frac{2}{3}\pi\right)r\left(|i_C|\right)\right) \quad (5.23)$$

Figures 5.53 and 5.54 show the experimental results of the same operating conditions as in Figures 5.18 and 5.19. The sensorless drive is operating in sensorless torque control at low/ zero speed at different load. The di_{d0}/dt compensation values are generated using the phase leg resistance function $r(|i|)$ shown in Figure 5.52 and equation (5.23).

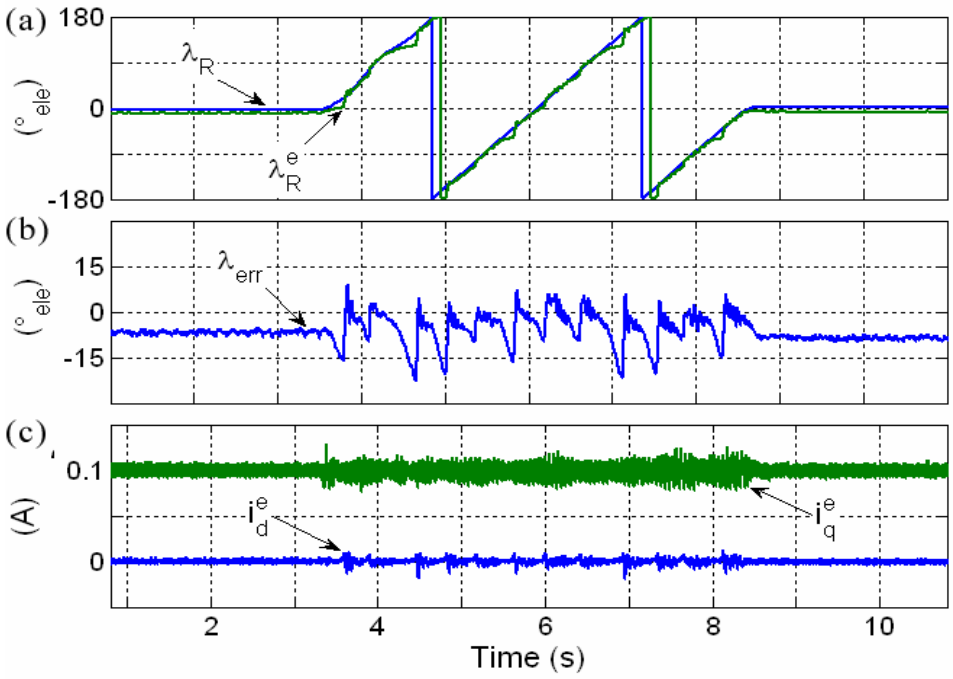

Figure 5.53: Sensorless operation at low torque (i_q^e = 0.1 A) and $r(|i|)$ compensation

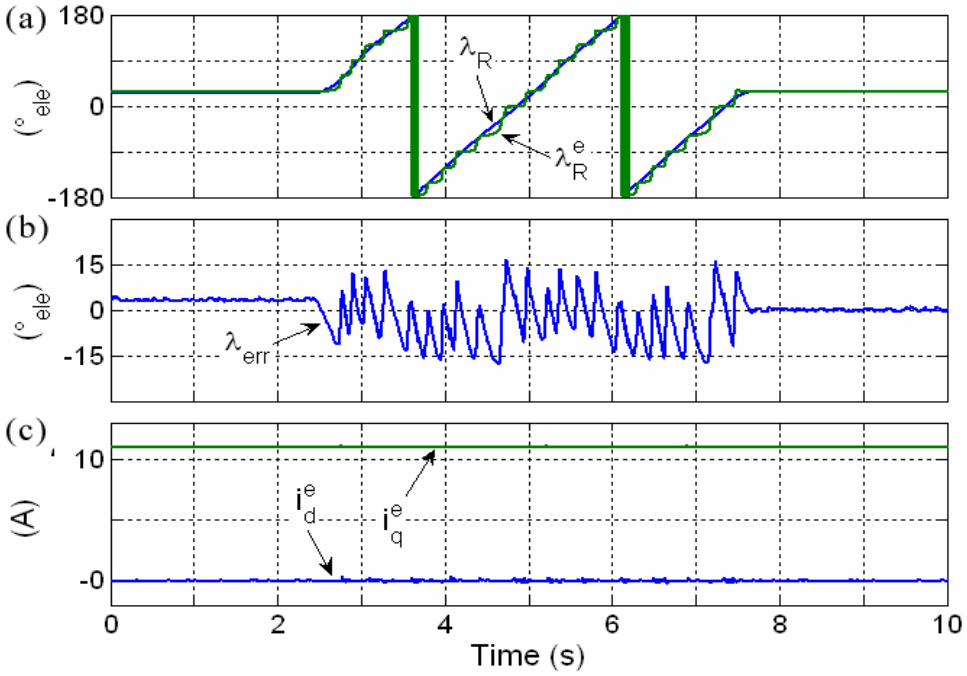

Figure 5.54: Sensorless operation at high torque (i_q^e = 11 A) and $r(|i|)$ compensation

As can be seen in the figures above, sensorless operation at very low and zero speed is also possible with the $r(|i|)$ compensation method. The position estimation errors obtained in these experiments are higher than those shown in Figures 5.18 and 5.19, which use the measured di_{d0}/dt compensation. This is expected, since the directly measured di_{d0}/dt function takes additional effects into account, e.g. current clamping. Furthermore the same $r(|i|)$ curve is used for each phase. Since in practice the real characteristics of the semiconductor devices are not 100 % identical, the three phase resistance functions are slightly different from each other, resulting in a larger error in the compensation [82].

5.8 Operation without Inverter Non-linearity Compensation

In the previous sections, operation of the sensorless drive using inverter non-linearity compensation was shown. The inverter effect is compensated by the directly measured $di_{d0}/dt(i_{\alpha\beta})$ function or the inverter resistance function $r(|i|)$. The inverter disturbance in the measured current derivative signals is speed independent, and depends only on the phase currents in the machine. It was explained in section 5.3 that at higher operation speeds the back EMF term in the $di_{d0}^{e}/dt(\lambda_{err})$ error signal is dominant and it only is used for the sensorless rotor position estimation. Since the back EMF $di_{d0}^{e}/dt(\lambda_{err})$ influence rises proportional with higher speed, the disturbances caused by the inverter non-linearity will be relatively small at higher speeds. Even if it was shown that the inverter non-linearity can be compensated, for a very simple low cost implementation, that requires no very low/ zero speed operation, the inverter non-linearity compensation can be left out. The expense of this simpler implementation will be larger estimation errors particular at lower speeds.

Figures 5.55 to 5.57 show the sensorless PMSM drive operating in torque control under various operation conditions. No inverter non-linearity compensation is used. The measured di_{d0}^{e}/dt signal is directly fed to the PLL structure as shown in Figure 5.4. The speed in the shown experiments is controlled by the coupled DC machine. Since the rotation direction in all three experiments is forward, the error signal polarity is set constant to positive. In the figures plot (a) shows the measured and estimated rotor position λ_R and λ_R^{e}, plot (b) shows the difference between the measured and estimated rotor position λ_{err} and plot (c) shows the applied machine currents in estimated dq^{e} reference frame. Figure 5.57 shows further in plot (d) the

measured mechanical rotor speed n_R (filtered by a 200 Hz low pass filter for noise reduction).

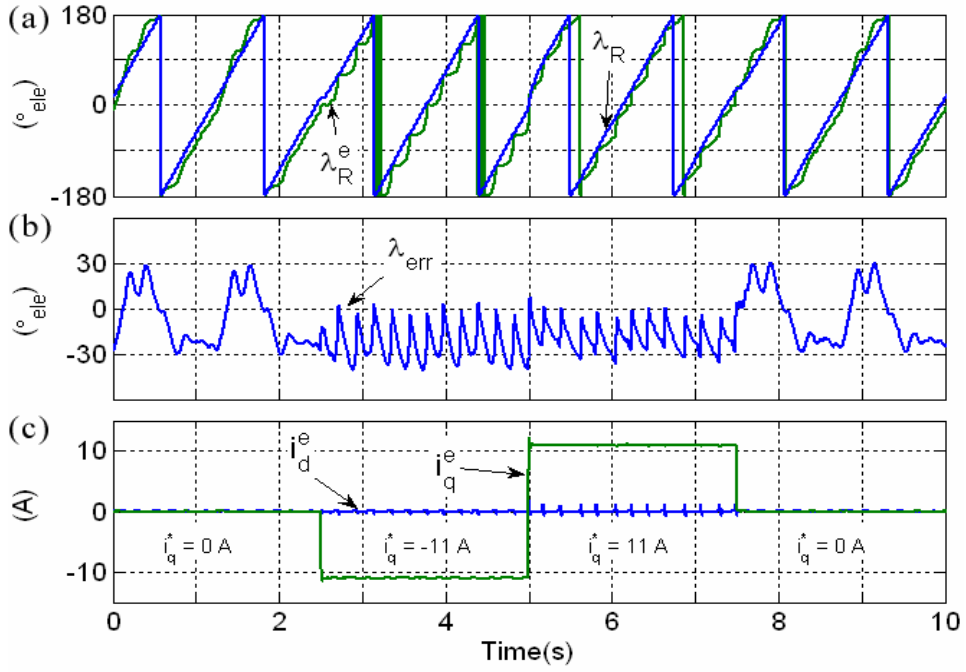

Figure 5.55: Sensorless operation without inverter non-linearity compensation and varying torque at 12 rpm (0.8 % of rated speed)

In Figure 5.55 the mechanical speed is set to 12 rpm. The i_q^* reference of the torque controlled sensorless PMSM drive is changed from 0 A to -11 A, to 11 A and back to 0 A. No ramp limitation is used for the i_q^* steps. The result in the figure shows that sensorless operation without inverter non-linearity compensation at zero and high torque is possible for speeds lower than 1 % of rated speed. From the position plot it can be seen that the estimation errors are rather large, but still the estimated position follows the measured rotor position. It can be seen that the estimator errors show a ripple function repeating with every current commutation sector. This is the influence of the uncompensated di_0/dt modulation effect due to the unbalanced resistances of the inverter legs. Figure 5.22 showed a similar test, but with di_{d0}/dt inverter non-linearity compensation. Comparing the two results shows that the

estimation error can be reduced by more then 70 % if inverter non-linearity compensation is used. It can also be seen that at zero current ($i_q^* = 0$ A) the position estimation quality is worse. This is due to the very strong current clamping effect since the current is always about zero during the zero vectors. The current clamping effect [34] blocks the inverter IGBT/ diode completely and changes therefore the internal resistance r_i of the inverter to a very high value. The same zero current condition was already shown in Figure 5.24 where only the back EMF provides the information for the position tracking.

Figure 5.56 shows the same experiment as Figure 5.55 repeated at a slightly higher speed. The set speed of 30 rpm corresponds to 2 % of rated speed. It can be seen that the rotor position estimation quality has improved significant compared to Figure 5.55. This is due to the larger back EMF amplitude at the higher speed. Therefore, the disturbances of the inverter non-linearity, which do not depend on speed, are relatively smaller and affect the position estimation less.

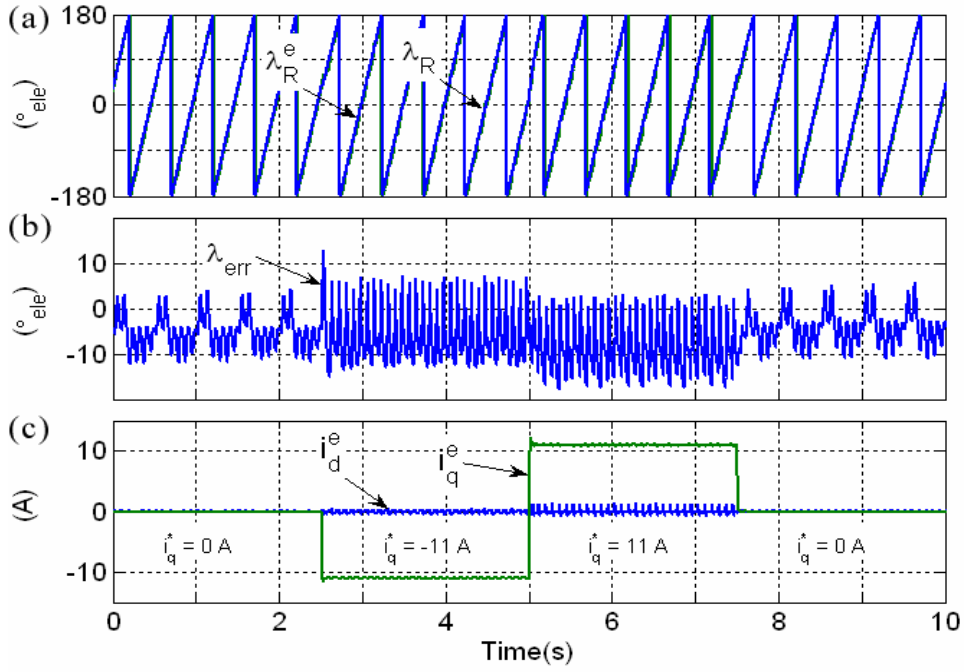

Figure 5.56: Sensorless operation without inverter non-linearity compensation and varying torque at 30 rpm (2 % of rated speed)

The experiment in Figure 5.57 demonstrates how the uncompensated inverter non-linearity affects the position estimation quality at high torque and different speeds. The sensorless drive is operated at high current amplitude (11 A). The speed is varied from 15 rpm to 375 rpm (1 to 25 % of rated speed). It can be seen in the figure below, that as expected the ripple in the estimated position decrease with higher speed.

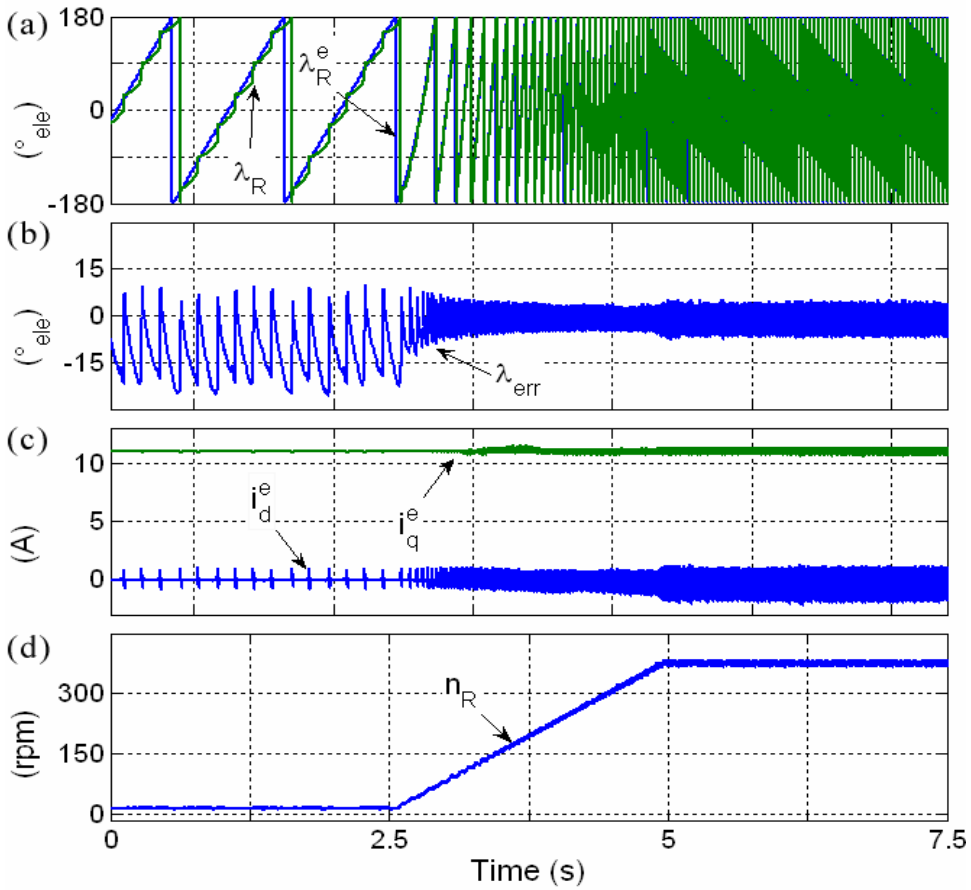

Figure 5.57: Sensorless operation without inverter non-linearity compensation and high torque at 15 to 375 rpm (1 to 25 % of rated speed)

Form the experiments shown above can be concluded that the strong back EMF in the implemented sensorless drive provides a good $di_{d0}^{e}/dt(\lambda_{err})$ signal for the rotor position estimation that does not require any inverter non-linearity compensation. Of course at very low and zero speed the inverter non-linearity di_{d0}^{e}/dt modulation will cause significant position estimation errors. However as shown above from an operation speed above 2 Hz electrical (2 % of rated value) the position estimation quality may be acceptable for certain applications. Therefore a much simpler implementation without any inverter non-linearity compensation can be achieved if maintained operation at speeds of less the 2 % of rated speed are not required.

5.9 Derivation of Zero Vector Current Derivative Method with Fundamental Cross Coupling Terms

As shown in the previous basic derivation of the zero vector current derivative (ZVCD) technique the cross coupling terms in the fundamental voltage equations were left out for simplicity. It was also found in practical experiments that the influence is not significant. However, for the completeness of the theoretical mathematical explanation, the derivation is repeated here including the cross coupling terms in the stator voltage equations. In the following equations the additional terms due to the cross coupling terms are marked in red to indicate their particular influence. As in section 5.2 the derivation starts from the fundamental voltage equations (5.24) and (5.25).

$$v_d = R i_d + L_d \frac{i_d}{dt} - L_q \omega_e i_q \tag{5.24}$$

$$v_q = R i_q + L_q \frac{i_q}{dt} + L_d \omega_e i_d + k_e \omega_R \tag{5.25}$$

At the zero voltage vectors v_d and v_q equal zero and equations (5.24) and (5.25) can be rearranged to:

$$\frac{i_{d0}}{dt} = -\frac{R}{L_d} i_d + \frac{L_q}{L_d} \omega_e i_q , \tag{5.26}$$

$$\frac{i_{q0}}{dt} = -\frac{R}{L_q} i_q - \frac{L_d}{L_q} \omega_e i_d - k_e \omega_R . \tag{5.27}$$

Equations (5.26) and (5.27) can be combined in matrix notation to:

$$\begin{bmatrix} \frac{i_{d0}}{dt} \\ \frac{i_{q0}}{dt} \end{bmatrix} = \begin{bmatrix} -\frac{R}{L_d} & \frac{L_q}{L_d}\omega_e \\ -\frac{L_d}{L_q}\omega_e & -\frac{R}{L_q} \end{bmatrix} \cdot \begin{bmatrix} i_d \\ i_q \end{bmatrix} - \begin{bmatrix} 0 \\ k_e \omega_R \end{bmatrix} . \tag{5.28}$$

Equation (5.30) gives the voltage equation system in the estimated reference frame. The reference frame transformation matrix is shown by equation (5.29). Equations (5.31) to (5.34) show the matrix factors c_{dq}^{e}, c_{dd}^{e}, c_{qd}^{e} and c_{qq}^{e}.

$$\mathbf{B}(\lambda_{err}) = \begin{bmatrix} \cos(\lambda_{err}) & \sin(\lambda_{err}) \\ -\sin(\lambda_{err}) & \cos(\lambda_{err}) \end{bmatrix} \tag{5.29}$$

$$\begin{aligned} \begin{bmatrix} \frac{i_{d0}^{e}}{dt} \\ \frac{i_{q0}^{e}}{dt} \end{bmatrix} &= \mathbf{B}(\lambda_{err}) \cdot \begin{bmatrix} -\frac{R}{L_d} & \frac{L_q}{L_d}\omega_e \\ -\frac{L_d}{L_q}\omega_e & -\frac{R}{L_q} \end{bmatrix} \cdot \mathbf{B}(\lambda_{err})^{-1} \cdot \begin{bmatrix} i_d^e \\ i_q^e \end{bmatrix} - \mathbf{B}(\lambda_{err}) \cdot \begin{bmatrix} 0 \\ k_e \omega_R \end{bmatrix} \\ &= \begin{bmatrix} c_{dd}^{e} & c_{dq}^{e} \\ c_{qd}^{e} & c_{qq}^{e} \end{bmatrix} \cdot \begin{bmatrix} i_d^e \\ i_q^e \end{bmatrix} - \begin{bmatrix} \sin(\lambda_{err}) \frac{k_e}{L_q} \omega_R \\ \cos(\lambda_{err}) \frac{k_e}{L_q} \omega_R \end{bmatrix} \end{aligned} \tag{5.30}$$

$$c_{dd}^{e} = -\frac{R}{L_d}\cos^2(\lambda_{err}) + \left(\frac{L_q}{L_d}\omega_e - \frac{L_d}{L_q}\omega_e\right)\sin(\lambda_{err})\cos(\lambda_{err}) - \frac{R}{L_q}\sin^2(\lambda_{err}) \tag{5.31}$$

$$c_{dq}^{e} = \frac{L_d}{L_q}\omega_e \sin^2(\lambda_{err}) + \left(\frac{R}{L_d} - \frac{R}{L_q}\right)\sin(\lambda_{err})\cos(\lambda_{err}) + \frac{L_q}{L_d}\omega_e \cos^2(\lambda_{err}) \tag{5.32}$$

$$c_{qd}^{e} = -\frac{L_d}{L_q}\omega_e \cos^2(\lambda_{err}) + \left(\frac{R}{L_d} - \frac{R}{L_q}\right)\sin(\lambda_{err})\cos(\lambda_{err}) - \frac{L_q}{L_d}\omega_e \sin^2(\lambda_{err}) \tag{5.33}$$

$$c^e_{qq} = -\frac{R}{L_d}\sin^2(\lambda_{err}) + \left(\frac{L_d}{L_q}\omega_e - \frac{L_q}{L_d}\omega_e\right)\sin(\lambda_{err})\cos(\lambda_{err}) - \frac{R}{L_q}\cos^2(\lambda_{err}) \quad (5.34)$$

In the position estimation algorithm only the current derivative in the estimated d^e axis is used and i^e_d is forced to zero by the current controller. Therefore the final equation for the error signal function $di_{d0}^e/dt(\lambda_{err})$ is:

$$\begin{aligned}
\frac{i^e_{d0}}{dt} &= d^e_{dq}\, i^e_q - \sin(\lambda_{err})\frac{k_e}{L_q}\omega_r \\
&= \left(\frac{L_d}{L_q}\omega_e \sin^2(\lambda_{err}) + \left(\frac{R}{L_d} - \frac{R}{L_q}\right)\sin(\lambda_{err})\cos(\lambda_{err}) + \frac{L_q}{L_d}\omega_e \cos^2(\lambda_{err})\right) i^e_q - \sin(\lambda_{err})\frac{k_e}{L_q}\omega_R \,. \\
&= \underbrace{\frac{R}{2}\left(\frac{1}{L_d} - \frac{1}{L_q}\right)\sin(2\lambda_{err})\, i^e_q}_{Saliency} + \underbrace{\left(\frac{L_q}{L_d} + \left(\frac{L_d}{L_q} - \frac{L_q}{L_d}\right)\sin^2(\lambda_{err})\right)\omega_e\, i^e_q}_{Cross\ coupling} \underbrace{- \sin(\lambda_{err})\frac{k_e}{L_q}\omega_R}_{Back\ EMF}
\end{aligned} \quad (5.35)$$

From equation (5.35) can be seen that the final current derivative is determined by three terms, a saliency, a cross coupling and a back EMF term. The cross coupling term and the back EMF term amplitudes are both linear with the speed ($\omega_e \approx \omega_R$). Therefore at very low speeds their effect can be neglected and only the saliency term is dominant. By contrast, the saliency term can be neglected at higher speeds. The cross coupling effect induces a voltage in the stator windings superimposed with the machine's back EMF.

If the condition $di^e_{d0}/dt = 0$ is still used for the sensorless position tracking algorithm the error at higher speeds can be evaluated from equation (5.36). In (5.36) the saliency term is neglected since higher speed operation is considered.

$$\frac{i_{d0}^{e}}{dt} = 0 = \underbrace{\left(\frac{L_q}{L_d} + \left(\frac{L_d}{L_q} - \frac{L_q}{L_d}\right)\sin^2\left(\lambda_{err}\right)\right)\omega_e\, i_q^e}_{Cross\ coupling} \underbrace{-\sin\left(\lambda_{err}\right)\frac{k_e}{L_q}\omega_R}_{Back\ EMF} \tag{5.36}$$

Equation (5.36) is a quadratic equation that gives two solutions for $\sin(\lambda_{err})$. However, it was found that only one solution for the condition $-1 \leq \sin(\lambda_{err}) \leq 1$ exists. Figure 5.58 shows the numerical solution for the theoretical position estimation error $\lambda_{err}(i^e_q)$ for the condition that $di^e_{d0}/dt = 0$ and the assumption that $\omega_e = \omega_R$ which is the case under locked position tracking. The machine parameters L_d, L_q and k_e stated in section 4.5 are used for the calculation. It can be seen that the error is an offset that increases almost linearly with the machine current amplitude. The theoretical expected error is about 8 electrical degrees at 11 A current amplitude.

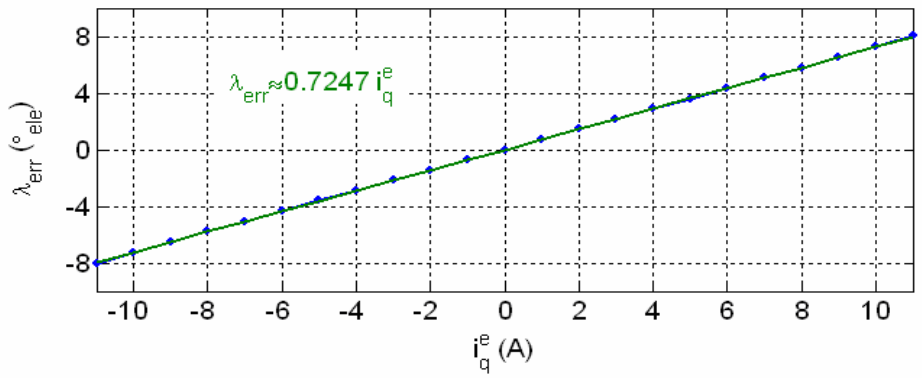

Figure 5.58: Theoretical solution and linear approximation for $\lambda_{err}(i^e_q)$ created by fundamental cross coupling effect

In Figure 5.58 the blue dots show the numerically calculated position errors and the green line shows a linear approximated function. The analytical linear approximation equation is also stated in Figure 5.58.

Setting λ_{err} in equation (5.35) to zero, which is the condition for true orientation, gives equation (5.37) as a solution for the zero vector current derivative in the d direction. It can be seen that the result is an offset value that arises in di^e_{d0}/dt. Therefore the tracking condition $di^e_{d0}/dt = 0$ for $\lambda_{err} = 0$ is not valid anymore. However, the offset value can be easily compensated in a feed forward manner in the tracking algorithm, since all the parameters of (5.37) are known.

$$\frac{i^e_{d0}}{dt}\left(\lambda_{err}=0\right) = \frac{L_q}{L_d}\omega_e\, i^e_q \tag{5.37}$$

However, in spite of the above theoretical derived influence of the cross coupling terms, in the practical implemented drive no significant offset errors in the estimated position were observed. Figures 5.59 and 5.60 show results for the sensorless PMSM drive operating from stand still to the maximum tested operation speed. In both experiments the sensorless PMSM drive is operated in torque control and the speed is set by the coupled DC machine. In both experiments the $di_{d0}/dt(\underline{i}_{\alpha\beta})$ compensation look up table shown in Figure 5.16 is used to decouple the inverter non-linearity modulation and enable zero speed operation. No compensation for the cross coupling terms is implemented and the position tracking controller is set to keep di^e_{d0}/dt to zero as in all experiments before. Figure 5.59 shows the operation at minimum torque producing current ($i_q^* = 0.1$ A) while Figure 5.60 shows the operation at high current ($i_q^* = 11$ A). In the figures plot (a) shows the measured and estimated rotor position λ_R and λ_R^e, plot (b) shows the difference between measured and estimated rotor position λ_{err}, plot (c) shows the applied machine currents in estimated dq^e reference frame and plot (d) shows the measured mechanical rotor speed n_R (filtered by a 200 Hz low pass filter for noise reduction).

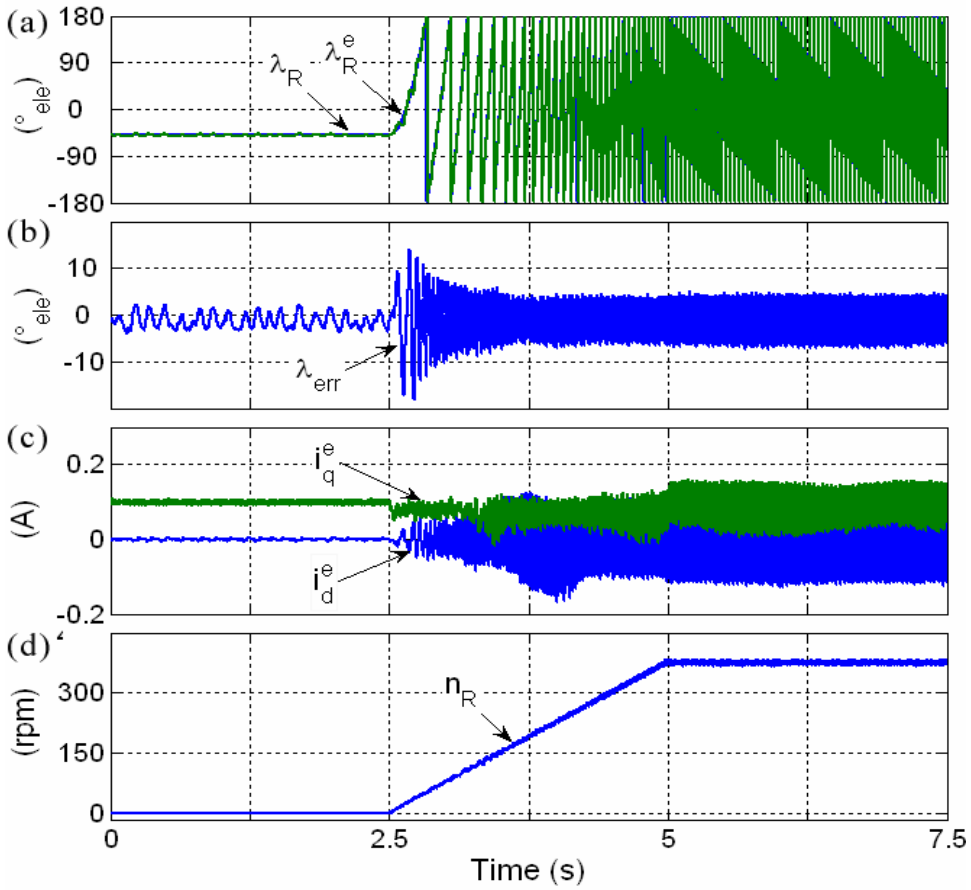

Figure 5.59: Sensorless operation from 0 to 375 rpm with $i_q^* = 0.1$ A

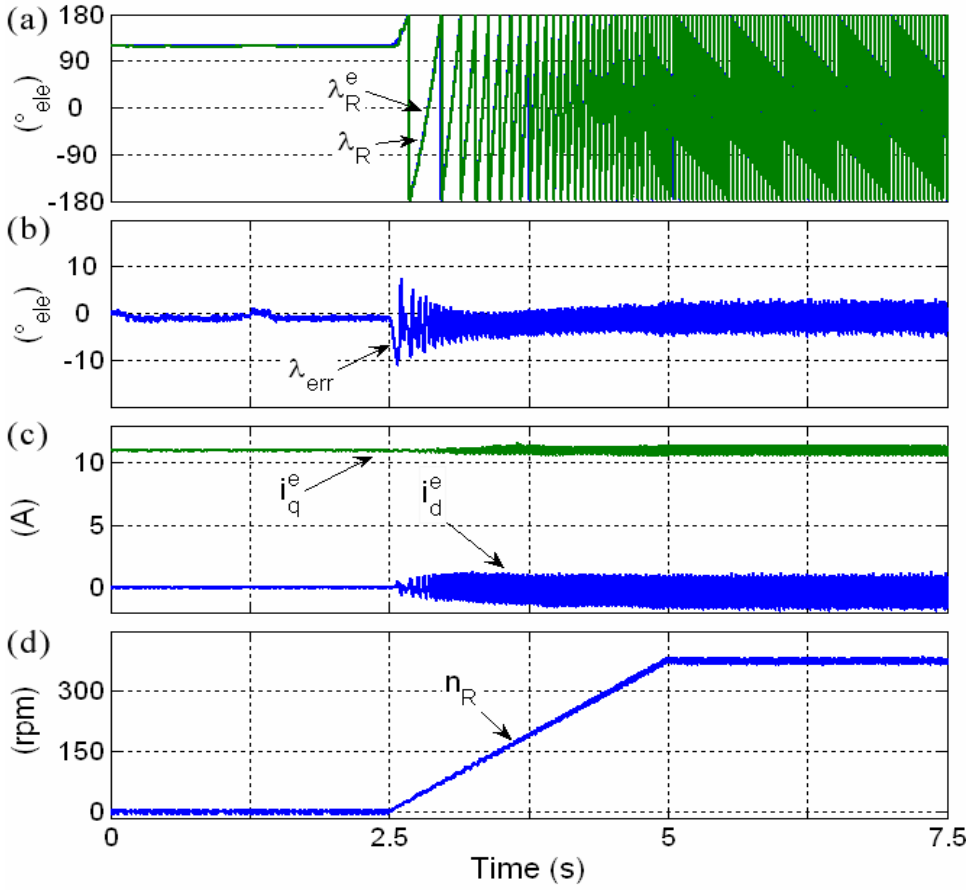

Figure 5.60: Sensorless operation from 0 to 375 rpm with $i_q^* = 11$ A

As can be seen from the figures above, the estimated position is quite noisy, but no offset error can be clearly identified in the estimated position. At zero speed ($\omega_e = 0$, $\omega_R = 0$) only the saliency term is present and the speed dependent back EMF and cross coupling terms are zero. Therefore the position estimation at zero speed is not affected by the cross coupling terms. At 375 rpm the electrical frequency is 25 Hz electrical for the 8 pole machine. Under this condition the saliency term influence is neglectable since the back EMF amplitude is much stronger at high speeds and the influence by the cross coupling terms should be visible. In the experiment of Figure 5.59 the machine current is quite small (0.1 A) and thus no significant offset error is expected. By contrast, from the theoretical derivation it is expected that the experiment with the current amplitude used in Figure 5.60 (11 A) shows a position

estimation error of about 8 electrical degrees as the cross coupling effect is not compensated. It can be concluded that the practical results show no significant offset in the estimated position occurs. Therefore no compensation of the cross coupling term is implemented in the set up sensorless drive.

5.10 Conclusions

A novel sensorless technique has been developed that measures the current derivative during the zero vectors. A novel hybrid position error signal is obtained without the introduction of additional test signal injection. The position error signal has both a back EMF based component and a machine saliency based component. Owing to the proposed method of measurement, the back EMF based component allows operation down to very low speed. The machine saliency based component then extends the operation down to zero speed. No additional sensors such as voltage or current derivative sensors are required. Only three standard current transducers are included in the system, which are also required for the fundamental current control. All the information for this algorithm is acquired from the current decay during the zero voltage vectors, which is digitally computed from two successive current samples. As only four current samples per PWM period are used, the ADC sampling needs only to run four times as fast as the PWM switching frequency. The overall cycle frequency of the sensorless algorithm can be set equal to the PWM frequency. The algorithm computational burden is low allowing implementation on low cost microcontrollers. For detecting the saliency component of the position error signal, a torque producing current needs to be applied which can be regarded as an inherent “test signal”. Proper operation of the sensorless drive down to zero speed has been achieved with torque producing currents as low as 0.1 A, which corresponds to less then 1 % of rated current. Practical results show a stable operation of the sensorless drive down to zero speed including low and high torque operation. Since no additional test signals were injected into the machine, the current controller can

operate at a very high bandwidth. It is further shown that the back EMF signal is quite strong even at low speeds thus providing the possibility of implementing the algorithm in any PMSM, even if no saliency is available.

Also the limitation of the method in the very low speed region in two of the four quadrants of operation is presented. There the zero vector current derivative gives no useful position tracking signal due to the similar amplitude, but different polarities of the saliency and the back EMF term. However, it is shown that it is possible to pass through this small unstable operation area without the drive losing stability. It is further shown that the error signal polarity has to be adjusted according to the quadrant of operation.

The ZVCD technique is also machine parameter independent, only a difference in L_d and L_q is required if zero speed is demanded. Further for very low speed operation compensation of an inverter non-linearity effect is required. It has been shown that the variation of the semiconductor on–resistance has a detrimental effect on the position signals. It is more pronounced in this case as the measurement is done during non–active voltage vectors. Two methods of compensation for the inverter non-linearity are shown. One is based on the inverter leg resistance function dependent on the phase current that could be easily derived from the inverter semiconductor voltage-current characteristic if enough information is available. The other method uses a two dimensional look up table that contains directly the influence on the measured zero vector current derivatives in dependency on the stator current vector amplitude and position. This allows a better performance, but requires a larger amount of memory. As is shown the necessary compensation is directly related to the inverter leg resistances and is machine parameter independent. Therefore the compensation function could be generated with any load. Once the inverter non-linearity function is identified, this function could be used for the operation of different machines. The inverter non-linearity compensation can be also

left out for the simplest implementation. However, operation at very low/ zero speed will then not be possible.

It is further shown that the general increase of the resistance at smaller currents is advantageous to the position estimation method, since it amplifies the saliency di_0/dt signal, making it detectable even at very low torque operation.

From the theoretical derivation it can be seen that the fundamental cross coupling terms can be regarded as a back EMF effect that influences the zero vector current derivative (ZVCD) signal by an offset value proportional to the current vector amplitude. This cross coupling influence is more pronounced at higher speeds when the back EMF effect is used for the position estimation. In the theoretical derivation it is shown that the resulting offset value can be easily determined and compensated in the online algorithm. However, practical experiments show that there is no significant influence in the sensorless PMSM drive operation. Therefore no cross coupling compensation is implemented in the practical drive and the simpler derivation of the method, by leaving out the cross coupling terms, can be used.

Experimental sensorless results with zero speed are shown at very low and high load operation which proves the feasibility of the proposed compensation schemes. Experimental results show sensorless torque and speed control of the PMSM in forward and reverse rotation.

Chapter 6
Using PWM Harmonics for Rotor Bar Saliency Tracking

Recent approaches to sensorless control of AC motors have tracked the machine saliency by using an additional test signal injection. As a result, the motor currents contain a strong distortion which causes additional losses, vibrations and unwanted audible noise.

With standard voltage source inverters the variable AC voltage generation is achieved by applying pulse width modulation (PWM) to a DC voltage source. For the fundamental control of the machine only the low frequency component of the generated output voltage is important. However, there are also high frequency switching harmonics included in the PWM voltages which are unavoidable, and usually undesirable. The technique presented here proposes the use of these inherent high frequency PWM harmonics as the test signal. The idea is very similar to standard high frequency injection methods. The major difference is that the high frequency exitation voltage amplitude and position cannot be independently set. It depends directly on the fundamental voltage demanded by the motor's current controller, and therefore the torque and flux settings. The high frequency currents, resulting from the PWM harmonic frequencies, should show some modulation in the impedance of the stator windings due to magnetic saliency. The saliency modulation is then used for the rotor position reconstruction for the sensorless control of AC drives [84].

In this chapter a new position estimation strategy for an induction motor is proposed which includes demodulation and compensation schemes. Before describing the control strategy, a theoretical analysis is made of the PWM frequency content. The sensorless control strategy is then derived, and experimental results from an off–the–shelf induction motor are shown. The results show the fully sensorless drive operating in torque-, speed-, and position control under different load conditions, and validate the proposed strategy.

In this chapter only stator quantities are considered. Therefore the index "*S*" to indicate stator variables, as used in Chapter 2, is omitted for simplicity.

6.1 Analysis of PWM Voltage Harmonics

To use AC motors as speed variable drives, a variable amplitude and frequency voltages needs to be applied to the machine terminals. For the fundamental three phase voltage generation the principle of pulse width modulation (PWM) is used. Therefore the inverter output is switched between the positive and negative potential of the DC link voltage with a much higher frequency (1 ... 20 kHz) than the fundamental machine voltage frequency (1 ... 50 Hz).

6.1.1 Theoretical Analysis

Figure 6.1 shows the principle of the PWM for one PWM period [12]. Plot (a) shows the PWM output pattern of the phase voltages and plot (b) shows the resulting components in the balanced system $\alpha\beta 0$ space [7], where:

$$\begin{bmatrix} v_a \\ v_\beta \\ v_0 \end{bmatrix} = \frac{2}{3} \begin{bmatrix} 1 & -1/2 & -1/2 \\ 0 & \sqrt{3}/2 & -\sqrt{3}/2 \\ 1/\sqrt{2} & 1/\sqrt{2} & 1/\sqrt{2} \end{bmatrix} \cdot \begin{bmatrix} v_A \\ v_B \\ v_C \end{bmatrix} \quad . \tag{6.1}$$

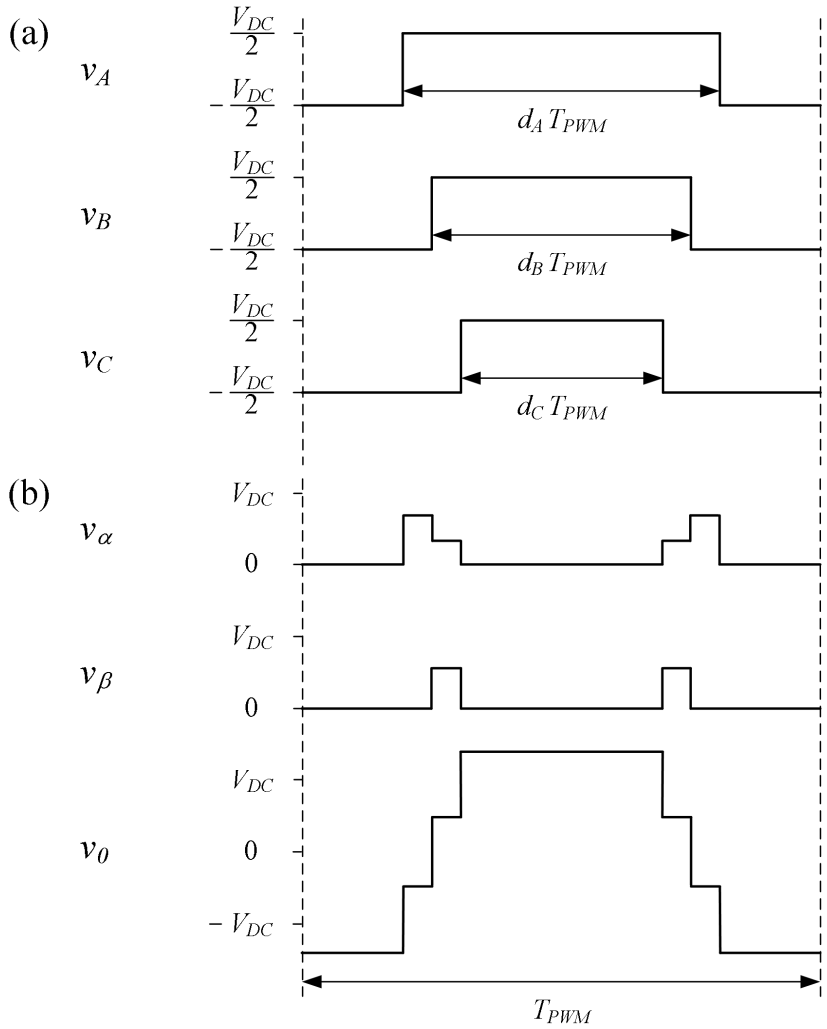

Figure 6.1: PWM voltage generation

The desired fundamental output voltage is the average of the PWM period. The PWM inverter voltage generation produces a switching voltage pattern with very sharp edges. This generated voltage signal has theoretical frequency components up to infinity [85]. Since the PWM period width is fixed and can be regarded as repeated pattern, the Fourier series can be calculated to investigate the frequency components. As basic rule of repeated patterns, only frequency components of multiple of the pattern frequency will be present in the Fourier series. That means that in this case the complete inverter output voltage can be fragmented into

frequency components of multiple the PWM switching frequency plus a DC component [85].

Only one PWM generation method as presented in section 2.5 is considered in this work, but the method can be extended to other PWM waveforms. The inverter leg switching duty cycle *d* is calculated using a simple sine weighted modulation [86] as follows:

$$d = \frac{1}{2} + \frac{m}{2} \quad . \tag{6.2}$$

where *m* is the normalized instantaneous line voltage demand (i.e. PWM modulation signal). It is derived from:

$$v = \frac{m V_{DC}}{2} \Rightarrow m = \frac{2v}{V_{DC}} \quad . \tag{6.3}$$

In (6.3) V_{DC} is the inverter DC link voltage and *v* the demanded instantaneous machine phase voltage. According to the general form of a Fourier series [85] the PWM output voltage per phase *v* can be described as:

$$v(t) = \frac{a_{PWM0}}{2} + \sum_{n=1}^{\infty} \left(a_{PWMn} \cos\left(n \omega_{PWM} t\right) + b_{PWMn} \sin\left(n \omega_{PWM} t\right) \right) \quad . \tag{6.4}$$

In equation (6.4) *n* represents the number of the PWM harmonic.

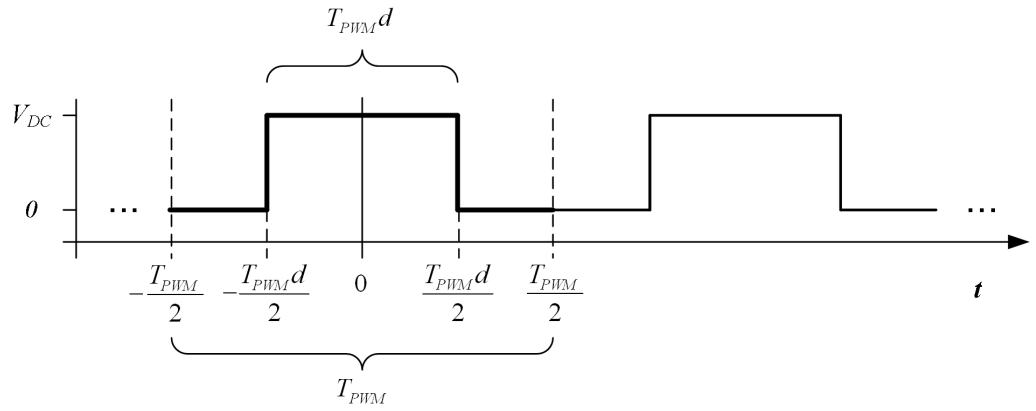

Figure 6.2: PWM considered for Fourier series calculation

The contribution to the desired fundamental AC output voltage is the component $a_{PWM0}/2$ which is dV_{DC}. Figure 6.2 shows a drawing of the PWM waveform used for the Fourier series calculation. The start point $t = 0$ is arbitrary selected for a convenient calculation. Since the signal is regarded as an even function [85] all b_{PWM0} coefficients are zero and the PWM harmonics are only defined by a_{PWMn}. Equations (6.5) to (6.8) give the derivation of the Fourier coefficients.

$$a_{PWMn} = \frac{2}{T_{PWM}} \int_{-\frac{T_{PWM}d}{2}}^{\frac{T_{PWM}d}{2}} V_{DC} \cos\left(n\,\omega_{PWM} t\right) dt \tag{6.5}$$

$$a_{PWMn} = \frac{2V_{DC}}{T_{PWM} n\,\omega_{PWM}} \left[\sin\left(n\,\omega_{PWM} t\right)\right]_{-\frac{T_{PWM}d}{2}}^{\frac{T_{PWM}d}{2}} \tag{6.6}$$

$$a_{PWMn} = \frac{V_{DC}}{n\pi}\left[\sin\left(n\pi d\right) - \sin\left(-n\pi d\right)\right] \tag{6.7}$$

$$a_{PWMn} = \frac{2V_{DC}}{n\pi}\sin\left(n\pi d\right) \tag{6.8}$$

Equation (6.8) as function to the phase modulation index m gives:

$$a_{PWMn} = \frac{2V_{DC}}{n\pi}\sin\left(n\pi\left(\frac{1}{2}+\frac{m}{2}\right)\right) . \quad (6.9)$$

Equations (6.10) to (6.13) show the resolved expressions for the first four PWM harmonics of the inverter output line voltages.

$$a_{PWM1} = \frac{2V_{DC}}{\pi}\cos\left(\frac{1}{2}\pi m\right) \quad (6.10)$$

$$a_{PWM2} = -\frac{V_{DC}}{\pi}\sin\left(\pi m\right) \quad (6.11)$$

$$a_{PWM3} = -\frac{2V_{DC}}{3\pi}\cos\left(\frac{3}{2}\pi m\right) \quad (6.12)$$

$$a_{PWM4} = \frac{V_{DC}}{2\pi}\sin\left(2\pi m\right) \quad (6.13)$$

Looking at the above equations (6.10) to (6.13) reveals some interesting properties. It can be seen that all odd PWM harmonic components are related with a cosine function to the actual phase voltage amplitude and all even harmonics are linked with a sine function. Visualising sine and cosine functions shows that the odd harmonics only depend on the modulation depth (amplitude of the phase voltages) and the even PWM harmonics are also affected by the sign of the phase voltages. That means that the odd PWM harmonics only contain information related to the rectified modulation depth.

It was found that at low speed the 2nd PWM harmonic shows the largest amplitude. Figure 6.1 illustrates this. It can be seen that in one PWM period the active voltage vectors, where v_α and v_β are not zero, occur twice and are positioned away from the

middle of the PWM cycle. Figure 6.1 also shows that the inverter phase output voltages v_A, v_B and v_C contain a very strong 1st PWM harmonic. However, since the first PWM harmonic in all three phases is almost the same, most of the first PWM harmonic results only in the common mode voltage component v_0. This common mode voltage will also produce common mode currents via parasitic capacitances that couple the machine to earth. These PWM harmonic common mode currents may also contain some position modulation [87] and might be useful for sensorless control of AC machines. However, in this work only the 2nd PWM harmonic is used for the sensorless position estimation. All variables referring to this PWM harmonic are further denoted as PWM2.

In the space vector approach [88] the fundamental three phase voltages can be combined to form a complex vector in the stator fixed $\alpha\beta$ frame:

$$\underline{v}_{\alpha\beta} = \frac{2}{3}\frac{V_{DC}}{2}\left(m_A + m_B e^{j\frac{2}{3}\pi} + m_C e^{j\frac{4}{3}\pi} \right) . \tag{6.14}$$

Therefore the three phase PWM carrier harmonic components can be also combined to form a complex vector in the $\alpha\beta$ reference frame:

$$\underline{a}_{PWMn\alpha\beta} = \frac{2}{3}\left(a_{PWMn\,A} + a_{PWMn\,B} e^{j\frac{2}{3}\pi} + a_{PWMn\,C} e^{j\frac{4}{3}\pi} \right) . \tag{6.15}$$

This gives for the 2nd PWM frequency harmonic the expression:

$$\underline{a}_{PWM2\alpha\beta} = -\frac{2}{3}\frac{V_{DC}}{\pi}\left(\sin(\pi m_A) + \sin(\pi m_B) e^{j\frac{2}{3}\pi} + \sin(\pi m_C) e^{j\frac{4}{3}\pi} \right) . \tag{6.16}$$

For a better understanding the negative polarity of equation (6.16) can be removed:

$$\underline{a}_{PWM2\alpha\beta} = \frac{2}{3}\frac{V_{DC}}{\pi}\left(\sin(\pi m_A)+\sin(\pi m_B)e^{j\frac{2}{3}\pi}+\sin(\pi m_C)e^{j\frac{4}{3}\pi}\right) \quad . \quad (6.17)$$

This change of polarity shifts only the reference phase of the pulsating signal by 180 degrees ($t = 0$ shifts by $T_{PWM}/4$ for the PWM2 harmonic) which is irrelevant for this analysis. A conclusion from equation (6.17) is that $\underline{a}_{PWM2\alpha\beta}$ describes a vector almost aligned with the fundamental voltage vector. Only a slight deviation due to the sine function non-linearity will appear. However, at low speed the fundamental voltage amplitude is small and this non-linearity should not be significant. Equation (6.18) states the final description of the 2nd PWM harmonic complex voltage vector in the stator $\alpha\beta$ frame which describes a pulsating high frequency vector rotating and synchronized with the fundamental voltage vector [84].

$$\begin{aligned}\underline{v}_{PWM2\alpha\beta} &= \underline{a}_{PWM2\alpha\beta}\cos(2\omega_{PWM}t)\\ &= \frac{2}{3}\frac{V_{DC}}{\pi}\left(\sin(\pi m_A)+\sin(\pi m_B)e^{j\frac{2}{3}\pi}+\sin(\pi m_C)e^{j\frac{4}{3}\pi}\right)\cos(2\omega_{PWM}t)\end{aligned} \quad (6.18)$$

6.1.2 Initial Experimental Analysis of the PWM Harmonics

In a first experiment the test machine is fed by the three phase inverter output voltages with a PWM switching frequency of 1.818 kHz. The machine is operated under sensored IRFO current control at constant rated torque. Therefore i_d^* is set to 7.6 A and i_q^* to 12.5 A. The mechanical speed is set by the coupled DC drive to 30 rpm. The resulting electrical frequency is approximately 2.7 Hz. All three measured line currents and voltages are filtered by a 4 pole analogue anti aliasing filter (f_c = 10 kHz) and then sampled at a frequency of 60 kHz. Figure 6.3 shows the experimental

results plotted over time. Plot (a) shows the rotor and rotor flux position λ_R and λ_{dq}, plot (b) shows the machine voltages v_α and v_β and plot (c) shows the machine currents i_α and i_β. In the plots the ripple due to the PWM switching can be clearly seen which are particularly large in the measured voltages. The current waveforms are sinusoidal with only a small ripple visible.

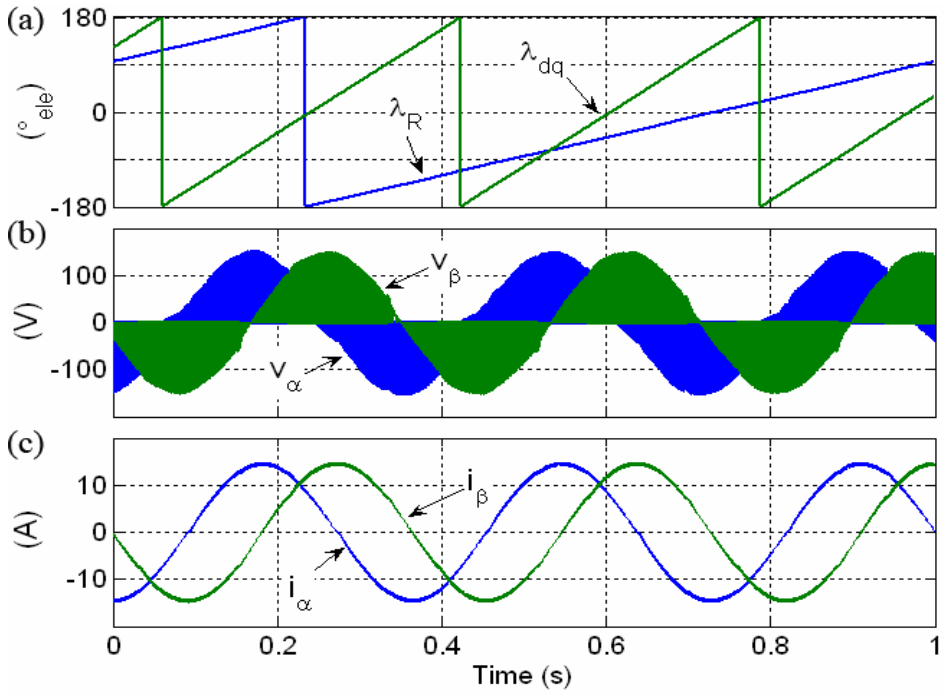

Figure 6.3: Flux and rotor position, measured voltages and current for an induction machine operating at rated torque, 30 rpm (all data sampled with 60 kHz)

A spectrum analysis was performed on the captured data using the Matlab FFT function [89]. The analysis was performed in data sets to demonstrate how the frequency components behave over time. For each analysis step 528 successive samples (16 PWM periods) are used for computing a single FFT. That means that every 8.8 ms the spectrum is calculated with a resolution of 113.63 Hz. Therefore in each time window the fundamental voltage vector is almost constant. Hence for each FFT the voltage signal is aproximately a static pulsating vector. The FFT is performed directly on the complex $\underline{v}_{\alpha\beta}$ and $\underline{i}_{\alpha\beta}$ vectors. Figures 6.4 and 6.5 show the

real and imaginary part of the time spectrum of the voltage vector $\underline{v}_{\alpha\beta}$. It can be seen that the positive and negative spectra are almost identical. It can be seen that the even PWM harmonics rotate, as explained before, and are almost synchronized with the fundamental voltage vector. By contrast the odd harmonics appear to rotate with double the fundamental frequency. It is also clearly visible that the even harmonics show much higher amplitude then the odd harmonics. In fact it can be seen that the 2nd PWM harmonic reaches almost the same amplitude as the fundamental machine voltage, visible in the DC component band (-56.8 Hz to 56.8 Hz) of the spectrum. Since the 2nd PWM harmonic is the stronges high frequency component it can be potentially used as "measurement" signal for the machine HF impedance.

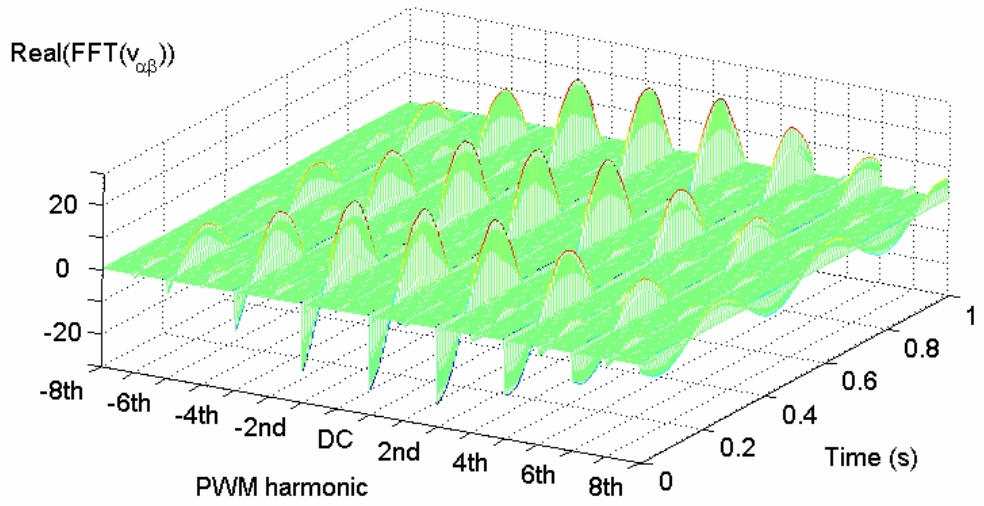

Figure 6.4: Real part of floating over time complex FFT spectrum of $\underline{v}_{\alpha\beta}$

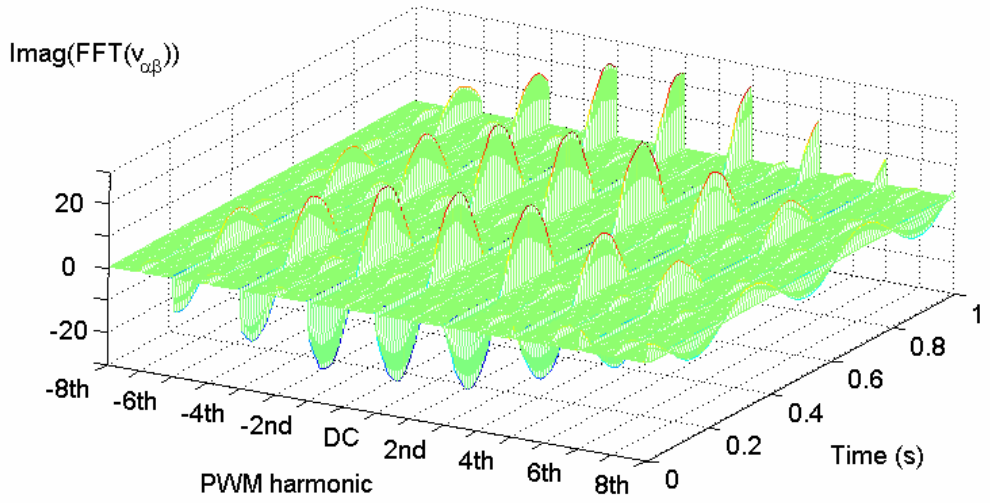

Figure 6.5: Imaginary part of floating over time complex FFT spectrum of $\underline{v}_{\alpha\beta}$

6.1.3 The Use of PWM harmonics for saliency detection

The PWM carrier frequency components in the voltage can be regarded as the injection of pulsating high frequency vectors. Hence, the resulting current PWM carrier harmonics together with the injected HF voltage vectors can be used for detecting the HF impedance inside the machine. In the following analysis only the 2nd PWM frequency harmonic is used, since it shows the largest amplitude. This 2nd PWM carrier harmonic component will be referred to as "PWM2" in the following explanation. The same analysis can also be made for the other PWM harmonics.

The 2nd PWM carrier harmonic component in the voltage and current signals is extracted by a heterodyning demodulation technique [6]. From the demodulated high frequency voltage and current PWM carrier harmonic vectors $\underline{v}'_{PWM2}$ and $\underline{i}'_{PWM2}$ an equivalent impedance vector $\underline{z}'_{PWM2}$ can be defined, which is described by equation (6.19). The complex vector division can be calculated in any reference frame. The result will be only affected by the phase and magnitude difference of the two vectors.

The apostrophe refers to the demodulated signals. The demodulation process is described in the next section.

$$\underline{z}'_{PWM2} = \frac{\underline{v}'_{PWM2}}{\underline{i}'_{PWM2}} \tag{6.19}$$

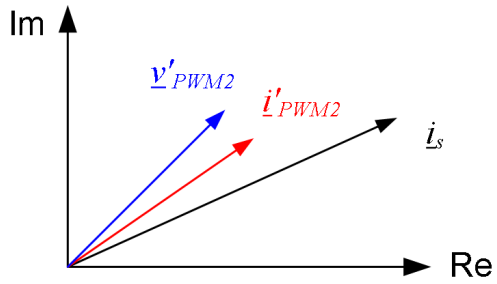

Figure 6.6: Principal illustration of PWM2 voltage and resulting PWM2 current vector

Figure 6.6 shows principally the position of the demodulated PWM2 high frequency voltage and current vectors $\underline{v}'_{PWM2}$ and $\underline{i}'_{PWM2}$ which are rotating with the fundamental machine voltage. Because of the vector division involved, the absolute position of the voltage and current vectors is not important and only the amplitude and phase difference will determine the equivalent impedance vector result $\underline{z}'_{PWM2}$. This will ease the practical implementation since this division can be made in any reference frame leading to the same result. The impedance of the machine will be almost constant. However, due to saliency effects in the machine the impedance will change with operation conditions. Thus it is expected that the magnitude and the phase of the measured impedance vector will show some modulation.

Figure 6.7 shows a block diagram of the signal processing. The measured three phase voltages and currents are sampled with 30 kHz and then directly combined in the time domain to the resulting stator voltage and current vectors ($\underline{v}_{\alpha\beta}$, $\underline{i}_{\alpha\beta}$). The $\alpha\beta$ components of the vectors are band pass filtered. The filters centre frequency is set to twice the PWM switching frequency (3.636 kHz). The width of the pass band needs

to be carefully selected. The band pass filter removes unwanted frequency components and reduces noise, but it also determined the maximum frequency of the detectable saliency signal modulation. In this implmentation a band width of 400 Hz is used for the pass band. The band pass filtered signals are demodulated by a heterodyning technique. The high frequency signals are directly multiplied by a f_{PWM2} sine reference signal [6]. The phase of the f_{PWM2} multiplication signal is adjusted manually. The adjusted phase shift compensates for the transducer delay and the approximate 90° phase shift in the current high frequency signal due to the predominantly inductive impedance. Therefore the resulting $\underline{z}'_{PWM2}$ vector does not describe the real machine impedance, since the phase information is manipulated due to the "rectification" process in the demodulation of $\underline{v}'_{PWM2}$ and $\underline{i}'_{PWM2}$. In the online implementation, the demodulation $\sin(2\pi f_{PWM2})$ signal is stored in a look up table inside the DSP control system. In the next stage the HF carrier frequency component, which has been converted to $2f_{PWM2}$, is removed by a discrete average filter. After exactly N HF signal periods the average of all samples is calculated. The average of the N carrier periods of the used averaging window will be zero. This means that running this algorithm every PWM period, the samples to be averaged contain exactly four $2f_{PWM2}$ signal periods, which will be completely removed. This forms a FIR filter with fixed small delay, which is the duration of the discrete down sampling. Therefore running this average filter every PWM period gives only one PWM period time delay in the position estimation information. The demodulated signals are then combined again to retrieve the vector modulation information. The final HF equivalent impedance vector $\underline{z}'_{PWM2}$ is calculated by the complex vector division (6.19) directly in the $\alpha\beta$ frame.

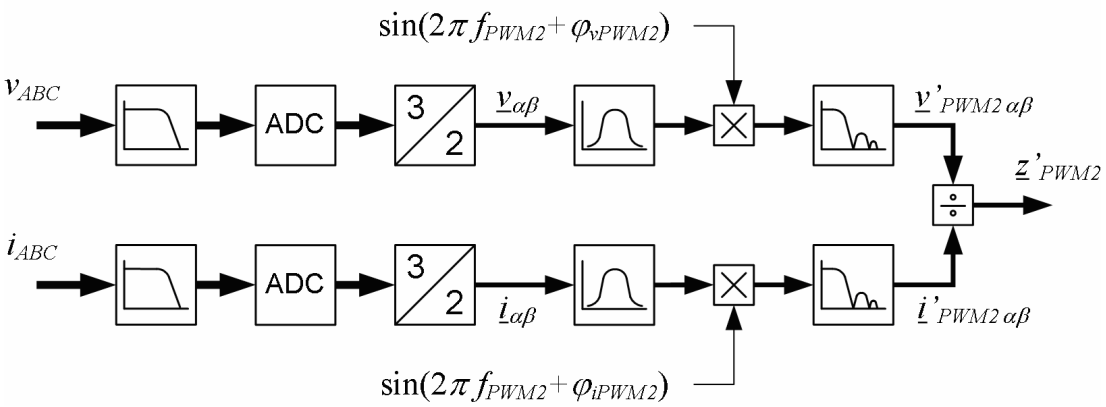

Figure 6.7: Block diagram of PWM2 signal demodulation

6.2 Experimental Implementation

For the experimental validation the standard of-the-shelf induction machine introduced in section 4.6 is used. All three phase voltages and currents are measured. The currents are measured with standard hall effect current transducers [69] used for the fundamental control of the machine. For the voltage measurement commercial differential probes [70] are used. The transducer signals are directly fed to the analogue inputs of the DSK periphery board introduces in section 4.2.

Figure 6.8 shows the configuration of the 4th order low pass filter (Bessel), implemented with two active multiple feedback (MFB) circuit stages in the analogue inputs. The cut off frequency is set to approximately 10 kHz. The operational amplifiers are OPA228 IC's [64] from Texas Instruments. The software TINA [90] from Texas Instruments is used to simulate the filter circuit shown in Figure 6.8.

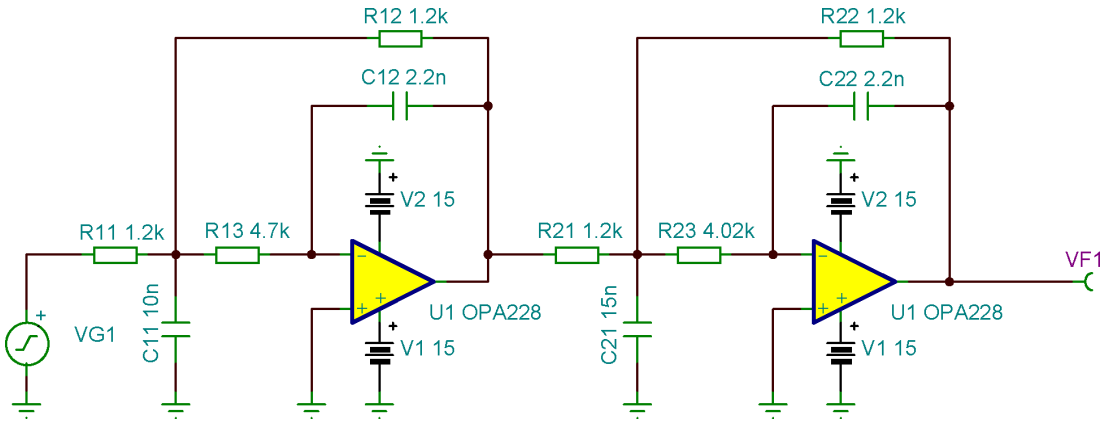

Figure 6.8: Schematic of anti aliasing filter

Figure 6.9 shows the filter characteristic plotted over the linear frequency. It can be seen that low frequency signals pass with low attenuation and small phase shift, while at higher frequencies stronger signal attenuation with increasing phase shift occurs.

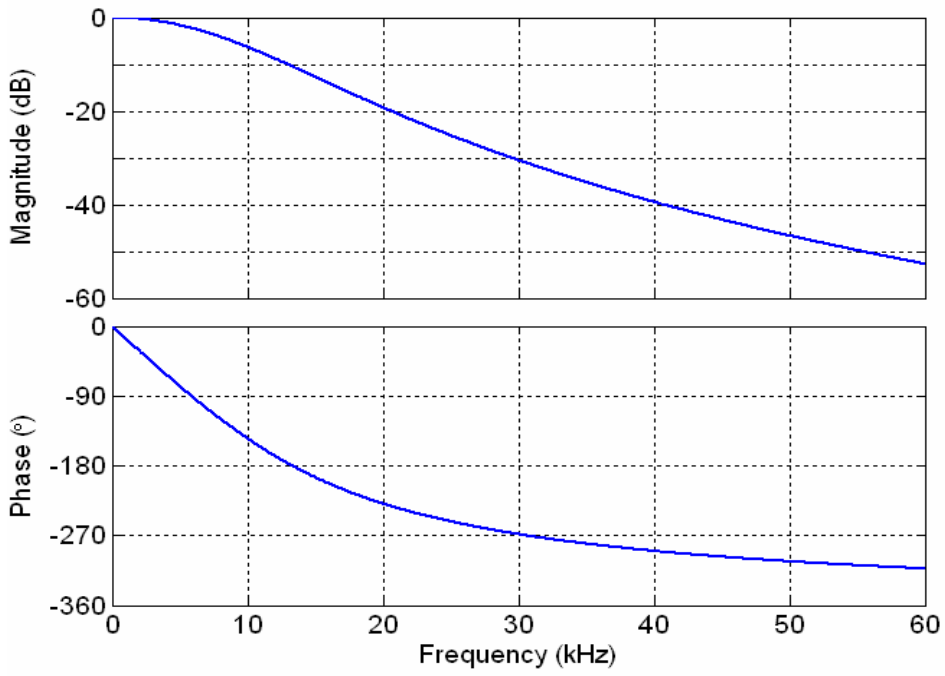

Figure 6.9: Characteristic of anti aliasing filter

The filtering of the PWM harmonics is demonstrated in Figure 6.10. The induction machine is run in sensored IRFO vector control to provide rated torque (i_d^* = 7.6 A, i_q^* = 12.5 A) and the speed is controlled by the coupled DC drive. The PWM switching frequency is set to 1.818 kHz and all voltage and current signals are sampled. The sampling frequency is set to 60 kHz for demonstration purpose, which is the maximum possible sampling frequency under sensored operation. The figure shows in plot (a) the measured rotor position λ_R and the resulting rotor flux position λ_{dq} used for the vector control, plot (b) shows the $\alpha\beta$ voltage vector components and plot (c) shows the resulting $\alpha\beta$ current vector components. As can be seen, under rated current condition the slip frequency of the induction machine is approximately 1.7 Hz electrical. From the plotted voltages and currents it can be seen that ripple due to the PMW switching are present in the drive. This is in particular pronounced in the voltages. However the effect of the analogue low pass filter can be seen. Without any low pass filtering the voltage signal would just show signal levels of the discrete inverter output space vectors. The low pass filter reduces the very high switching harmonics and a sinusoidal envelope is visible.

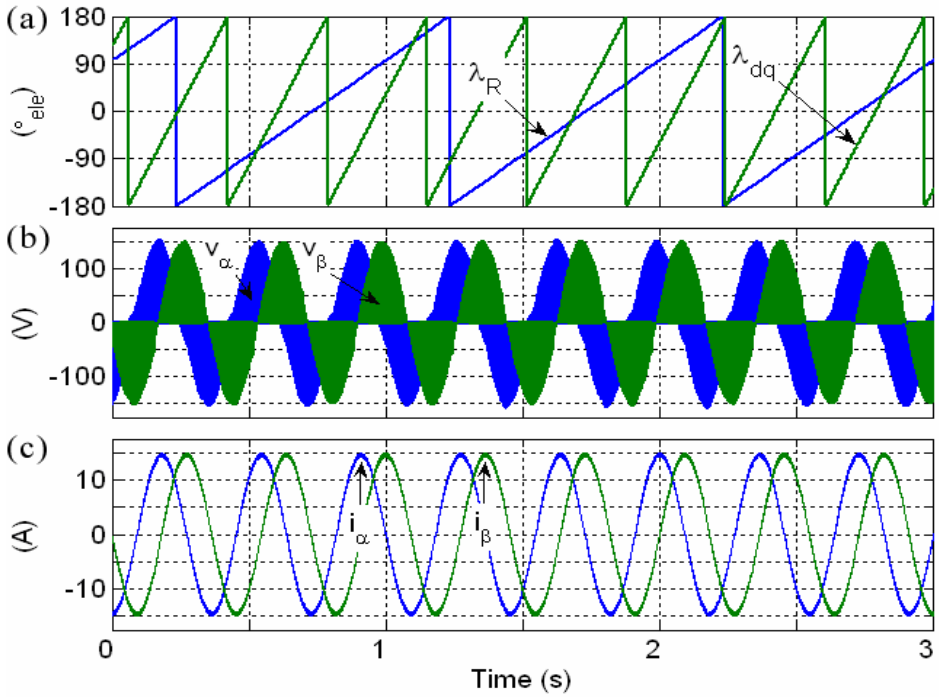

Figure 6.10: Test machine run with f_{PWM} = 1.818 kHz at f_R = 1 Hz electrical and rated current

Figure 6.11 shows the resulting FFT spectrum of the voltage vector $v_{\alpha\beta}$ (a) and current vector $i_{\alpha\beta}$ (b). It can be seen that the 2nd PWM frequency component in the positive and negative spectrum are the strongest PWM carrier harmonics in both plots. It can be seen in the voltage spectrum that this harmonic components shows a strength even greater then the generated fundamental machine voltage (peak at f_e = 2.7 Hz). The PWM2 harmonic peaks in the spectra are in fact not exactly at double the PWM frequency (3636.3 Hz), but shifted by +2.7 Hz which is the electrical frequency. Therefore the second PWM harmonic in the negativ spectrum is at 3633.7 Hz and the second PWM harmonic in the positive spectrum is at 3639.1 Hz. This confirms the derivation, that the 2nd PWM harmonic can be regarded as pulsating vector rotating at f_e.

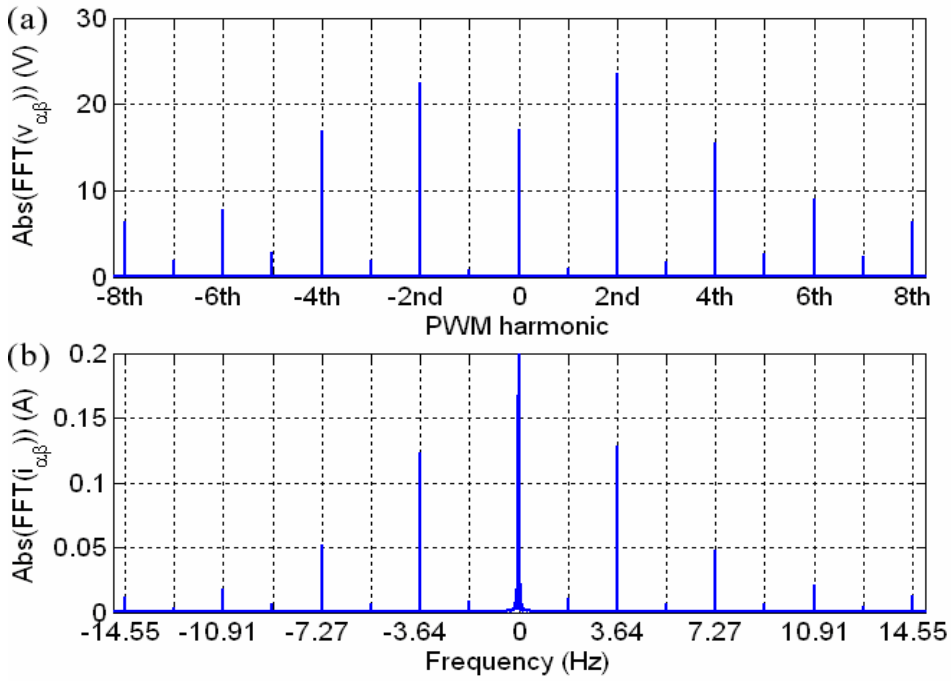

Figure 6.11: Spectrum of voltage and current vector with f_s = 60 kHz

For the practical implementation of the sensorless algorithm it was not possible to run the signal demodulation with a cycle frequency as high as 60 kHz. Therefore for the final implementation the analogue signal sampling is reduced to 30 kHz. Figure 6.12 shows the spectrum of the same voltage and current vectors sampled at only 30 kHz. At 30 kHz sampling frequency exactly 16.5 samples are made over each PWM period. Due to the lower sampling frequency the Nyquist frequency is only 15 kHz. As can be seen the attenuation of the analogue low pass filter at 15 kHz is only approximately -13 dB. That means that higher frequency components are not completely filtered off and aliasing effects occur. This is also visible in Figure 6.12. Looking closely at the voltage spectrum, it can be seen that there are additional frequency components between the original PWM harmonics peaks. These frequency components are aliased frequencies arising from PWM harmonics higher then the Nyquist frequency. The ratio of a 16.5 higher sampling frequency is selected on purpose to separate the aliasing frequency components from the original PWM harmonics. With the used sampling frequency/ PWM frequency ratio the aliasing

frequencies are exactly in the middle between two original PWM harmonics. Thus the distance between the original PWM harmonics and the aliasing frequencies is maximised. As explained in this work only the 2nd PWM harmonics are used. Therefore the aliasing effects of the 14th and 15th PWM harmonics are particular concerning since they are adjacent to the used 2nd PWM harmonics. These frequencies are indicated in Figure 6.12. However due to the sampling frequency/ PWM frequency ratio the distance between these frequencies is half the PWM frequency, i.e. 909.09 Hz.

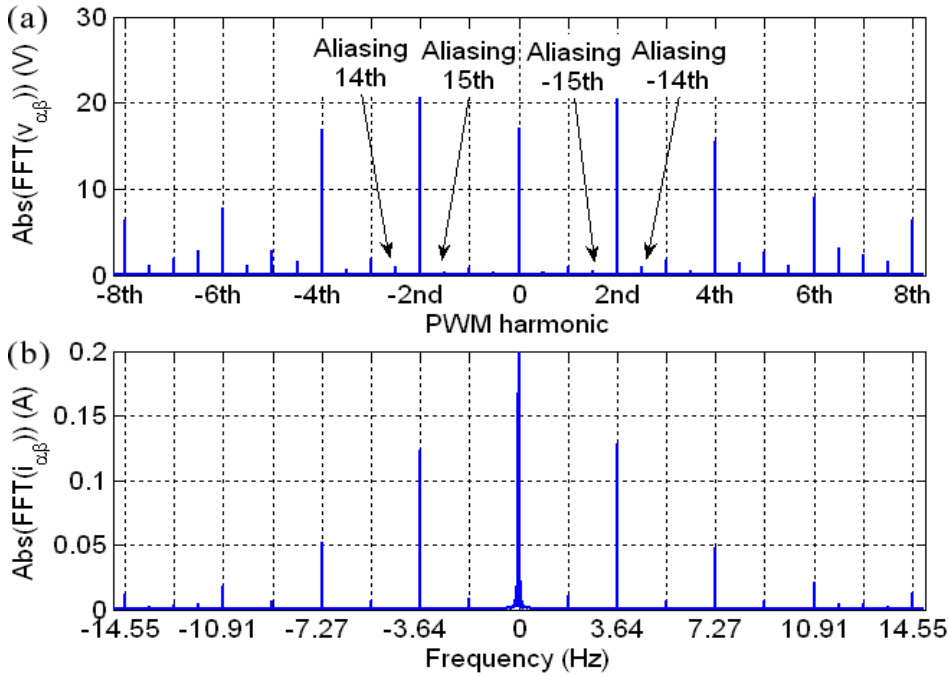

Figure 6.12: Spectrum of voltage and current vector with f_s = 30 kHz

As indicated in the signal processing block diagram of Figure 6.7, the discretised voltage and current signals are further band pass filtered digitally. The $\alpha\beta$ vector components are passed through a 4th order (Butterworth) IIR filter as shown in Figure 6.7. This filtering selects in particular the desired positive and negative 2nd PWM harmonic. Therefore the modulated information in the positive and negative 2nd PWM harmonic is used for the demodulation. The filter centre frequency is

therefore set to 3.636 kHz and the band width is set to 400 Hz. Therefore the sidebands up to +/- 200 Hz from the positive and negative 2nd PWM frequency are considered in the demodulation. Figure 6.13 shows the characteristic of this discrete band pass filter. Plot (a) shows the output signal magnitude and plot (b) shows the resulting filter phase shift. It can be seen that there is no attenuation at the PWM2 frequency. Further it can be seen that the phase shift at this frequency is zero. Therefore no addition filter delay occurs to the f_{PWM2} signal, apart from one discrete sample time of 33.3 µs. At 2727.3 kHz and 4545.5 kHz the attenuation is approximately -25 dB. Therefore aliasing frequencies adjacent to the f_{PWM2} frequency should be further reduced by approximately 95%.

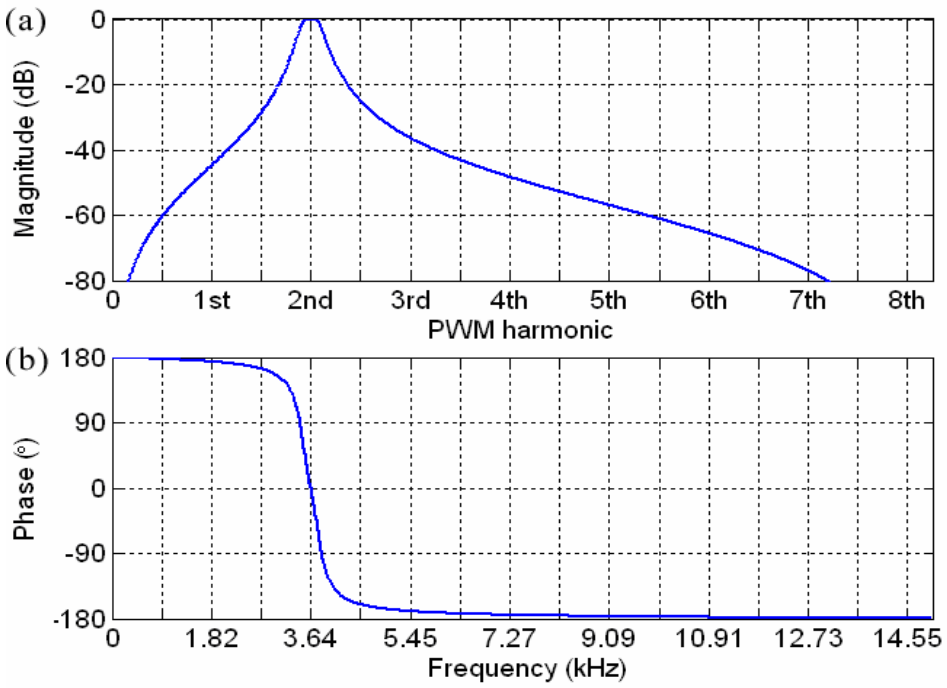

Figure 6.13: Characteristic of discrete band pass filter

Figure 6.14 shows the voltage spectrum (a) and current spectrum (b) for the $\alpha\beta$ vectors of Figure 6.10 after they have passed through the band pass filter. It can be seen that only the desired f_{PWM2} frequency remains. It can be assumed that all other frequencies are reduced to values that will not cause significant disturbances to the

signal demodulation. Comparing Figure 6.14 to 6.11 shows that the f_{PWM2} signals still have the same amplitudes. In these figures the voltage magnitude $|\underline{v}'_{PWM2}|$ is 2 x 23.6 V and the $|\underline{i}'_{PWM2}|$ signal is 2 x 128.2 mA. Therefore under this machine operating condition the average stator winding impedance at 3.636 kHz is 184 V/A. The desired machine impedance modulation occurs as small side bands of the 2nd PWM current harmonics.

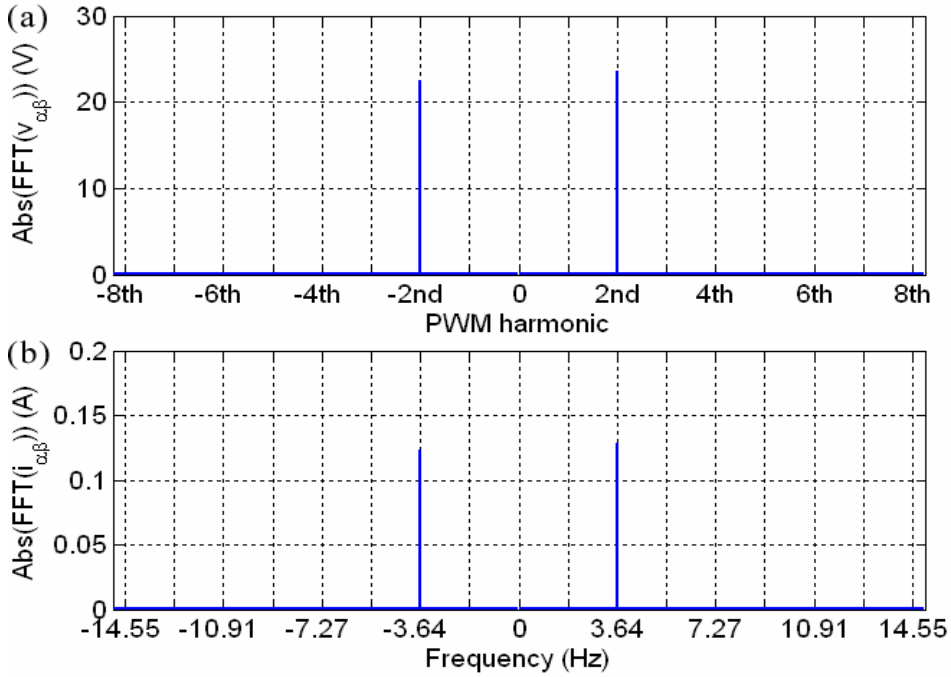

Figure 6.14: Voltage and current spectrum after band pass filter

The filtered signals are then multiplied with a $\sin(2\pi f_{PWM2})$ reference signal as shown in Figure 6.7. To remove the high frequency component the discrete average filter at the end of the signal demodulation process, shown in Figure 6.7, calculates the average over the samples of two PWM periods. Therefore the average is calculated over the last 33 samples. Figure 6.15 shows the characteristic of the implemented discrete average filter. Plot (a) shows the filter signal magnitude and plot (b) displays the output phase shift. It can be clearly seen from the magnitude plot that all multiple frequencies of 909.09 Hz are completely removed. Therefore all carried frequency

components and aliasing frequencies should be reduced to a minimum and not influence the final demodulated signal.

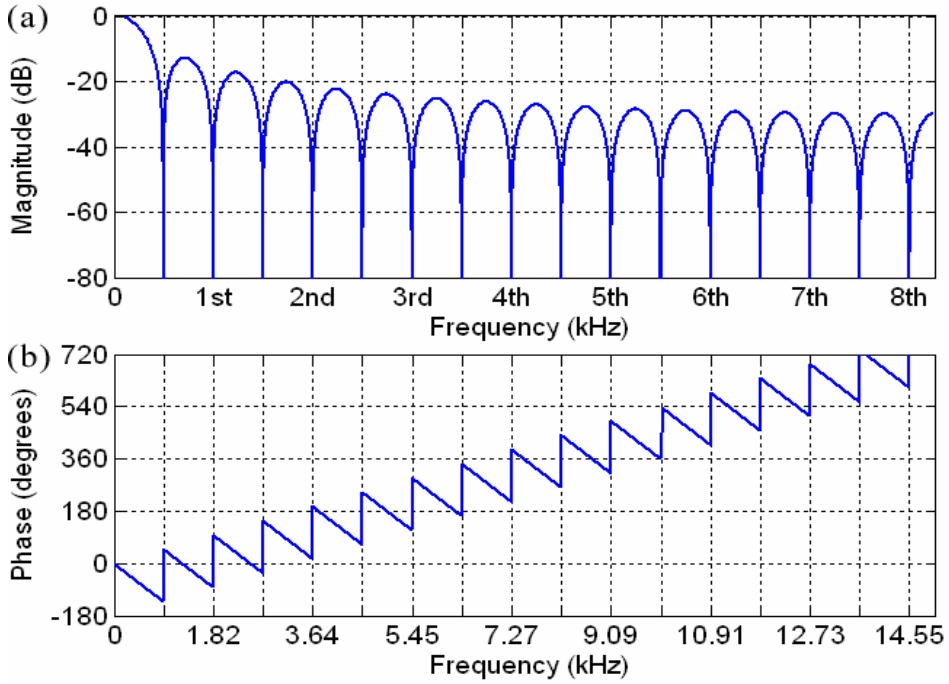

Figure 6.15: Characteristic of average filter for PWM2 voltage and current demodulation

Since the averaging for the high frequency removal is performed over 33 samples, the demodulation result is updated every 2nd PWM cycle and the final cycle frequency of the sensorless algorithm is 909.09 Hz. Due to this down sampling a discrete delay of 1.1 ms occurs. This is in fact the major delay of the sensorless position estimation, as the previously shown filter delays are very small. Therefore the resulting position estimation delay will be less then 2 mechanical degrees up to 300 rpm, which is the maximum tested motor speed. The focus in this work is only on the zero and low speed region since for higher speed operation well established sensorless techniques exist as explained in section 3.1.

6.3 Variation of Measured Impedance due to Rotor Bar Slotting

6.3.1 Theoretical Analysis

In this work the objective is to detect the permanence modulation due to the aluminium or copper conductor bars embedded in the rotor of the machine. The impedance of the stator windings at high frequency is dominantly determined by the inductance of the machine. As shown in section 3.2.1 the inductance is affected by the magnetic permeability of the flux path. The iron of the rotor has a different permeability than the aluminium or copper of the rotor bars. Therefore the total permeability of the flux path per stator coil will change slightly dependent on the position of the rotor bars. It is expected that the measured equivalent impedance is almost constant. However it is assumed that the rotor bar slotting causes an impedance modulation $\Delta Z'_{RB}$ (6.20). The assumed equivalent impedance tensor $\mathbf{Z'}$ in the $\alpha\beta$ stator frame is stated by (6.21) [5], [6]. The angle λ_{RB} is the rotor bar position within one rotor bar period. The resulting voltage equation system for the PWM2 harmonic is shown by equation (6.22). Equation (6.22) describes the relationship between the high frequency voltage vector $\underline{v}'_{PWM2\alpha\beta}$ and current vector $\underline{i}'_{PWM2\,\alpha\beta}$, which is defined by the modulated high frequency equivalent impedance tensor $\mathbf{Z'}_{\alpha\beta}$ of the stator windings.

$$\mathbf{Z}' = \mathbf{Z}'_{Offset} + \Delta\mathbf{Z}'_{RB} \tag{6.20}$$

$$\mathbf{Z}'_{\alpha\beta} = \begin{bmatrix} Z' & 0 \\ 0 & Z' \end{bmatrix} + \begin{bmatrix} -\Delta Z'_{RB}\cos(\lambda_{RB}) & \Delta Z'_{RB}\sin(\lambda_{RB}) \\ \Delta Z'_{RB}\sin(\lambda_{RB}) & \Delta Z'_{RB}\cos(\lambda_{RB}) \end{bmatrix} \tag{6.21}$$

$$\begin{bmatrix} v'_{PWM2\alpha} \\ v'_{PWM2\beta} \end{bmatrix} = \begin{bmatrix} Z' - \Delta Z' \cos(\lambda_{RB}) & \Delta Z' \sin(\lambda_{RB}) \\ \Delta Z' \sin(\lambda_{RB}) & Z' + \Delta Z' \cos(\lambda_{RB}) \end{bmatrix} \cdot \begin{bmatrix} i'_{PWM2\alpha} \\ i'_{PWM2\beta} \end{bmatrix} \tag{6.22}$$

Figure 6.16 visualizes the normalised equivalent impedance modulation for several rotor bar positions. The 2nd PWM harmonic voltage and current vectors $\underline{v}'_{PWM2}$ and $\underline{i}'_{PWM2}$ are shown for the condition that $\angle \underline{v}'_{PWM2}$ is fixed to be constant at 45 ° electrical as measured in the stator $\alpha\beta$ frame. The "injected" pulsating HF voltage vector $\underline{v}'_{PWM2}$ (blue vector) rotates with the fundamental frequency. In steady state the amplitude of this vector is approximately constant and the locus is almost circular in the $\alpha\beta$ frame (blue dashed line). The resulting HF current vector $\underline{i}'_{PWM2}$ (red vector) follows the imposed voltage vector. However, due to the impedance variation in the machine windings the current vector locus will be slightly different as indicated by the oval shape (red dashed line). The difference between the HF voltage and current vector is proportional to the impedance modulation $\Delta Z'_{RB}$ (green vectors). The measured equivalent impedance modulation is shown in the drawings for different positions of the PWM2 vectors in the $\alpha\beta$ frame (grey circles). The oval $\underline{i}'_{PWM2}$ locus will rotate by 180 °$_{ele}$ per rotor bar period (360 °$_{RB}$).

Impedance defines the voltage drop caused by a certain current. Thus, by using the measured impedance, the PWM2 current can be regarded as the HF excitation signal and the PWM2 voltage as the response. Therefore in the drawings the equivalent impedance vector modulation points from the PWM2 current vector $\underline{i}'_{PWM2}$ to the PWM2 voltage vector $\underline{v}'_{PWM2}$. In should be noted here that the same analysis can also be done by using the admittance of the machine which is $\underline{i}'_{PWM2}$ over $\underline{v}'_{PWM2}$. The admittance describes the resulting current caused by a particular voltage excitation. Therefore if considering the admittance, the admittance vector modulation would point from the voltage vector to the current vector.

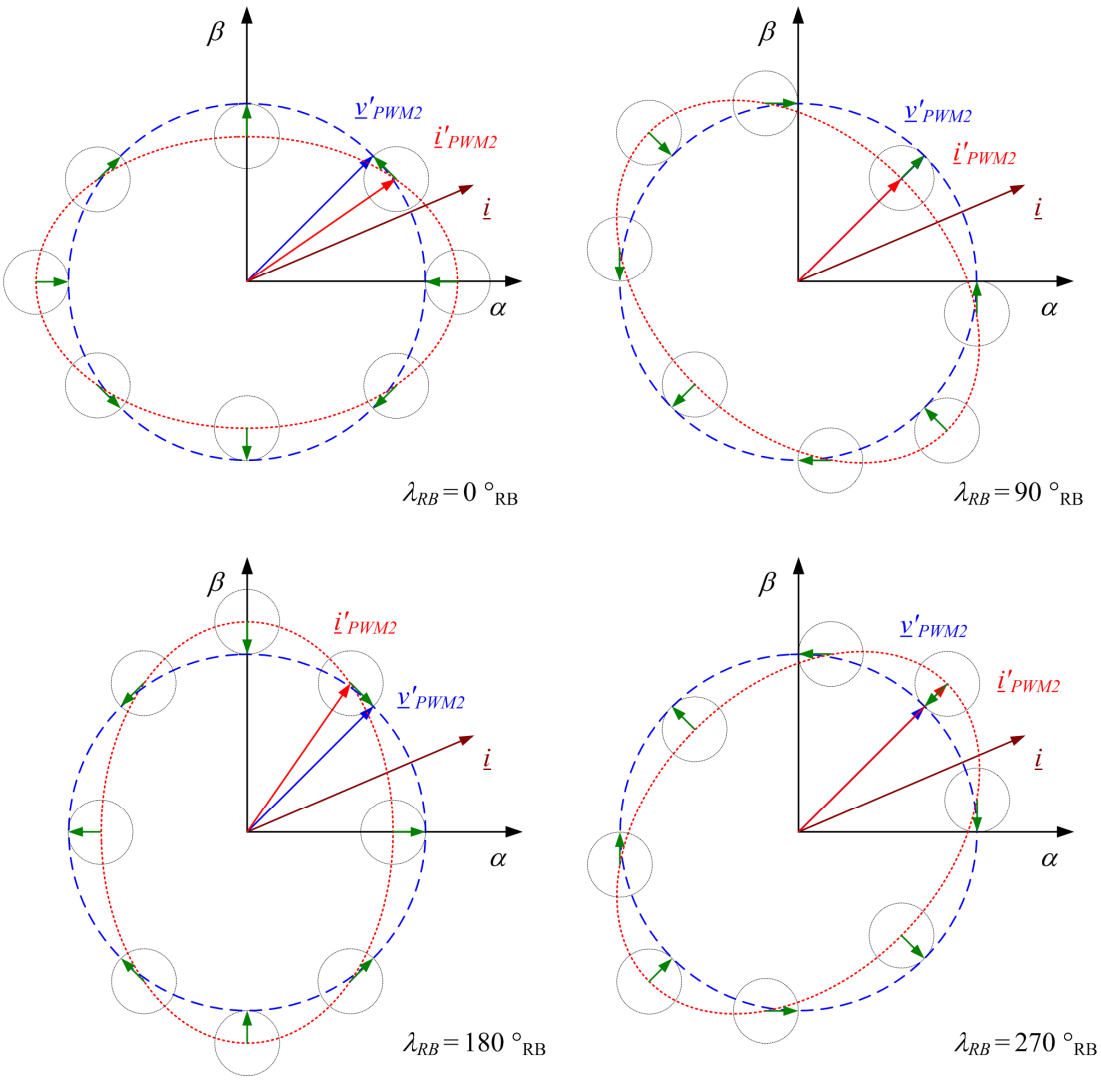

Figure 6.16: Detected machine impedance with $\underline{v}'_{PWM2}$ and $\underline{i}'_{PWM2}$ dependent on rotor bar position λ_{RB}

It can be noticed from Figure 6.16, that also an additional rotation occurs in the $\Delta Z'_{RB}$ impedance modulation, depending on the position of the PWM2 vector positions in the stator $\alpha\beta$ frame. The additional modulation is explained by equation (6.23). The vector division applies a transformation of the measured impedance into the $\underline{i}'_{PWM2}$ vector position defined xy reference frame. The definition of the $\underline{i}'_{PWM2}$ vector xy reference frame is shown in Figure 6.17.

$$
\begin{aligned}
\underline{z}'_{PWM2} &= \frac{\underline{v}'_{PWM2\alpha\beta}}{\underline{i}'_{PWM2\alpha\beta}} \\
&= \frac{\left|\underline{v}'_{PWM2}\right|}{\left|\underline{i}'_{PWM2}\right|} e^{j\angle \underline{v}'_{PWM2\alpha\beta}} \underbrace{e^{-j\angle \underline{i}'_{PWM2\alpha\beta}}}_{\substack{xy\ frame \\ transformation}} \\
&= \frac{\left|\underline{v}'_{PWM2}\right| e^{j\angle \underline{v}'_{PWM2xy}}}{\left|\underline{i}'_{PWM2}\right|} \\
&= \frac{\underline{v}'_{PWM2xy}}{\underline{i}'_{PWM2xy}}
\end{aligned}
\tag{6.23}
$$

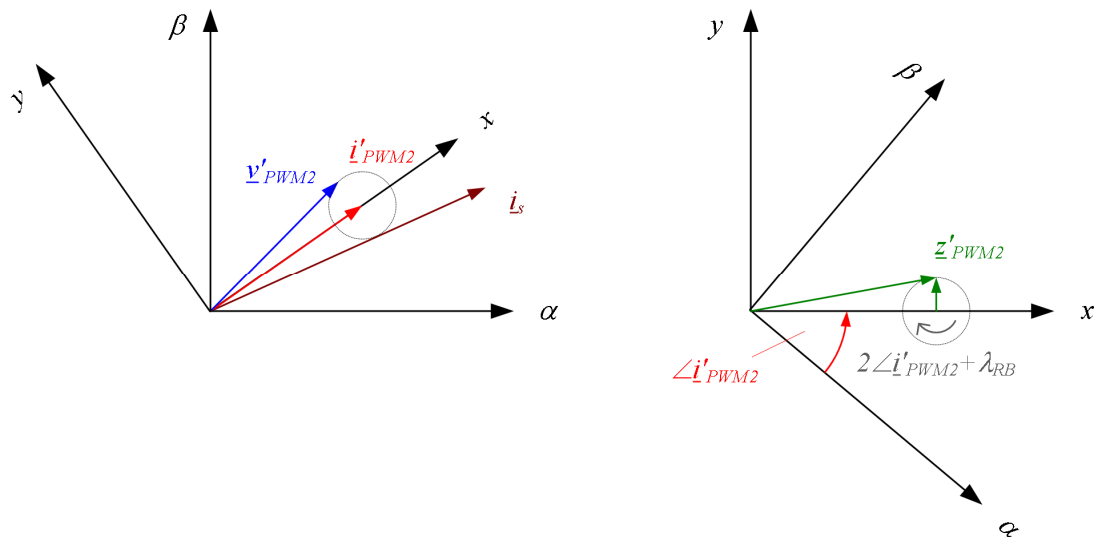

Figure 6.17: $\underline{v}'_{PWM2}$, $\underline{i}'_{PWM2}$ and the resulting HF impedance vector $\underline{z}'_{PWM2}$ in $\alpha\beta$ and xy reference frame

The 2nd PWM harmonic creates a pulsating HF vector with varying position in the $\alpha\beta$ frame. Therefore the detected impedance $\underline{z}'_{PWM2}$ is referred to the xy measurement frame. The detected impedance in the xy frame is shown in equation (6.25) after applying the transformation matrix $\mathbf{B}_{\alpha\beta\rightarrow xy}$ (6.24).

$$\mathbf{B}_{\alpha\beta\to xy} = \begin{bmatrix} \cos\left(\angle \underline{i}'_{PWM2\alpha\beta}\right) & \sin\left(\angle \underline{i}'_{PWM2\alpha\beta}\right) \\ -\sin\left(\angle \underline{i}'_{PWM2\alpha\beta}\right) & \cos\left(\angle \underline{i}'_{PWM2\alpha\beta}\right) \end{bmatrix} \tag{6.24}$$

$$\begin{aligned} \mathbf{Z}'_{xy} &= \mathbf{B}_{\alpha\beta\to xy} \cdot \mathbf{Z}'_{\alpha\beta} \cdot \mathbf{B}^{T}_{\alpha\beta\to xy} \\ &= \begin{bmatrix} Z' - \Delta Z'_{RB} \cos\left(\lambda_{RB} + 2\angle \underline{i}'_{PWM2\alpha\beta}\right) & \Delta Z'_{RB} \sin\left(\lambda_{RB} + 2\angle \underline{i}'_{PWM2\alpha\beta}\right) \\ \Delta Z'_{RB} \sin\left(\lambda_{RB} + 2\angle \underline{i}'_{PWM2\alpha\beta}\right) & Z' + \Delta Z'_{RB} \cos\left(\lambda_{RB} + 2\angle \underline{i}'_{PWM2\alpha\beta}\right) \end{bmatrix} \end{aligned} \tag{6.25}$$

The resulting voltage equation system in the *xy* frame is given by equation (6.26), which yields equation (6.27) for the applied complex vector division.

$$\begin{bmatrix} v'_{PWM2x} \\ v'_{PWM2y} \end{bmatrix} = \begin{bmatrix} Z' - \Delta Z'_{RB} \cos\left(\lambda_{RB} + 2\angle \underline{i}'_{PWM2\alpha\beta}\right) & \Delta Z'_{RB} \sin\left(\lambda_{RB} + 2\angle \underline{i}'_{PWM2\alpha\beta}\right) \\ \Delta Z'_{RB} \sin\left(\lambda_{RB} + 2\angle \underline{i}'_{PWM2\alpha\beta}\right) & Z' + \Delta Z'_{RB} \cos\left(\lambda_{RB} + 2\angle \underline{i}'_{PWM2\alpha\beta}\right) \end{bmatrix} \cdot \begin{bmatrix} \left|\underline{i}'_{PWM2}\right| \\ 0 \end{bmatrix} \tag{6.26}$$

$$\begin{aligned} \underline{z}'_{PWM2} &= \frac{\underline{v}'_{PWM2xy}}{\underline{i}'_{PWM2xy}} \\ &= \frac{v'_{PWM2x}}{\left|\underline{i}'_{PWM2}\right|} + j\frac{v'_{PWM2y}}{\left|\underline{i}'_{PWM2}\right|} \\ &= Z' - \Delta Z'_{RB} \cos\left(\lambda_{RB} + 2\angle \underline{i}'_{PWM2\alpha\beta}\right) + j\Delta Z'_{RB} \sin\left(\lambda_{RB} + 2\angle \underline{i}'_{PWM2\alpha\beta}\right) \end{aligned} \tag{6.27}$$

The result of the complex vector division gives an impedance vector with an offset Z' and a circular modulation with the radius $\Delta Z'_{RB}$ rotating backwards with an instantaneous angle of $\lambda_{RB}+2\angle \underline{i}'_{PWM2\,\alpha\beta}$. The additional $2\angle \underline{i}'_{PWM2\,\alpha\beta}$ phase modulation is known since the HF current vector $\underline{i}'_{PWM2\,\alpha\beta}$ is directly measured and can therefore be easily removed. Figure 6.18 shows the block diagram of the system proposed for the rotor bar position construction. From the estimated rotor bar position, a rotor

position and speed estimate can be derived as illustrated in the block diagram of Figure 6.19. From the modulation frequency of the 16 rotor bars per pole pair a rotor speed estimate ω_R^e is derived, which when integrated, gives the estimated rotor position λ_R^e. For a smoother speed signal feedback the filtered estimated speed $\omega_R^e{}_F$ is provided.

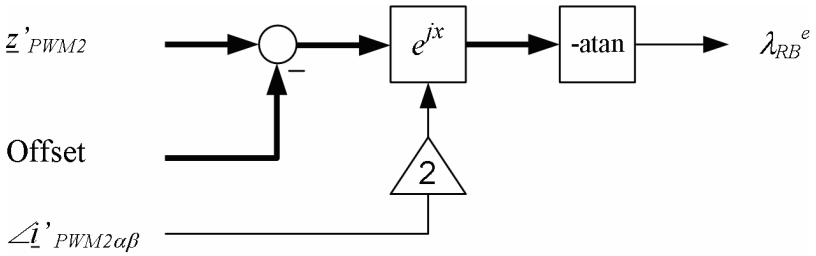

Figure 6.18: Principal reconstruction of the rotor bar position

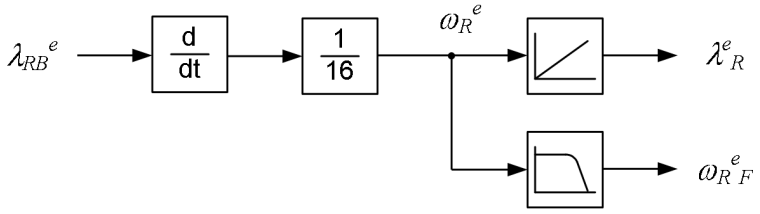

Figure 6.19: Block diagram of possible rotor position and speed reconstruction from estimated rotor bar position

The above shown theoretical explanation considers only the saliency modulation due to rotor bar slotting. In practical induction machines saturation saliency also occurs. The saturation in the machine is rotating with the stator current vector $i_{\alpha\beta}$ at the fundamental frequency. Since the $\underline{v}'_{PWM2\alpha\beta}$ and $\underline{i}'_{PWM2\alpha\beta}$ vectors are also rotating with the fundamental frequency it can be assumed that the saturation effect is static under steady state operation, resulting only in an offset in the measured equivalent impedance. Therefore the saturation saliency affects only the total offset value and can be included into the offset compensation as shown in Figure 6.18.

6.3.2 Impedance Modulation due to Rotor Bar Slotting as Measured on the Experimental System

In the experiment described below the general effect of rotor bar slotting modulation on the measured $\underline{z}'_{PWM2}$ equivalent impedance is tested. For this purpose the vector controller for the induction motor is set to maintain a fixed DC current vector of rated amplitude in the $\alpha\beta$ frame. The coupled DC machine is moving the rotor with constant reverse speed (-52 rpm), equal to the slip frequency (1.73 Hz electrical). Therefore, this condition emulates the operating point where the drive is operating at zero excitation frequency and non-zero rotor speed. The purpose of this experiment is to acquire an equivalent impedance vector measurement that is only affected by modulation due to the mechanical rotor position. Since the current is DC it is assumed that $\angle\underline{i}'_{PWM2\alpha\beta}$ is constant and no further modulation due to the $\underline{i}'_{PWM2\alpha\beta}$ vector position occurs in the measured $\underline{z}'_{PWM2}$. Figure 6.20 shows the resulting experimental data plotted over time. Plot (a) shows the rotor and rotor flux position λ_R and λ_{dq}, plot (b) shows the machine currents i_α and i_β, plot (c) shows the demodulated PWM2 harmonic voltage vector components $v'_{PWM2\alpha}$ and $v'_{PWM2\beta}$, plot (d) shows the demodulated PWM2 harmonic current vector components $i'_{PWM2\alpha}$ and $i'_{PWM2\beta}$ and plot (e) contains the measured equivalence impedance vector $\underline{z}'_{PWM2}$. All variables are sampled with 909.09 Hz.

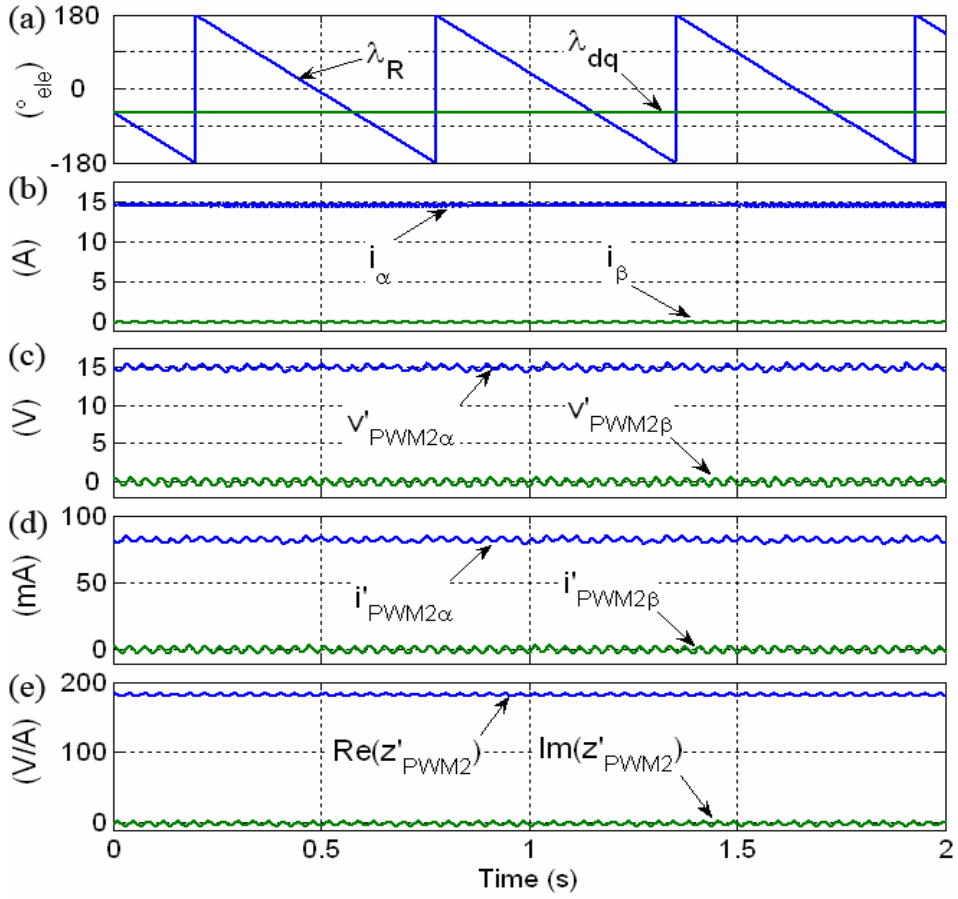

Figure 6.20: Induction machine with rated current (rated torque) at -52 rpm

Figure 6.21 shows the calculated $\underline{z}'_{PWM2}$ impedance vector for this experiment plotted over the measured electrical rotor position. Plot (a) shows the real part of $\underline{z}'_{PWM2}$ and plot (b) the imaginary part of $\underline{z}'_{PWM2}$. In both of the above plots one can observe a significant modulation pattern with 16 cycles over one complete electrical rotor revolution. This equivalent impedance variation is caused by the 16 rotor bar slots per pole pair of the machine. Although the modulation amplitude is only about 1.1 % of the average impedance vector magnitude the signal is quite clear. It should be pointed out here that a standard off-the-shelf induction machine with semi opened skewed rotor bars has been used. A particular feature of the modulation information is that there is a phase shift between the real and imaginary part of the PWM2 equivalent impedance vector modulation. Hence the complete modulation effect

forms a two dimensional locus. The tracking of this locus may allow not only a detection of how much the rotor bar position is changing, but also in what direction.

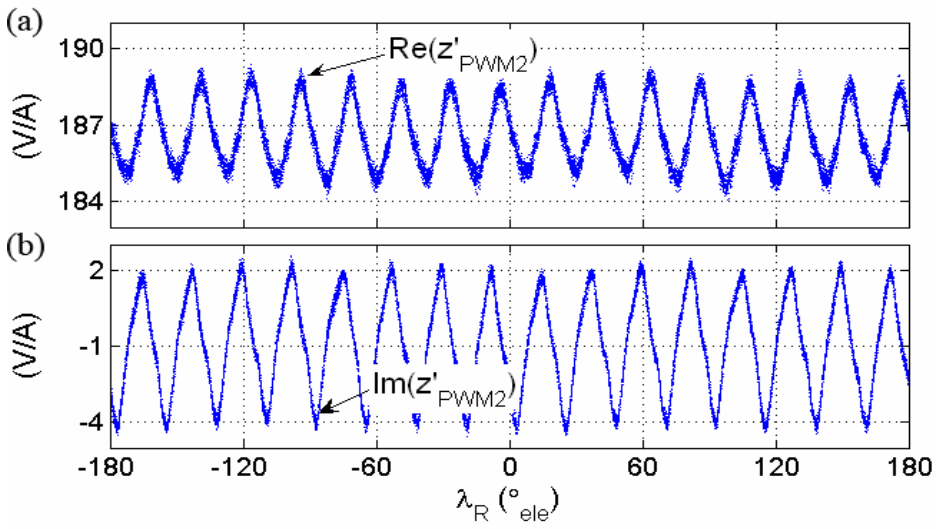

Figure 6.21: Measured equivalent impedance vector plotted over the rotor position λ_R

Figure 6.22 shows the measured $\underline{z}'_{PWM2}$ equivalence impedance vector modulation locus in the complex plane. As expected from the theoretical derivation, the equivalent impedance vector modulation is near to a circular shape.

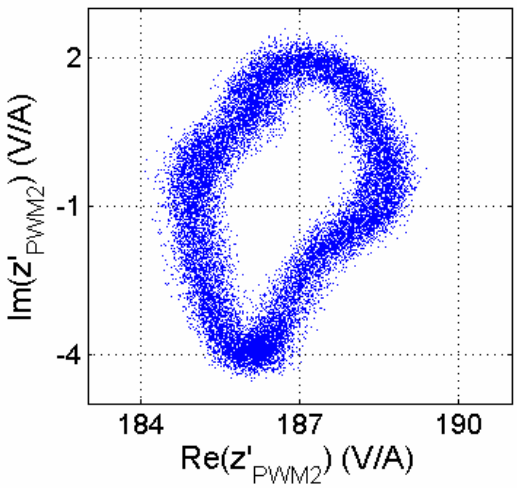

Figure 6.22: Rotor bar modulation locus of $\underline{z}'_{PWM2}$ in complex plane

In the next experiment the machine is operated under non-zero electrical frequency. The induction machine vector controller is set to rated current (i_d^* = 7.6 A and i_q^* = 12.5 A). The mechanical speed is set by the coupled DC machine to 30 rpm. Figure 6.23 shows the measured data over time. Plot (a) shows the rotor and rotor flux position λ_R and λ_{dq}, plot (b) shows the machine currents i_α and i_β, plot (c) shows the demodulated PWM2 voltage vector components $v'_{PWM2\alpha}$ and $v'_{PWM2\beta}$, plot (d) shows the demodulated PWM2 current vector components $i'_{PWM2\alpha}$ and $i'_{PWM2\beta}$, and plot (e) shows the measured equivalent impedance vector $\underline{z}'_{PWM2}$. All variables shown in Figure 6.23 are sampled with the demodulation frequency of 909.09 Hz.

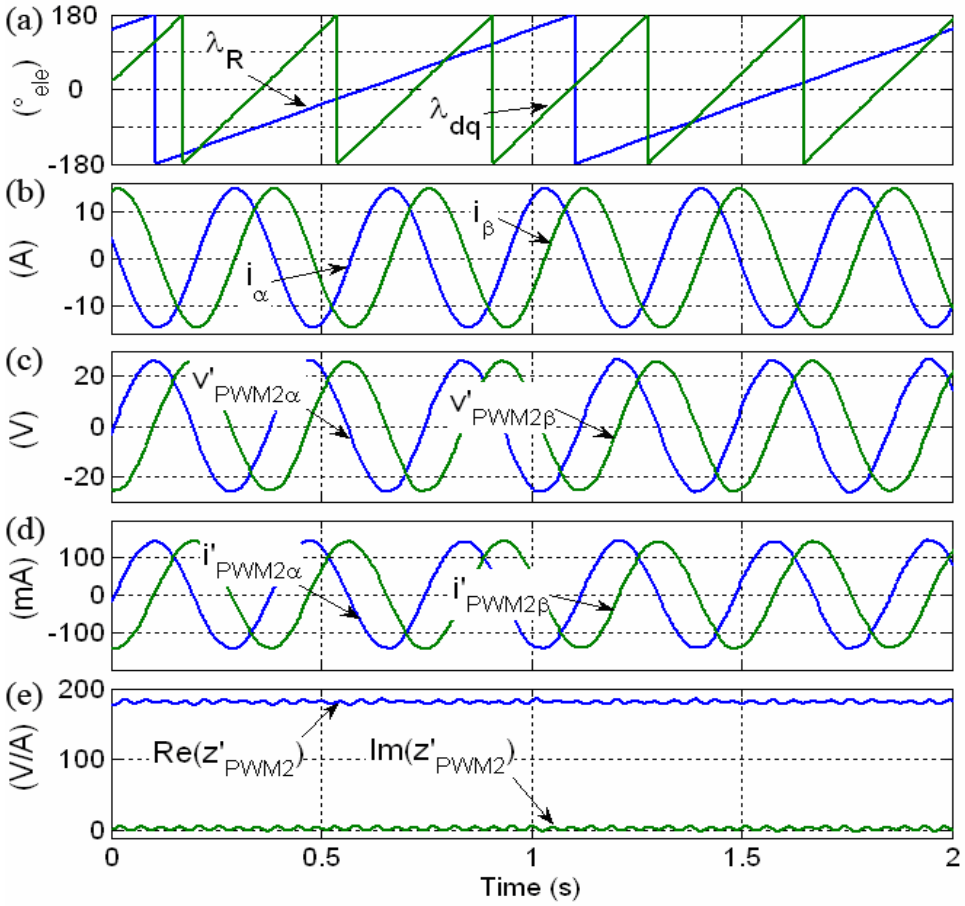

Figure 6.23: Induction machine running with rated torque at 30rpm

Since the electrical frequency is not zero in this experiment, i.e. $\underline{i}'_{PWM2}$ is moving in the $\alpha\beta$ frame, a further modulation depending on $\angle\underline{i}'_{PWM2\alpha\beta}$, additional to the rotor slotting modulation occurs. Figures 6.24 and 6.25 show the measured equivalent impedance saliency profile $\underline{z}'_{PWM2}$ as a function of $\angle\underline{i}'_{PWM2\alpha\beta}$ and the rotor position λ_R. The mechanical rotor position and the $\underline{i}'_{PWM2\alpha\beta}$ position are discretised by steps of 2° electrical and all data samples with the same position index are averaged. It can be seen that a sinusoidal modulation pattern of 16 periods is present which is due to the 16 rotor bars per electrical pole pair. A skew of two rotor bar modulation pattern periods as a function of $\angle\underline{i}'_{PWM2\alpha\beta}$ can be seen. This verifies the aforementioned influence of the rotating xy measurement frame relative to the stator equivalent impedance tensor in the $\alpha\beta$ frame. It can also be seen from Figure 6.25 that there is a small offset in the imaginary part of $\underline{z}'_{PWM2}$. This is due to the saturation effect on the measured equivalent impedance as mentioned before. The figures also show an additional modulation of six times the electrical frequency. This is assumed to be due to inverter non-linearity effects, for example dead time and zero crossing effects [6], [23].

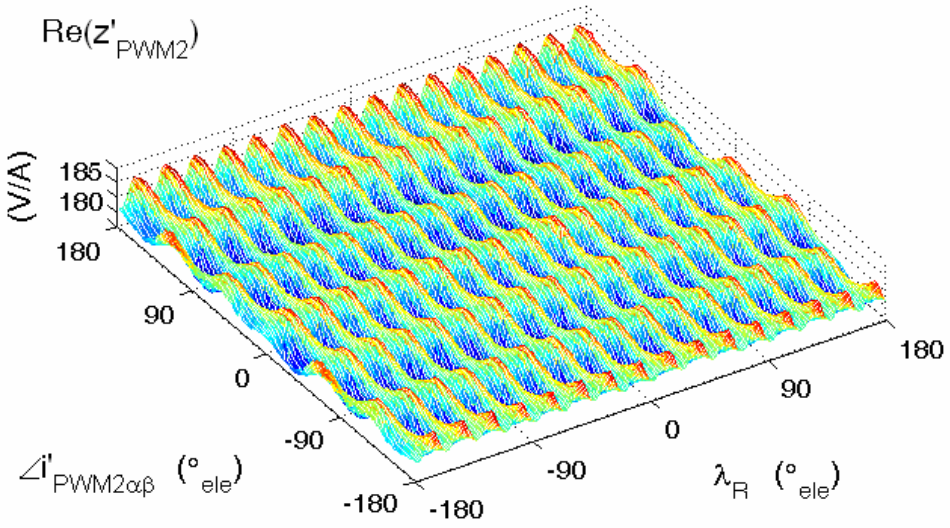

Figure 6.24: Real part of machine $\underline{z}'_{PWM2}$ saliency profile in dependency of rotor position λ_R and $\angle\underline{i}'_{PWM2\alpha\beta}$

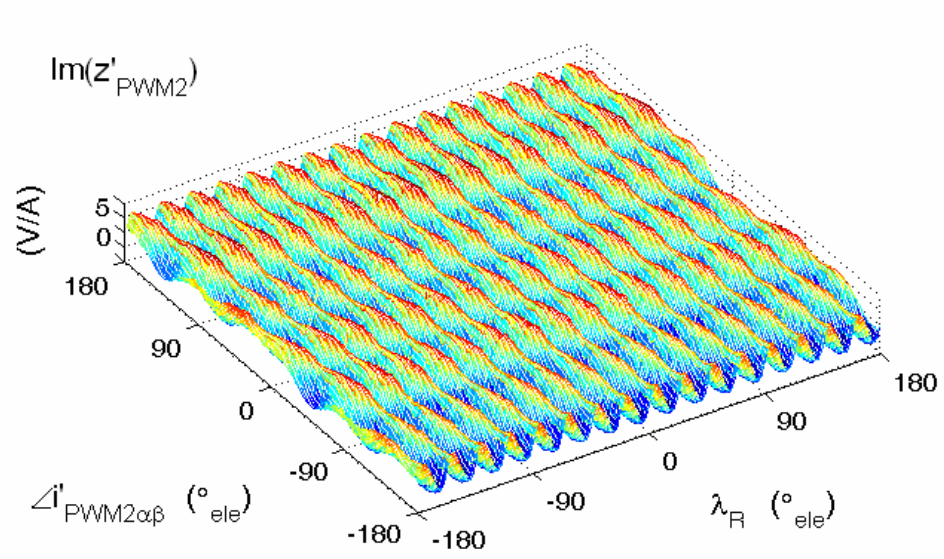

Figure 6.25: Imaginary part of machine $\underline{z}'_{PWM2}$ saliency profile dependency of rotor position λ_R and $\angle\underline{i}'_{PWM2\alpha\beta}$.

Figure 6.26 shows the offline estimated rotor position from the experimental data shown in Figure 6.23. The rotor position estimation algorithm shown in Figures 6.18 and 6.19 is used. For the offset compensation the mean of the measured $\underline{z}_{PWM2}$ equivalent impedance values is used. As can be seen in Figures 6.24 and 6.25, this is 181 V/A for the real part and 3 V/A for the imaginary part. In Figure 6.26 plot (a) shows the measured rotor position λ_R, plot (b) shows the measured equivalent impedance $\underline{z}_{PWM2}$ minus the used offset value and plot (c) shows the estimated rotor bar position λ_{RB} value within one rotor bar period. Plot (d) shows the final estimated rotor position λ_R^e and plot (e) shows the difference between the rotor position estimate and the real measured rotor position.

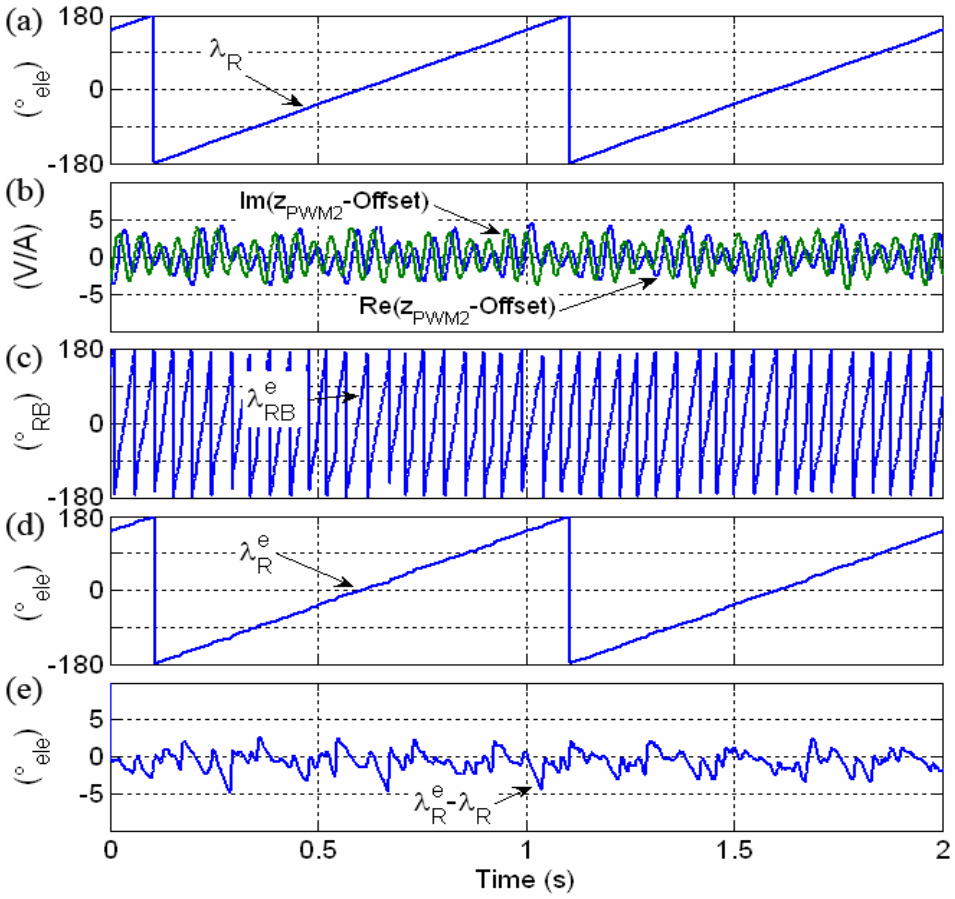

Figure 6.26: Induction machine running with rated torque at 30rpm

In Figure 6.26 it can be seen that it is possible to estimate the mechanical rotor position from the rotor bar modulation signal detected in the measured $\underline{z}_{PWM2}$ equivalent impedance. The estimated rotor position follows the measured rotor position and the estimation error is in the range of +/-5 electrical degrees. It should be noted that the rotor position can be only incremental measured and is derived from the detected rotor bar modulation signal. In Figure 6.26 the offset error is manually set to zero in order to illustrate the principle of the rotor position estimation.

6.3.3 Sensorless Control in the Steady State by Using Rotor Bar Slotting Impedance Modulation

Figure 6.27 shows results when the drive is operated in sensorless control mode using the proposed algorithm. The induction machine drive is operating in torque control and the DC machine is setting the speed to 30 rpm. The current reference values are set to rated values (i_d^* = 7.6 A and i_q^* = 12.5 A). Plot (a) shows the measured rotor position λ_R, plot (b) shows the estimated rotor bar position λ_{RB}^e, plot (c) shows the reconstructed rotor position λ_R^e, plot (d) shows the position estimation error λ_R^e - λ_R and plot (e) shows the estimated speed, filtered by 10 Hz low pass filter. The estimated rotor position is smoothed by a 30 Hz low pass filter and fed directly to the IRFO vector control system. The required $\underline{z}'_{PWM2}$ offset was measured in a prior experiment under sensored conditions. The rotor bar position is directly derived from the measured $\underline{z}'_{PWM2}$ as shown in Figure 6.18. The algorithm shown in Figure 6.19 is then used to reconstruct a mechanical rotor position estimate from the measured rotor bar position. Only incremental position can be measured but for vector torque and speed control this is not problematic, since the absolute rotor position is not required. In Figure 6.27 the offset error is manually set to zero in order to illustrate the principle of the rotor position estimation. Having a constant λ_R^e - λ_R shows the quality of the tracking here.

As can be seen, the position signal can be derived from the measured $\underline{z}'_{PWM2}$ equivalent impedance rotor bar modulation. The rotor position can then be reconstructed and shows a good estimate to the real position. The error may be due to noise in the measured PWM2 quantities and influences. However, in practice the rotor bar modulation is not expected to be ideally sinusoidal

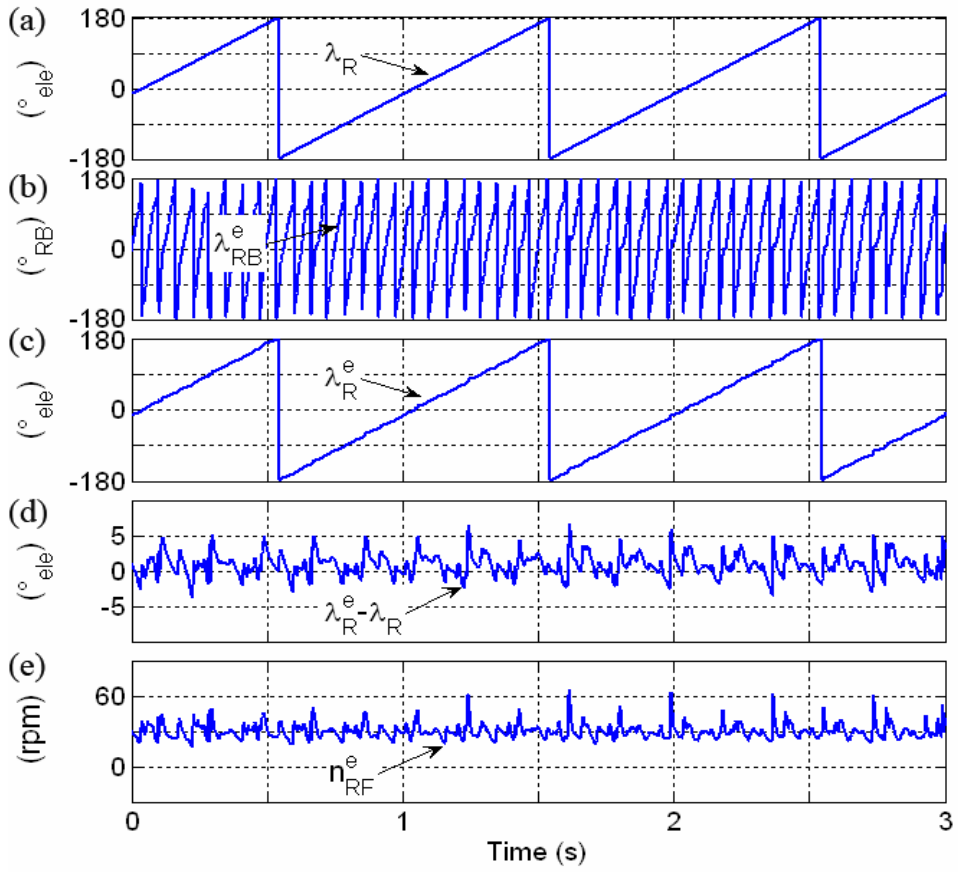

Figure 6.27: Sensorless control at steady at rated torque and 30 rpm

.

The shown results in Figure 6.27 consider only steady state operation with constant torque and speed. It was found that the $\underline{z}'_{PWM2}$ offset, which must be removed for the rotor bar modulation extraction, varies under varying operation conditions. This is due to the operation point dependent saturation effect in the machine. For the operation shown only a single value for the offset compensation is used and this was determined beforehand for one particular steady state operation point. If the $\underline{z}'_{PWM2}$ offset can be described as function of directly known quantities, the required compensation value can be generated for each independent operation point and sensorless control under dynamic operation can be achieved. This has to be considered for dynamic operation of the drive and is discussed in the next section.

6.4 Practical Implementation of the Sensorless Drive for Dynamic Operation

As has been shown the rotor bar modulation in the measured $\underline{z}'_{PWM2}$ equivalent impedance can be used for the mechanical rotor position. However it was shown that for the used standard off-the-shelf the useful rotor bar modulation is very small. Under dynamic operation additional modulation effects to the useful rotor bar modulation occur that have even larger amplitude, i.e. magnetic saturation and inverter non-linearity effects. These addition modulation effects have to be suppressed, which forms a challenging task [21], [22], [30]. The behaviour of these additional modulations is non-linear over the operation range. Therefore a look up table is used for the compensation similar to the space modulation profile used in [6], [23]. However, even with the used complex look up table compensation the signal to noise ration of the rotor bar modulation is low. Therefore a phase locked loop structure is used to enhance the tracking of the small rotor bar modulation position signal [91].

6.5 Additional Modulation Effects

In standard induction machines strong magnetic saturation effects are present as well as rotor bar modulation effects. For simplicity it can be assumed that the saturation modulation effects on the impedance $\Delta\mathbf{Z}'_{Sat}$ are superimposed to the rotor bar modulation $\Delta\mathbf{Z}'_{RB}$ (6.28).

$$\mathbf{Z}' = \mathbf{Z}'_{Offset} + \Delta\mathbf{Z}'_{RB} + \Delta\mathbf{Z}'_{Sat} \tag{6.28}$$

The saturation impedance modulation is also theoretically modelled as an oval shape [23], rotating with the fundamental flux in the $\alpha\beta$ frame. As the PWM2 voltage and

current vectors are also rotating with the fundamental frequency, it can be assumed that the resulting saturation effect on the $\underline{z}'_{PWM2}$ impedance vector is static. Therefore under steady state conditions the magnetic saturation will only affect the DC component of the impedance vector $\underline{z}'_{PWM2}$. Figure 6.28 (a) shows visually the effect of the magnetic saturation influence on the $\underline{z}'_{PWM2}$ measurement.

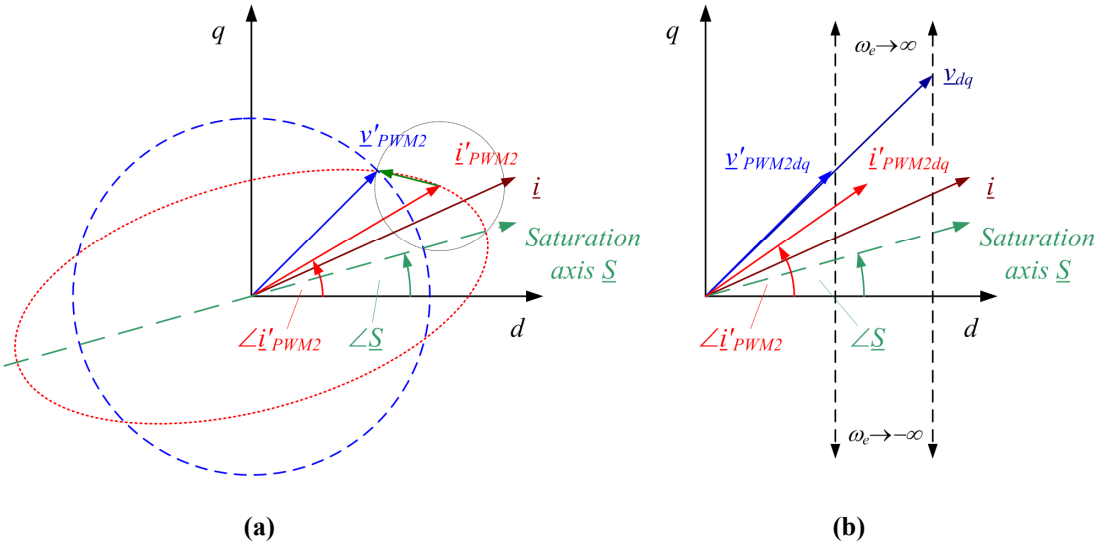

Figure 6.28: (a) Saturation HF impedance modulation, (b) Locus of fundamental voltage vector and PWM2 vectors dependent on speed in *dq* frame

In Figure 6.28 (a) the axis of the oval (the assumed saturation tensor $\Delta\mathbf{Z}'_{Sat}$) is defined by the maximum magnetic saturation axis $\underline{S}$. The position of the maximum saturation is affected by the position of the machine flux and magnetic saturation due to the stator currents in the machine. A change of the fundamental current vector position will therefore affect the position of the saturation tensor. The amplitude of the imposed current will further affect the total saturation of the machine iron and thus change the diameter of the saturation equivalent impedance tensor. This affects also the total offset in the detected impedance $\underline{z}'_{PWM2}$. For normal operation, the rotor flux producing current i_d is kept constantly at rated value and the torque producing current component i_q is changed with varying load. Therefore the saturation equivalent impedance tensor is a function of i_q. Under steady state the position of the

high frequency impedance *xy* measurement frame ($\angle \underline{i}'_{PWM2}$) with respect to the saturation axis $\underline{S}(i_q)$ is constant. However, under different speed operation the position of the fundamental voltage vector changes with respect to the rotor flux orientated *dq* frame. This is mostly due to the speed dependent back EMF voltage into *q* axis direction. Therefore also the position of the PWM2 voltage and current vectors change in the *dq* frame, since they are dependent on the fundamental PMW. Figure 6.28 (b) shows a simplified speed dependent locus (cross coupling terms neglected) for the fundamental voltage vector $\underline{v}_{dq}$ and the resulting PWM2 vectors $\underline{v}'_{PWM2}$ and $\underline{i}'_{PWM2}$ in the *dq* frame. Therefore, the relative position $\angle \underline{i}'_{PWM2}$ - $\angle \underline{S}$ changes and the detected $\underline{z}'_{PWM2}$ impedance saturation influence will not be constant under dynamic operation. Equation (6.29) shows the voltage equation system for the assumed saturation modulation, measured by the vectors $\underline{v}'_{PWM2}$ and $\underline{i}'_{PWM2}$ in the measurement *xy* frame. Equation (6.30) shows the resulting equation for the complex number vector division. Since the saturation tensor is affected by the torque producing current, the resulting saturation effect is also i_q dependent. The offset Z'_{Sat} determines the total machine saturation and influences the average equivalent impedance. The modulation term $\Delta Z'_{Sat}$ describes the saturation saliency that creates the oval shape of saturation equivalent impedance tensor.

$$\begin{bmatrix} v'_{PWM2x} \\ v'_{PWM2y} \end{bmatrix} = \begin{bmatrix} Z'_{Sat} - \Delta Z'_{Sat}\cos\left(2\left(\angle \underline{i}'_{PWM2} - \angle \underline{S}\right)\right) & \Delta Z'_{Sat}\sin\left(2\left(\angle \underline{i}'_{PWM2} - \angle \underline{S}\right)\right) \\ \Delta Z'_{Sat}\sin\left(2\left(\angle \underline{i}'_{PWM2} - \angle \underline{S}\right)\right) & Z'_{Sat} + \Delta Z'_{Sat}\cos\left(2\left(\angle \underline{i}'_{PWM2} - \angle \underline{S}\right)\right) \end{bmatrix} \cdot \begin{bmatrix} \left|\underline{i}'_{PWM2}\right| \\ 0 \end{bmatrix} \tag{6.29}$$

$$\begin{aligned} \underline{z}'_{PWM2Sat} &= \frac{\underline{v}'_{PWM2xy}}{\underline{i}'_{PWM2xy}} \\ &= \frac{v'_{PWM2x}}{\left|\underline{i}'_{PWM2}\right|} + j\frac{v'_{PWM2y}}{\left|\underline{i}'_{PWM2}\right|} \\ &= Z'_{Sat} - \Delta Z'_{Sat}\cos\left(2\left(\angle \underline{i}'_{PWM2} - \angle \underline{S}\right)\right) + j\Delta Z'_{Sat}\sin\left(2\left(\angle \underline{i}'_{PWM2} - \angle \underline{S}\right)\right) \end{aligned} \tag{6.30}$$

6.5.1 Decoupling of the Rotor Bar Modulation

In the theoretical explanation it is assumed that the offset machine impedance Z' and the modulation effects are superimposed as stated in equation (6.31). In the machine used the measured rotor bar modulation $\Delta Z'_{RB}$ is only about 1 to 1.5 % of the average stator equivalent impedance. The saturation modulation $\Delta Z'_{Sat}$ is about 4 % of the average stator equivalence impedance. It was observed that a further modulation occurs with each current commutation sector. This effect is assumed to be due to inverter non-linearity. The amplitude of this inverter impedance modulation $\Delta \underline{z}'_{PWM2\ Inv}$ is in the range of about 2 to 3 % of the average stator equivalence impedance. As shown here, with the standard off-the-shelf induction machine used, the required useful rotor bar position signal is the smallest modulation of all. Therefore the decoupling of the desired signal for the rotor position estimation forms a critical task.

$$\underline{z}'_{PWM2} = Z' + \Delta \underline{z}'_{PWM2\,RB} + \Delta \underline{z}'_{PWM2\,Sat} + \Delta \underline{z}'_{PWM2\,Inv} \tag{6.31}$$

In this work a basic three dimensional look up table (LUT) compensation scheme is implemented to extract only the desired rotor bar modulation. The unwanted impedance offset Z', the saturation modulation $\Delta \underline{z}'_{PWM2\ Sat}$ and the inverter modulation $\Delta \underline{z}'_{PWM2\,Inv}$ is subtracted from the measured PWM2 impedance $\underline{z}'_{PWM2}$:

$$\Delta \underline{z}'_{PWM2\,RB} = \underline{z}'_{PWM2} - \left(Z' + \Delta \underline{z}'_{PWM2\,Sat} + \Delta \underline{z}'_{PWM2\,Inv} \right) \ . \tag{6.32}$$

As stated before, the influence of the saturation modulation depends on the imposed stator currents and the relative position of $\underline{i}'_{PWM2}$ to the saturation axis $\underline{S}$. For this project i_d is kept constant and thus the total machine current amplitude variation depends directly on the torque producing current component i_q. Since the current controller has a high dynamic response i_q^* is used as the first pointer value to access

the LUT, as it has a low noise content. A further compensation dimension is $\angle \underline{i}'_{PWM2}$ - $\angle \underline{S}$. The position of the saturation axis $\underline{S}$ is not known, but it is assumed that it is directly related to the fundamental machine stator current vector $\underline{i}$. Therefore $\angle \underline{i}'_{PWM2}$ - $\angle \underline{i}$ is used as the second pointer value for referencing the LUT. For the compensation of the inverter non-linearity effect $\angle \underline{i}_{\alpha\beta}$ is used as the third pointer value to reference the LUT. The final implemented LUT contains the values of $\underline{z}'_{PWM2\,LUT}$ addressed by the three reference pointers:

$$\underline{z}'_{PWM2\,LUT}\left(i_q, \angle i_{\alpha\beta}, \angle \underline{i}'_{PWM2} - \angle i\right) = Z' + \Delta \underline{z}'_{PWM2\,Sat} + \Delta \underline{z}'_{PWM2\,Inv} \quad . \qquad (6.33)$$

Figure 6.29 shows the block diagram of the principal for the rotor bar position estimation algorithm with the look up table (LUT) compensation scheme for the impedance offset, saturation and inverter modulation decoupling from $\underline{z}'_{PWM2}$.

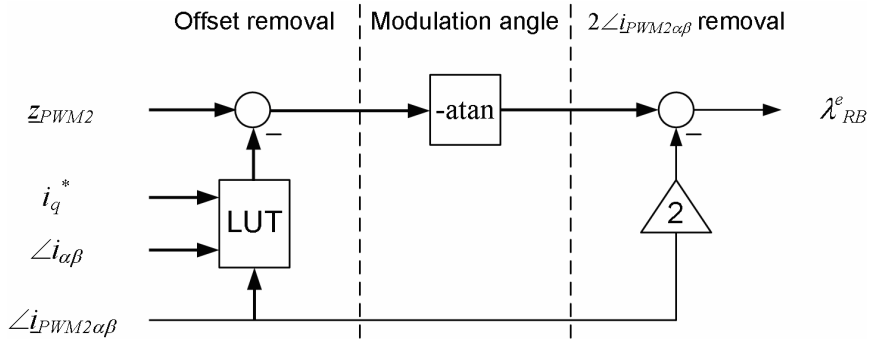

Figure 6.29: Principal reconstruction of the rotor bar position with LUT compensation

For the generation of the look up table the machine is run in sensored mode in all operation conditions (variable speed and i_q) and the complete saturation profile is acquired. This is later used for the look up table compensation process. The creation of the look up table will be discussed in more detail in the next section.

6.5.2 Generation of the Compensation Look up Table

The measured machine impedance is a composition of an offset impedance plus several modulation effects. Only the rotor bar modulation is required for control in this work. Therefore the other effects need to be removed. Even if in theory some simplified mathematical models for the saturation can be derived, the real observed function seems more complicated. Since the precise decoupling of the very small rotor bar modulation is crucial, $\underline{z}'_{PWM2}$ is measured during sensored operation over the entire operation range (variable speed and i_q) and the complete impedance profile $\underline{z}'_{PWM2\ LUT}(i_q,\ \angle\underline{i}'_{PWM2} - \angle\underline{i},\ \angle\underline{i}_{\alpha\beta})$ excluding the rotor bar modulation component $\Delta\underline{z}'_{PWM2\ RB}$ is generated. This profile is stored into a look up table (LUT) in the DSP memory. During online sensorless operation, the algorithm accesses this LUT using the known parameters i_q^*, $\angle\underline{i}'_{PWM2} - \angle\underline{i}$ and $\angle\underline{i}_{\alpha\beta}$. To create the look up table, several experiments are performed at constant torque. The coupled DC machine is controlling the speed of the rig. The speed is constantly varied over the desired speed range. Figure 6.30 shows a section of data captured when the induction machine is operated at rated torque (i_q = 12.5 A). Plot (a) shows the measured rotor position λ_R and the stator current vector position $\angle\underline{i}_{\alpha\beta}$, which is the first LUT addressing variable. Plot (b) shows the mechanical and electrical frequency and plot (c) shows $\angle\underline{i}'_{PWM2} - \angle\underline{i}$, which is the second LUT reference variable. One can notice that as explained earlier, this parameter varies with the speed of the machine. Plot (d) shows the measured impedance vector $\underline{z}'_{PWM2}$. The collected data is sorted as a function of the LUT addressing parameters $\angle\underline{i}_{\alpha\beta}$ and $\angle\underline{i}'_{PWM2} - \angle\underline{i}$ with a resolution of 2 ° electrical. Data points with the same addressing index were averaged. The experiment takes a long time to execute. Thus it is ensured that each LUT index constellation ($\angle\underline{i}_{\alpha\beta}$, $\angle\underline{i}'_{PWM2} - \angle\underline{i}$) occurs several times. Since the rotor speed is asynchronous to the electrical frequency it can be assumed that all samples of $\underline{z}'_{PWM2}$ per index constellation ($\angle\underline{i}_{\alpha\beta}$, $\angle\underline{i}'_{PWM2} - \angle\underline{i}$) are measured at different rotor bar

positions. Therefore the average of the high number of samples should give an equivalent value with decoupled rotor bar modulation.

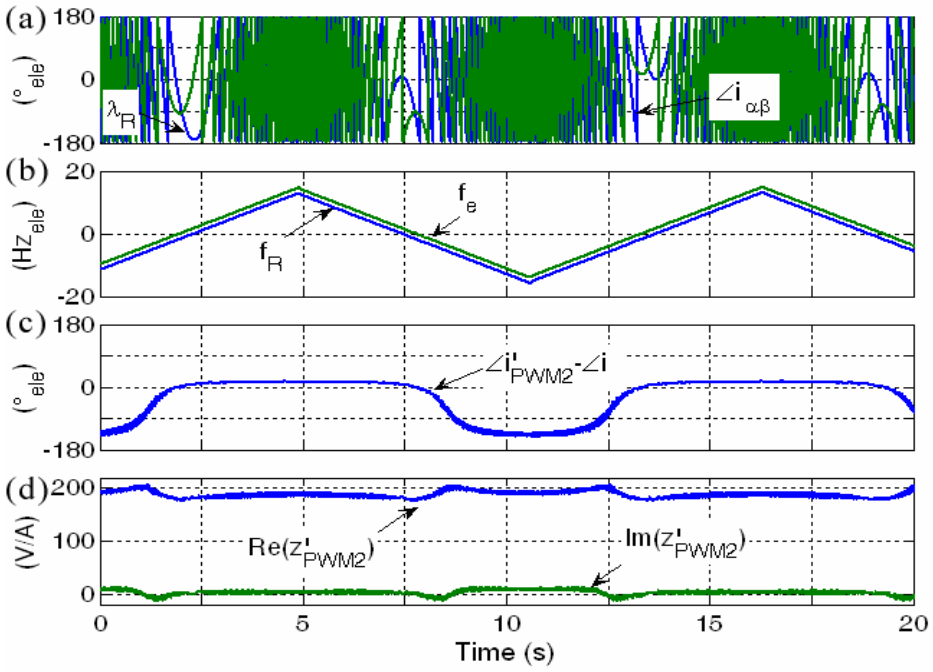

Figure 6.30: Induction machine in sensored torque control mode and varying speed

Figures 6.31 and 6.32 show the real and imaginary parts of the measured $\underline{z}'_{PWM2\ LUT}$ profile for variations in $\angle\underline{i}_{\alpha\beta}$ and $\angle\underline{i}'_{PWM2}$ - $\angle\underline{i}$ for machine operation with rated torque (i_q = 12.5 A) as shown in Figure 6.30. The flat sections in the figures show data points that did not occur during the experiment. The $\angle\underline{i}'_{PWM2}$ - $\angle\underline{i}$ range is limited due to the fundamental operation of the machine and therefore the saliency function is only detected in a small section of the 360 ° electrical range. However during sensorless operation, the drive can operate only at the points in the detected section and thus the knowledge of this part of the compensation look up table is sufficient.

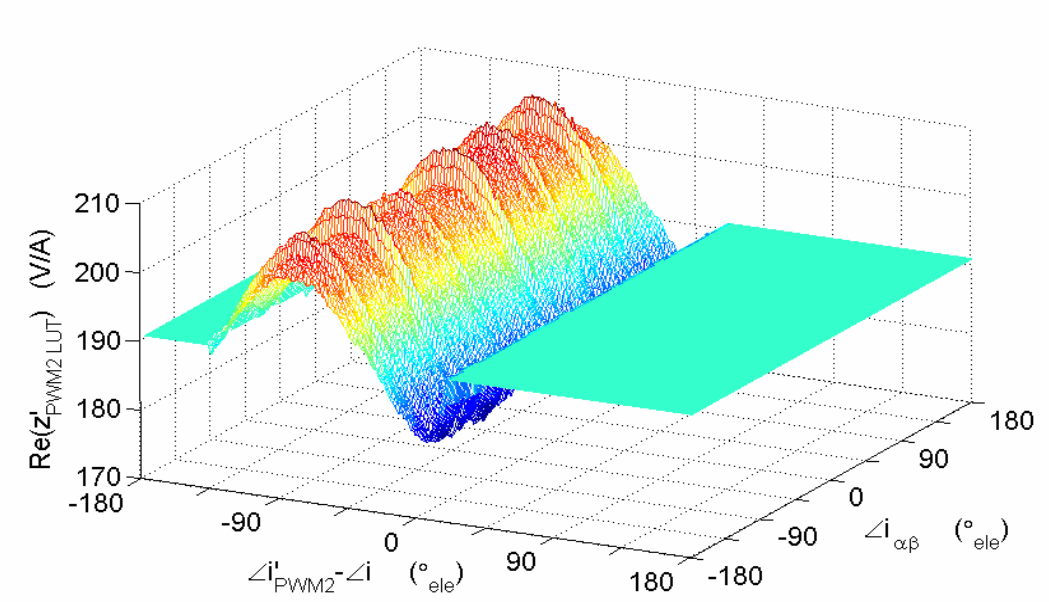

Figure 6.31: Real part of measured impedance profile

$\underline{z}'_{PWM2\ LUT}(i_q = 12.5\ \text{A}, \angle\underline{i}_{\alpha\beta}, \angle\underline{i}'_{PWM2} - \angle\underline{i})$

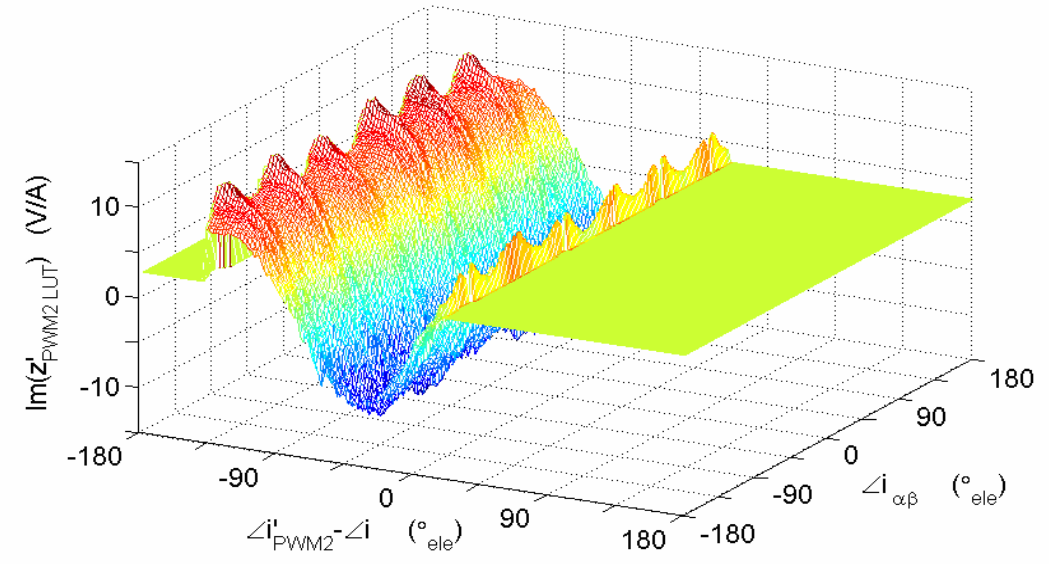

Figure 6.32: Imaginary part of measured impedance profile

$\underline{z}'_{PWM2\ LUT}(i_q = 12.5\ \text{A}, \angle\underline{i}_{\alpha\beta}, \angle\underline{i}'_{PWM2} - \angle\underline{i})$

In the impedance profile of $\underline{z}'_{PWM2\ LUT}$ one can see the parameter dependency of $\angle\underline{i}_{\alpha\beta}$ and $\angle\underline{i}'_{PWM2} - \angle\underline{i}$. It can be seen that the real part offset Z' is about 190 V/A for the given i_q. Also the modulation pattern as a function of $\angle\underline{i}_{\alpha\beta}$ for the current commutation sectors can be seen. The magnetic saturation saliency modulation $\Delta\underline{z}'_{PWM2\ Sat}$ shows a shape as expected for the assumed model. From the figures it can be seen that $\Delta Z'_{Sat}$ is about 10 V/A. The real part of $\underline{z}'_{PWM2\ LUT}$ shows a $-\Delta Z'_{Sat}$ $\cos(2(\angle\underline{i}'_{PWM2} - \angle\underline{S}))$ modulation and imaginary part shows a $\Delta Z'_{Sat}$ $\sin(2(\angle\underline{i}'_{PWM2} - \angle\underline{S}))$ modulation. The saturation axis, where the real part of $\Delta\underline{z}'_{PWM2}$ is minimum and imaginary part is zero, is approximately at $\angle\underline{i}'_{PWM2} - \angle\underline{i} = 0$. That indicates that the magnetic saturation axis $\underline{S}$ is very close to the stator current vector position $\angle\underline{i}$.

Figure 6.33 shows the effectiveness of the look up table compensation. The same data from Figure 6.30 is used, but zoomed to a smaller time window. Plot (a) shows the mechanical rotor and stator current vector position. Plot (b) and (c) shows the real and imaginary part of the measured impedance vector $\underline{z}'_{PWM2}$ and the LUT compensation values $\underline{z}'_{PWM2\ LUT}(i_q, \angle\underline{i}'_{PWM2} - \angle\underline{i}, \angle\underline{i}_{\alpha\beta})$. It can be seen that the LUT compensation values follow the average of the measured equivalent impedance $\underline{z}'_{PWM2}$. Plot (d) shows the $\underline{z}'_{PWM2}$ vector minus the LUT compensation values. This is the desired decoupled rotor bar impedance modulation $\underline{z}'_{PWM2\ RB}$ (6.32). It can be seen from the plotted signal that the rotor bar equivalence impedance modulation amplitude $\Delta Z'_{RB}$ is only approximately 2 V/A which is 1.1 % of the average equivalent impedance.

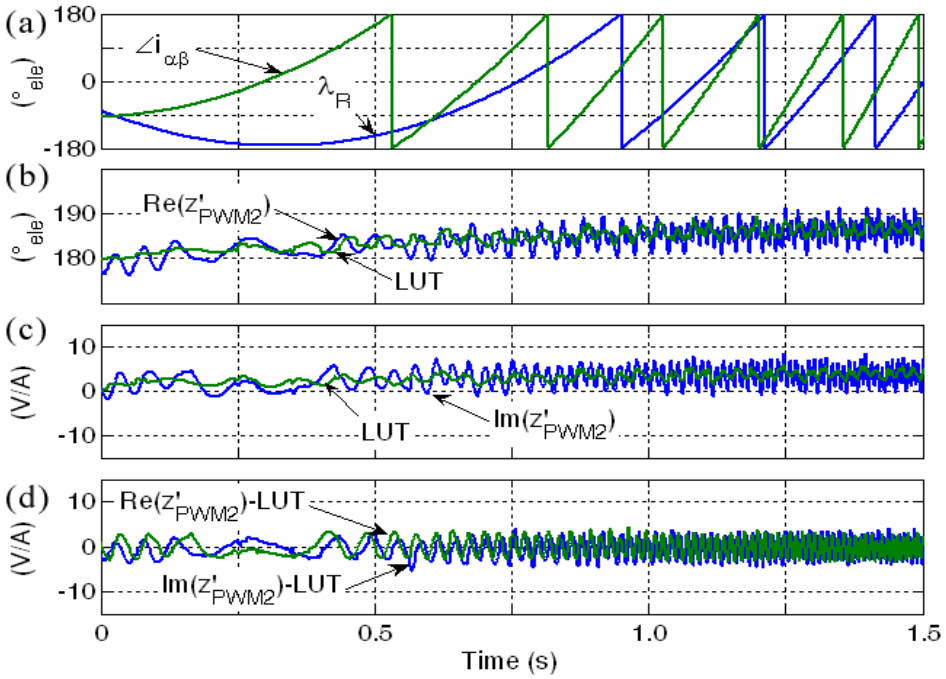

Figure 6.33: Applied LUT compensation

Figures 6.34 and 6.35 show the decoupled rotor bar impedance modulation $\Delta\underline{z}'_{PWM2\,RB}$ plotted over the mechanical rotor position and the *xy* reference frame position $\angle\underline{i}'_{PWM2\alpha\beta}$. The same experimental data as in the plots above is used. In Figures 6.34 and 6.35 the mechanical rotor position and $\underline{i}'_{PWM2\alpha\beta}$ position are discretised by steps of 2 ° electrical and all data samples with the same position index are averaged. It can be seen that there are clearly 16 sinusoidal modulation patterns which depend directly on the mechanical rotor position, which are due to the 16 rotor bars per electrical pole pair. Looking at the high frequency current vector position $\angle\underline{i}'_{PWM2\alpha\beta}$ a twist of two periods of the rotor bar modulation pattern can be seen. This verifies the theoretical derived influence of the rotating *xy* measurement frame relative to the stator $\alpha\beta$ reference frame (6.27). The offset in Figures 6.34 and 6.35 is zero. Also no inverter non-linearity influences are visible anymore. This is due to the inverter modulation included in the compensation look up table.

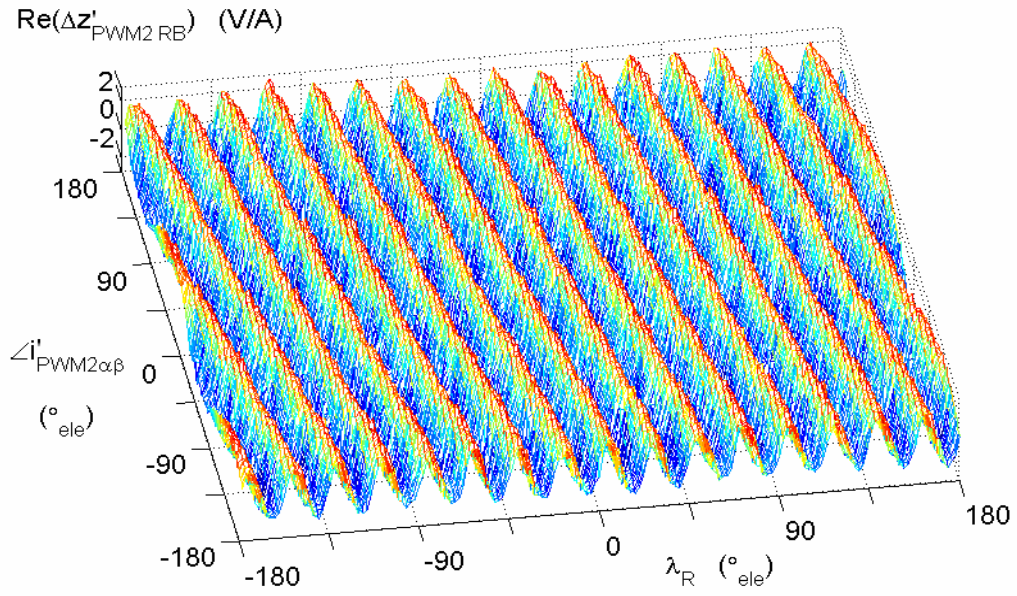

Figure 6.34: Real part of decoupled $\Delta\underline{z}'_{PWM2\,RB}$ in dependency of λ_{RB} and $\angle\underline{i}'_{PWM2\alpha\beta}$

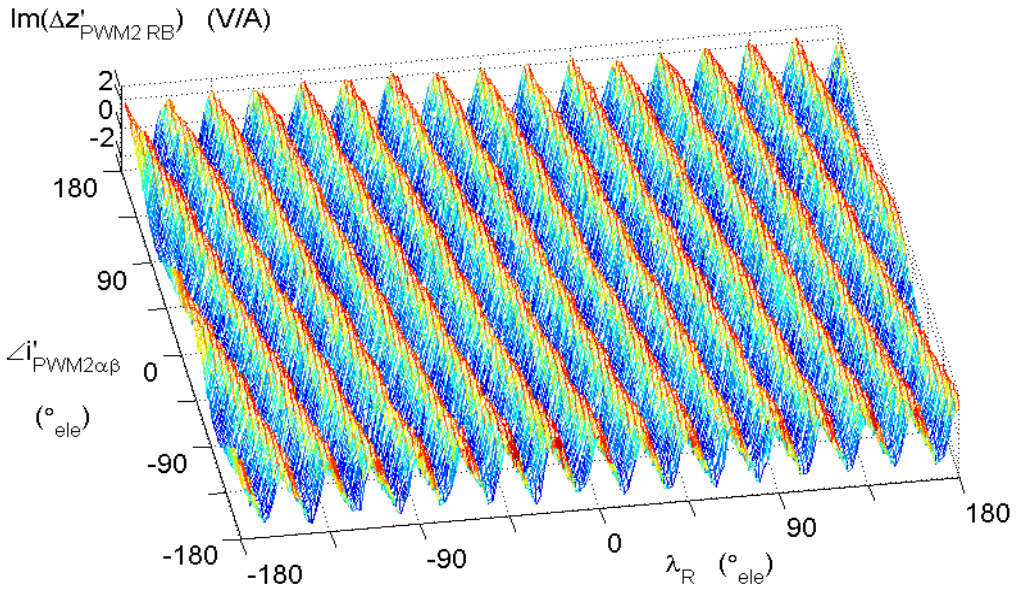

Figure 6.35: Imaginary part of decoupled $\Delta\underline{z}'_{PWM2\,RB}$ in dependency of λ_{RB} and $\angle\underline{i}'_{PWM2\alpha\beta}$

The magnetic saturation in the machine depends also on the imposed torque producing current i_q. The look up table for the impedance decoupling as shown in

Figures 6.31 and 6.32 are generated for the entire torque range in steps of 5 % rated i_q. The resulting compensation profiles are then combined to generate the complete $\underline{z}'_{PWM2\ LUT}(i_q,\ \angle\underline{i}'_{PWM2} - \angle\underline{i},\ \angle\underline{i}_{\alpha\beta})$ profile for variable torque operation of the sensorless IM drive. Figures 6.36 and 6.37 show the measured compensation impedance $\underline{z}'_{PWM2\ LUT}$ for the i_q range of 1 % to 100 % rated torque for the stator current vector position $\angle\underline{i}_{\alpha\beta} = 0$ ° electrical. The $\underline{z}'_{PWM2\ LUT}$ profile generation for zero torque is not possible with the described procedure. At zero speed the slip frequency is zero and the fundamental current vector rotates synchronised with the rotor. Therefore the measured $\underline{z}'_{PWM2}$ rotor position saliency modulation would be synchronized with the $\underline{i}_{\alpha\beta}$ vector position and even an averaging of many samples would not filter out the rotor bar slotting effect. Therefore $\underline{z}'_{PWM2RB}$ would be included in the generated $\underline{z}_{PWM2\ LUT}$ profile in $\angle\underline{i}_{\alpha\beta}$ direction, and it therefore cannot be used for the signal decoupling. Figures 6.36 and 6.37 show the impedance compensation values in dependency of i_q and $\angle\underline{i}_{PWM2} - \angle\underline{i}$. These graphs shows the data for the fundamental stator current position $\angle\underline{i}_{\alpha\beta} = 0$ ° electrical. It can be seen from Figures 6.36 and 6.37 that the machine impedance is significantly affected by the amount of i_q forced into the machine. As can be seen in the real part of $\underline{z}'_{PWM2\ LUT}$ the total impedance decreases as rated current is approached. This is theoretical expected since a larger amount of current causes more magnetic saturation and therefore a smaller permeability resulting into a lower inductance. However it can also be seen that the measured PWM2 impedance drops at very low currents; this contradicts what is theoretically predicted. The reason for this might be due to the practical machine design which is usually much more complex then any assumed model. Figures 6.36 and 6.37 show as Figures 6.31 and 6.32 that the minimum value of the real part of $\underline{z}'_{PWM2\ LUT}$ and the condition that the imaginary part equals zero occurs at approximately $\angle\underline{i}'_{PWM2} - \angle\underline{i} = 0$. Referring to the assumed mathematical model of equation (6.30) shows that the total saturation axis is very close to the fundamental stator current vector. Hence it is concluded that the measured saturation effect in $\underline{z}'_{PWM2}$ is mainly caused by local saturation due to the stator currents.

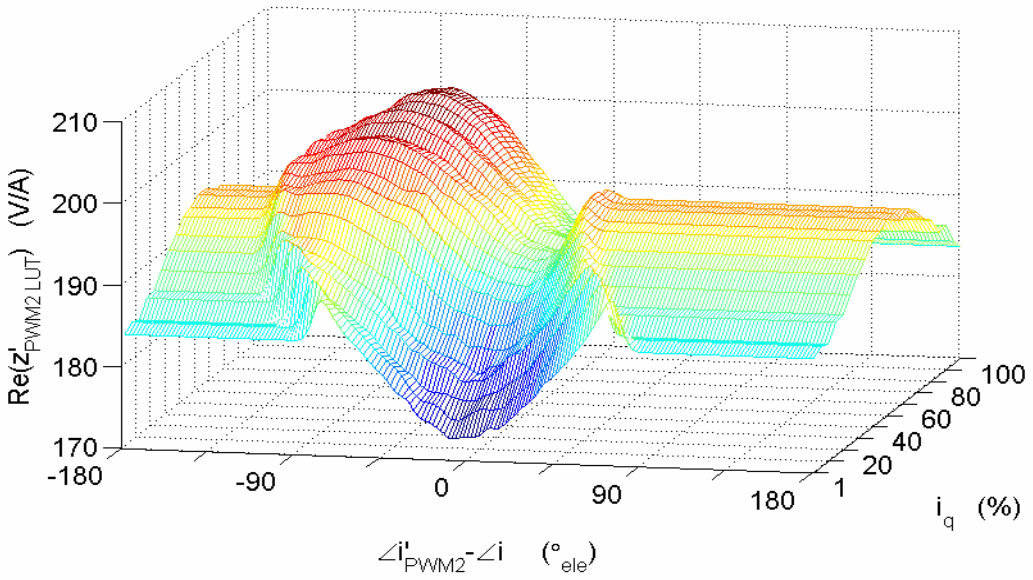

Figure 6.36: Real part of measured impedance profile

$\underline{z}'_{PWM2\ LUT}(i_q, \angle\underline{i}_{\alpha\beta} = 0\ °_{ele}, \angle\underline{i}'_{PWM2} - \angle\underline{i})$

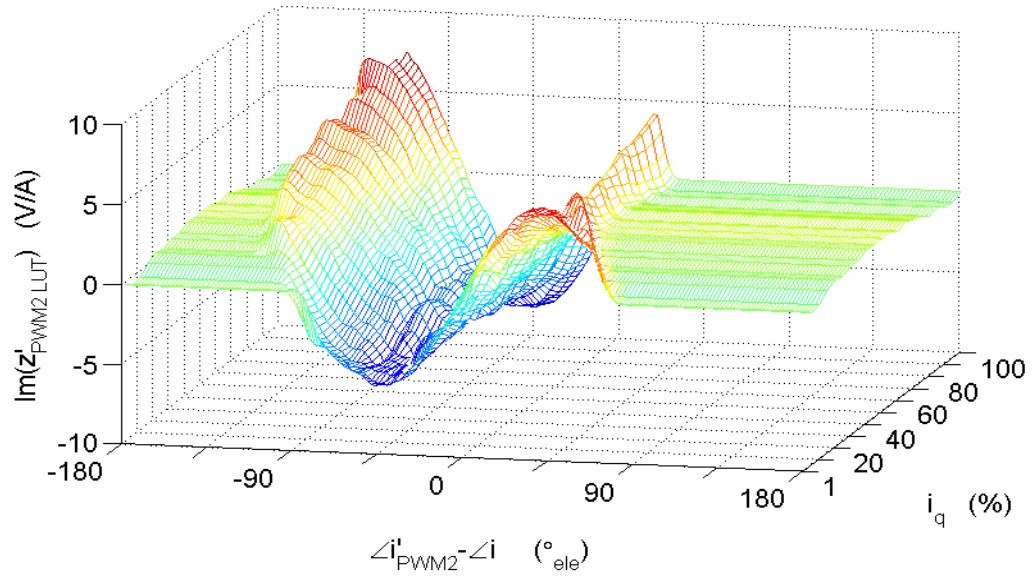

Figure 6.37: Imaginary part of measured impedance profile

$\underline{z}'_{PWM2\ LUT}(i_q, \angle\underline{i}_{\alpha\beta} = 0\ °_{ele}, \angle\underline{i}'_{PWM2} - \angle\underline{i})$

The variation of the impedance profile as a function of i_q looks smooth. To reduce the number of elements to be stored in the DSP memory this dimension is

approximated by a linear polynomial of degree 6. The final look up table contains for each $\angle \underline{i}_{\alpha\beta}$, $\angle \underline{i}'_{PWM2} - \angle \underline{i}$ constellation a set of polynomial coefficients as a function of i_q as stated in equation (6.34) and (6.35).

$$\mathrm{Re}\left(\underline{z}'_{PWM2\,LUT}\right) = a6_{Re}\, i_q^{*6} + a5_{Re}\, i_q^{*5} + a4_{Re}\, i_q^{*4} + a3_{Re}\, i_q^{*3} + a2_{Re}\, i_q^{*2} + a1_{Re}\, i_q^{*} + a0_{Re} \quad (6.34)$$

$$\mathrm{Im}\left(\underline{z}'_{PWM2\,LUT}\right) = a6_{Im}\, i_q^{*6} + a5_{Im}\, i_q^{*5} + a4_{Im}\, i_q^{*4} + a3_{Im}\, i_q^{*3} + a2_{Im}\, i_q^{*2} + a1_{Im}\, i_q^{*} + a0_{Im} \quad (6.35)$$

The LUT resolution as functions of $\angle \underline{i}_{\alpha\beta}$ and $\angle \underline{i}'_{PWM2} - \angle \underline{i}$ is 2 ° electrical. Thus 180 x 180 sets of a_{Re} and a_{Im} coefficients are stored in the look up table. Therefore the LUT consists of 180 x 180 x 14 values which takes (for 16-bit numbers representation) 907200 bytes of memory. The look up table size could be further reduced by leaving out the range of the $\angle \underline{i}'_{PWM2} - \angle \underline{i}$ values which are never used in the practical drive. However in this DSP system the memory size is not a problem. For practical implementation the size of the look up table seems also to become less significant due to the decreasing costs of memory (e.g. Flash). Figures 6.38 and 6.39 show the polynomial approximation of the $\underline{z}'_{PWM2\,LUT}$ profile shown above.

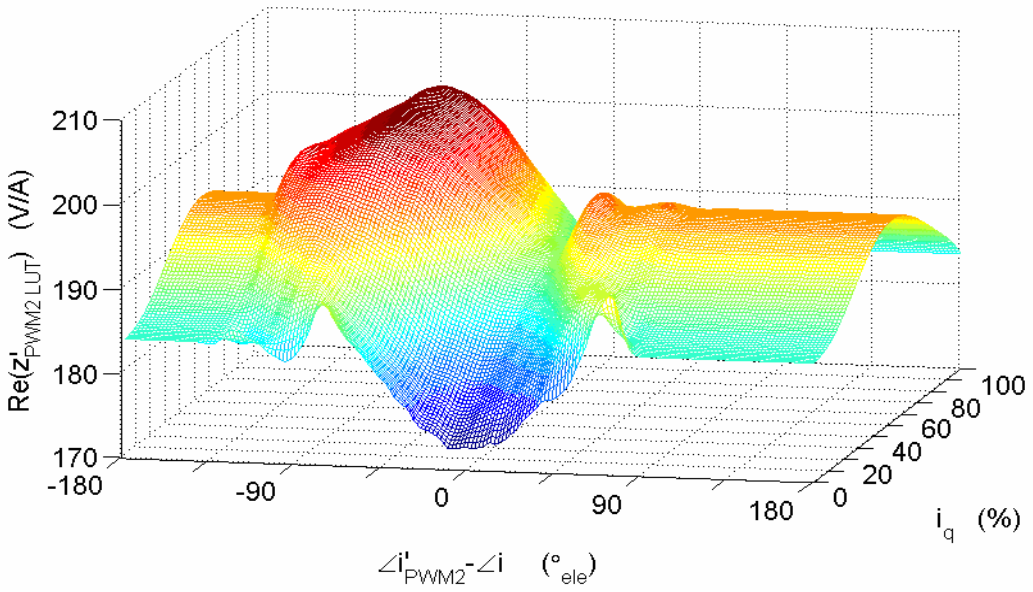

Figure 6.38: Real part of polynomial approximated impedance profile

$\underline{z}'_{PWM2\ LUT}(i_q, \angle\underline{i}_{\alpha\beta} = 0\ °_{ele}, \angle\underline{i}'_{PWM2} - \angle\underline{i})$

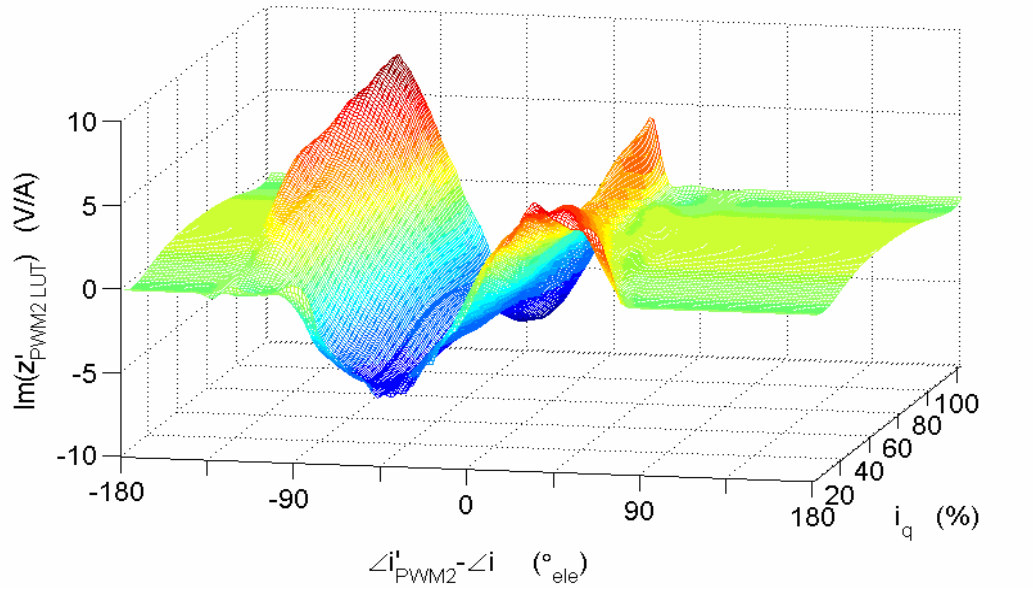

Figure 6.39: Imaginary part of polynomial approximated impedance profile

$\underline{z}'_{PWM2\ LUT}(i_q, \angle\underline{i}_{\alpha\beta} = 0°_{ele}, \angle\underline{i}'_{PWM2} - \angle\underline{i})$

6.5.3 Position Tracking using a Phase Locked Loop

As shown before, the rotor bar impedance modulation is fairly small compared with the other $\underline{z}'_{PWM2}$ components. Therefore the decoupling of the rotor bar modulation signal is corrupted by noise. Strong disturbances were observed in the rotor position reconstruction scheme shown in Figure 6.29, particular under transient conditions. The disturbances are usually only of small time duration. The worst case disturbance happens when the position estimator misses a rotor bar period (rotor bar skipping). This causes a position error step of one rotor bar period in the mechanical estimated position (22.5 ° electrical for the used machine). Since the estimated rotor position is directly used as feed back for the *dq* current transformation in the IRFO vector controller, this error step may cause instability of the sensorless control system. To reduce the likely hood of rotor bar skipping the principle of phase locked loops (PLL's) is applied. A PLL has the capability of tracking an AC signal by locking to the phase of the signal [92]. The PLL proportional plus integral (PI) controller defines the dynamic response of the tracking system. If the PLL dynamic is slower than the disturbances of the input signals, the output reconstructed signal will be less affected by the disturbance and can be regarded as filtered [93]. A very important advantage to general low pass filters is that PLL's do not cause steady state delays in the position tracking since the phase detector and the PI controller forces the phase error to a minimum.

Figure 6.40 shows were PLL's were placed in the sensorless rotor position estimator. One PLL (PLL 1) is used to track and filter the directly measured $\Delta\underline{z}'_{PWM2\ RB}$ modulation which contains the rotor bar modulation signal $\lambda_{RB} + 2\angle\underline{i}'_{PWM2\alpha\beta}$. A second PLL (PLL 2) is used to condition the final rotor bar position signal λ_{RB}. The second PLL block gives the mechanical position $\lambda_R{}^e$ and a filtered speed estimate $\omega_R{}^e{}_F$ as its outputs.

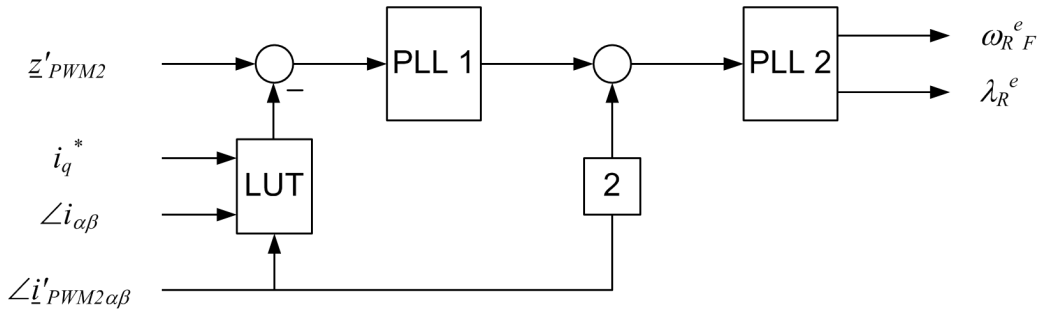

Figure 6.40: Signal tracking PLL's in the sensorless algorithm

Figures 6.41 and 6.42 show the two PLL structures in detail. Both PLL blocks are quadrature input signal PLL's. For the first PLL (PLL 1) the real and imaginary part of the decoupled $\Delta\underline{z}'_{PWM2\ RB}$ are directly used as input signals. The output is the position and frequency of the $\Delta\underline{z}'_{PWM2\ RB}$ modulation $\lambda_{RB} + 2\angle\underline{i}'_{PWM2\alpha\beta}$. It was observed that the real part of the measured impedance vector $\Delta\underline{z}_{PWM2\ RB}$ is more corrupted by disturbances then the imaginary part. As explained before the real part has a very large offset compared to the rotor bar modulation amplitude (1 – 1.5 % of offset value Z'). Therefore the offset compensation is very sensitive. Particularly under dynamic operation it was observed that the look up table compensation did not provide a perfect signal decoupling. Even if the offset compensation error is always smaller then 3 % of Z' it could reach absolute values larger than the rotor bar modulation amplitude $\Delta Z'_{RB}$. The $\underline{z}'_{PWM2}$ imaginary part offset (mostly caused by the magnetic saturation saliency) is small. Therefore even if the relative offset compensation error is the same, the absolute error is much smaller and the rotor bar modulation is still clearly detectable. As result the quadrature PLL 1 error signals derived from the real and imaginary part of $\Delta\underline{z}'_{PWM2\ RB}$ are conditioned by the scaling factors k_{Re} and k_{Im}. k_{Im} is set to a larger value then k_{Re}, since the imaginary part of $\Delta\underline{z}'_{PWM2\ RB}$ is less affected by noise. The k_{Re} / k_{Im} ratio is empirically adjusted in the range of 1 / 5 to 1 / 50. Hence the combined error signal to the PI controller is mainly derived from the imaginary part of $\Delta\underline{z}'_{PWM2\ RB}$. The trade off for doing this is that even under correct lock in of the PLL an error signal of twice the input frequency

occurs. This approach pushes the system towards a single input signal PLL. If only one input frequency signal is present, a very strong doubling of the input frequency component in the error signal occurs. The phase error is only determined by the average offset of the error signal. To reduce the effect of this error signal ripple a low pass filter has to be integrated into the PLL feedback path or the bandwidth of the PLL PI controller needs to be lower than the additional error signal frequency [92]. In this implementation, the quadrature input signal (real part of $\Delta\underline{z}'_{PWM2\ RB}$) is still used, which reduces the error ripple effect and additionally, gives an indication of the rotational direction of the two dimensional rotating position signal.

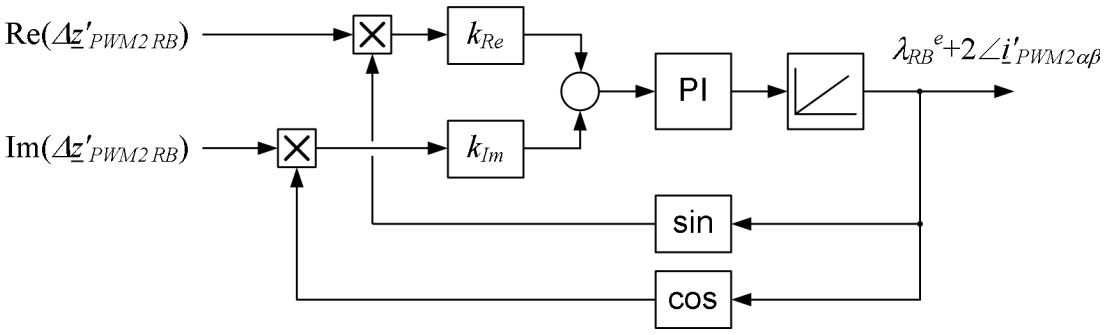

Figure 6.41: PLL 1, tracking of $\underline{z}'_{PWM2\ RB}$ modulation signal

The second PLL (PPL 2) is applied after the $2\angle\underline{i}'_{PWM2\alpha\beta}$ phase modulation has been removed. Here no scaling of the quadrature input signals is required. The input sine and cosine signals are directly derived from the reconstructed rotor bar position λ_{RB}^{e}. Therefore their quality is the same. In fact this PLL serves only for filtering the estimated rotor bar position signal again. This reduces further the effect of the incurred ripple $2(\lambda_{RB}+2\angle\underline{i}'_{PWM2\alpha\beta})$ in PLL 1 and smoothes noise that might be introduced by the $2\angle\underline{i}'_{PWM2\alpha\beta}$ phase removal. The tracking signal of PLL 2 is directly converted into a mechanical speed estimate and integrated to the final estimated rotor position λ_{R}^{e}. The speed signal is further conditioned by an additional low pass filter which provides a smoothed speed signal $\omega_{R}^{e}{}_{F}$, that is used for sensorless speed

control of the drive. The cut of frequency of the digital 1st order low pass filter (Butterworth) is set to 5 Hz.

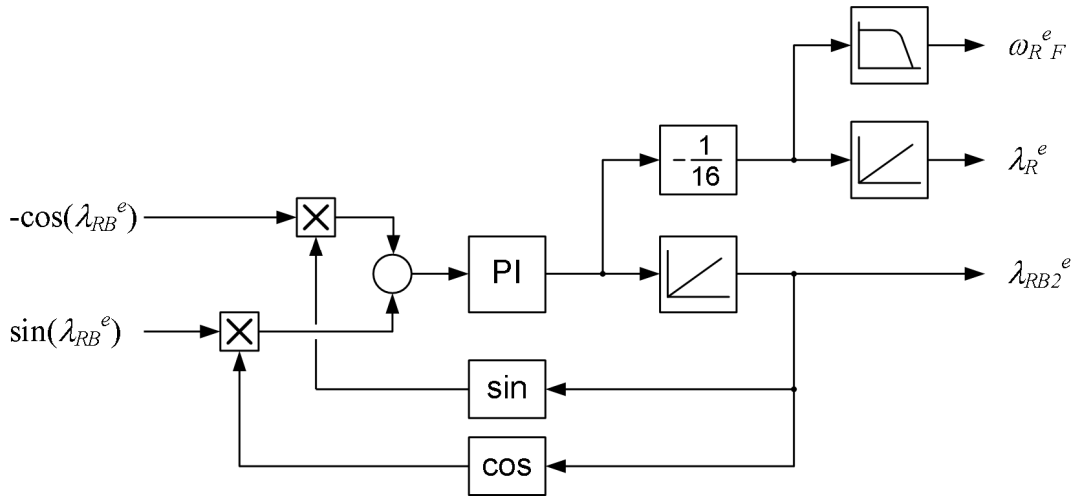

Figure 6.42: PLL 2, conditioning of final rotor bar modulation and mechanical rotor speed and position reconstruction

The explained PLL structure showed the most stable operation when implemented. The gain parameters of the PLL's are empirically adjusted for their best performance. K_P and T_I of PLL's are set in the range of 3 ... 20 and 0.01 ... 0.03 s respectively. The PLL system used for the signal conditioning shows a significant improvement on rotor bar position tracking. It reduces the occurrences of rotor bar skipping and smoothes noise. This stabilizes significantly the sensorless operation since noise in the estimated position causes further amplified feedback noise through the current controllers.

6.5.4 Experimental Results for the Sensorless Drive under Dynamic Operation Conditions

In this section the results of the final sensorless drive operating in torque, speed and position control are shown. The induction machine under test is coupled to a DC drive which acts as a controlled load. The DC drive is either set to speed control or to a constant current level to provide a constant electrical torque. All data shown in the figures is sampled at the cycle frequency of the sensorless algorithm which is 909.09 Hz.

6.5.5 Sensorless Torque Control

Figures 6.43 to 6.48 show results with the induction motor drive in sensorless torque control mode. For the vector control of the sensorless induction machine the estimated mechanical position is directly fed to the IRFO model for the rotor flux position orientation. The speed is controlled by the coupled DC load machine.

Figures 6.43 to 6.45 show experiments under constant speed and torque transitions. In each figure, plot (a) shows the measured mechanical rotor position λ_R and the estimated rotor position λ_R^e and plot (b) shows the difference between these position signals. Plot (c) shows the $\underline{i}_{dq}^e$ current components of the vector controlled sensorless drive. The flux producing component i_d^e is always keeps constant at rated value and i_q^e is varied proportional to the demanded electrical torque. Plot (d) shows the measured stator current vector $\underline{i}_{\alpha\beta}$ components and plot (e) shows the resulting frequency of the stator currents. Plot (f) and (g) show the measured $\underline{z}'_{PWM2}$ components (blue lines) and the look up table (LUT) compensation components (green lines). In the figures it can be seen that the LUT compensation values of $\underline{z}'_{PWM2\ LUT}$ follow the average of the measured equivalent impedance vector $\underline{z}'_{PWM2}$. However, it can be seen that during the transitions of i_q^e this condition is not always

met. Therefore the correct rotor bar impedance modulation $\Delta\underline{z}'_{PWM2\ RB}$ decoupling is not always ensured. The look up table for the impedance modulation decoupling is generated using many experiments with constant i_q. However it was observed that under torque (i_q) transients the saturation impedance modulation behaves differently to steady state. The assumed explanation is that the saturation impedance modulation $\Delta\underline{z}'_{PWM2\ Sat}$ changes not instantly with the machine currents. The LUT is referenced only by the known machine currents and transient conditions are not included in the static compensation LUT. One option considered was to filter the LUT reference variable i_q^* to compensate for a transient delay. However the $\Delta\underline{z}'_{PWM2\ Sat}$ transient behaviour under i_q^* steps is not adaptable using a simple 1st order low pass filter. Since the LUT compensation is not 100 % precise errors arise in the decoupled $\Delta\underline{z}'_{PWM2\ RB}$ signal. However the PLL signal conditioning allows the tracking of the correct rotor position to be achieved even under torque transient conditions. As can be seen the LUT compensation in the real part of $\underline{z}'_{PWM2}$ shows large errors during the torque transients. The compensation of the imaginary part of $\underline{z}'_{PWM2}$ has less error. This is taken into account in the weighting of the input signals for PLL 1 as explained previously. The error of the $\underline{z}'_{PWM2}$ compensation is dependent on the step amplitude and rate of change of i_q.

Figure 6.43 shows results where the coupled DC machine sets the speed to –30 rpm. The i_q demand for the sensorless drive is changed between 0 and 100 %. The transitions are limited by a ramp of 100 % rated i_q per second (12.5 A/s). As can be seen the $\underline{z}'_{PWM2\ LUT}$ compensation shows some errors during the transients. This is the reason for the dynamic limitation of the i_q transients. The rotor position tracking during the compensation error is only possible with the aid of the implemented PLL structure. At torque steps of less amplitude a higher rate of change in i_q could be applied resulting in smaller $\underline{z}'_{PWM2}$ compensation errors. The frequency of the current changes as a function of the demand torque. Since the mechanical speed is only slightly negative the current vector $i_{\alpha\beta}$ rotates in a forward direction at higher torque

values. Therefore this experiment shows the condition when the electrical frequency changes between positive and negative rotation with constant mechanical speed.

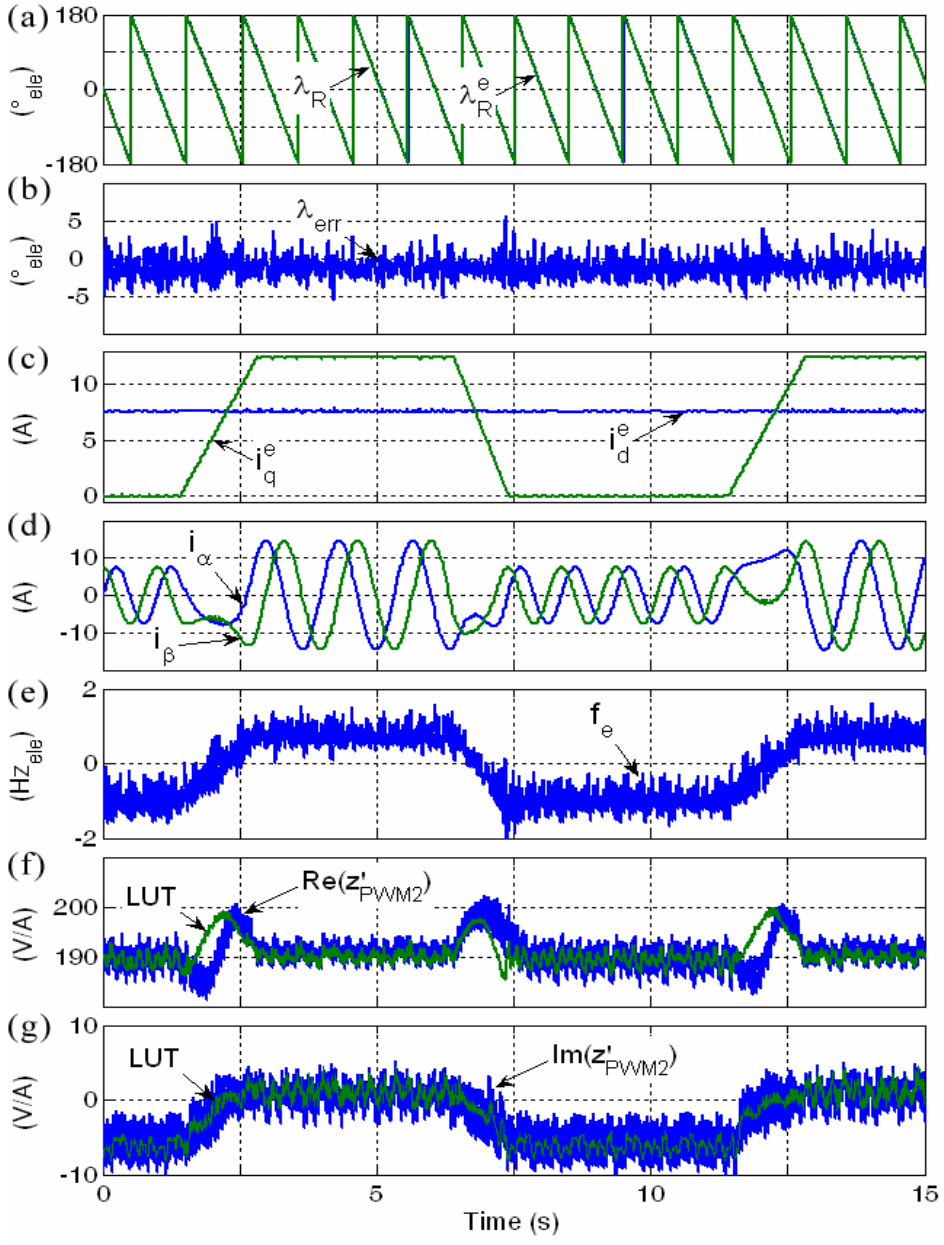

Figure 6.43: Torque transition from 0 to 100 % at -30 rpm

In Figure 6.44 the mechanical rotor speed is set to -52 rpm. The IM drive i_q demand is again changed between 0 to 100 % by a 12.5 A/s ramp. At the maximum applied i_q the slip frequency is approximately the same value as the mechanical speed but of opposite polarity. Therefore the condition when the sensorless drive is operating at rated torque and approximately zero electrical frequency is shown. It can be seen from the figure that the position estimation error is very low. The ripple in the error ripple amplitude in the estimated rotor position is only about +/-2 electrical degrees.

In the experiment shown in Figure 6.45 the DC machine is set to keep the mechanical speed to zero. Therefore at $i_q^e = 0$ A the electrical frequency is also set to zero by the vector current controller. At zero mechanical speed and zero electrical frequency the $\Delta\underline{z}'_{PWM2\ RB}$ modulation $\lambda_{RB} + 2\angle\underline{i}'_{PWM2\alpha\beta}$ shows also at zero frequency. The incurred double frequency PLL 1 error ripple $\lambda_{RB} + 2\angle\underline{i}'_{PWM2\alpha\beta}$ is also zero frequency and hence not suppressed by the PLL 1 bandwidth limitation. Thus the resulting error ripple caused by the k_{Re} and k_{Im} weighting becomes more significant. In this experiment the ratio between the scaling factors k_{Re} and k_{Im} is set to a lower value (5 / 1). As result the $\underline{z}'_{PWM2}$ compensation error during the i_q^e transients affects the position tracking more and as can be seen in Figure 6.45 the transient of i_q^* from 0 to 100 % had to be limited to 33 % of rated i_q per second (4.2 A/s). The sensorless algorithm is capable of tracking the correct rotor position and the resulting rotor position error is in the range of approximately +/-3 mechanical degrees. The ripple in the estimated position is due to the scaling of the PLL 1 input signals and occurs at a frequency of $2f_e$, since f_{RB} is zero.

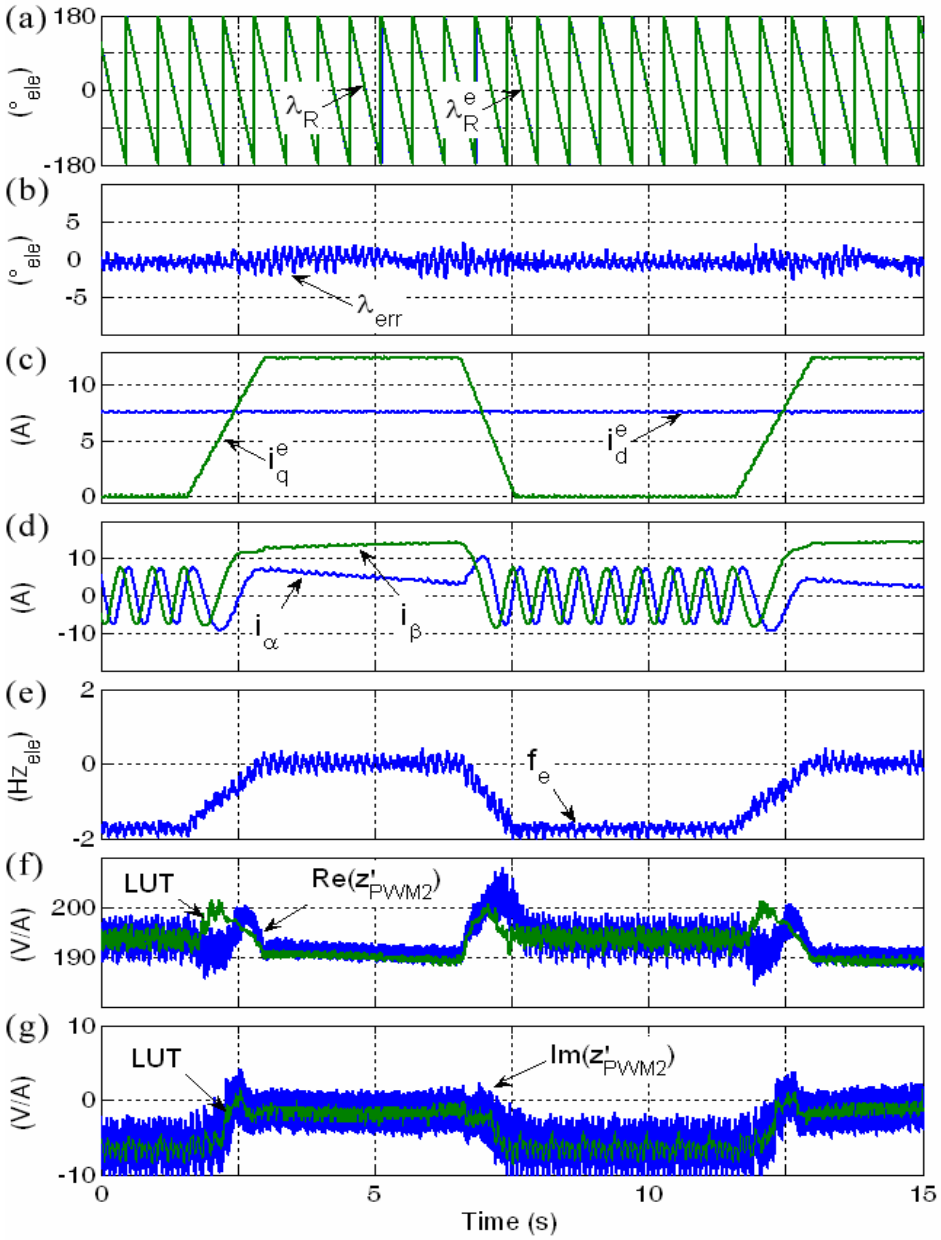

Figure 6.44: Torque transition from 0 to 100 % at -52 rpm

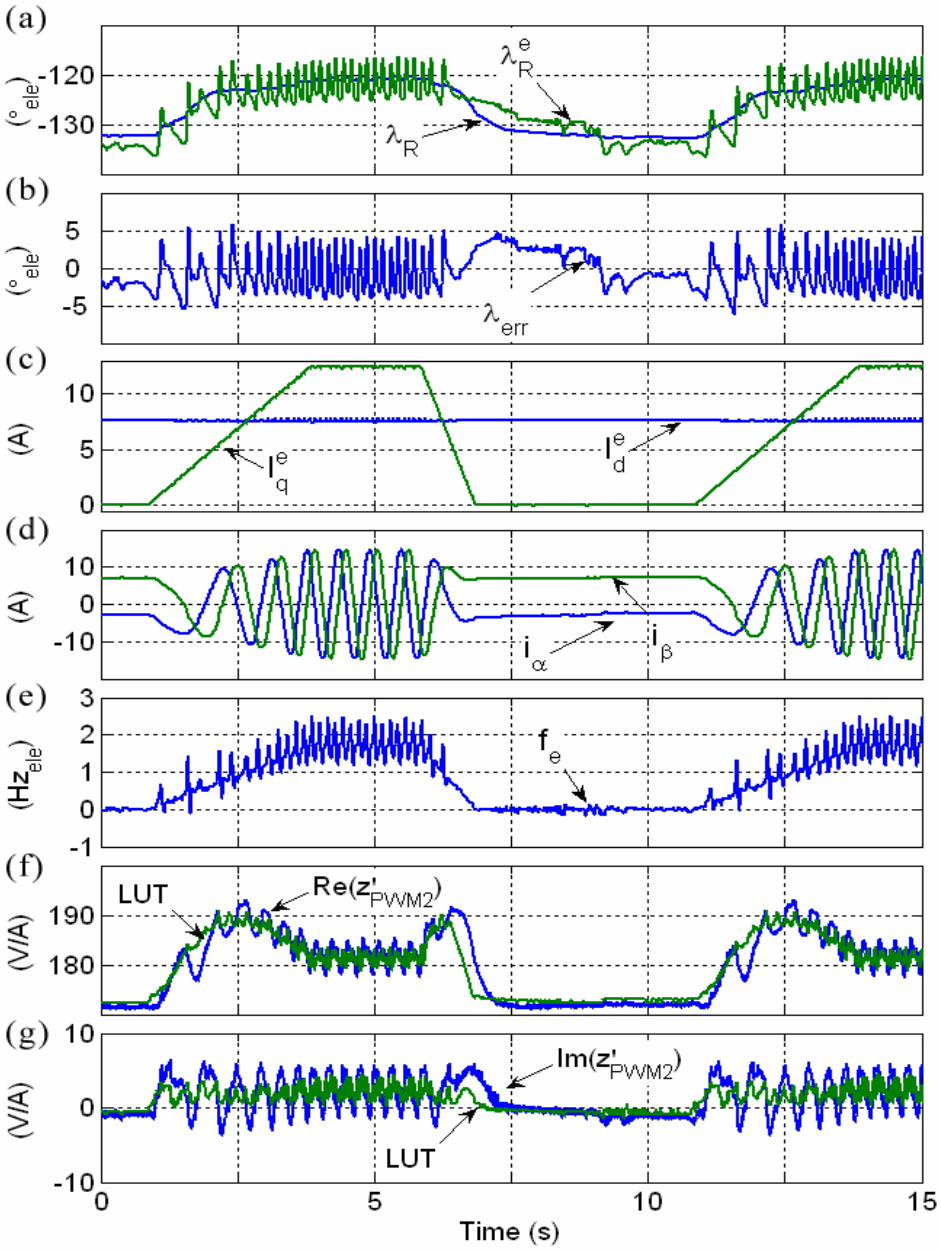

Figure 6.45: Torque transition from 0 to 100 % at stand still

Figures 6.46 and 6.47 show the sensorless IM drive operating with no load and rated torque respectively. The speed is varied by the coupled DC machine between +/-300 rpm. In Figures 6.46 and 6.47, plot (a) shows the measured mechanical rotor position λ_R and the estimated rotor position λ_R^e and plot (b) shows the difference between these position signals. Plot (c) shows i_d^e and i_q^e of the vector controlled sensorless IRFO drive, plot (d) shows the measured (blue) and estimated (green) mechanical speed n_R and n_R^e, plot (e) shows the resulting electrical frequency of the stator currents and plot (f) and (g) contain the measured $\underline{z}'_{PWM2}$ components (blue lines) and the look up table (LUT) compensation values (green lines).

In Figure 6.46 the torque demand is set to zero ($i_q^* = 0$). The coupled DC machine is changing the speed from zero to 300 rpm, to -300 rpm and back to zero. The speed transitions are limited to 600 rpm per second. This experiment shows the operation where only a flux producing current i_d^e is imposed on the machine. At zero mechanical speed the back EMF amplitude is zero too. This demonstrates the condition where the minimum voltage vector is applied to the machine and therefore the minimum $\underline{v}'_{PWM2}$ voltage amplitude is imposed. At zero speed the amplitude $|\underline{v}'_{PWM2}|$ is only 8.7 V and $|\underline{i}'_{PWM2}|$ is only 50 mA. It can be seen that the PWM2 high frequency harmonics are still strong enough to detect the machine impedance reliable. Thus it can be concluded that, under vector control, if no field weakening is applied, there is always a sufficiently strong PWM2 HF signals in the machine to provide a reliable $\underline{z}'_{PWM2}$ measurement. Therefore, the experimental results of Figure 6.46 show that the sensorless algorithm can follow the correct rotor position under the speed transients.

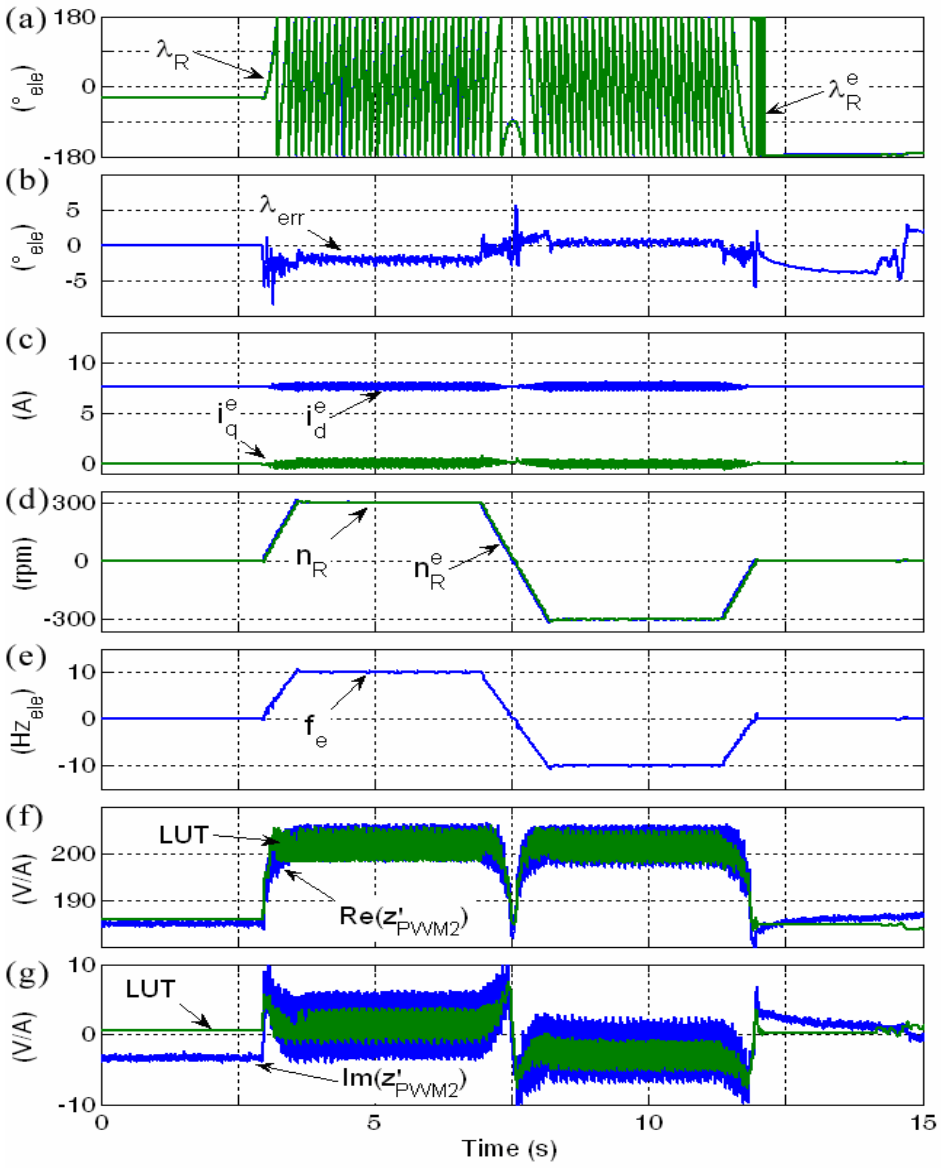

Figure 6.46: Speed transition between -300 to 300 rpm at zero torque

Figure 6.47 shows the same speed transients experiment, but with rated torque imposed by the induction motor drive. It can be seen that the sensorless IM drive is again reliable, even if the position estimation error ripple is larger at zero speed. These experiments show the highest tested speed - 300 rpm. At rated toque and 300 rpm the $\Delta\underline{z}'_{PWM2\ RB}$ modulation frequency $\lambda_{RB} + 2\angle\underline{i}'_{PWM2\alpha\beta}$ is 163.5 Hz. The sensorless algorithm is running at 909.09 Hz. Therefore at 300 rpm the detected rotor

bar modulation signal is only sampled about 5.5 times per period. Since several samples should be made during each rotor bar modulation period the speed should not be increased much higher unless the execution frequency of the sensorless algorithm is increased as well. However, the scope of this work is only the zero and low speed operation and therefore test with larger speeds are omitted.

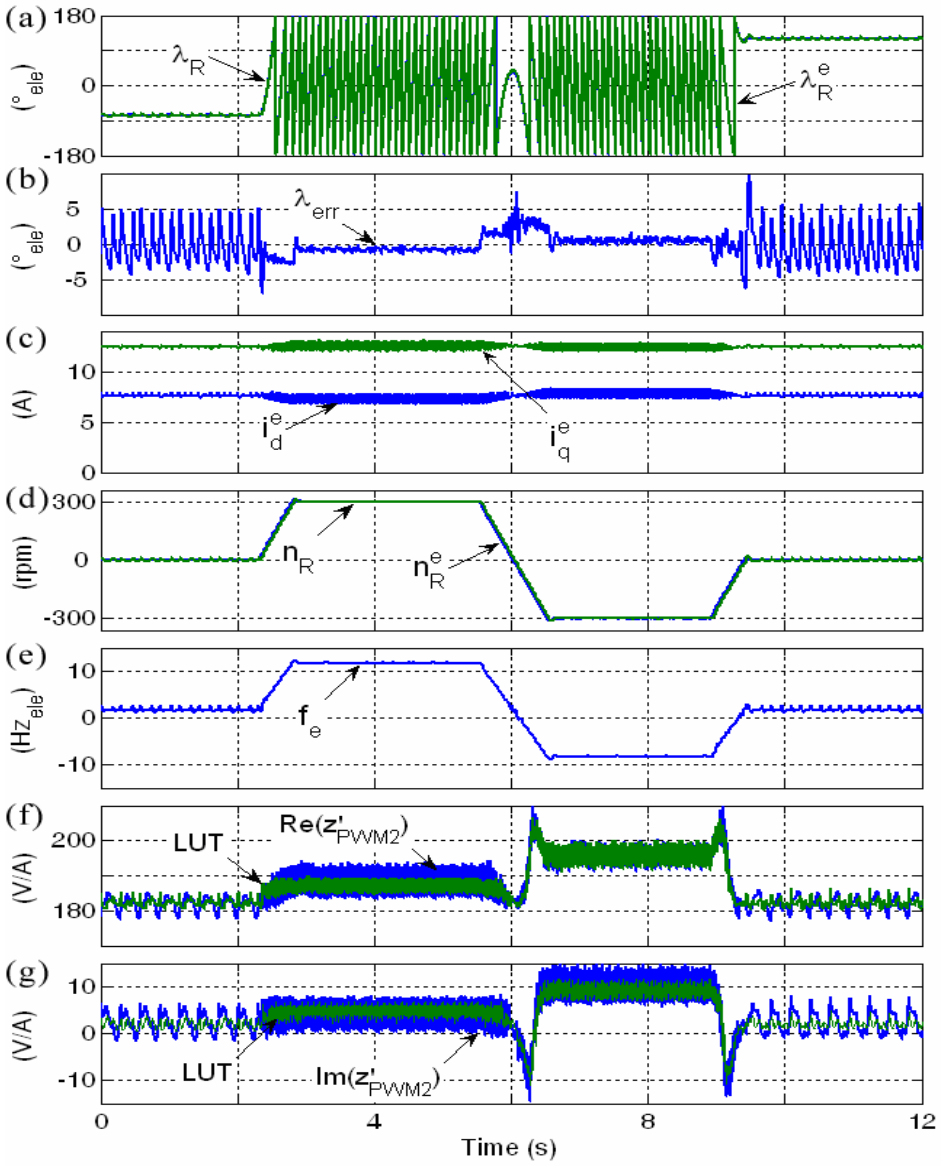

Figure 6.47: Speed transition between -300 to 300 rpm at rated torque

In Figures 6.46 and 6.47 the estimation errors are fairly low in the range of approximately +/-6 electrical degrees. It can be seen that the error ripple in the estimated position become much less at higher speeds. This is due to the filter effect of the PLL at higher frequencies. Also the error ripple incurred due to the k_{Re} and k_{Im} scaling in PLL1 are well filtered. During speed transients a small delay can be seen, which is introduced by the PLL position tracking. This error is small under the shown speed transitions. It can be also seen that a small steady state delay occurs in the estimated position at high speeds. This is due to the small delay in the sensorless position estimation algorithm by one cycle time, as explained in section 6.2, which is approximately 1.1 ms.

In Figure 6.48 the mechanical speed is changed between 0 and -52 rpm. The sensorless drive is operated at rated torque. Plot (a) shows the measured λ_R and the estimated λ^e_R mechanical rotor position, plot (b) shows the position estimation error, plot (c) shows i_d^e and i_q^e of the vector controlled sensorless drive and plot (d) shows the measured stator current vector components i_α and i_β. Plot (e) shows the measured and estimated mechanical speed n_R and n_R^e while plot (f) shows the resulting electrical frequency of the stator currents. Plot (g) and (h) contain the measured equivalent impedance vector components and the look up table (LUT) compensation values. It can be seen that at zero mechanical speed the stator current vector is rotating with rated slip frequency (1.74 Hz electrical) and at -52 rpm the imposed fundamental stator currents are approximately DC. This experiment shows the operation points where the sensorless drive is operating under rated torque with zero mechanical and zero electrical frequency. These two conditions reflect the most challenging operating points for sensorless AC drives.

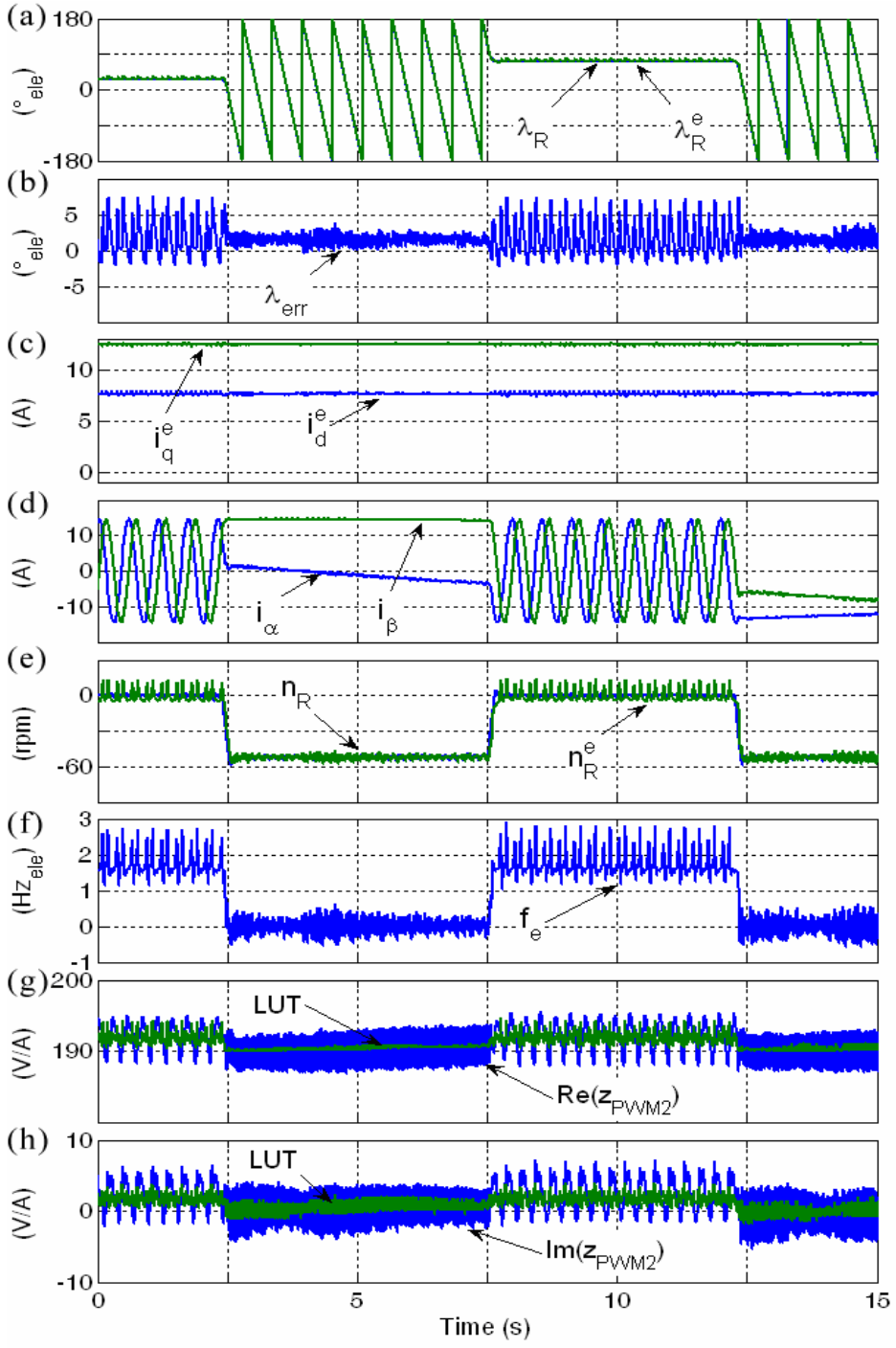

Figure 6.48: Operation with rated torque at zero electrical and mechanical speed

From the impedance $\underline{z}'_{PWM2}$ diagrams of the figures above it can be seen that the LUT compensation scheme tracks the floating mean of the impedance vector precisely even under dynamic speed transients. Only small deviations are visible. It can be seen that the speed variations cause less disturbances in the $\Delta\underline{z}'_{PWM2RB}$ decoupling than torque transitions, even if the stator current frequency changes are quite dynamic. Therefore it can be concluded that the transient disturbances in $\underline{z}'_{PWM2}$ are more related to the i_q transitions. One reason could be that the stator current vector amplitude changes with a change in i_q and thus the total magnetic saturation of the machine. Furthermore i_q changes proportional the slip frequency and therefore the frequency and amplitude of the rotor currents. The change of the rotor currents will also change the magnetic field build up by the rotor currents, which may not follow instantaneously, but follow with a lag. This effect could be similar to the relationship of the rotor flux to i_d which is defined by the rotor time constant. It was found that very high steps of i_q cause not only a delay in the offset settling, but also increased oscillations in $\underline{z}'_{PWM2}$.

6.5.6 Sensorless Speed Control

Figures 6.49 to 6.56 show results of the IM drive operating with sensorless speed control. The coupled DC machine is set to a constant armature and field current. The sensorless IM drive is controlling the speed by an implemented speed cascade loop which sets the reference torque (i_q^*). The filtered estimated speed output of PLL 2 is used as speed feedback for the speed controller. The speed reference in each experiment is toggled between two reference values. The transitions of the reference speed are limited to 120 rpm per second. The speed controller dynamic is set to a low value due to the transient limitations of the rotor bar modulation decoupling. No ramp limitation in the generated reference torque is applied. The parameters of the used PI controller are adjusted experimentally to achieve best performance. K_p of the

speed controller was set in the range of 0.5 to 1.5 As/ rad and T_I in the range of 0.5 to 3 s.

Figures 6.49 to 6.50 and 6.53 to 6.56 show in plot (a) the measured λ_R and the estimated λ^e_R rotor position and plot (b) shows the difference between the position signals. Plot (c) shows i_d^e and i_q^e of the sensorless IRFO drive, plot (d) shows the measured (blue) and estimated (green) mechanical speed n_R and n_R^e and plot (e) shows the resulting frequency of the stator currents. In plot (f) and (g) of the figures are the measured equivalent impedance vector components and the look up table compensation values shown.

Figure 6.49 shows the result when the reference speed is changed between -60 and 60 rpm for a low load. The armature current of the DC machine is set constantly to 6 A, which provides approximately 6.7 Nm electrical torque. The torque applied by the sensorless drive is almost constant (i_q^e). Only a slight increase/ decrease is visible during the acceleration/ deceleration. As can be seen the position estimation error is very low. Only during the transients the estimation noise increases slightly.

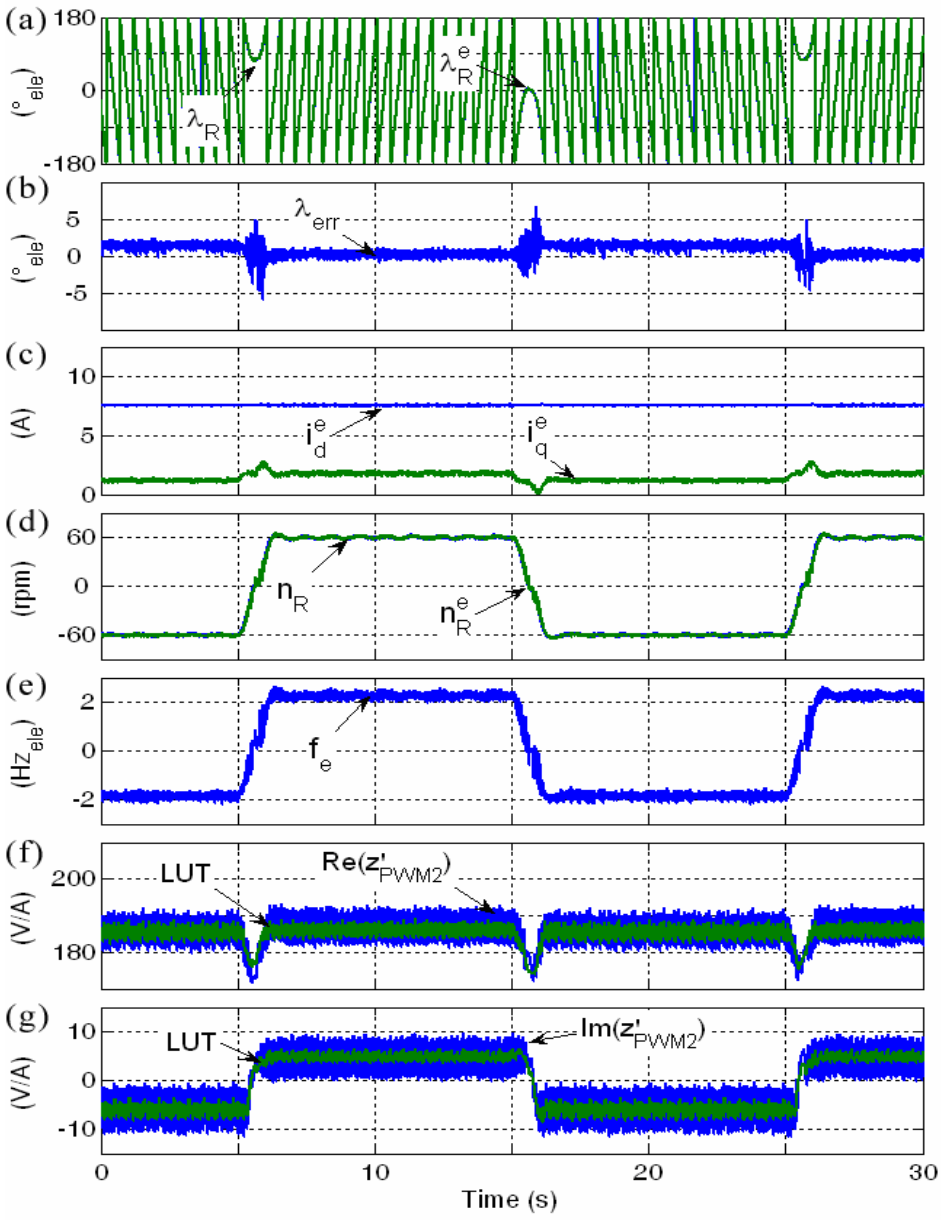

Figure 6.49: Sensorless speed control between -60 and 60 rpm at low load

In Figure 6.50 the same experiment as before is carrier out, but with a higher load. The armature current reference of the DC machine is set to 15 A, therefore the DC machine provides an electrical torque of 17.25 Nm. From the i_q^e graph can be seen that the torque applied by the sensorless IM drive varies with different speeds. The peak i_q^e is about 100 % of rated value (12.5 A). The strong variation of the torque

producing current is due to strong friction losses in the mechanical coupling of the DC and induction machine. The speed transient is slow due to the limited i_q^* dynamic of the sensorless algorithm and the hence set low bandwidth of the seed loop. However it can be seen that the reference speed is reached correctly.

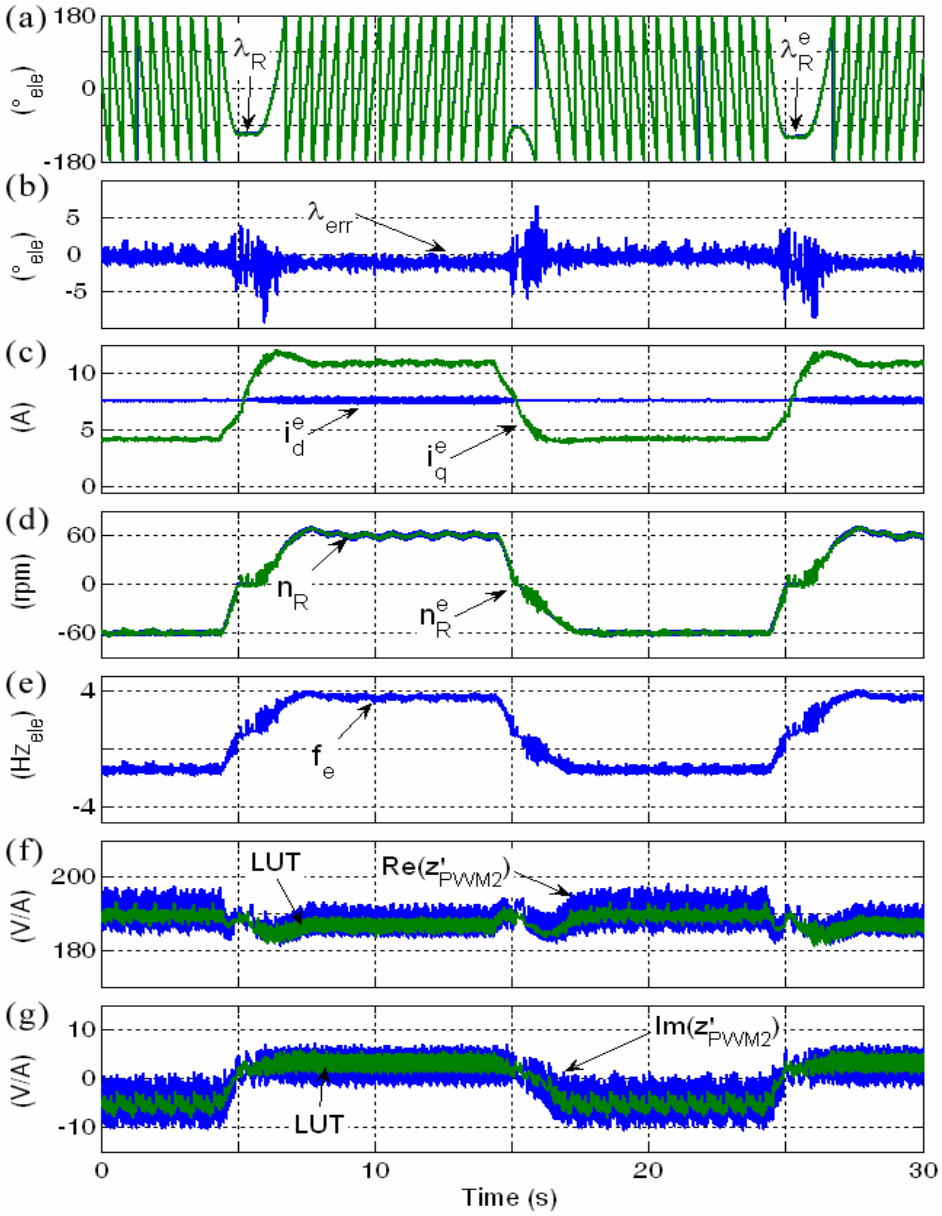

Figure 6.50: Sensorless speed control between -60 and 60 rpm at high load

Figures 6.51 and 6.52 show for comparison the same experiments of Figures 6.49 and 6.50 under sensored condition. It can be seen that the results look similar and the speed transients show the same dynamic characteristic. It can be seen that i_q changes also with the rotational speed and that the speed tends to stick at zero. That affirms that the i_q variations are not caused by the sensorless operation but rather come from mechanical load variations (friction losses). Small differences between the results are due since the experiments in Figures 6.51 and 6.52 were carried out at a later stage and the test machine was removed and reattached again to the rig in between. Therefore the coupling was not exactly adjusted as in the experiments in Figures 6.49 and 6.50. It can be seen in Figure 6.52 that the clamping of the speed at zero is worse than in Figure 6.50. This indicates that the coupling at the sensored experiments was less accurate aligned than at the experiments under sensorless condition. However, the purpose of Figures 6.51 and 6.52 is only to explain in general the reason of the i_q variation over the operation speed.

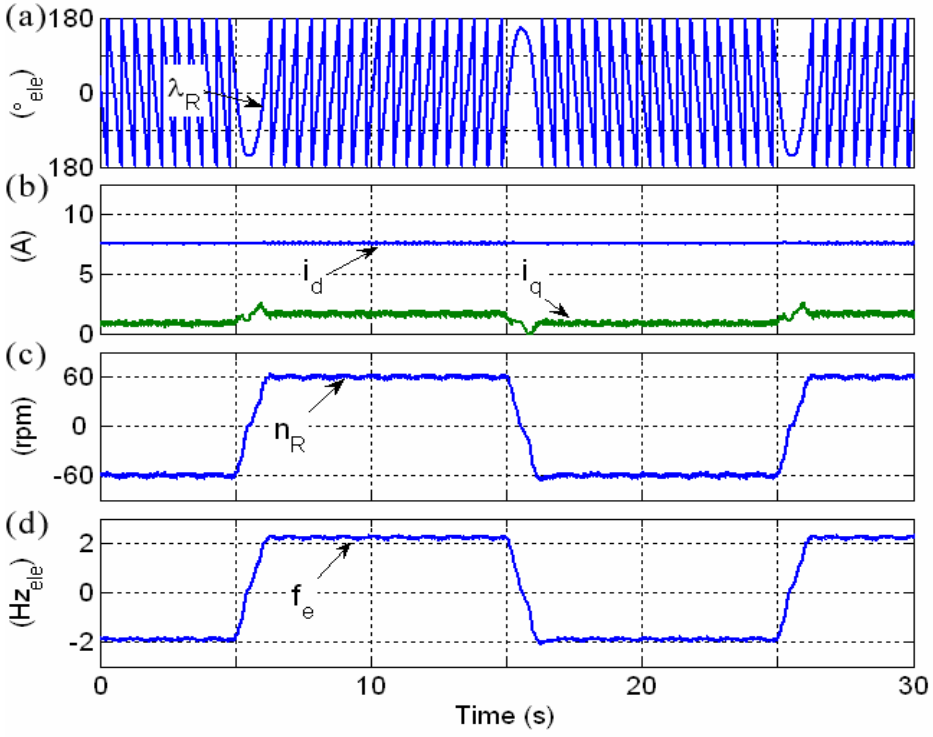

Figure 6.51: Sensored speed control between -60 and 60 rpm at low load

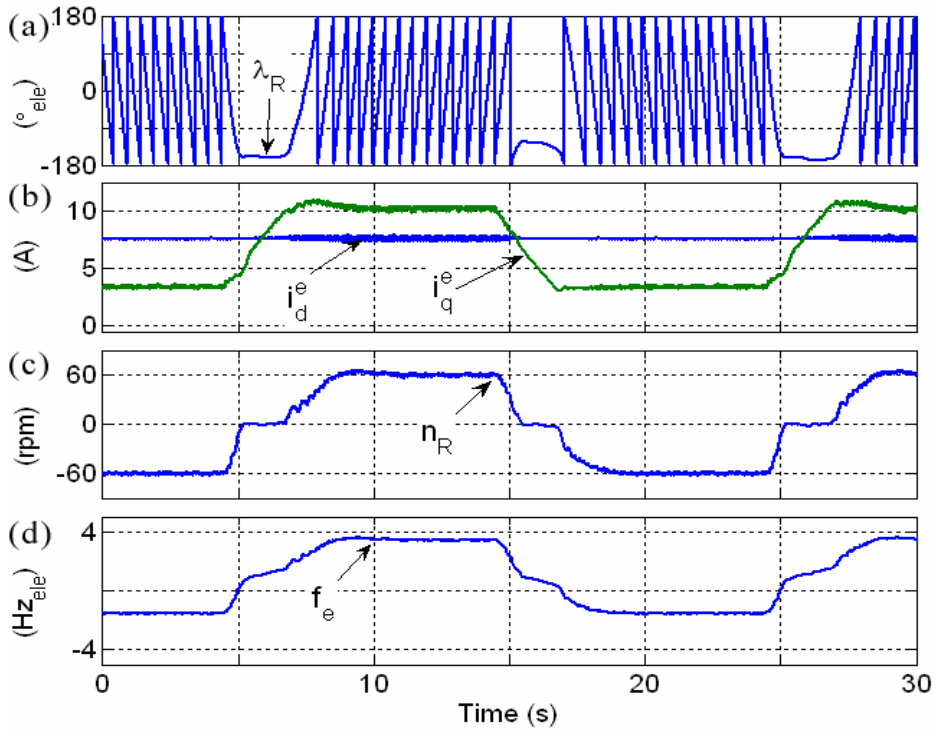

Figure 6.52: Sensorless speed control between -60 and 60 rpm at low load

Figure 6.53 shows results when the reference speed is toggled between 0 and 120 rpm. The mechanical load is set to a low value. During acceleration and deceleration the changes in i_q^e can be observed. The experiment shows the behaviour of the drive at zero mechanical speed in speed control and low load condition.

Figure 6.54 shows the same results as Figure 6.53 at high load. As can be seen during the acceleration transients the torque producing current component of the sensorless drive i_q^e reaches up to 100 % of rated value. The experiment shows the behaviour of the drive at zero mechanical speed in speed control and high load condition.

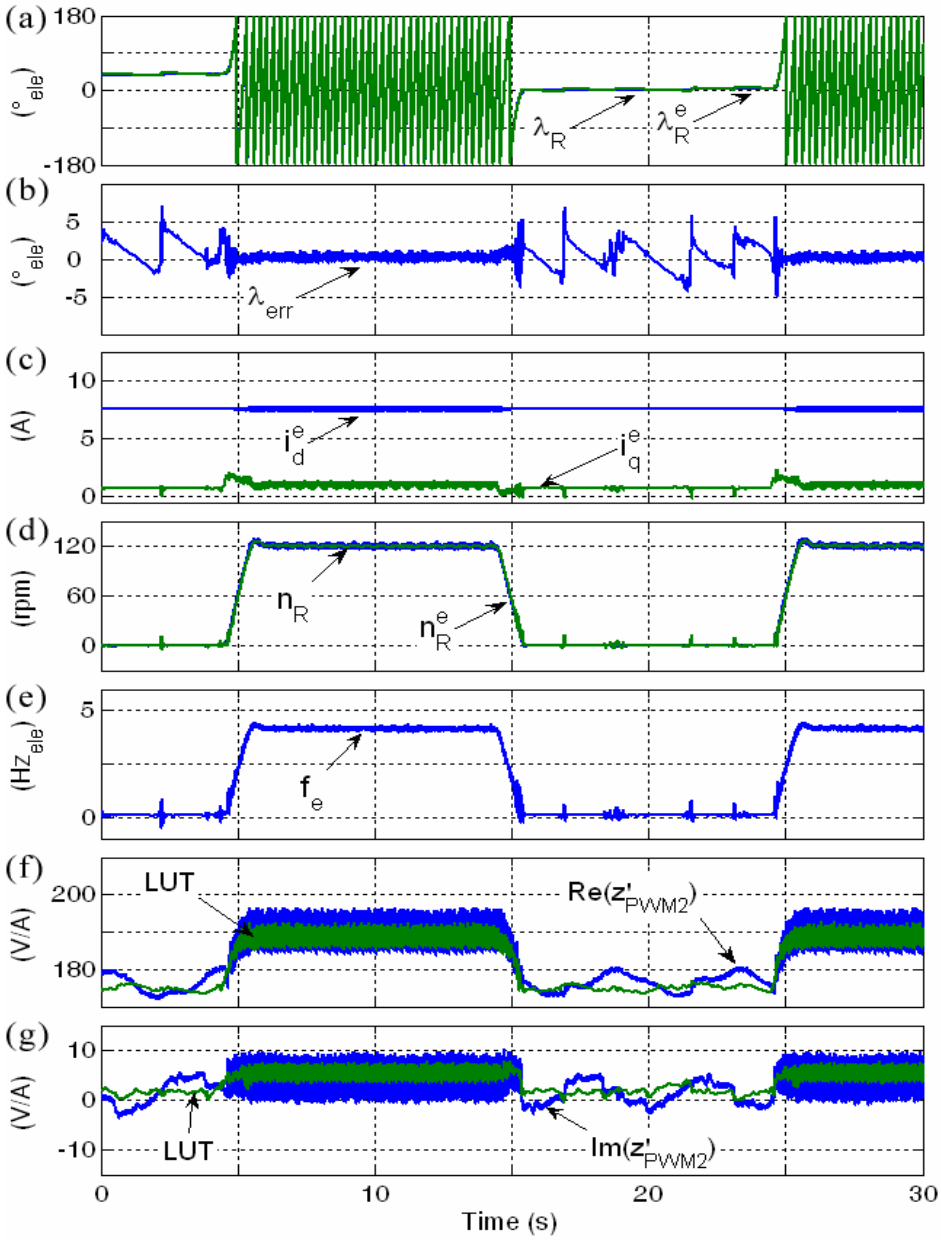

Figure 6.53: Sensorless speed control between 0 and 120 rpm at low load

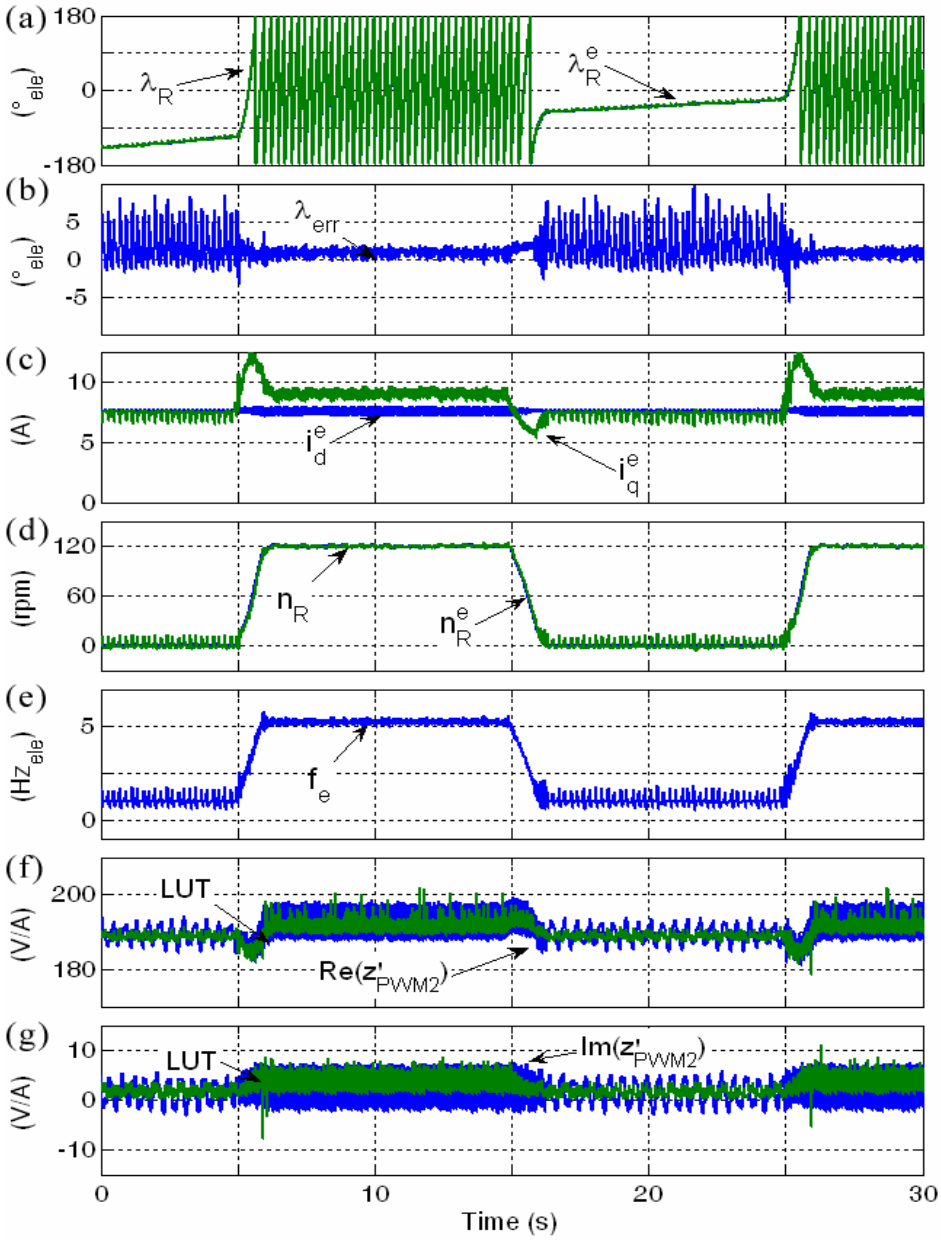

Figure 6.54: Sensorless speed control between 0 and 120 rpm at high load

Figures 6.55 and 6.56 shows the result when the speed reference is changed between 0 and -120 rpm at low torque and at high load condition, similar to Figures 6.53 and 6.54.

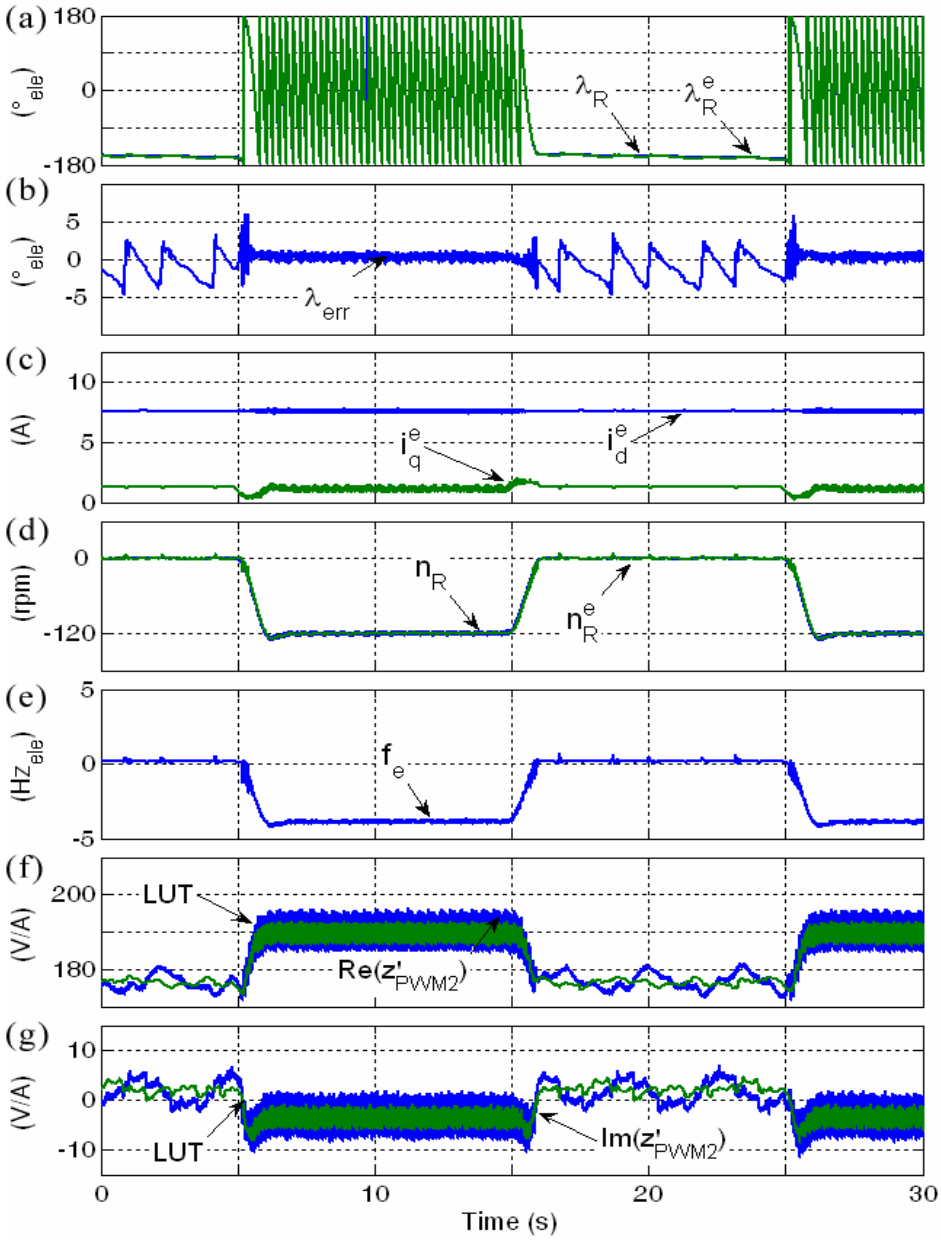

Figure 6.55: Sensorless speed control between 0 and -120 rpm at low load

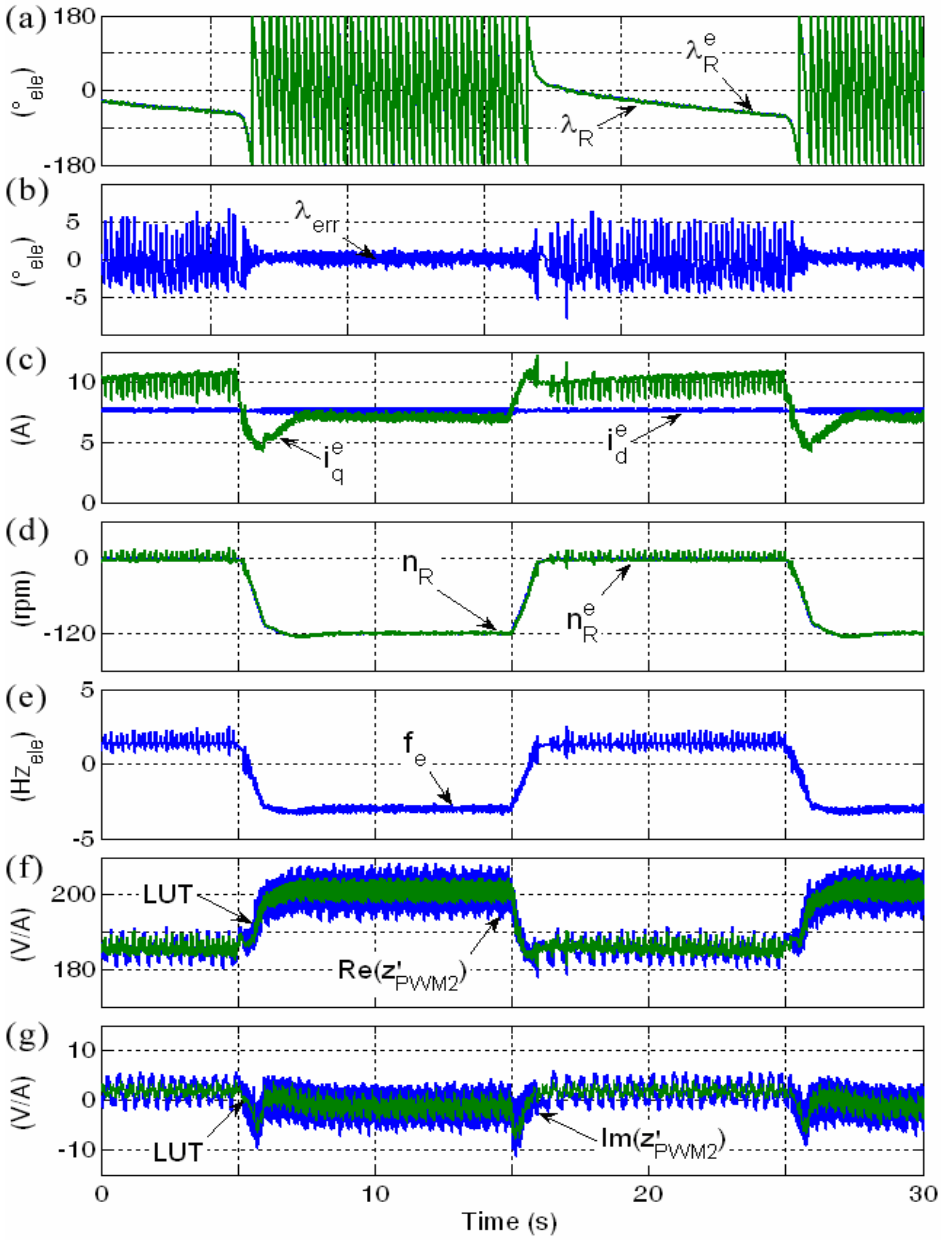

Figure 6.56: Sensorless speed control between 0 and -120 rpm at high load

In the experiments above it has been shown that sensorless speed control operation is possible with the implemented induction machine. The dynamic is low due to the torque transient limitations. However the set reference speed is precisely set, even at very low and zero speed. No steady state errors occur and the noise is in the range of +/-6 rpm.

6.5.7 Sensorless Position Control

Figures 6.57 and 6.58 show results of the implemented sensorless induction motor drive operating with position control. The coupled DC machine is again set to provide a constant load torque. The estimated position signal is used as the position signal feedback. The position controller of the sensorless IM drive provides a reference ω_R^* for the internal speed cascade control loop as explained in section 2.4.1. In the control structure the same speed controller as implemented in the previous section is used. Neither the reference speed output of the position controller ω_R^* nor the reference torque output of the speed controller i_q^* is limited by a ramp. The position control loop contains only a P controller since the position transfer function provides already a pure integral term to ensure no steady state error. K_P of the speed controller is set in the range of 0.5 to 1.5 1/ s. The parameter of the P position controller and the PI speed controller were adjusted experimentally to achieve the best performance.

It should be noted that only incremental position can be measured from the rotor bar modulation. Therefore the absolute rotor position is not known and the position control is also only achieved incrementally. For the experiments the zero position value was initialised manually. The reference position is changed to one mechanical revolution (2 electrical periods) forward and backwards. The reference position ramp is set to 360 electrical degrees per second. Figures 6.57 and 6.58 show in plot (a) the measured mechanical rotor position λ_R and the estimated rotor position λ^e_R, and plot (b) shows the difference between the position signals. Plot (c) shows i_d^e and i_q^e of the vector controlled sensorless drive and plot (d) shows the measured currents in the $\alpha\beta$ frame. Plot (e) shows the measured and estimated mechanical speed n_R and n_R^e. Plot (f) shows the resulting frequency of the stator currents. In plots (g) and (h) are the measured equivalent impedance vector $\underline{z}'_{PWM2}$ components and the look up table compensation values (LUT) shown.

Figure 6.57 shows the result of the experiment performed with low load. It can be seen that the sensorless drive follows the reference position and keeps the operation stable at zero speed at the demanded position value. The position error is, as in the most experiments before, in the range of +/-6 electrical degrees.

Figure 6.58 shows the same experiment as in Figure 6.57 but with high load torque. It can be seen that the torque producing current component i_q^e reaches up to 100 % of rated value. The settling to the final position value takes longer than in the experiment with no load. This is due to the limited acceleration torque capability of the sensorless drive and the resulting low speed controller dynamic. However, the demanded position value is reached. The position estimation error is slightly higher than in the experiment with low torque.

The results of Figures 6.57 and 6.58 show that the sensorless position control of the implemented drive is achieved. The dynamic is not very high due to the torque response limitation in the rotor bar modulation decoupling described before. However, it is shown that a relatively precise position control of the induction machine is possible by using only the small saliency modulation information of the rotor bar slotting.

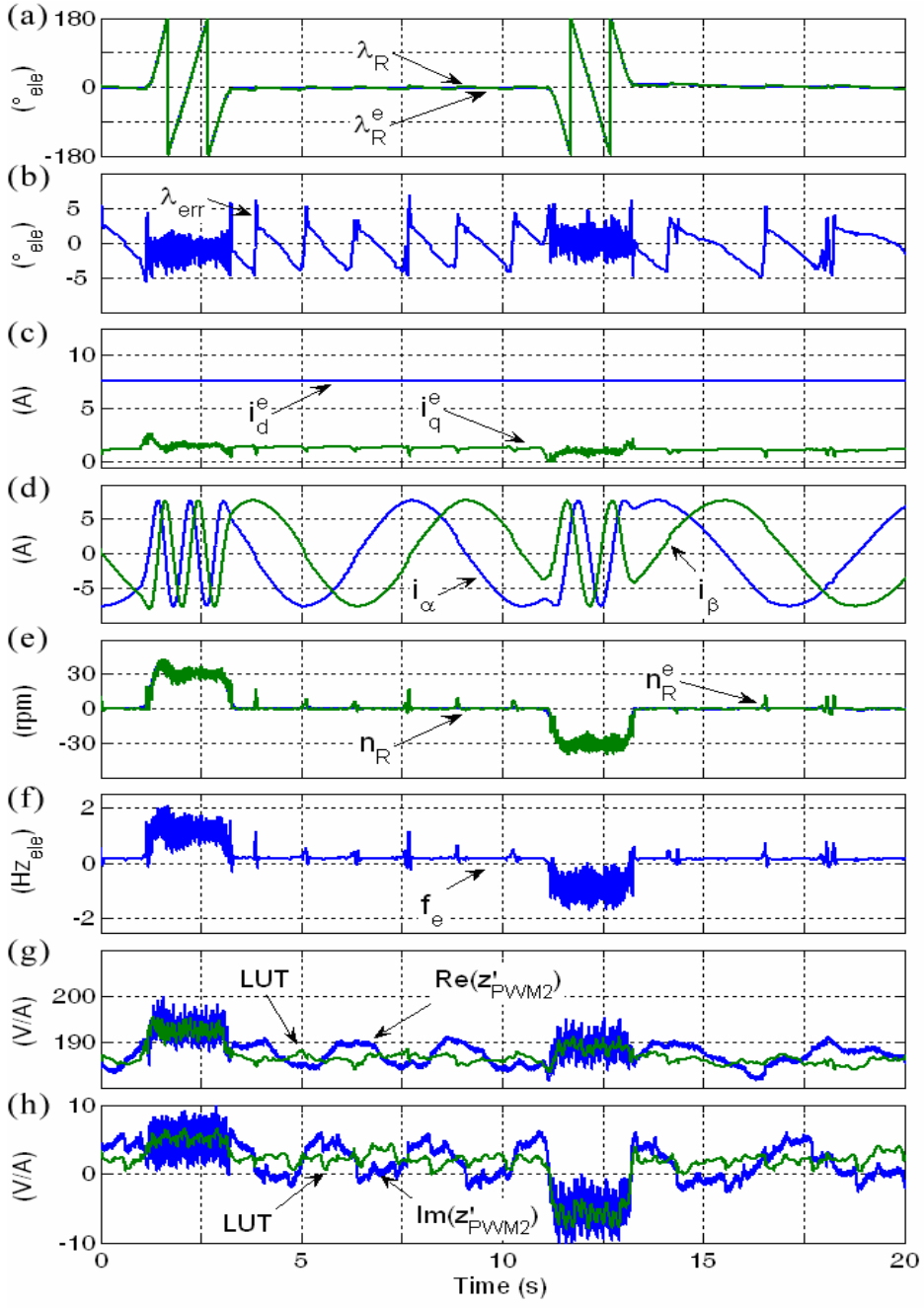

Figure 6.57: Sensorless position control of one mechanical revolution forward and backward at low load

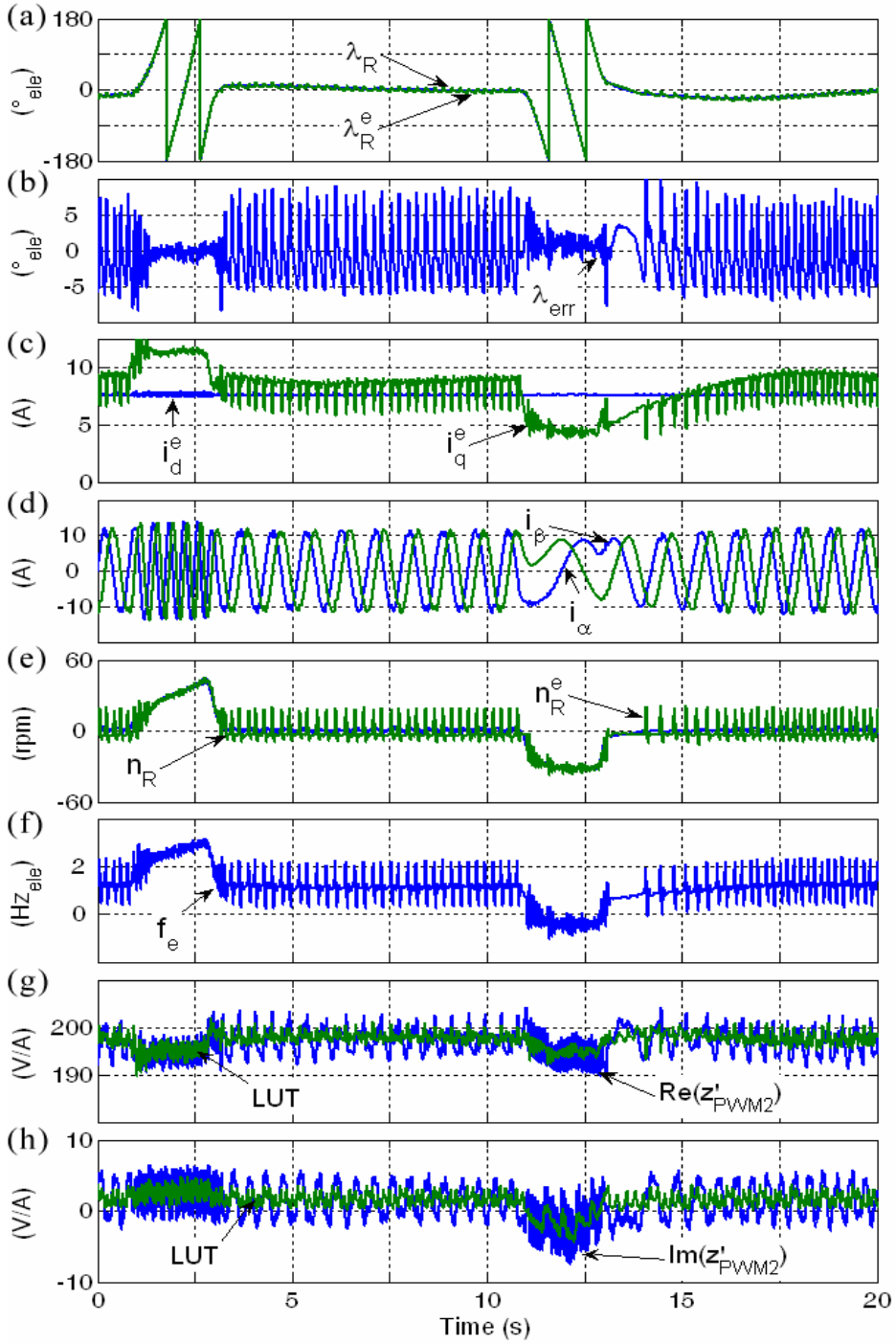

Figure 6.58: Sensorless position control of one mechanical revolution forward and backward at high load

6.6 Conclusions

In this chapter it was shown that the natural switching related harmonics contained in PWM voltages can be used for the sensorless control of induction machines. Hence no additional test signal injection is required and the fundamental control of the drive will be unaffected. The theory was developed to show that the principle is very similar to standard high frequency injection methods. A high frequency AC signal is used to detect the predominantly inductive impedance saliency of the machine windings. The major difference here is that no additional HF signal is injected into the machine, but only part of the inherit PWM ripple is used as HF signal. The nature of the PWM carrier harmonics is analyzed and it is shown that using a basic pulse width modulation strategy the 2^{nd} PWM carrier harmonic gives the best option to detect the machine equivalent impedance. It is shown that the PWM harmonics do not form a constant signal, but that they are directly dependent on the required fundamental voltage, i.e. the required torque, flux and speed. However, this is taken into account by measuring both the voltages and the currents. The high frequency excitation due to the 2^{nd} harmonic of the PWM voltage waveform is used for the detection of an equivalent impedance. The equivalent impedance is calculated by a complex division using the demodulated high frequency voltage and current vector variables. The measured equivalent impedance shows several modulation effects due to the rotor bar slotting, saturation and inverter non-linearity. It is shown that a precise decoupling of the rotor bar position saliency from all other effects is required. A simple look up table compensation scheme is implemented to decouple the wanted rotor bar modulation from other effects. Even though the rotor bar modulation in the used standard off-the-shelf induction machine is very small, sufficient position information can be retrieved for position and speed estimation. Furthermore, a dual PLL structure can be used to improve the signal tracking [91]. Experimental results for torque, speed and position sensorless drive control including zero electrical and mechanical speed under rated torque validate the proposed technique.

Chapter 7

Final Conclusions and Discussions

In recent research several sensorless techniques for low and zero speed operation have been successfully implemented that use the magnetic saliency information of the machine. High frequency signals or active test voltage vectors are injected on the machine for the saliency detection. The problem remaining is that the machine currents show significant distortions due to the injected test signals. This causes several disadvantages, i.e. additional losses, torque ripple and EMV problems. The main disadvantage is however audible noise, that makes these techniques unattractive for many applications, i.e. in automotive applications.

The aim of this work was to develop new sensorless strategies for low and zero speed operation, but without additional test signals injected on the machine. The main idea is to use the natural PWM voltage, generated by the inverter for the fundamental control of the machine, as signal excitation for the saliency detection. The inverter switches the voltage between several voltage vectors during each PWM cycle. The current response to these voltage vectors can be analysed in the time domain. Further the resulting PWM frequency carrier harmonics can be analysed in the frequency domain. Two methods have been developed and successfully implemented in an experimental rig. No modifications of the fundamental PWM are made. Therefore only the fundamental voltage for the machine operation in field orientated vector control is applied on the machines.

One method works for sensorless control of permanent magnet synchronous machines. In there the current derivative during the PWM period zero vectors is measured. The resulting position tracking signal is a combination of a back EMF and a saliency term. With the used machine, in motoring operation both terms reinforce each other, while in regenerative mode both terms oppose each other. Operation down to zero speed has been achieved with the sensorless drive in motoring mode. However, a small operation range in the regenerative operation exists, where no stable steady state operation is possible.

It was found that the measured current derivative signal used for the position tracking is significantly affect by inverter non-linearity. The effect was analysed in detail and it was found that the resistance of the inverter switching devices have a detrimental effect on the position error signal. The resistance of the inverter semiconductors is non-linear dependant on the currents in the devices and the analytical compensation is rather difficult. Therefore an inverter non-linearity compensation look up table is used. It was shown that the precision of the inverter non-linearity compensation has a direct effect on the quality of the position tracking, particular at low and zero speed. The inverter non-linearity effect becomes less significant at higher speeds when the back EMF error signal rises. However, at low and zero speed operation the compensation for inverter non-linearity is essential. Results have been shown with the implemented sensorless PMSM drive in toque and speed control with low and high load.

A second technique has been developed for the sensorless control of induction machines. The natural second PWM carrier harmonic is used to measure a stator equivalent impedance. The principle is similar to standard high frequency injection methods. The main difference is that the amplitude and direction of the "injected" high frequency voltage depends directly on the fundamental machine voltage. Therefore the measured stator voltages and currents are used for the calculation of the complex equivalent impedance vector. The tip of the resulting equivalent impedance vector shows modulation due to rotor bar slotting. Even if the rotor bar

modulation is only about 1 to 1.5 % of the average stator equivalent impedance vector magnitude, the rotor bar modulation allows tracking of the mechanical rotor movement.

The measured equivalent impedance vector is further significantly affected by saturation and inverter non-linearity effects. A look up table is used to decouple the desired rotor bar modulation from all other effects. The look up table was generated for the entire operation range of the drive and is referenced by three input variables. The decoupling of the rotor bar modulation has been achieved with the simple static look up table. However the signal to noise ratio of the small rotor slotting effect is rather poor. Particular dynamic effects during torque transients show strong disturbances. A phase locked loop structure has been developed that enhances the rotor bar position tracking quality. Results are presented of the sensorless induction machine drive in torque, speed and position control. The drive shows stable operation in all operation points including zero electrical and mechanical frequency with no and high load.

It has been shown in this work that the natural PWM of the voltage source inverter provides the possibility of retrieving saliency based rotor position information without additional test signal injection. Since the PWM voltage generation is not modified by the sensorless estimation techniques the operation of the drive is not affected. The disadvantage of excessive current ripples caused by additional test signal injection has been removed. For the implementations at this experimental stage the PWM switching frequencies were set to a rather low value. Of course this causes larger natural PWM harmonics than at higher PWM switching frequencies. However, for large drives the used low PWM switching frequencies are realistic values. The resulting total current ripples are still much less than with methods that use additional high frequency injection. Therefore also the audible noise is lower, within an acceptable range.

In this research inverter non-linearity effects have been identified as the main problem. Further multiple saliency effects in the induction machine (rotor bar slotting, saturation modulation) cause difficulties in the signal decoupling. These problems have been reported in most works that use additional test signal injection. The conclusion is that in this work techniques have been developed that remove the problems associated with addition test signal injection. No additional high frequency current ripple, due to a sinusoidal test voltage injection, or current spices, due to the application of active voltage test vector, exist. Thus additional losses, torque ripple and increased EMV problems, causes by the current disturbances associated with additional test signal injections, are avoided. As main improvement the unwanted audible noise due to additional test signal injections is avoided. However, the well known problems of inverter non-linearity disturbances and multiple saliencies in induction machines are still present. Look up table compensation schemes have been used for the compensation of the disturbing effects. Even if these look up tables are quite complex, the required memory space is not problematic in modern microcontroller systems. However the commissioning of the look up tables might be problematic in practical sensorless drive applications.

7.1 Future Work

As is shown there is a small operation range in the ZeroVector Current Derivative method where the zero vector current derivative signal provides no useful position tracking information. Further the error signal polarity has to be adjusted according to the drive current and speed. This information is available by the sensorless controller. However, due to the noise in the estimate speed, the speed feedback has to be low pass filtered. This low pass filtering produces an undesired delay. The speed signal could be improved by implementing a mechanical observer. That could provide a smoother speed signal with no delay in the estimated rotor speed. The task

is made more complex, since the parameter of the mechanical model (inertia, friction, load torque) should be known.

The current derivative is derived from discrete current samples. In order to ensure a good measurement, a minimum duration between the two successive is required. Therefore the maximal used output voltage is limited to approximately 30 % of rated value. That means that rated speed and high load can not be achieved with this voltage limitation. This limitation could be extended by implementing for instance a different PWM technique that provides longer zero vectors or using dedicated *di/dt* sensors that measure the current derivative over a shorter period of time. It would also possible to extent the machine operation at high speed by complementing the drive by an additional model based sensorless technique.

An inverter non-linearity compensation function needs to be implemented if operation at very low/ zero speed is required. In this work the used look up table is generated from experiments under sensored condition. This procedure is not desirable in a commercial drive. However, it is shown that this inverter non-linearity signal is independent on the rotor speed. Therefore the compensation profile could be measured at higher speed by operating the machine by e.g. a sensorless model based method. It was also shown that this inverter non-linearity is caused mainly by the unbalanced resistances in the inverter legs. It could be investigated if a commission procedure can be developed that determines this inverter specific compensation function with a different load. Therefore the compensation function could be acquired and stored into the inverters control system directly after manufacturing. Ones the resistance unbalance function is determined it should be load independent, as long as the load consists of a balanced set of resistances.

In the developed technique for the sensorless control of induction machines by using PWM harmonics for rotor bar saliency tracking the PWM harmonic HF voltage excitation is varying with the fundamental voltage generation. Therefore the three phase voltages are measured by using three voltage transducers. The introduction of additional voltage sensors is undesirable, mostly because it will increase the cost of

the system. However, the drive reference voltage and the generated PWM switching pattern is known by the DSP control system. Therefore the require PWM2 voltage vector can be mathematically derived from the reference PWM duty cycles. It is expected that the task is made more complex since inverter non-linearity effects like dead time, current clamping and voltage drops over the switching devises change the real output voltage from the generated reference voltage. However, noise and oscillations that might be due to the voltage measurement would be removed. Therefore a reconstructed voltage HF signal from the reference PWM duty cycles could get even a better result then the direct measured voltage PWM2 harmonic.

For the practical implementation only a standard off-the-shelf induction machine was available. Such kind of machine is usually bound to show very small rotor slotting effects due to the rotor bar skewing and the semi-closed or closed rotor bars. It has been realised by researchers [22], [25], [27], [45], [53] that a non-skewed squirrel cage design with open rotor bars should give naturally a larger detectable stator impedance modulation. The tracked rotor bar modulation signal of the used machine is only 1 to 1.5 %. With a machine design that gives a larger rotor bar modulation, the signal to noise ration of the wanted modulation could be significant improved.

The used look up table for the rotor bar modulation decoupling has been created by running the drive under sensored condition by using an encoder. For a practical implementation this is highly undesirable. Since no continuous zero speed operation is required for the look up table generation, a model based sensorless technique could be used to sweep trough the required operation conditions for the compensation look up table generation. Therefore the required compensation look up table could also be generated in an auto commissioning procedure under sensorless condition.

As was shown, transient effects deteriorate the static look up table compensation. This is already significant improved by the used PLL structure. However, by including more information about the drive system into the signal conditioning, for instance by using a mechanical observer, the dynamic performance and stability of the drive could be probable further increased.

The dynamic conditions in the compensation look up table could be further investigated. A better knowledge of the nature in the offset dynamics during the drive transients could provide solutions to take the transient behaviour additional into account to the static look up table compensation.

In this work only one PWM generation scheme is implemented. However, a big variety of pulse width modulation techniques has been reported in literature. An investigation of several PWM strategies could be carried out. The result could be that a different PWM strategy would allow a simpler implementation with better performance.

In the here presented work it was only attempt to track the rotor bar slotting modulation in an induction machine. However, the same idea of using the PWM harmonics for saliency detection could be transferred to other machine designs, i.e. permanent magnet synchronous machines or switched reluctance motors.

7.2 Publications

The present work has resulted in five papers [74], [75], [82], [84] and [91] published at international conferences.

Appendix A
Determination of Induction Machine Parameters

Not all information required for the implementation of the in section 2.3.2 explained vector control scheme was available from the machine nameplate. Particular the rated machine stator currents i_{Sd}, i_{Sq} and the rotor time constant τ_R need to be known. The other parameters referring to the equivalent circuit shown in Figure 2.7 are also derived from three simple tests. The test are: DC test, locked rotor and no load test. Since the ohmic machine resistance are temperature dependent the tests were carried out when the machine was warm after some loaded operation. Thus the measured parameters reflect values approximately at operation temperature.

A.1 DC Test

The DC test is used to measure the stator windings ohmic resistance. The principle is very basic. A constant DC voltage is applied to two stator terminals and the current is measured. The ratio of the resulting DC current to the constant DC voltage gives the ohmic stator resistance. The ohmic resistance could be also simpler measured with a standard multi meter. However, since the resistance value is small a measurement at a large current level gives a more reliable result.

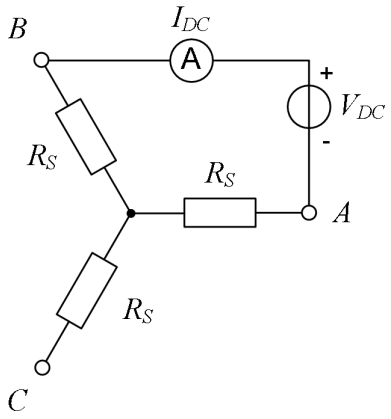

Figure A.1: Circuit of induction machine DC test

Figure A.1 shows a schematic of the DC test circuit. The same measurement was repeated for all three phase combinations. Table A.1 states the measured values and the used average values for the stator winding resistance calculation.

	V_{DC} (V)	I_{DC} (A)
AB	30.65	4.5
BC	30.64	4.53
CA	30.65	4.56
Average	30.65	4.53

Table A.1: Measurements of induction machine DC test

The stator winding resistance is then simply calculated by:

$$R_S = \frac{1}{2}\frac{V_{DC}}{I_{DC}} = \frac{1}{2}\frac{30.65\,\mathrm{V}}{4.53\,\mathrm{A}} = 3.38\,\Omega \qquad \text{(A.1)}$$

A.2 Locked Rotor Test

The locked rotor test is used to determine the rotor resistance and the leakage impedances. For the test the rotor is mechanical locked and the machine is fed by a three phase AC voltage with rated frequency and rated current. The voltage is provided by a variable transformer. The machine voltage is slightly increased until the rated machine current is reached. Figure A.2 shows the connection of the used measurement device (Fluke 39 Power meter) [94]. With the Fluke 39 Power meter the voltage and current is measured simultaneous for each phase. The power meter measures also the phase shift between the AC current and voltage. The measurement is repeated for all three phases and for the calculation the average of the measurement values is used.

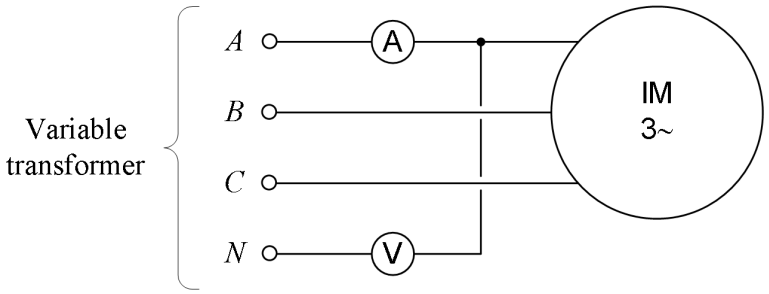

Figure A.2: Connection of power meter for measurement of phase voltage and phase current

Form the measured phase voltage and phase current the power and reactive power per phase is calculated. The resulting impedance parameters Z' refers then to the machine equivalent circuit in wye connection shown in Figure A.3 (a). The impedance values of the real machine windings, which are connected in delta as shown in Figure A.3 (b), can be easily calculated by equation (A.2). The superscript "Y" is used to mark the machine impedances referred to the wye equivalent circuit.

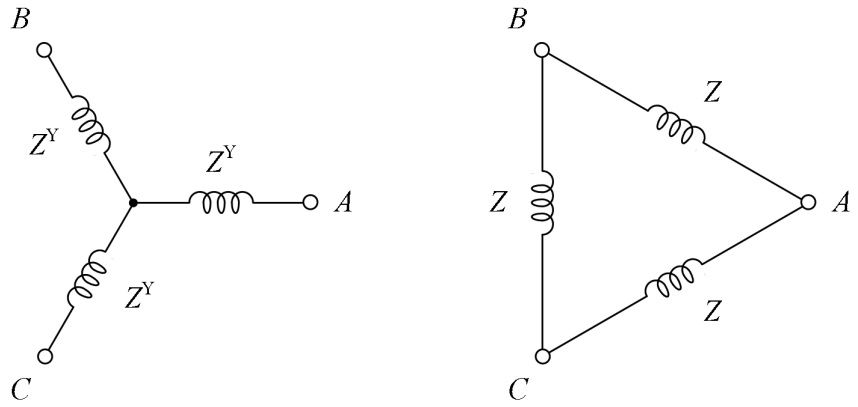

Figure A.3: Windings impedances, (a) wye equivalent impedances, (b) in delta connection

$$Z = 3Z^Y \tag{A.2}$$

Table A.2 shows the measured values with the connected power meter. The voltage and current values are RMS values.

	P (W)	S (VA)	Q (VAR)	cos(φ)	v_S (V)	i_S (A)
A	170	460	430	0.38	44.6	10.32
B	240	560	500	0.44	53.9	10.32
C	250	490	430	0.51	47.9	10.30
Average	220	503	453	0.44	48.8	10.31

Table A.2: Measurements of induction machine locked rotor test

The equivalent circuit shown in Figure A.4 is used for the calculation of the rotor resistance and leakage inductance values. It is assumed that under the locked rotor experiment most of the current is directly transformed into the rotor side and the magnetizing current is small. Therefore the magnetizing inductance branch of the

induction machine equivalent circuit is left out for simplicity. From the measured phase voltage and phase current the phase equivalence impedance Z^Y is calculated as shown by equation (A.3). The resistive part is the sum of the stator and rotor resistances R_S and R_R whereas the reactive part of the impedance is the sum of the stator and rotor leakage inductance $L_{S\sigma}$ and $L_{R\sigma}$. As the stator resistance is already determined in the DC experiment, the rotor resistance can be easily calculated from equation (A.4). From equation (A.5) and (A.6) the total leakage inductance value can be calculated. It is not exactly known which portion belongs to the stator and which portion belongs to the rotor side. According to [95] it is assumed that the total leakage inductance is split equal to the rotor and stator side. The stator and rotor impedance is therefore calculated by equation (A.7).

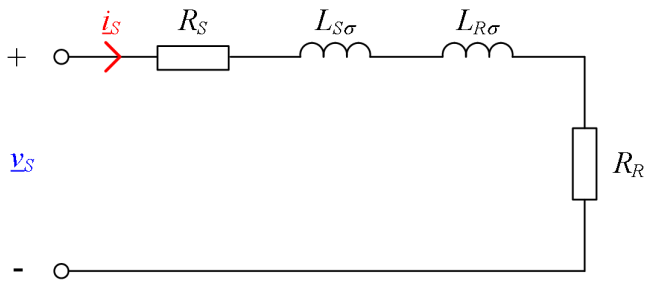

Figure A.4: Induction machine equivalent circuit for locked rotor test

$$Z^{\mathrm{Y}} = \frac{\underline{v}_S}{\underline{i}_S} = \frac{48.8\,\mathrm{V}}{10.31\,\mathrm{A}\,\mathrm{e}^{\mathrm{j}63.7°}} = (2.098 + j4.241)\frac{\mathrm{V}}{\mathrm{A}} \tag{A.3}$$

$$R_R{}^{\mathrm{Y}} = 2.098\Omega - R_S{}^{\mathrm{Y}} = 1.128\Omega \tag{A.4}$$

$$X_\sigma{}^{\mathrm{Y}} = \left(L_{S\sigma}{}^{\mathrm{Y}} + L_{R\sigma}{}^{\mathrm{Y}}\right)2\pi\,50\,\mathrm{Hz} = 4.241\frac{\mathrm{V}}{\mathrm{A}} \tag{A.5}$$

$$L_{S\sigma}{}^{\mathrm{Y}} + L_{R\sigma}{}^{\mathrm{Y}} = \frac{X_{\sigma}{}^{\mathrm{Y}}}{2\pi\,50\,\mathrm{Hz}} = 13.5\,\mathrm{mH} \tag{A.6}$$

$$L_{S\sigma}{}^{\mathrm{Y}} = L_{R\sigma}{}^{\mathrm{Y}} = \frac{13.5\,\mathrm{mH}}{2} = 6.75\,\mathrm{mH} \tag{A.7}$$

A.3 No Load Test

The no load experiment is used to calculate the parameter of the magnetising impedance and rated i_{Sd} and i_{Sq}. The rated supply voltage is applied to the machine. Under no load condition the rotor is rotating almost at synchronous speed and the slip frequency is near zero. Therefore the rotor currents are approximately zero and the entire machine current is passing though the magnetising inductance. In the test the machine is not loaded by an external load, but the internal friction losses of the rotor bearings causes a small slip frequency and hence also small rotor currents. However these effects are small and therefore neglected to simplify the calculations. The equivalent circuit shown in Figure A.5 is used for the calculation. The rotor branch is simply left out. The measurement of the machine phase voltage and phase current is also done as shown in Figure A.2. Table A.3 shows the measured and average values. The voltage and current values are RMS values.

	P (W)	S (VA)	Q (VAR)	cos(φ)	v_S (V)	i_S (A)
A	170	1300	1290	0.13	244	5.34
B	190	1310	130	0.14	242	5.46
C	150	1290	1280	0.12	244	5.29
Average	170	1300	1290	0.13	243.3	5.36

Table A.3: Measurements of induction machine no load test

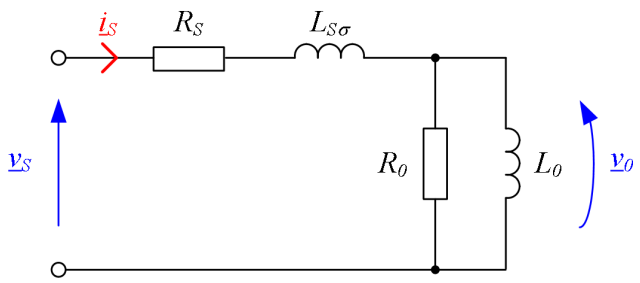

Figure A.5: Induction machine equivalent circuit for no load test

The values of the stator resistance and leakage stator impedance are already determined in the DC and locked rotor test. Subtracting the voltage drop over these impedance values, the voltage over the magnetising inductance v_0 can be calculated as:

$$\begin{aligned}\underline{v}_0 &= \underline{v}_S - \left(R_S{}^{\mathrm{Y}} + jX_{S\sigma}{}^{\mathrm{Y}}\right)\underline{i}_S = 243.3\,\mathrm{V} - \left(1.128 + j2.12\right)\frac{\mathrm{V}}{\mathrm{A}}5.36\,\mathrm{A}\,e^{-j82.5°} \\ &= 231.3\,\mathrm{V}\,e^{j1.12°}\end{aligned} \quad . \tag{A.8}$$

The real and reactive power of the magnetising air gap impedance can be calculated by equations (A.9) and (A.11). $R_0{}^{\mathrm{Y}}$ and $X_0{}^{\mathrm{Y}}$ can then be calculated by equation (A.10) and (A.12). From $X_0{}^{\mathrm{Y}}$ the magnetising inductance $L_0{}^{\mathrm{Y}}$ is derived from equation (A.13).

$$\begin{aligned}P_0 &= P_S - R_S{}^{\mathrm{Y}}\, i_S{}^2 = 170\,\mathrm{W} - 1.128\,\Omega\left(5.363\,\mathrm{A}\right)^2 \\ &= 137.3\,\mathrm{W}\end{aligned} \tag{A.9}$$

$$\begin{aligned}R_0{}^{\mathrm{Y}} &= \frac{v_0{}^2}{P_0} = \frac{\left(231.3\,\mathrm{V}\right)^2}{137.3\,\mathrm{W}} \\ &= 388.9\,\Omega\end{aligned} \tag{A.10}$$

$$\begin{aligned} Q_0 &= Q_S - X_{S\sigma}{}^{\mathrm{Y}}\, i_S{}^2 = 1290\,\mathrm{VAR} - 2.12\,\frac{\mathrm{V}}{\mathrm{A}}\left(5.363\,\mathrm{A}\right)^2 \\ &= 1229\,\mathrm{VAR} \end{aligned} \tag{A.11}$$

$$\begin{aligned} X_0{}^{\mathrm{Y}} &= \frac{v_0{}^2}{Q_0} = \frac{\left(231.3\,\mathrm{V}\right)^2}{1229\,\mathrm{VAR}} \\ &= 43.53\,\frac{\mathrm{V}}{\mathrm{A}} \end{aligned} \tag{A.12}$$

$$L_0{}^{\mathrm{Y}} = \frac{X_0{}^{\mathrm{Y}}}{2\pi\,50\,\mathrm{Hz}} = 138.5\,\mathrm{mH} \tag{A.13}$$

From the magnetising inductance, the beforehand determined rotor leakage impedance and rotor resistance the rotor time constant can be calculated by:

$$\begin{aligned} \tau_R{}^{\mathrm{Y}} &= \frac{L_0{}^{\mathrm{Y}} + L_{R\sigma}{}^{\mathrm{Y}}}{R_R{}^{\mathrm{Y}}} = \frac{138.5\,\mathrm{mH} + 6.75\,\mathrm{mH}}{0.97\,\Omega} \\ &= 150\,\mathrm{ms} \end{aligned} \quad . \tag{A.14}$$

Table A.4 summarises the determined machine impedance parameters. The values for the wye equivalent circuit and the parameter values to the in delta connected windings are given.

	Wye equivalent circuit	Winding value
Stator resistance	R_S^{Y} = 1.13 Ω	R_S = 3.38 Ω
Rotor resistance	R_R^{Y} = 0.97 Ω	R_R = 2.91 Ω
Stator leakage impedance	$L_{S\sigma}^{Y}$ = 6.75 mH	$L_{S\sigma}$ = 20.25 mH
Rotor leakage impedance	$L_{R\sigma}^{Y}$ = 6.75 mH	$L_{R\sigma}$ = 20.25 mH
Air gap resistance	R_0^{Y} = 388.9 Ω	R_0 = 1166.7 Ω
Air gap inductance	L_0^{Y} = 138.5 mH	L_0 = 415.5 mH
Stator time constant	τ_R^{Y} = 150 ms	τ_R = 150 ms

Table A.4: Summary of determined machine parameters

The current flowing at no load condition is only the magnetising current. Therefore i_{Sd} under rated condition can be derived, which is defined to be the amplitude of the measured sinusoidal AC current. Therefore i_{Sd} is set to 7.6 A in vector control. Knowing the value of rated i_{Sd} and the rated current vector amplitude gives further the result of i_{Sq}. The rated current amplitude is 14.6 A, therefore i_{Sq} is 12.5 A.

.

Appendix B
PCB Design of FPGA Periphery Control Board

The designed FPGA periphery control board provides a flexible and robust solution for integrating the C6713 DSK development board [55] into real time motor control applications. The C6713 DSK board accommodates a 32-bit floating point DSP (TMS320C6713 [56]) by Texas Instruments running at 225 MHz clock frequency. Additional are 16 MB synchronous DRAM available on the TMS320C6713 DSK board. This provides a powerful real time standalone controller platform. However, for integration of the C6713 DSK board into practical motor control application, several interfaces such as PWM outputs and multi channel A/D converters are required. The C6713 DSK periphery board has been designed to provide adequate hardware periphery for motor control systems. The two 80-pin connectors External Memory Interface (EMI) and External Peripheral Interface (EPI) are used for a memory mapped integration of the FPGA periphery control board to the C6713 DSK micro processor platform. For achieving a highly integrated design a FPGA is used in which the periphery control functions are implemented. Only the A/D and D/A converters are implemented in external circuits. A flash reprogrammable FPGA (Actel A3PE600) [59] has been selected, providing the possibility of in line reprogramming. Thus the peripheral configuration and the included hardware

functionality of the FPGA periphery control board is reconfigurable, providing a maximum of flexibility.

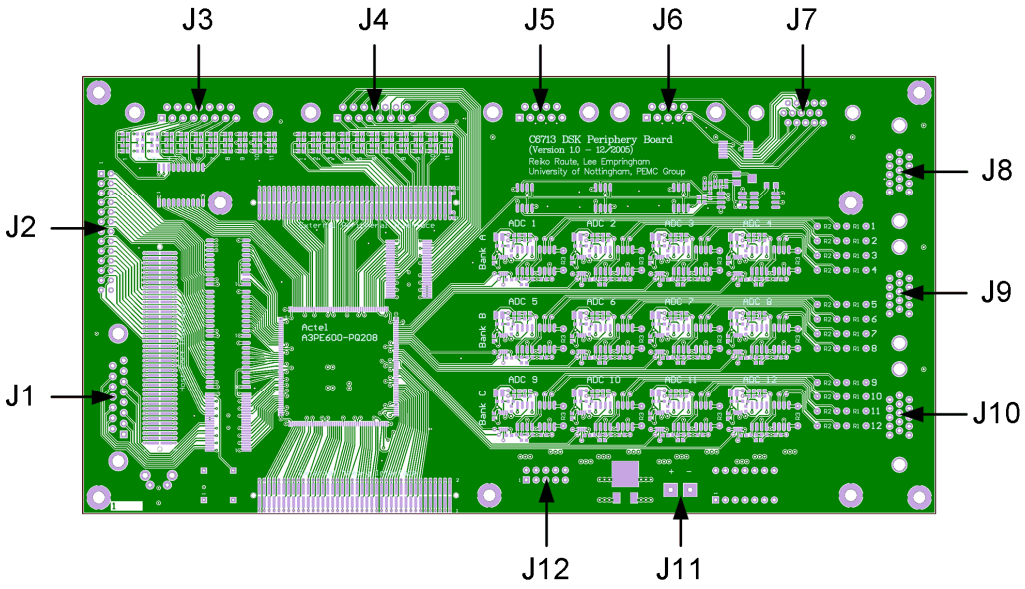

Figure B.1: Outline of the PCB

The FPGA periphery control board digital and analogue interfaces are provided at several connectors accommodated onto the PCB shown in Figure B.1.

B.1 Inverter Interface

The inverter interface J1 is a 26-pin 0.1 IDC connector. It provides 18 digital output signal suitable for controlling 18 inverter switching devices. Therefore this interface unit is capable of driving standard 6 switch inverters, as well as 3-phase to 3-phase matrix converters and other multi switch power electronics units such as multilevel and multiphase inverters. There are also 5 digital input signals provided, usable for inverter feedback signal such as trip and operation state signals. The output signals are 5V TTL level. For the input signals 3.3 V LVTTL and 5 TTL levels are accepted. +5V, +3.3V and digital ground from the C6713 DSK periphery board are also available on the inverter interface connector. Table B.1 shows the signal allocation of

the inverter interface connector. The column "I/O" symbolised if the signal is an input or output of the FPGA periphery control board. "I" means the signal is an input signal and "O" means the signal is an output of the FPGA periphery control board.

Pin	**I/O**	**Signal**	**Description**
1	O	+5V	Power output
2	O	PWM1	PWM Switching signal 1
3	O	PWM2	PWM Switching signal 2
4	O	PWM3	PWM Switching signal 3
5	O	PWM4	PWM Switching signal 4
6	O	PWM5	PWM Switching signal 5
7	O	PWM6	PWM Switching signal 6
8	O	PWM7	PWM Switching signal 7
9	O	PWM8	PWM Switching signal 8
10	O	PWM9	PWM Switching signal 9
11	O	PWM10	PWM Switching signal 10
12	O	PWM11	PWM Switching signal 11
13	O	PWM12	PWM Switching signal 12
14	O	+3.3 V	Power output
15	O	PWM13	PWM Switching signal 13
16	O	PWM14	PWM Switching signal 14
17	O	PWM15	PWM Switching signal 15
18	O	PWM16	PWM Switching signal 16

19	O	PWM17	PWM Switching signal 17
20	O	PWM18	PWM Switching signal 18
21	I	II_in1	Inverter Interface Input signal 1
22	I	II_in2	Inverter Interface Input signal 2
23	I	II_in3	Inverter Interface Input signal 3
24	I	II_in4	Inverter Interface Input signal 4
25	I	II_in5	Inverter Interface Input signal 5
26	O	DGND	System ground

Table B.1: Inverter Interface (J2)

B.2 Encoder Interface

The encoder interface (J2) provides 8 digital inputs via a 15-way Sub-D connector. As input four differential signals of a quadrature encoder, i.e. track A (A), track B (B), zero marker (Z) and strobe signal (S) are provided. 5 V TTL and 3.3 V LVTTL voltage signals can be used. Additional +5 V, +3.3 V and digital ground are provided on the connector. Table B.2 shows the signal allocations of the encoder interface connector J2.

Pin	I/O	Signal	Description
1	O	+5 V	Power output
2	I	A	Encoder track A signal
3	I	/A	Encoder track /A signal
4	O	+5 V	Power output
5	I	B	Encoder track B signal

6	I	/B	Encoder track /B signal
7	O	+5 V	Power output
8	O	+3.3 V	Power output
9	O	DGND	System ground
10	I	Z	Encoder track Z signal
11	I	/Z	Encoder track /Z signal
12	O	DGND	System ground
13	I	S	Encoder track S signal
14	I	/S	Encoder track /S signal
15	O	DGND	System ground

Table B.2: Encoder Interface (J1)

B.3 General Purpose Digital I/O Connectors

Connectors J3 and J4 provide each 11 digital input or output pins. The digital output signals are 5 V TTL level. The input signals can be 3.3 V LVTTL or 5 V TTL logic. +5 V, +3.3 V and digital ground are also provided on the general purpose digital I/O interface connectors. Table B.3 and Table B.4 show the pin allocations of the general purpose I/O connectors J3 and J4. The logical stated of the digital signals are indicated by the LED's next to the connectors. As driver circuits are 74ABT541 ICs [96] used which have a driving capability of up to 32 mA for high level and 64 mA for low level. The LED's on the digital outputs are directly driven by the output buffer circuits. The LED's consume already approximately 7 mA for high and approximately 4 mA for low level.

Pin	I/O	Signal	Description
1	O	DOUT bit 1	Digital Output bit 1
2	O	DOUT bit 2	Digital Output bit 2
3	O	DOUT bit 3	Digital Output bit 3
4	O	DOUT bit 4	Digital Output bit 4
5	O	DOUT bit 5	Digital Output bit 5
6	O	DOUT bit 6	Digital Output bit 6
7	O	DOUT bit 7	Digital Output bit 7
8	O	DOUT bit 8	Digital Output bit 8
9	O	DOUT bit 9	Digital Output bit 9
10	O	DOUT bit 10	Digital Output bit 10
11	O	DOUT bit 11	Digital Output bit 11
12	O	+3.3 V	Power output
13	O	+5 V	Power output
14	O	DGND	System ground
15	O	DGND	System ground

Table B.3: Digital OUT (J3)

Pin	I/O	Signal	Description
1	I	DIN bit 1	Digital Input bit 1
2	I	DIN bit 2	Digital Input bit 2
3	I	DIN bit 3	Digital Input bit 3

4	I	DIN bit 4	Digital Input bit 4
5	I	DIN bit 5	Digital Input bit 5
6	I	DIN bit 6	Digital Input bit 6
7	I	DIN bit 7	Digital Input bit 7
8	I	DIN bit 8	Digital Input bit 8
9	I	DIN bit 9	Digital Input bit 9
10	I	DIN bit 10	Digital Input bit 10
11	I	DIN bit 11	Digital Input bit 11
12	O	+3.3 V	Power output
13	O	+5 V	Power output
14	O	DGND	System ground
15	O	DGND	System ground

Table B.4: Digital IN (J4)

B.4 Serial Ports

The two serial ports McBSP0 and McBSP1 of the C6713 DSK development board are directly connected through to J5 and J6. On each 9-pole Sub-D connector are all McBSP signals of one DSP serial interface available. Additional are +5 V and digital ground per serial interface connector provided. Table B.5 and Table B.6 show the signal allocations of the serial interface connectors J5 and J6.

Pin	I/O	Signal	Description
1	I	DR0	McBSP0 receive data (EPI#30)

2	I/O	FSR0	McBSP0 receive frame sync (EPI#29)
3	I/O	CLKR0	McBSP0 receive clock (EPI#27)
4	O	DX0	McBSP0 transmit data (EPI#24)
5	I/O	FSX0	McBSP0 transmit frame sync (EPI#23)
6	I	CLKS0	McBSP0 clock source (EPI#22)
7	I/O	CLKX0	McBSP0 transmit clock (EPI#21)
8	O	+5 V	Power output
9	O	DGND	System ground

Table B.5: Serial 0 (J5)

Pin	**I/O**	**Signal**	**Description**
1	I	DR1	McBSP1 receive data (EPI#42)
2	I/O	FSR1	McBSP1 receive frame sync (EPI#41)
3	I/O	CLKR1	McBSP1 receive clock (EPI#39)
4	O	DX1	McBSP1 transmit data (EPI#36)
5	I/O	FSX1	McBSP1 transmit frame sync (EPI#35)
6	I	CLKS1	McBSP1 clock source (EPI#34)
7	I/O	CLKX1	McBSP1 transmit clock (EPI#33)
8	O	+5 V	Power output
9	O	DGND	System ground

Table B.6: Serial 1 (J6)

All signals of the McBSP1 serial interface are also connected to the FPGA IC. The signals of McBSP0 are in parallel connected to the on board DAC AD5668 [62].

B.5 Analogue Outputs

For convenience an analogue output unit is provided. As D/A converter the AD5668 [62] is used which offers 8 analogue output channels providing voltage signals in the range of 0 ... +5 V. The digital input values are transmitted by a basic 3 wire synchronous serial interface. The input serial interface is directly connected to the McBSP0 port of the C6713 DSK development board. The analogue output signals are connected to the 15-way HD Sub-D connector J7. Furthermore are +5 V, analogue ground and +/-12 V from the C6713 DSK board connected. Table B.7 shows the signal allocations of the analogue output connector J7.

Pin	I/O	Signal	Description
1	O	AOUT1	Analogue output 1
2	O	AOUT2	Analogue output 2
3	O	+5 V	Power output
4	O	AOUT3	Analogue output 3
5	O	AOUT4	Analogue output 4
6	O	+5 V	Power output
7	O	AOUT5	Analogue output 5
8	O	AOUT6	Analogue output 6
9	O	AGND	Analogue ground
10	O	AGND	Analogue ground
11	O	AGND	Analogue ground
12	O	AOUT7	Analogue output 7
13	O	AOUT8	Analogue output 8

14	O	+12 V DSK	Power output
15	O	-12 V DSK	Power output

Table B.7: Analogue OUT (J7)

B.6 Analogue Inputs

The FPGA periphery control board offers 12 16-bit A/D converters arranged into 3 banks of 4 ADCs. Each analogue input channel has a differential input circuit. For each bank is one dedicated 15-way HD Sub-D connector (J8 to J10) provided. Additional to the analogue input signals are +5 V, analogue ground, +12 V and -12 V of the C6713 DSK board provided.

Pin	I/O	Signal	Description
1	I	AIN1+	Analogue input 1 +
2	I	AIN1-	Analogue input 1 -
3	O	+5 V	Power output
4	I	AIN2+	Analogue input 2 +
5	I	AIN2-	Analogue input 2 -
6	O	+5 V	Power output
7	I	AIN3+	Analogue input 3 +
8	I	AIN3-	Analogue input 3 -
9	O	AGND	Analogue ground
10	O	AGND	Analogue ground
11	O	AGND	Analogue ground

12	I	AIN4+	Analogue input 4 +
13	I	AIN4-	Analogue input 4 -
14	O	+12 V DSK	Power output
15	O	-12 V DSK	Power output

Table B.8: Analogue IN A (J8)

Pin	I/O	Signal	Description
1	I	AIN5+	Analogue input 5 +
2	I	AIN5-	Analogue input 5 -
3	O	+5 V	Power output
4	I	AIN6+	Analogue input 6 +
5	I	AIN6-	Analogue input 6 -
6	O	+5 V	Power output
7	I	AIN7+	Analogue input 7 +
8	I	AIN7-	Analogue input 7 -
9	O	AGND	Analogue ground
10	O	AGND	Analogue ground
11	O	AGND	Analogue ground
12	I	AIN8+	Analogue input 8 +
13	I	AIN8-	Analogue input 8 -
14	O	+12 V DSK	Power output
15	O	-12 V DSK	Power output

Table B.9: Analogue IN B (J9)

Pin	I/O	Signal	Description
1	I	AIN9+	Analogue input 9 +
2	I	AIN9-	Analogue input 9 -
3	O	+5 V	Power output
4	I	AIN10+	Analogue input 10 +
5	I	AIN10-	Analogue input 10 -
6	O	+5 V	Power output
7	I	AIN11+	Analogue input 11 +
8	I	AIN11-	Analogue input 1 -
9	O	AGND	Analogue ground
10	O	AGND	Analogue ground
11	O	AGND	Analogue ground
12	I	AIN12+	Analogue input 12 +
13	I	AIN12-	Analogue input 12 -
14	O	+12 V DSK	Power output
15	O	-12 V DSK	Power output

Table B.10: Analogue IN C (J10)

For the analogue signal acquisition are AD7668 [62] analogue to digital converter devices used. +4.096 V, provided by an ADR434 IC [97], is used as measurement reference voltage. The analogue input signals are passed through several signal conditioning stages before reaching the ADC input, a voltage divider, an instrumentation amplifier, an active 4^{th} order op-amp filter stage and a passive 1^{st} order RC low pass filter. For debugging purpose several test points are provided on

the PCB. Test points are available for several analogue and digital signals. The test point locations are illustrated in Figure B.2 for one ADC circuit cluster. The detailed circuit functionality is shown in the attached schematics of Figures B.4 to B.10.

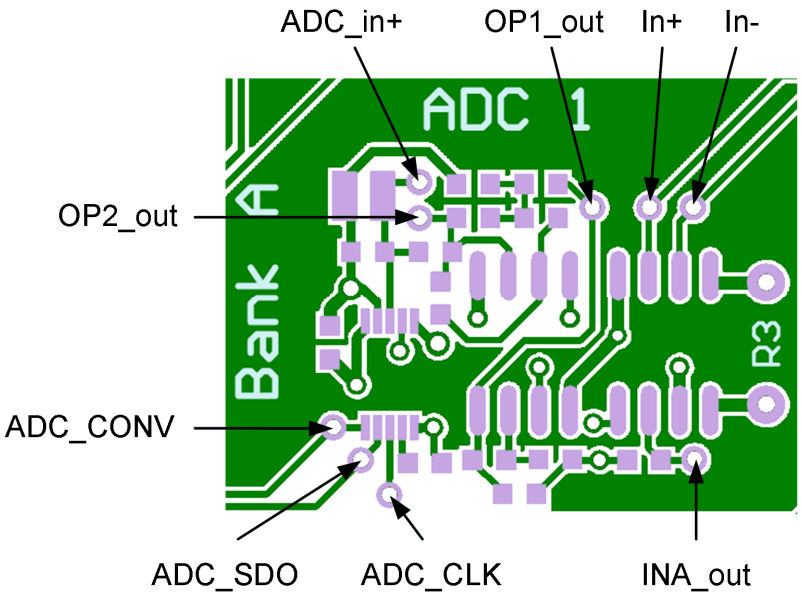

Figure B.2: Test points of analogue inputs circuit

The input voltage divider consists of two basic resistors R1 and R2. Due to the very high instrumentation amplifier input impedance the voltage divider can be regarded as not loaded. Thus, the input voltage divider gain G_1 can be set to any value ≤1 according to:

$$G_1 = \frac{R_2}{R_1 + R_2} \quad . \tag{B.1}$$

In the case of measuring current input signals R2 can be considered as measurement shunt. The instrumentation amplifier gain can be adjusted by adding an external resistor R3 giving the instrumentation amplifier stage gain:

$$G_2 = 1 + \frac{50\,\text{k}\Omega}{R_3} \quad . \tag{B.2}$$

The total gain of the analogue circuit can be calculated by:

$$G_{total} = \frac{R_2}{R_1 + R_2} \cdot \left(1 + \frac{50\,\text{k}\Omega}{R_3} \right) \quad . \tag{B.3}$$

The 12 on board A/D converter are divided into 3 banks. For each bank one common convert start signal is used. All ADC's in one bank are triggered simultaneously. ADC 1 to 4 are regarded as bank A, ADC 5 to 8 as bank B and ADC 9 to 12 as bank C. Each ADC bank has its own connector (J8 to J10). The digital results are uploaded to the FPGA via a basic unidirectional 2 wire synchronous serial interface [62]. Each ADC data signal is connected to a dedicated digital input pin of the FPGA. The data transmit clock signal is commonly provided to all ADC's by only one FPGA output pin.

B.7 External Power Supply

Table B.11 shows the signals of the extra +5 V power supply terminal J11. This terminal is directly connected to the +5 V and digital ground and can be used to power the entire DSK/ FPGA board system. This power terminal is also useful if the FPGA periphery control board is used as stand alone application without the C6713 DSK development board connected.

Pin	I/O	Signal	Description
1	I	+5 V	System Power
2	I	DGND	System Power

Table B.11: 5 V power supply (J11)

B.8 FPGA Programming Header

The 10-way 0.1 IDC header J12 is directly connected to the JTAG interface pins of the A3PE600 FPGA chip. This header is used to connect the FPGA programming device Flash Pro 3 [60]. It can also be used for connecting any other JTAG device interacting with the Actel FPGA chip.

B.9 Hardware Over Current Trip

The analogue input signal level of the analogue input channels 1, 2 and 3 are monitored by hardware comparators [98]. The threshold of the analogue signal level can be adjusted by a potentiometer on the PCB. The 6 comparator open collector outputs are connected together to a FPGA input pin equipped with a pull up resistor, creating a logical OR gate. This FPGA input pin can be analysed as hardware over current trip signal.

B.10 FPGA Circuit

The used Actel AP3E600 FPGA [59] is purely digital signal IC. With the selected package PQ 208 are 147 digital I/O pins available. Figure B.3 shows the how these digital I/O signals are used.

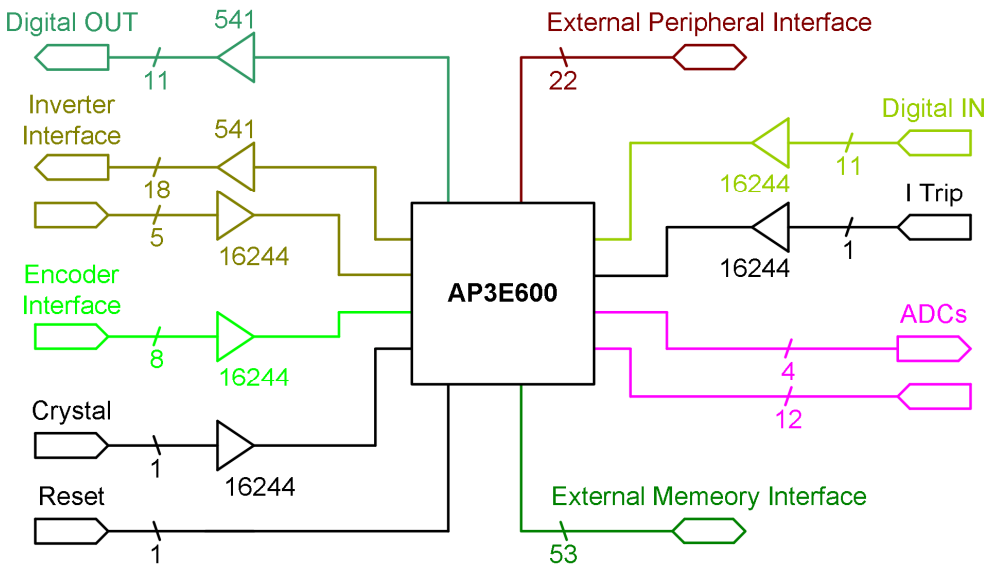

Figure B.3: FPGA signals

All FPGA I/O signals are 3.3 V LVTTL logic level. Buffers are used for the FPGA I/O protection and as level converters to 5 V TTL. The 16244 buffers convert any external 5 V TTL or 3.3 V LVTTL signal to the required 3.3 V LVTTL level. As output buffers are 541 (TTL family devices only, ABT, HCT, ACT) used to generate 5 V TTL level signals for all digital outputs. Table B.12 shows all signals connected to the FPGA IC.

Pin	I/O	Signal	Description
1	I	DGND	Power Supply
2	I	DGND	Power Supply
3	I	+3.3 V	Power Supply
4	O	DOUT bit 9	Digital Output bit 9
5	O	DOUT bit 10	Digital Output bit 10
6	O	DOUT bit 11	Digital Output bit 11

7	O	PWM 1	PWM Switching signal 1
8	O	PWM 2	PWM Switching signal 2
9	O	PWM 3	PWM Switching signal 3
10	O	PWM 4	PWM Switching signal 4
11	O	PWM 5	PWM Switching signal 5
12	O	PWM 6	PWM Switching signal 6
13	O	PWM 7	PWM Switching signal 7
14	O	PWM 8	PWM Switching signal 8
15	O	PWM 9	PWM Switching signal 9
16	I	+1.5 V	Power Supply
17	I	DGND	Power Supply
18	I	+3.3 V	Power Supply
19	O	PWM 10	PWM Switching signal 10
20	O	PWM 11	PWM Switching signal 11
21	O	PWM 12	PWM Switching signal 12
22	O	PWM 13	PWM Switching signal 13
23	O	PWM 14	PWM Switching signal 14
24	O	PWM 15	PWM Switching signal 15
25	I	DGND	Power Supply
26	I	CLK_board	On board crystal clock source
27	I	+1.5 V	Power Supply
28	O	PWM 16	PWM Switching signal 16

29	I	DGND	Power Supply
30	O	PWM 17	PWM Switching signal 17
31	O	PWM 18	PWM Switching signal 18
32	I	II_in 1	Inverter Interface Input signal 1
33	I	RST_board	On board reset circuit
34	I	II_in 2	Inverter Interface Input signal 2
35	I	II_in 3	Inverter Interface Input signal 3
36	I	+1.5 V	Power Supply
37	I	II_in 4	Inverter Interface Input signal 4
38	I	II_in 5	Inverter Interface Input signal 5
39	I	Encoder A	Encoder track A signal
40	I	+3.3 V	Power Supply
41	I	DGND	Power Supply
42	I	Encoder /A	Encoder track /A signal
43	I	Encoder B	Encoder track B signal
44	I	Encoder /B	Encoder track /B signal
45	I	Encoder Z	Encoder track Z signal
46	I	Encoder /Z	Encoder track /Z signal
47	I	Encoder S	Encoder track S signal
48	I	Encoder /S	Encoder track /S signal
49	I	ACE2# (EMI#78)	Chip enable 2
50	I	+3.3 V	Power Supply

51	I	DGND	Power Supply
52	I	DGND	Power Supply
53	I	+3.3 V	Power Supply
54	I	DGND	Power Supply
55	I	ACE3# (EMI#77)	Chip enable 3
56	O	AARDY (EMI#76)	EMIF asynchronous ready
57	I	AAOE# (EMI#75)	EMIF async output enable
58	I	AAWE# (EMI#74)	EMIF async write enable
59	I	AARE# (EMI#73)	EMIF async read enable
60	I/O	AED0 (EMI#70)	EMIF data pin 0
61	I/O	AED1 (EMI#69)	EMIF data pin 1
62	I	+3.3 V	Power Supply
63	I/O	AED2 (EMI#68)	EMIF data pin 2
64	I/O	AED3 (EMI#67)	EMIF data pin 3
65	I	DGND	Power Supply
66	I/O	AED4 (EMI#66)	EMIF data pin 4
67	I/O	AED5 (EMI#65)	EMIF data pin 5
68	I/O	AED6 (EMI#64)	EMIF data pin 6
69	I/O	AED7 (EMI#63)	EMIF data pin 7
70	I/O	AED8 (EMI#60)	EMIF data pin 8
71	I	+1.5 V	Power Supply
72	I	+3.3 V	Power Supply

73	I/O	AED9 (EMI#59)	EMIF data pin 9
74	I/O	AED10 (EMI#58)	EMIF data pin 10
75	I/O	AED11 (EMI#57)	EMIF data pin 11
76	I/O	AED12 (EMI#56)	EMIF data pin 12
77	I/O	AED13 (EMI#55)	EMIF data pin 13
78	I/O	AED14 (EMI#54)	EMIF data pin 14
79	I/O	AED15 (EMI#53)	EMIF data pin 15
80	I/O	AED16 (EMI#50)	EMIF data pin 16
81	I	DGND	Power Supply
82	I/O	AED17 (EMI#49)	EMIF data pin 17
83	I/O	AED18 (EMI#48)	EMIF data pin 18
84	I/O	AED19 (EMI#47)	EMIF data pin 19
85	I/O	AED20 (EMI#46)	EMIF data pin 20
86	I/O	AED21 (EMI#45)	EMIF data pin 21
87	I/O	AED22 (EMI#44)	EMIF data pin 22
88	I	+1.5 V	Power Supply
89	I	+3.3 V	Power Supply
90	I/O	AED23 (EMI#43)	EMIF data pin 23
91	I/O	AED24 (EMI#40)	EMIF data pin 24
92	I/O	AED25 (EMI#39)	EMIF data pin 25
93	I/O	AED26 (EMI#38)	EMIF data pin 26
94	I/O	AED27 (EMI#37)	EMIF data pin 27

95	I/O	AED28 (EMI#36)	EMIF data pin 28
96	I/O	AED29 (EMI#35)	EMIF data pin 29
97	I	DGND	Power Supply
98	I/O	AED30 (EMI#34)	EMIF data pin 30
99	I/O	AED31 (EMI#33)	EMIF data pin 31
100	I	DGND	Power Supply
101	I	TCK	JTAG Clock
102	I	TDI	Test Data Input
103	I	TMS	Test Mode Select
104	I	+3.3 V	Power Supply
105	I	DGND	Power Supply
106	I	Vpump	Programming Supply Voltage
107	I	DGND	Power Supply
108	O	TDO	Test Data Output
109	I	TRST	JTAG Test Reset
110	I	+3.3 V	Power Supply
111	I	+3.3 V	Power Supply
112	I	ABE0# (EMI#30)	EMIF byte enable 0
113	I	ABE1# (EMI#29)	EMIF byte enable 1
114	I	ABE2# (EMI#28)	EMIF byte enable 2
115	I	ABE3# (EMI#27)	EMIF byte enable 3
116	I	AEA2 (EMI#26)	EMIF address pin 2

117	I	AEA3 (EMI#25)	EMIF address pin 3
118	I	AEA4 (EMI#24)	EMIF address pin 4
119	I	AEA5 (EMI#23)	EMIF address pin 5
120	I	AEA6 (EMI#20)	EMIF address pin 6
121	I	AEA7 (EMI#19)	EMIF address pin 7
122	I	DGND	Power Supply
123	I	+3.3 V	Power Supply
124	I	RESET_DSK (EPI#59)	DSK System reset
125	I	AEA8 (EMI#18)	EMIF address pin 8
126		NC	
127	I	AEA9 (EMI#17)	EMIF address pin 9
128	I	AEA10 (EMI#16)	EMIF address pin 10
129	I	AEA11 (EMI#15)	EMIF address pin 11
130	I	DGND	Power Supply
131	I	+1.5 V	Power Supply
132	I	ECLKOUT (EPI#78)	EMIF Clock
133	I	DGND	Power Supply
134	I	AEA12 (EMI#14)	EMIF address pin 12
135	I	ADC12_SDO	Serial Data ADC12
136	I	ADC11_SDO	Serial Data ADC11
137	I	ADC10_SDO	Serial Data ADC10
138	I	ADC9_SDO	Serial Data ADC9

139	O	CONV_C	Convert Trigger Signal ADC Bank C
140	I	+3.3 V	Power Supply
141	I	DGND	Power Supply
142	I	+1.5 V	Power Supply
143	I	ADC8_SDO	Serial Data ADC8
144	I	ADC7_SDO	Serial Data ADC7
145	I	ADC6_SDO	Serial Data ADC6
146	I	ADC5_SDO	Serial Data ADC5
147	O	CONV_B	Convert Trigger Signal ADC Bank B
148	I	ADC4_SDO	Serial Data ADC4
149	I	ADC3_SDO	Serial Data ADC3
150	I	ADC2_SDO	Serial Data ADC2
151	I	ADC1_SDO	Serial Data ADC1
152	O	CONV_A	Convert Trigger Signal ADC Bank A
153	O	ADC_CLK	Serial Data Clock ADCs
154	I	+3.3 V	Power Supply
155	I	DGND	Power Supply
156	I	DGND	Power Supply
157	I	+3.3 V	Power Supply
158	I	DGND	Power Supply
159	I	I_TRIP	Hardware Over Current Trip (ADC 1,2,3)
160	I	DIN bit 11	Digital Input bit 11

161	I	DIN bit 10	Digital Input bit 10
162	I	DGND	Power Supply
163	I	DIN bit 9	Digital Input bit 9
164	I	DIN bit 8	Digital Input bit 8
165	I	DIN bit 7	Digital Input bit 7
166	I	DIN bit 6	Digital Input bit 6
167	I	DIN bit 5	Digital Input bit 5
168	I	DIN bit 4	Digital Input bit 4
169	I	DIN bit 3	Digital Input bit 3
170	I	+3.3 V	Power Supply
171	I	+1.5 V	Power Supply
172	I	DIN bit 2	Digital Input bit 2
173	I	DIN bit 1	Digital Input bit 1
174	I/O	CLKX1 (EPI#33)	McBSP1 transmit clock
175	O	CLKS1 (EPI#34)	McBSP1 clock source
176	I/O	FSX1 (EPI#35)	McBSP1 transmit frame sync
177	I	DX1 (EPI#36)	McBSP1 transmit data
178	I	DGND	Power Supply
179	I/O	CLKR1 (EPI#39)	McBSP1 receive clock
180	I/O	FSR1 (EPI#41)	McBSP1 receive frame sync
181	O	DR1 (EPI#42)	McBSP1 receive data
182	I	TOUT0 (EPI#45)	Timer 0 output

183	O	TINP0 (EPI#46)	Timer 0 input
184	O	EXT_INT5 (EPI#48)	External interrupt 5
185	I	TOUT1 (EPI#49)	Timer 1 output
186	I	+3.3 V	Power Supply
187	I	+1.5 V	Power Supply
188	O	TINP1 (EPI#50)	Timer 1 input
189	O	EXT_INT4 (EPI#53)	External interrupt 4
190	I	CNTL1 (EPI#63)	Daughtercard control 1
191	I	CNTL0 (EPI#64)	Daughtercard control 0
192	O	STAT1 (EPI#65)	Daughtercard status 1
193	O	STAT0 (EPI#66)	Daughtercard status 0
194	O	EXT_INT6 (EPI#67)	External interrupt 6
195	I	DGND	Power Supply
196	O	EXT_INT7 (EPI#68)	External interrupt 7
197	I	ACE3# (EPI#69)	Chip enable 3
198	O	DOUT bit8	Digital Output bit 8
199	O	DOUT bit7	Digital Output bit 7
200	I	+3.3 V	Power Supply
201	O	DOUT bit 6	Digital Output bit 6
202	O	DOUT bit 5	Digital Output bit 5
203	O	DOUT bit 4	Digital Output bit 4
204	O	DOUT bit 3	Digital Output bit 3

205	O	DOUT bit 2	Digital Output bit 2
206	O	DOUT bit 1	Digital Output bit 1
207	I	DGND	Power Supply
208	I	+3.3 V	Power Supply

Table B.12: FPGA AP3E600 pin connections

B.11 Schematics

Figures B.4 to B.10 show the schematics of the designed FPGA periphery control board. Figure B.5 shows also a fix that has been implemented on the prototype board. Two tracks are cut on the PCB and reconnected, indicated by the green lines. The dark green lines with the capture "Cut" show the position of the cut tracks. The light green lines show the reconnection implemented by some wires soldered on the prototype PCB.

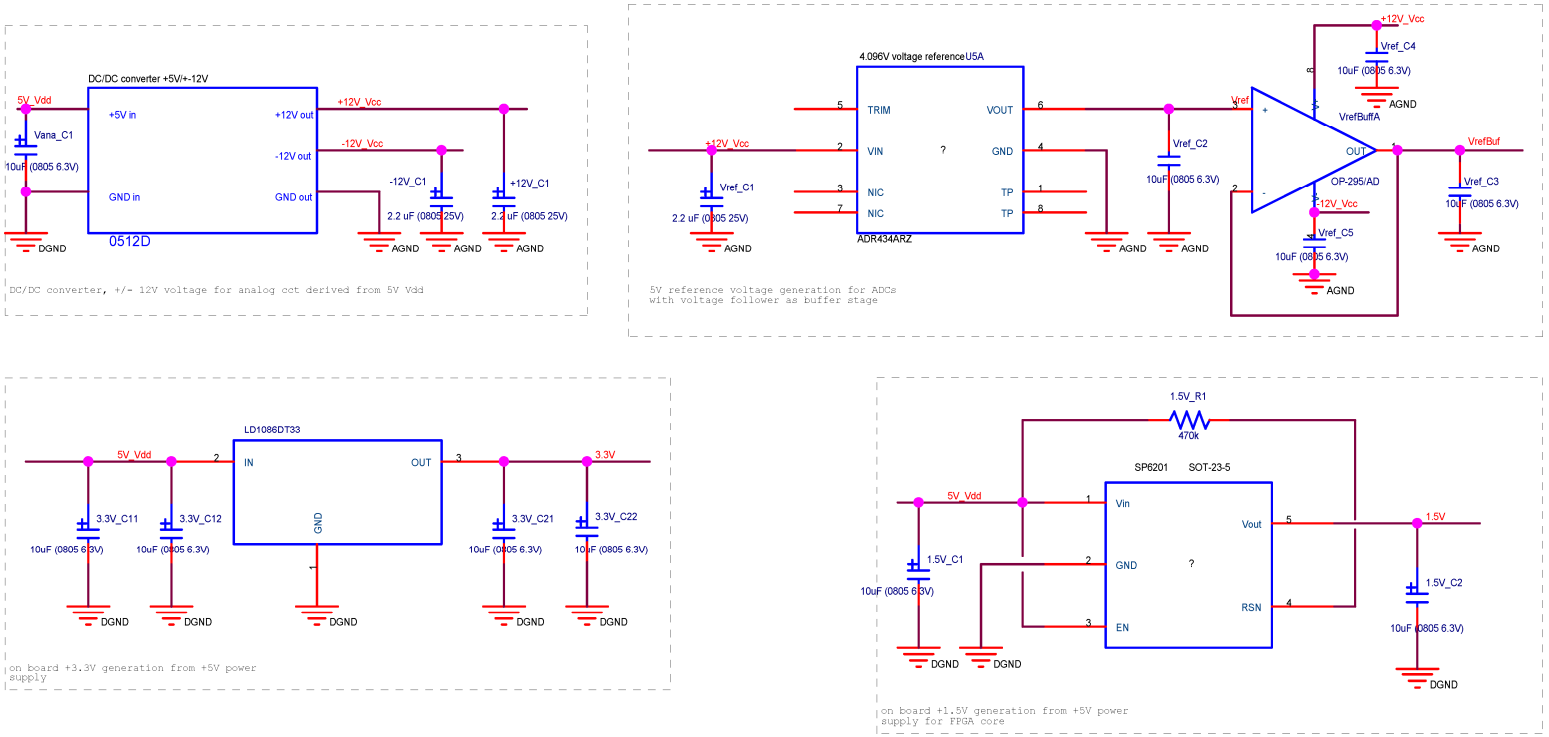

Figure B.4: Board voltage supply

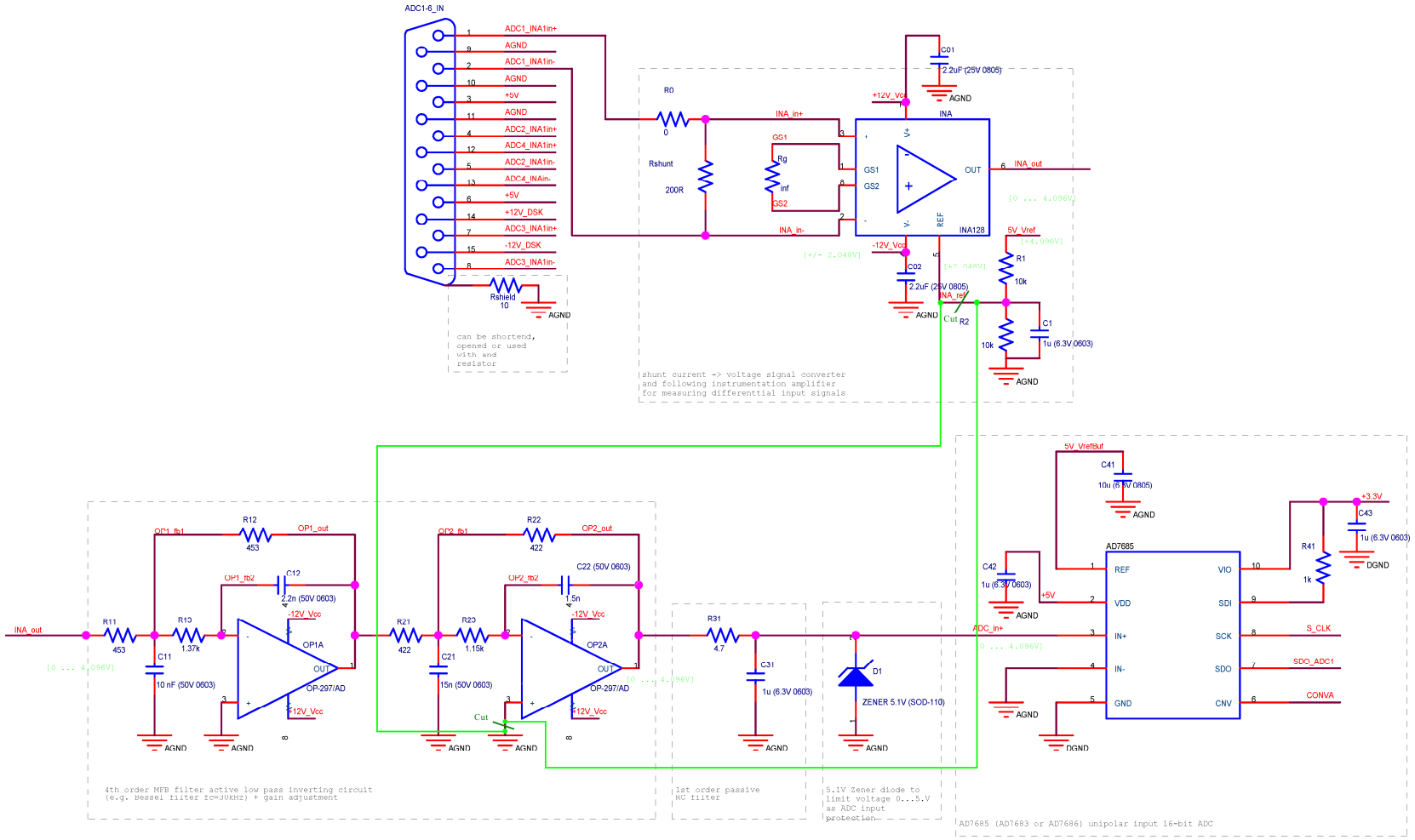

Figure B.5: Analogue inputs circuit

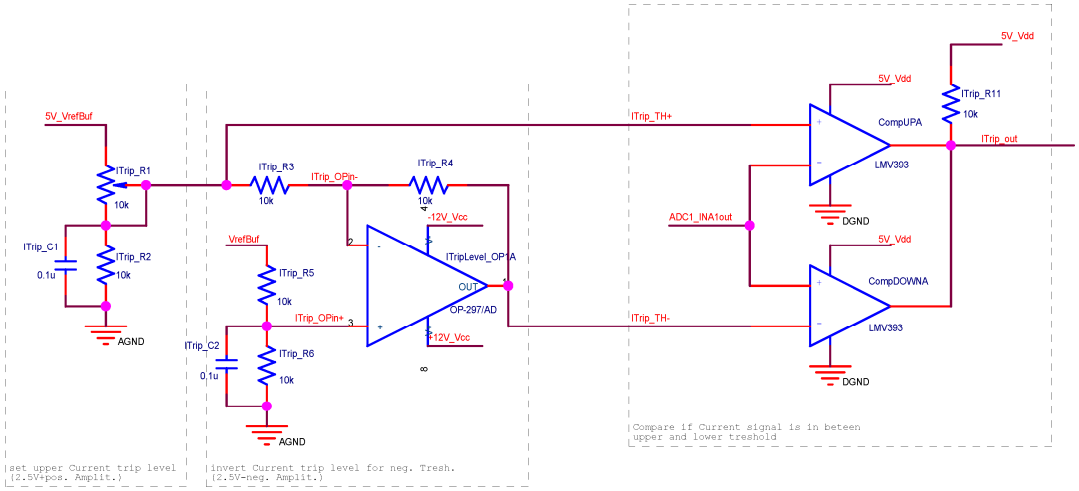

Figure B.6: Comparator circuit for over current detection

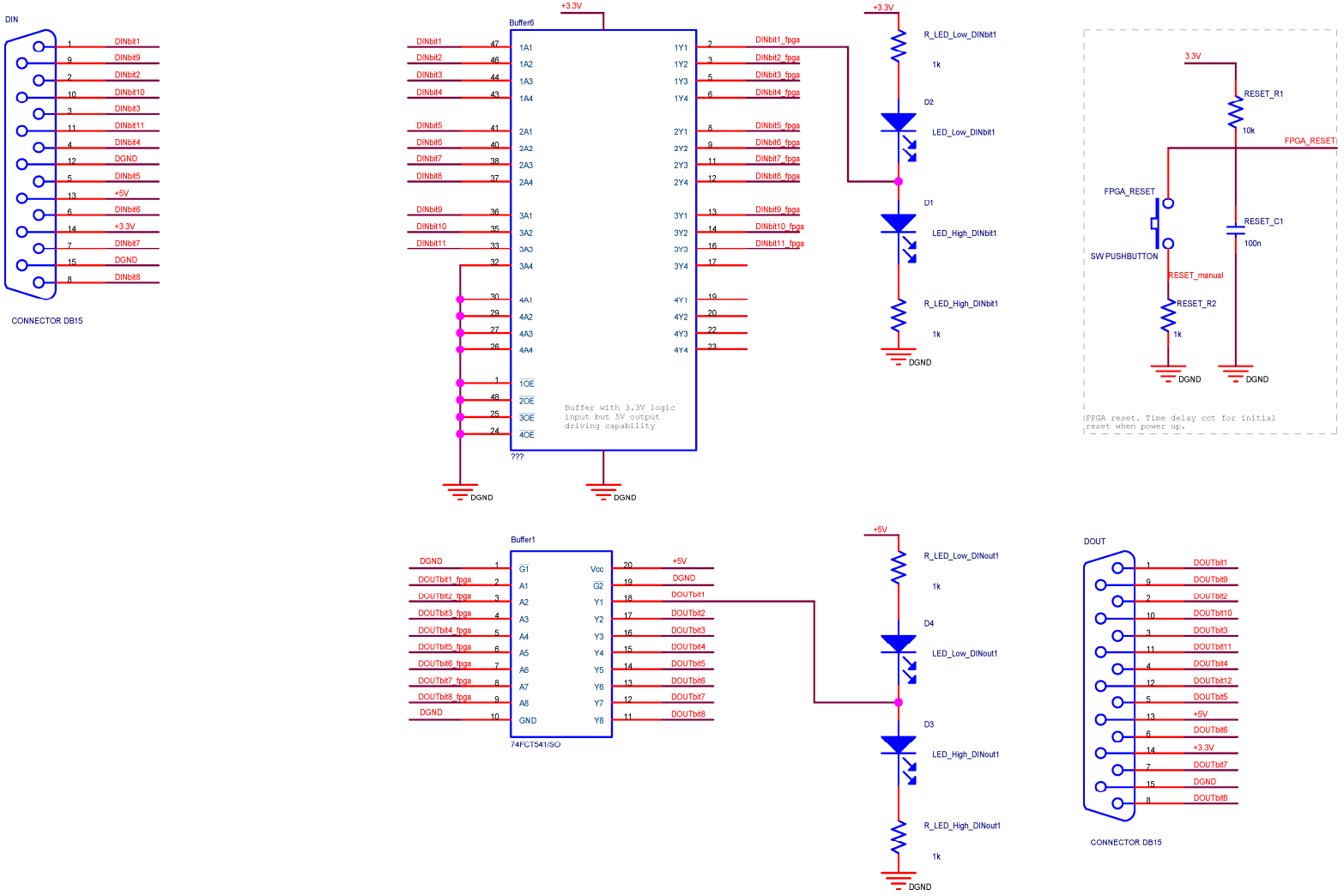

Figure B.7: Digital in and outputs

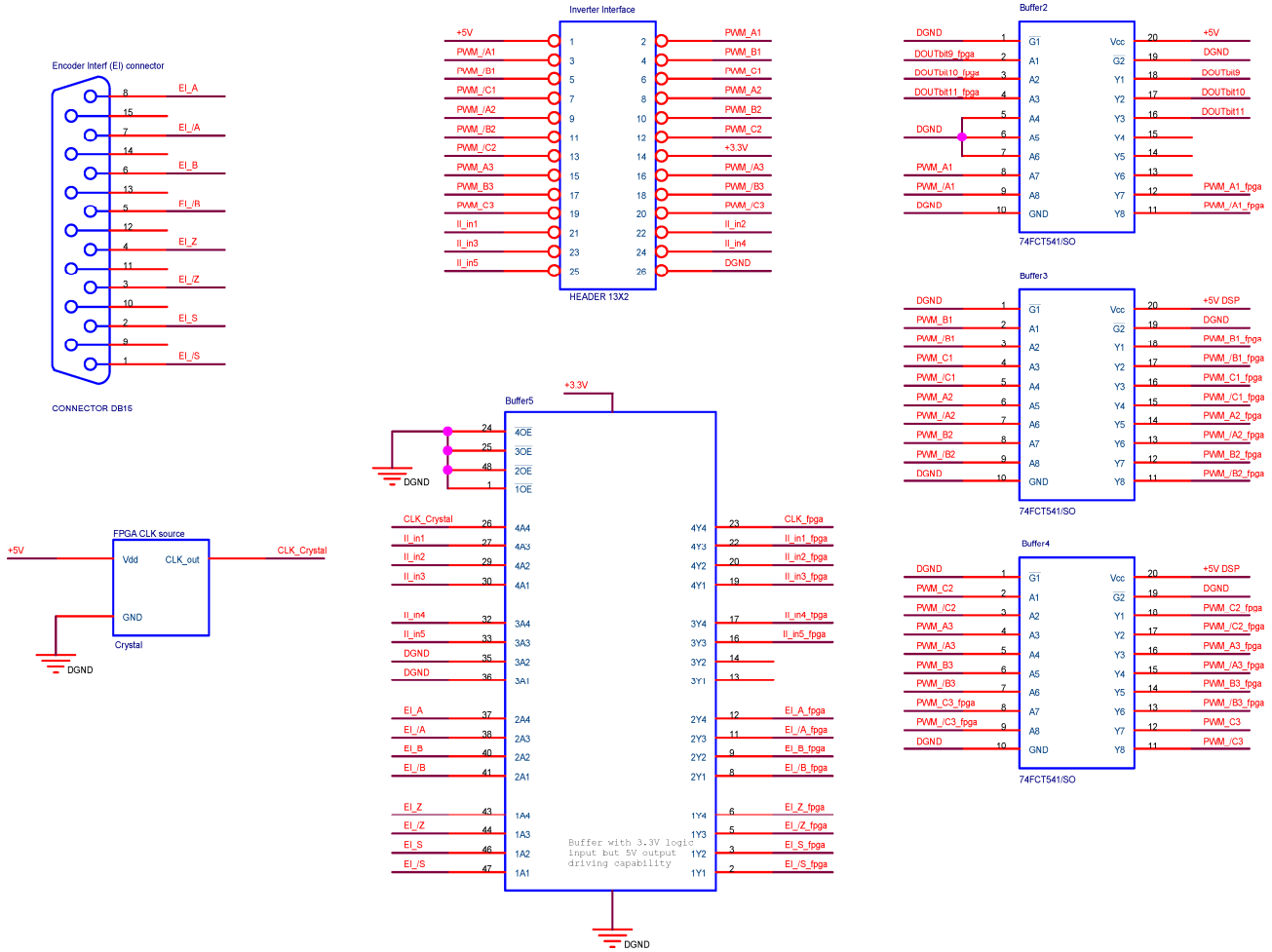

Figure B.8: Digital buffer IC's

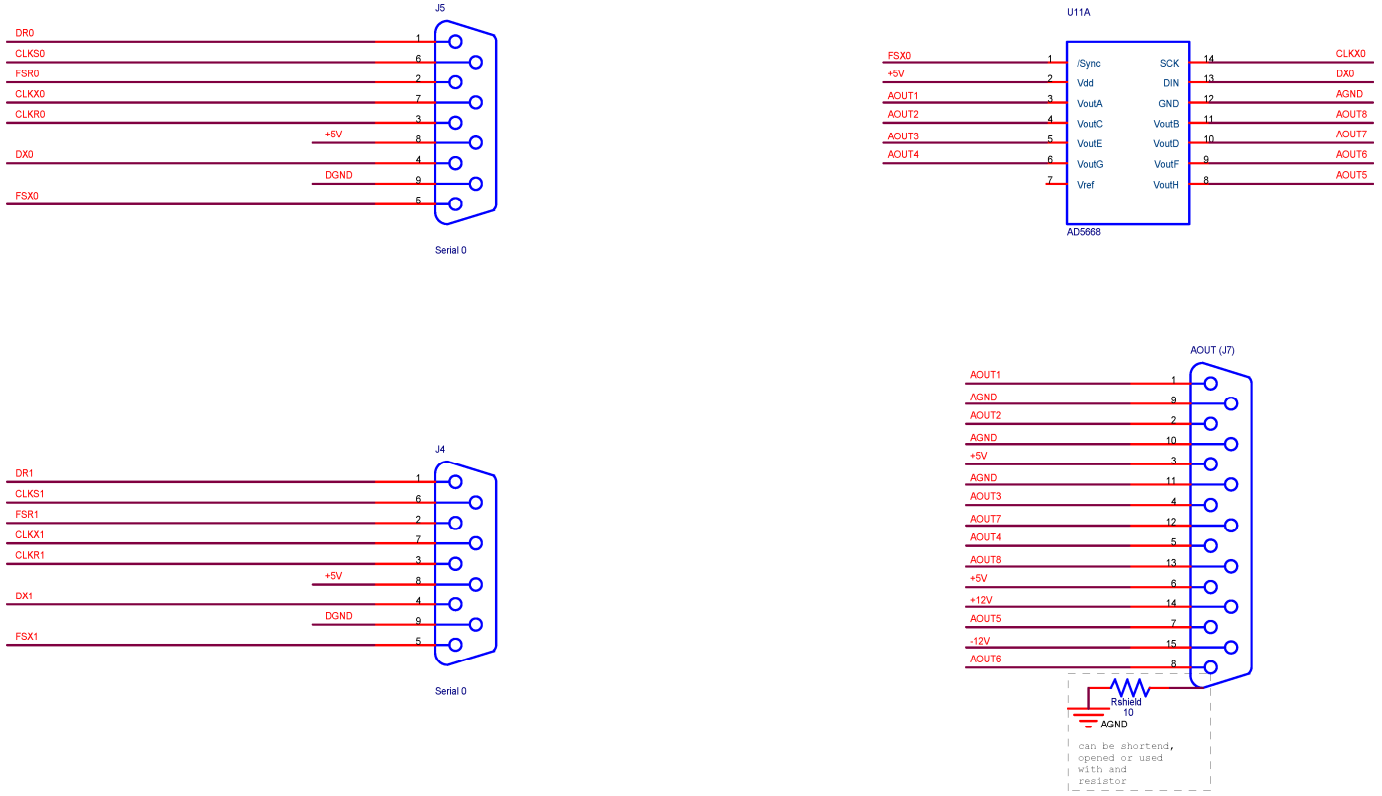

Figure B.9: Connectors

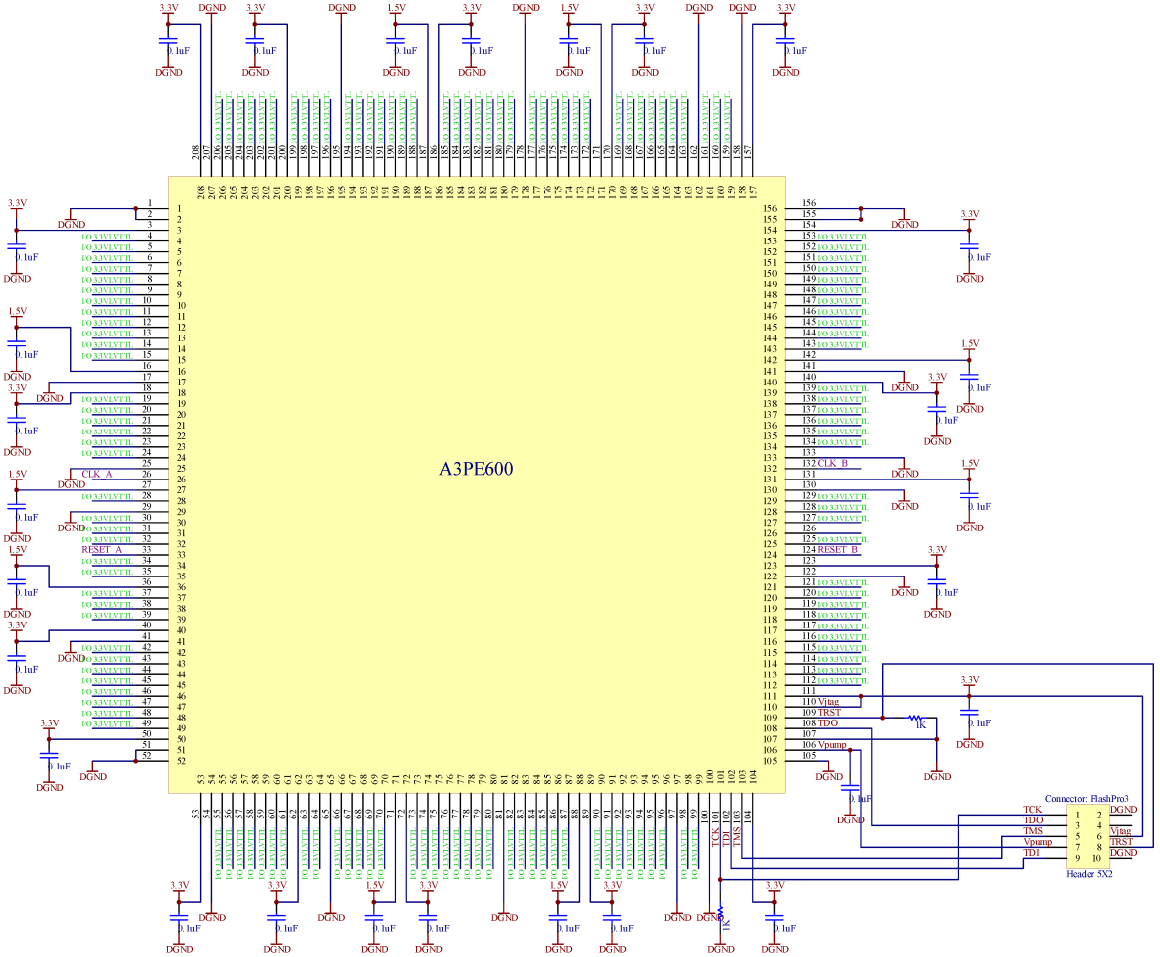

Figure B.10: FPGA (Actel A3PE600) circuit

Bibliography

[1] P. Vas, *Vector Control of AC Machines*. Oxford: Oxford University Press, 1990.

[2] K. Rajashekara, A. Kawamura, and K. Matsuse, *Sensorless Control of AC Motors*. New York: IEEE Press, 1996.

[3] J. Holtz, "Sensorless Control of Induction Machines—With or Without Signal Injection?," *IEEE Trans. Ind. Electron.*, vol. 53, no. 1, pp. 7-30, Feb. 2006.

[4] J. W. Finch and D. Giaouris, "Controlled AC Electrical Drives," *IEEE Trans. Ind. Electron.*, vol. 55, No. 2, pp. 481-491, Feb. 2008.

[5] M. W. Degner, "Flux, Position, and Velocity Estimation in AC Machines Using Carrier Signal Injection," University of Wisconsin-Madison, 1998.

[6] N. Teske, "Sensorless Position Control of Induction Machines using High Frequency Signal Injection," PhD. Thesis, Department of Electrical and Electronic Engineering, University of Nottingham, Nottingham, UK, 2001.

[7] D. O'Kelly and S. Simmons, *Introduction to Generalized Electrical Machine Theory*. Maidenhead: McGraw- Hill, 1968.

[8] D. W. Novotny and T. A. Lipo, *Vector Control and Dynamics of AC Drives*. Oxford: Oxford University Press, 1996.

[9] W. Leonhard, *Control of Electrical Drives*: Springer Verlag, 1985.

[10] J. Holtz, "Sensorless control of induction motor drives," *Proceedings of the IEEE*, vol. 90, no. 8, pp. 1359-1394, Aug. 2002.

[11] O. Nelles, *Nonlinear system identification*: Springer, 2001.

[12] B. K. Bose, *Power Electronics and Variable Frequency Drives*, 1st ed. New York: IEEE Press, 1996.

[13] G. Asher, "Vector Control of Induction Motor Drives," University of Nottingham, 2003.

[14] J. Holtz and J. Quan, "Sensorless Vector Control of Induction Motors at Very Low Speed Using a Nonlinear Inverter Model and Parameter Identification," *IEEE Trans. Ind. Appl.*, vol. 38, no. 4, pp. 1087-1094, July-Aug. 2002.

[15] G. Guidi and H. Umida, "A Sensorless Induction Motor Drive For Low Speed Applications Using a Novel Stator Resistance Estimation Method," in *Proc. IEEE IAS Annu. Meeting*, Phoenix, USA, pp. 180-186, Oct. 3.–7., 1999.

[16] K. Akatsu and A. Kawamura, "Sensorless Very Low-Speed and Zero-Speed Estimations with Online Rotor Resistance Estimation of Induction Motor Without Signal Injection," *IEEE Trans. Ind. Appl.*, vol. 36, no. 3, pp. 764-771, May/June 2000.

[17] K.-W. Lee, D.-H. Jung, and H. I.-J., "An Online Identification Method for Both Stator Resistance and Back-EMF Coefficient of PMSMs Without Rotational Transducers," *IEEE Trans. Ind. Electron.*, vol. 51, no. 2, pp. 507-510, Apr. 2004.

[18] J. Holtz and J. Quan, "Drift- and Parameter-Compensated Flux Estimator for Persistent Zero-Stator-Frequency Operation of Sensorless-Controlled Induction Motors," *IEEE Trans. Ind. Appl.*, vol. 39, no. 4, pp. 1052-1060, July/Aug. 2003.

[19] J. Cilia, "Sensorless Speed and Position Control of Induction Motor Drives," PhD. Thesis, Department of Electrical and Electronic Engineering, University of Nottingham, 1997.

[20] M. W. Degner and R. D. Lorenz, "Using Multiple Saliencies for the Estimation of Flux, Position, and Velocity in AC Machines," *IEEE Trans. Ind. Appl.*, vol. 34, no. 5, pp. 1097-1104, Sept./Oct. 1998.

[21] N. Teske, G. M. Asher, M. Sumner, and K. J. Bradley, "Suppression of Saturation Saliency Effects for the Sensorless Position Control of Induction Motor Drives Under Loaded Conditions," *IEEE Transactions on Industrial Electronics*, vol. 47, No. 5, pp. 1142-1150, Oct. 2000.

[22] N. Teske, G. M. Asher, M. Sumner, and K. J. Bradley, "Analysis and Suppression of High-Frequency Inverter Modulation in Sensorless Position-Controlled Induction Machine Drives," *IEEE Trans. Ind. Appl.*, vol. 39, no. 1, pp. 10-18, Jan./Feb. 2003.

[23] C. Caruana, "Sensorless Vector Control of Cage Induction Machines using Signal Injection Techniques," PhD. Thesis, Department of Electrical and Electronic Engineering, University of Nottingham, Nottingham, UK, 2003.

[24] C. Caruana, G. M. Asher, and M. Sumner, "Performance of HF Signal Injection Techniques for Zero-Low-Frequency Vector Control of Induction Machines Under Sensorless Conditions," *IEEE Trans. Ind. Appl.*, vol. 53, no. 1, pp. 225-238, Sept./Oct. 2006.

[25] Q. Gao, G. Asher, and M. Sumner, "Sensorless Position and Speed Control of Induction Motors Using High-Frequency Injection and Without Offline Precommissioning," *IEEE Trans. Ind. Electron.*, vol. 54, no. 5, pp. 2474-2481, Oct. 2007.

[26] C. Caruana, G. M. Asher, and J. C. Clare, "Sensorless Flux Position Estimation at Low and Zero Frequency by Measuring Zero-Sequence Current in Delta-Connected Cage Induction Machines," *IEEE Trans. Ind. Appl.*, vol. 41, no. 2, pp. 609-617, Mar./Apr. 2005.

[27] M. W. Degner and R. D. Lorenz, "Position Estimation in Induction Machines Utilizing Rotor Bar Slot Harmonics and Carrier-Frequency Signal Injection," *IEEE Trans. Ind. Appl.*, vol. 36, no. 3, pp. 736-742, May/June 2000.

[28] N. Teske, G. M. Asher, M. Sumner, and K. J. Bradley, "Encoderless Position Control of Induction Machines," in *Proc. EPE*, Graz, Austria, 2001.

[29] N. Teske, G. M. Asher, M. Sumner, and K. J. Bradley, "Analysis and Suppression of Inverter Clamping Saliency in Sensorless Position Controlled Induction Machine Drives," in *Proc. Industry Applications Annual Meeting*, Chicago, USA, 2001.

[30] N. Teske, G. M. Asher, M. Sumner, and K. J. Bradley, "Encoderless Position Estimation for Symmetric Cage Induction Machines Under Loaded Conditions," *IEEE Trans. Ind. Appl.*, vol. 37, no. 6, pp. 1793-1800, Nov./Dec. 2001.

[31] F. Briz, A. Diez, and M. W. Degner, "Dynamic Operation of Carrier-Signal-Injection-Based Sensorless Direct Field-Oriented AC Drives," *IEEE Transactions on Industry Applications*, vol. 36, no. 5, pp. 1360-1368, Sept.-Oct. 2000.

[32] F. Briz, M. W. Degner, A. Diez, and R. D. Lorenz, "Measuring, Modeling, and Decoupling of Saturation-Induced Saliencies in Carrier-Signal Injection-Based Sensorless AC Drives," *IEEE Transactions on Industry Applications*, vol. 37, No. 5, pp. 1356-1364, Sept.-Oct. 2001.

[33] F. Briz, M. W. Degner, A. Diez, and R. D. Lorenz, "Static and Dynamic Behavior of Saturation-Induced Saliencies and Their Effect on Carrier-Signal-Based Sensorless AC Drives," *IEEE Transactions on Industry Applications*, vol. 38, No. 3, pp. 670-678, May-June 2002.

[34] J. M. Guerrero, et al., "Inverter Nonlinearity Effects in High-Frequency Signal-Injection-Based Sensorless Control Methods," *IEEE Trans. Ind. Appl.*, vol. 41, No.2, pp. 618-626, Mar./Apr. 2005.

[35] P. L. Jansen and R. D. Lorenz, "Transducerless Position and Velocity Estimation in Induction and Salienct AC Machines," *IEEE Trans. Ind. Appl.*, vol. 31, No. 2, pp. 240-247, March/April 1995.

[36] A. Consoli, G. Scarcella, and A. Testa, "Industry Application of Zero-Speed Sensorless Control Techniques for PM Synchronous Motors," *IEEE Trans. Ind. Appl*, vol. 37, No. 2, pp. 513-520, Mar/Apr 2001.

[37] A. Consoli, G. Scarcella, and A. Testa, "A New Zero-Frequency Flux-Position Detection Approach for Direct-Field-Oriented-Control Drives," *IEEE Trans. Ind. Appl*, vol. 36, No. 3, pp. 797-804, May/June 2000.

[38] F. Briz, W. Degner, P. García, and J. M. Guerrero, "Rotor Position Estimation of AC Machines Using the Zero-Sequence Carrier-Signal Voltage," *IEEE Trans. Ind. Appl.*, vol. 41, no. 6, pp. 1637-1646, Nov./Dec. 2005.

[39] A. Consoli, G. Scarcella, A. Testa, and T. A. Lipo, "Air-gap flux position estimation of inaccessible neutral induction machines by zero sequence voltage," *Elect. Mach. Power Syst.*, vol. 30, No. 1, pp. 77–88, Jan. 2002.

[40] F. Briz, W. Degner, P. G. Fernández, and A. B. Diez, "Rotor and Flux Position Estimation in Delta-Connected AC Machines Using the Zero-Sequence Carrier-Signal Current," *IEEE Trans. Ind. Appl.*, vol. 42, no. 2, pp. 495-503, March-April 2006.

[41] J.-i. Ha and S.-K. Sul, "Sensorless Field-Orientation Control of an Induction Machine by High-Frequency Signal Injection," *IEEE Trans. Ind. Appl.*, vol. 35, no.1, pp. 45-51, Jan./Feb. 1999.

[42] M. J. Corley and R. D. Lorenz, "Rotor Position and Velocity Estimation for a Salient-Pole Permanent Magnet Synchronous Machine at Standstill and High Speeds," *IEEE Trans. Ind. Appl.*, vol. 34, no. 4, pp. 784-789, July-Aug. 1998.

[43] J.-H. Jang, et al., "Sensorless Drive of Surface-Mounted Permanent-Magnet Motor by High-Frequency Signal Injection Based on Magnetic Saliency," *IEEE Trans. Ind. Appl.*, vol. 39, no. 4, pp. 1031-1038, July-Aug. 2003.

[44] M. Linke, R. Kennel, and J. Holtz, "Sensorless position control of permanent magnet synchronous machines without limitation at zero speed," in *Proc. IECON*, Sevilla, Spain, pp. 674 - 679, 2002.

[45] J. Holtz, "Acquisition of Position Error and Magnet Polarity for Sensorless Control of PM Synchronous Machines," *IEEE Trans. Ind. Appl.*, vol. 44, no. 4, pp. 11721180, July/Aug. 2008.

[46] R. Kennel, "Tutorial: Sensorless Motor Drives," York, UK, 2.-4. April.

[47] M. Schroedl, "Sensorless Control of AC Machines at Low Speed and Standstill Based on the "INFORM" Method," in *Proc. IEEE IAS Annu. Meeting*, San Diego, CA, pp. 270-277, Oct. 6.-10., 1996.

[48] E. Robeischl and M. Schroedl, "Optimized INFORM Measurement Sequence for Sensorless PM Synchronous Motor Drives With Respect to Minimum Current Distortion," *IEEE Trans. Ind. Appl.*, vol. 40, no. 2, pp. 591-598, Mar./Apr. 2004.

[49] J. Holtz, "Sensorless Position Control of Induction Motors—An Emerging Technology," *IEEE Trans. Ind. Electron.*, vol. 45, no. 6, pp. 840-852, Dec. 1998.

[50] J. Holtz and H. Pan, "Elimination of Saturation Effects in Sensorless Position-Controlled Induction Motors," *IEEE Trans. Ind. Appl.*, vol. 40, no. 2, pp. 623-631, Mar./Apr. 2004.

[51] J. Holtz and H. Pan, "Acquisition of Rotor Anisotropy Signals in Sensorless Position Control Systems," *IEEE Trans. Ind. Appl.*, vol. 40, no. 5, pp. 1377-1387, Sep./Oct. 2004.

[52] J. Holtz and J. Juliet, "Sensorless Acquisition of the Rotor Position Angle of Induction Motors With Arbitrary Stator Windings," *IEEE Trans. Ind. Appl.*, vol. 41, no. 6, pp. 1675-1682, Nov./Dec. 2005.

[53] Q. Gao, G. M. Asher, M. Sumner, and P. Makys, "Position Estimation of AC Machines Over a Wide Frequency Range Based on Space Vector PWM Excitation," *IEEE Trans. Ind. Appl.*, vol. 43, no. 4, pp. 1001-1011, July/Aug. 2007.

[54] P. García, F. Briz, M. W. Degner, and D. Díaz-Reigosa, "Accuracy, Bandwidth, and Stability Limits of Carrier-Signal-Injection-Based Sensorless Control Methods," *IEEE Trans. Ind. Appl.*, vol. 43, no. 4, pp. 990-999, July/Aug. 2007.

[55] "TMS320C6713 DSK DSP Development Systems," Spectrum Digital, Technical Reference

[56] "TMS320C6713 Floating-Point Digital Signal Processor," Texas Instruments, Data Sheet

[57] "Synchronous DRAM MT48LC2M32B2," Micron, Data Sheet

[58] "Code Composer Studio," Texas Instruments, 3.1.0

[59] "ProASIC3E Flash Family FPGAs," Actel

[60] "In-System Programming (ISP) in ProASIC3/E Using FlashPro3," Actel

[61] "Libero IDE," Actel Corporation, 7.0.0.11

[62] "AD7686, 16-Bit, 500 kSPS PulSAR ADC in MSOP/QFN," Analog Devices, Data Sheet

[63] "Precision, Low Power INSTRUMENTATION AMPLIFIERS INA128, INA129," Burr Brown, Data sheet

[64] "OPA228, High Precision, Low Noise OPERATIONAL AMPLIFIERS," Texas Instruments, Data sheet

[65] "Texas Instruments DSK to USB 2.0 Daughtercard," Avnet, User Guide

[66] "CY7C68001, EZ-USB SX2™ High-Speed USB Interface Device," Cypress Semiconductor Corporation, Data Sheet

[67] "Dev-C++," Bloodshed Software, 4.9.9.0

[68] "584 S," Eurothern Drives, Manual

[69] "Current Transducer LAH-25NP," LEM, Data Sheet

[70] "HAMEG probes," Hameg, Data Sheet

[71] M. Apap, "Vector Control of a Permanent Magnet Synchronous Machine," MSc. Thesis, Department of Electrical Power and Control, University of Malta, 2001.

[72] "DCS Thyristor power converter," ABB, Manual

[73] "Drive Window Light," ABB

[74] R. Raute, et al., "A Zero Speed Operation Sensorless PMSM Drive Without Additional Test Signal Injection," in *Proc. EPE*, Aalborg, Denmark, pp. CD-ROM, 2-5 Sept., 2007.

[75] R. Raute, et al., "Operation of a Sensorless PMSM Drive Without Additional Test Signal Injection," in *Proc. PEMD*, York, UK, pp. 616-620, 2-4 April 2008, 2008.

[76] S. Nakashima, Y. Inagaki, and I. Miki, "Sensorless Initial Rotor Position Estimation of Surface Permanent-Magnet Synchronous Motor," *IEEE Trans. Ind. Appl.*, vol. 36, no. 6, pp. 1598-1603, Nov./Dec. 2000.

[77] M. Tursini, R. Petrella, and F. Parasiliti, "Initial Rotor Position Estimation Method for PM Motors," *IEEE Trans. Ind. Appl.*, vol. 39, no. 6, pp. 1630-1640, Nov./Dec. 2003.

[78] H. Kim, K.-K. Huh, R. D. Lorenz, and T. M. Jahns, "A Novel Method for Initial Rotor Position Estimation for IPM Synchronous Machine Drives," *IEEE Trans. Ind. Appl.*, vol. 40, no. 5, pp. 1369-1378, Sep./Oct. 2004.

[79] Y.-S. Jeong, R. D. Lorenz, T. M. Jahns, and S.-K. Sul, "Initial Rotor Position Estimation of an Interior Permanent-Magnet Synchronous Machine Using Carrier-Frequency Injection Methods," *IEEE Trans. Ind. Appl.*, vol. 41, no. 1, pp. 38-45, Jan./Feb. 2005.

[80] J. B. Bartolo, C. Spiteri Staines, and C. Caruana, "An Investigation on the Performance of Current Derivative Sensors for the Sensorless Control of A.C. Drives," in *Proc. PEMD*, York, UK, pp. 532-536, 2008.

[81] T. M. Wolbank, J. L. Machl, and H. Hauser, "Closed-Loop Compensating Sensors Versus New Current Derivative Sensors for Shaft-Sensorless Control of Inverter Fed Induction Machines," *IEEE Trans. Instrum. and Measurem.*, vol. 53, no. 4, pp. 1311-1315, Aug. 2004.

[82] R. Raute, et al., "Inverter Non-linearity Effects on a Sensorless PMSM Drive Without Additional Test Signal Injection and Zero Speed Operation," in *Proc. IEEE ISIE*, Cambridge, pp. 552-557, 30.June-2.July, 2008.

[83] TOSHIBA, "MG25Q6ES42," Data sheet, 3. Mar. 1997, Available: www.alldatasheet.com.

[84] R. Raute, et al., "Impedance saliency detection for sensorless control of AC machines utilizing existing PWM switching harmonics," in *Proc. PEMD*, York, UK, pp. 557-561, 2-4 April 2008, 2008.

[85] H.-J. Bartsch, *Taschenbuch Mathematischer Formeln*. Leipzig: Fachbuchverlag Leipzig, 1999.

[86] "Three-Phase Sine-Wave Generation using the PWM Unit of the ADMC331," Analog Devices, Application Note, Application Note AN331-03, Jan.

[87] A. Consoli, G. Scarcella, G. Tutino, and A. Testa, "Sensorless Field Oriented Control Using Common Mode Currents," in *Proc. IEEE IAS Annu. Meeting*, Rome, Italy, pp. 1866-1873, Oct. 8-12, 2000.

[88] P. Vas, *Electrical Machines and Drives, A Space- Vector Theory Approach*, 1 ed. Oxford: Oxford Science Publications, 1992.

[89] T. Mathworks, "Matlab," 7

[90] "TINA for Windows, The Complete Electronic Lab," Texas Instruments, 6.02.002SF-TI

[91] R. Raute, et al., "Sensorless Control of Induction Machines by Using PWM Harmonics for Rotor Bar Slotting Detection," in *Proc. IEEE IAS Annu. Meeting*, Edmonton, Canada, pp. CD-ROM, 5-9 Oct., 2008.

[92] G.-C. Hsieh and J. C. Hung, "Phase-Locked Loop Techniques- A Survey," *IEEE Trans. Ind. Electron.*, vol. 43, No. 6, pp. 609-615, Dec. 1996.

[93] F. M. Gardner, *Phaselock Techniques*. New York, 1979.

[94] "Fluke 39/41B Power Harmonics Tester," Fluke, Users Manual

[95] *IEEE Standard Test Procedure for Polyphase Induction Motors and Generators*: IEEE, 2004.

[96] "74ABT541," Philips, Data Sheet

[97] FTDI, "FT2232C Dual USB UART/FIFO I.C., DS2232C Version 1.3," Future Technology Devices International Ldt.

[98] "LMV393," National Semiconductor, Data Sheet